ABSTRACT

Title of dissertation: INVESTIGATING THE ORIGIN OF GAMMA-RAY EMISSION IN NON-BLAZAR AGN WITH THE FERMI LARGE AREA TELESCOPE

William Francis McConville, Doctor of Philosophy, 2014

Dissertation directed by: Professor Julie McEnery
Department of Physics

The Fermi Large Area Telescope (Fermi-LAT) has detected a small sample of γ-ray loud non-blazar Active Galactic Nuclei (AGN), including the so-called misaligned AGN, whose radio jets are believed to be pointed off-axis with respect to the observer's line of sight, in contrast to the far more populous γ-ray loud blazars, whose jets are pointed directly toward the line of sight of the observer. The origin of the γ-ray emission in these misaligned sources has been widely attributed to the so-called "blazar zone" under the pretense of AGN unification, in which the misaligned Fanaroff-Riley type I and II objects are purported to make up the parent population of the BL Lac and FSRQ blazars, respectively. For a number of misaligned sources, the observations prove to be consistent under this scenario, in that the sources demonstrate short timescale γ-ray variability, thus confining the emission region to a size scale consistent with the inner parsec-scale regions of the jet.

Representing an even smaller percentage of non-blazar sources are those that

exhibit no evidence of variable γ-ray emission over timescales of > 3 years. Steady high energy (HE) emission over these timescales, if proven to be statistically significant, relaxes the constraint that would place the γ-ray emission within a < 1 parsec region consistent with the size scale of the blazar zone. Three sources in particular that have demonstrated no evidence of variability in the LAT range are 4C +55.17, Fornax A, and M87. Each of these objects further demonstrates a unique set of multiwavelength properties that could potentially give rise to γ-ray emission that is produced outside of the blazar zone. In this thesis, I conduct a detailed investigation into the origin of γ-rays from each of these objects, and I discuss the multiwavelength properties that could give rise to a steady γ-ray component consistent with non-blazar emission. Further improvements in LAT analysis techniques are also briefly discussed.

INVESTIGATING THE ORIGIN OF GAMMA-RAY EMISSION IN NON-BLAZAR AGN WITH THE FERMI LARGE AREA TELESCOPE

by

William Francis McConville

Dissertation submitted to the Faculty of the Graduate School of the
University of Maryland, College Park in partial fulfillment
of the requirements for the degree of
Doctor of Philosophy
2014

Advisory Committee:
Professor Jordan Goodman, Chair, Department of Physics
Professor Julie McEnery, Co-chair/Advisor, Department of Physics
Professor Cole Miller, Department of Astronomy
Professor Peter Shawhan, Department of Physics
Professor Kara Hoffman, Department of Physics

For my parents.

Acknowledgments

Thank you to all who have lent their support and encouragement toward the completion of this thesis, from my co-workers, to my family and friends. I truly am fortunate to have you in my life.

In particular, I wish first and foremost to thank my advisor, Julie McEnery, for her unrelenting support and encouragement. I couldn't have asked for a more personable, intelligent, and supportive advisor as you have been to me. You were there for me through thick and thin, and I owe you my thanks both as a professional and as a colleague and friend.

Secondly, I wish to thank Teddy Cheung, for being such an important influence and mentor in much of my early work as a graduate student. Your insight and extensive knowledge across such a diverse spectrum of astronomical fields was truly an inspiration to me, and this played a key role in guiding me toward much of the work that is presented in this thesis.

I also wish to thank Lukasz Stawarz for his collaborative work during my time as a graduate student. I learned a great deal from the discussions that we had over particular sources, and although we've only had a few chances to speak in person, I feel as if we've worked together in the same building for years. You were always there to answer emails, and to discuss many details of AGN physics that would seek to answer even the most subtle of questions.

In addition, I would like to thank Jeremy Perkins and Dave Thompson for your helpful comments with regard to this thesis, and for always being there to

offer your help and support. Your encouragement, especially toward the final throes of my thesis writing, was tremendously important, and for that I can't thank you enough.

I'd also like to thank Sylvia Zhu and David Green, for your supply of life-saving cookies during some of the most critical junctions of my career as a graduate student. Your friendship was an essential ingredient in the completion of this thesis.

I'd also like to thank the members of my committee, for taking the time from your busy schedules to read my thesis and to offer to sit in on my defense.

Lastly, I'd like to thank my parents, for their love and support.

Table of Contents

List of Tables ix

List of Figures x

List of Abbreviations xvii

1 Introduction 1
1.1 History of γ-ray Astronomy . . . 1
1.2 Physical & Radiative Processes in γ-ray Astronomy . . . 2
1.2.0.1 Synchrotron Radiation . . . 3
1.2.0.2 Compton Scattering . . . 6
1.2.0.3 Bremsstrahlung Radiation . . . 9
1.2.0.4 Particle Acceleration . . . 10
1.2.0.5 Pair Production . . . 11
1.2.0.6 Electromagnetic Cascades . . . 13
1.2.0.7 Čerenkov Radiation . . . 13
1.3 Detecting γ-rays . . . 14
1.3.1 Space-based . . . 14
1.3.2 Ground-based . . . 16
1.3.2.1 Atmospheric Čerenkov Telescopes . . . 16
1.3.2.2 Extensive Air Shower Arrays . . . 18
1.4 Organization of the Thesis . . . 18

2 The Astrophysics of Active Galactic Nuclei 20
2.1 AGN Paradigm . . . 20
2.1.1 Black Hole & Accretion Disk . . . 20
2.1.2 Torus & Broad / Narrow Line Regions . . . 20
2.1.3 Jets . . . 22
2.1.4 Relativistic Doppler Boosting . . . 22
2.1.5 Giant Radio Bubbles . . . 25
2.2 Taxonomy of AGN . . . 25
2.2.1 Radio Quiet AGN: Seyferts & QSO's . . . 28
2.2.2 Radio Loud AGN . . . 29
2.2.2.1 Radio Galaxies . . . 29
2.2.2.2 Broad Line Radio Galaxies & Radio Loud Quasars . . . 29
2.2.2.3 Radio Loud Narrow-Line Seyfert 1 Galaxies . . . 31
2.2.2.4 Blazars . . . 31
2.2.2.5 Young Radio Sources (CSO / MSO / CSS / GPS Sources) . . . 32
2.2.3 SED Classification & The Blazar Sequence . . . 34
2.3 Models of Gamma-ray Emission from AGN . . . 36
2.3.1 Synchrotron Self-Compton Radiation . . . 36
2.3.2 External Compton Process . . . 38

2.3.3 Proton Based Models . . . 40
2.3.4 Spectral Attenuation in AGN . . . 40
2.3.4.1 Internal $\gamma\gamma$ Absorption . . . 41
2.3.4.2 External Absorption and the Extragalactic Background Light . . . 42

3 The Fermi Gamma-ray Space Telescope Large Area Telescope 44
3.1 Fermi Large Area Telescope Design . . . 44
3.1.1 LAT Modular Design . . . 44
3.1.2 Tracker . . . 44
3.1.3 Calorimeter . . . 47
3.1.4 Anti-coincidence Detector & Micrometeriod Shield . . . 50
3.2 Data Aquisition and Event Processing . . . 54
3.2.1 Trigger Filter & Data Aquisition . . . 54
3.2.2 Data Quality & Instrument Operations . . . 57
3.2.2.1 Onboard Filter . . . 57
3.2.2.2 Downlink & Event Processing . . . 58
3.3 LAT Event Reconstruction . . . 59
3.3.1 Track and Vertex Reconstruction: A General Overview . . . 59
3.3.2 LAT Directional Reconstruction . . . 60
3.3.2.1 Track Finding . . . 60
3.3.2.2 Track Fitting & The Kalman Filter . . . 61
3.3.2.3 Vertex Reconstruction . . . 63
3.3.3 Energy Reconstruction . . . 63
3.3.4 Background Rejection . . . 64
3.3.5 Event Classification . . . 65
3.4 LAT Instrument Performance . . . 66
3.4.1 GLEAM Simulation Software . . . 66
3.4.2 Effective Area . . . 66
3.4.3 Point Spread Function . . . 68
3.4.3.1 Monte Carlo Derived PSF . . . 68
3.4.3.2 In-flight Derived PSF . . . 70
3.5 Likelihood Analysis Technique . . . 70
3.5.1 Statistical Likelihood . . . 70
3.5.2 Modeling γ-ray emission using the LAT data . . . 74
3.5.2.1 Event Selection and Exposure . . . 74
3.5.2.2 Spectral & Temporal Analysis . . . 75
3.5.2.3 Localization & Source Association . . . 77
3.5.2.4 Pointlike Method . . . 78

4 Observations of non-blazar emission in Fermi-LAT AGN 80
4.1 A Search for Extended γ-ray Emission from the Radio Galaxy Fornax A 81
4.1.1 Introduction . . . 81
4.1.2 Observations . . . 82
4.1.3 Monte Carlo Simulations . . . 84

4.1.4 Discussion . . . 84
4.1.4.1 LAT Results . . . 84
4.1.4.2 Future Outlook: High Resolution Imaging with the NuSTAR Telescope . . . 88
4.1.5 Conclusions . . . 89
4.2 Nonblazar properties of the gamma-ray AGN 4C+55.17 . . . 89
4.2.1 Introduction . . . 89
4.2.2 Observations . . . 95
4.2.2.1 *Fermi*/LAT Observations . . . 95
4.2.3 Multiwavelength Data . . . 99
4.2.3.1 X-ray . . . 99
4.2.3.2 Optical & Infrared . . . 99
4.2.3.3 Radio . . . 100
4.2.4 Modeling & Classification . . . 101
4.2.4.1 CSO Modeling . . . 101
4.2.4.2 Blazar Modeling . . . 106
4.2.5 High Energy γ-ray Continuum of 4C +55.17 . . . 109
4.2.6 Conclusions . . . 113
4.3 The Origin of Gamma-ray Emission from the radio galaxy M87 . . . 113
4.3.1 Introduction . . . 113
4.3.2 Observations . . . 114
4.3.2.1 10 Month Initial Detection . . . 114
4.3.2.2 MAGIC & VERITAS Multiwavelength Campaign . . . 116
4.3.2.3 Four Year Very High Energy Detection . . . 117
4.4 Discussion . . . 119

5 Development of Analysis Methods for the LAT Pass 8 Instrument Response Functions 124
5.1 Introduction . . . 124
5.2 Implementation & Development of Event-by-Event Covariant Errors . 124
5.2.1 Overview of the 2d Covariance Matrix . . . 124
5.2.2 Likelihood with Covariance Matrix . . . 127
5.2.3 Covariance Analysis Using HEALpix software . . . 130
5.2.4 Initial Results: Covariance-Smoothed Counts Maps . . . 131
5.3 Development of CAL-only Error Reconstruction for Pass 8 . . . 132
5.3.1 Overview of Calorimeter Clustering Methods . . . 132
5.3.2 Implementation of the Error for CAL-only Events . . . 135
5.3.3 Results & Conclusions . . . 137

6 Final Thoughts 140

A Preparation of the 20 cm VLA Radio Image of Fornax A 142

B Association of the 145 GeV photon with 4C +55.17 144

C Calculation of the MAGIC II Differential Flux Sensitivity 146

Bibliography 147

List of Tables

2.1 Taxonomy of AGN according to their radio luminosity and optical emission line properties. 28

3.1 Table of trigger engines and their respective primitives. Listed are the conditions of the trigger primitives belonging to each trigger engine: 1 = asserted, 0 = not asserted, and x = don't care, along with the readout instructions for each engine (zero-suppression enable/disable, CAL 4-range/1-range), and whether the event readout has been prescaled to a particular value. Table taken from [143]. . . . 55

3.2 Table of analytic parameters for the energy scaling function $S(E)$ (See Equation 3.11)[113]. 69

4.1 Spectral parameters for the `gtlike` analysis of Fornax A using 44 months of data for both the observed source as well as the monte carlo simulations of a point source emission, extended lobe emission, and an even distribution between lobe and point source. A value of "NC" indicates a failure of the fit parameters to converge within the allowed bounds. [a]Flux is given above 100 MeV in units of $[10^{-9}\,\mathrm{cm}^{-2}\,\mathrm{s}^{-1}]$. [b]A larger statistical error in the integral flux than the value itself is a consequence of the low detection significance combined with a large covariance between the index and prefactor parameters. In this case, the parameters are not well constrained and should be considered largely uncertain. 87

4.2 Spectral parameters for the `pointlike` analysis of Fornax A comparing the spatial models of a circular disk, elliptical disk, circular gaussian, and elliptical gaussian. [a]Flux is given above 100 MeV in units of $[10^{-9}\,\mathrm{cm}^{-2}\,\mathrm{s}^{-1}]$. [b]Semimajor and semiminor axes are given in units of degrees. 88

4.3 *Swift*/UVOT observation of 4C +55.17. The observations were obtained on 2009 March 5 (ep1), Nov 11 (ep2), and Nov 26 (ep3). . . . 100

4.4 De-absorption of γ-ray flux using different EBL models with fixed $\tau_{\gamma\gamma}$ normalization. [a]Flux is given above 100 MeV in units of $[10^{-8}\,\mathrm{cm}^{-2}\,\mathrm{s}^{-1}]$. 111

List of Figures

1.1 The electromagnetic spectrum as a function of frequency (top), energy (middle), and electron rest mass ($\epsilon = h\nu/m_e c^2$; top), along with some important astronomical lines and features (adapted from [95]). 2

1.2 Synchrotron spectrum (in log-log representation), from a powerlaw distrubution of electrons (From [261]). 6

1.3 Compton scattering of an incident photon ϵ in the electron rest frame. The photon scatters with energy ϵ_s at angle χ, while the electron is scattered at angle θ_e with lorentz factor γ_e [95]. 7

1.4 The behavior of $f(q)$ as a function of the lower energy photon, for an incident γ-ray with energy 100 GeV at collision angles $\theta = \pi, \pi/2, \pi/4$ (adapted from [254]). 12

1.5 Diagram of a pair-conversion telescope. 15

1.6 Schematic diagram of the two methods for ground-based detection of astrophysical γ-rays. Atmospheric Čerenkov Telescopes (ACTs; left) measure the Čerenkov radiation produced in the electromagnetic cascade, while Extensive Air-Shower (EAS; right) arrays directly detect the secondary particles from showers of sufficient energy to reach the ground. Adapted from [187]. 17

2.1 Anatomy of an Active Galactic Nucleus. Observed properties and behavior of AGN can vary considerably depending upon the observer's line of sight, despite many objects sharing the same intrinsic characteristics (from [186]). 21

2.2 Illustration of the Doppler factor δ as a function of viewing angle θ for various values of the Lorentz factor γ (From [305]). 23

2.3 Archetypal core jet morphology of a 15 GHz VLBI image of the blazar 0003+380. The unresolved Doppler boosted core dominates the total emission (from [192]). 26

2.4 Fermi-LAT observation of γ-ray emission from the giant radio lobes of the nearby radio galaxy Centaurus A. The white circle with diameter 1° represents approximately the scale of the LAT point spread function (PSF). Adapted from [110]. 27

2.5 VLA radio morphology of the FR II radio galaxy Cygnus A at 6 cm (left) [237], compared to the 1.4 GHz ATCA enhanced image of the nearby FR I radio galaxy Centaurus A (right) [108]. 30

2.6 Characteristic morphologies of the Compact Symmetric Objects. a) 0108+388 at 8.4 GHz [316], b) 0404+768 at 1.6 GHz [245], c) 0710+439 at 8.4 GHz [316], d) 1358+624 at 8.4 GHz [297], e) 2352+495 at 1.6 GHz [249], f) 2352+495 at 0.610 GHz [249] (Adapted from [249]). 33

2.7 The average SED of blazars studied by [123], which shows a distinct double peak for all sources, widely attributed to the synchrotron and inverse Compton processes [101]. The apparent anti-correlation between the low energy synchrotron peak and the bolometric luminosity has historically been referred to as the blazar sequence [249]. Adapted from [101]. 35
2.8 Diagram of the synchrotron self-Compton process in a conical jet, as originally proposed by [206]. Relativistic electrons are injected at an axial distance R_0 from the vertex of the cone, resulting in the formation of a shock. Accelerated electrons from within the shock produce synchrotron emission, which is then reprocessed into X-ray / γ-ray energies through inverse Compton scattering of the same electron population off of the synchrotron photons. 37
2.9 Diagram of the external Compton process. Relativistic electrons are accelerated along the jet direction away from the black hole, with the radiating region (short cylinder of dimension a) moving with pattern Lorentz factor Γ_p. Rescattered emission from the surrounding UV disk, broad line region, and dusty torus act as the primary source of seed photons, and dominate over the self-Compton emission if the energy density of the rescattered emission exceeds that of the internally produced synchrotron radiation in the comoving frame [274]. 39

3.1 Modular design of the LAT tracker [47]. 45
3.2 Schematic of one corner of the silicon detector. Each strip is biased through a polysilicon resistor and extends underneath the resistor itself in order maximize the active area. The Al readout electrodes include two AC pads for wire bonding to the front end electronics and one DC pad for testing purposes. The guard ring serves to minimize the insensitive area at the detector edge. [47]. 46
3.3 Inverted side view of one tracker module. Each side houses nine MCMs and 2 flex-circuit cables which extend to the tower electronics located below the calorimeter (not shown) [40]. 48
3.4 The LAT hodoscopic calorimeter design [37]. 49
3.5 Diagram of one calorimeter FREE board [163]. 50
3.6 LAT ACD tile layout, taken from [37]. 51
3.7 (a) Stacking of tiles along a single dimension on the top of the LAT ACD. (b) Cross section of ribbon placement for gaps in the remaining dimension [215]. 52
3.8 Illustration of the trigger timing for a 6-fold coincidence of three adjacent tracker planes. Only the strips that remain above threshold after event readout (T_2 to the right of the vertical green line) are successfully captured [64]. 56

3.9 Average rate of primitives received after passage of the onboard gamma filter during nominal science operations. Individual primitives for each event are subsequently categorized into trigger engines, which encode the trigger context information and trigger accept message (see Table 3.1) 57
3.10 Illustration of the Kalman Filter Process [286]. The state vector $\boldsymbol{q}$ is propagated from layer $k-1$ to layer k, taking into account the multiple scattering through the detector material. The measured position $\boldsymbol{m}_k$ is then used as a correction to the predicted state $\boldsymbol{q}_{k|k-1}$ to obtain the final filtered state $\boldsymbol{q}_{k|k}$. 63
3.11 LAT effective area for front (left) and back (right) events, as a function of monte carlo energy and $\cos(\theta)$ [113]. 67
3.12 (a) Histogram of scaled angular deviation. (b) Angular density histogram fit to LAT psf using events from from `P7SOURCE_V6` event class, $5.6 < E < 10\,\mathrm{GeV}$, and $26^\circ < \theta < 37^\circ$ [113]. 69

4.1 Test Statistic maps and associated localization contours (black) representing the 68%, 95%, and 99% confidence regions for the observed data (upper left), compared against the simulated confidence regions from an even distribution between lobes and core (upper right), pure lobe emission (lower left), and pure point source emission (lower right). Contours from the 20 cm image from [120] are included for reference (cyan). 86
4.2 44-month light curve of Fornax A, modeled as a point source to a power law spectrum with photon index $\Gamma = 2.25$. The points were divided into 225 day bins, with the dashed horizontal line and dark gray region representing the weighted mean and corresponding error over the period of observation. Each point falling below a 2σ detection was plotted as an upper limit. 88
4.3 NuSTAR Field of View (FOV) at 68 keV (black) and 10 keV (blue), compared to the total size scale of the lobes of Fornax A. The FOV is defined by the radius at which the off-axis effective area falls to 50% of its on-axis value. 90
4.4 Preliminary modeling of the extended γ-ray emission from Fornax A, along with archival data of the lobe (triangle) and LINER core (square) emission. The historical EGRET upper limit is also plotted. The blue line is the IC emission due to the COB and the host galaxy optical photons, the red line is the IC emission due to the CIB, and the black line is the total SED due to CMB (left IC peak), and EBL and host galaxy seed photons (right IC peak). The dashed black like represents the extrapolation of the core flux through the NuSTAR energy range (gray shaded area) and into the LAT spectrum (thick black lines). A well measured spectrum of the Fornax A lobe and core emission in the NuSTAR energy range would provide important constraints to the spectral modeling of each source. 91

4.5 Radio core brightness temperature of the 15 GHz MOJAVE northern hemisphere VLBA blazar monitoring program, plotted against γ-ray SED peak frequency(from [191]). The filled circles represent BL Lac objects, divided into high synchrotron peaked (orange), and low synchrotron peaked (blue). Open circles represent quasars, the green diamonds radio galaxies, and purple crosses optically unidentified objects. The plot includes all sources from the MOJAVE sample detailed in [191], with the single exception of 4C +55.17. At a synchrotron peak frequency of $10^{13.77}$ Hz, with brightness temperature $T_b = 10^{8.46}$ K, 4C +55.14 falls several orders of magnitute below the sample population. 93
4.6 VLBA 5 GHz map (left) featuring the inner parsec-scale radio structure of 4C +55.17, reimaged using data from [153]. The beam size is 2.0 mas × 1.6 mas (position angle = $-29.6°$), and the contour levels increase by factors of $\sqrt{2}$ beginning at 1 mJy/beam. The resolved morphology has a total angular size of 53 mas (413 pc). The VLA 5 GHz map (right) with a $0.4''$ beam (lowest contour is 2 mJy/beam increasing by factors of $\sqrt{2}$) shows the large scale radio structure (from[295]). 94
4.7 Fermi-LAT 5 year γ-ray light curve of 4C +55.17 divided into 14 day bins. All points represent $> 3\sigma$ detections and are plotted along with their statistical errors. The dashed horizontal line and gray region represent the weighted mean and corresponding error derived from all $> 3\sigma$ detections over the observing period. 97
4.8 Energy Flux over the LAT energy range versus variability index for AGN associations using a four year internal LAT catalog. The dashed black line represents the 99% confidence threshold for variability, following the official 2FGL catalog. The dashed blue line represents a more conservative 5σ confidence level. 4C +55.17 currently stands as the most luminous non-variable AGN across the LAT energy range. . 98
4.9 Conceptual diagram of the model proposed by Stawarz et al. (2008)[281]. A broken power law electron energy distribution is injected from the terminal jet shock into the expanding lobe. The electron population undergoes adiabatic and radiative cooling effects, producing synchrotron emission from the internal magnetic field, and IC emission from scattering off of the photon fields produced within the active center. 103

4.10 The CSO model of 4C +55.17 versus multiwavelength data, including the new LAT spectrum along with contemporaneous data with *Swift* XRT, BAT, and UVOT (black bullets). Archival detections (gray) with EGRET [151], ROSAT, Chandra, SDSS, 2MASS, 5-year integrated WMAP, and historic radio data are also included, as well as archival VLA measurements (black triangles) of the inner $\sim$ 400pc radio structure (see § 4.2.3). De-absorption of the observed *Fermi* spectral points using the [118] EBL model was applied in order to properly model the intrinsic γ-ray spectrum. Black curves indicate the total non-thermal emission of the lobes, with the long-dashed/green representing the contribution from synchrotron self-Compton (SSC). Dashed/pink, dash-dot-dotted/gray, and dash-dotted/blue blackbody-type peaks represent the dusty torus, starlight, and the UV disk emission components, respectively, along with their corresponding inverse-Compton components as required by the model. 105
4.11 Blazar fit using multi-wavelength data for 4C +55.17. Indicated are the individual contributions from synchrotron and SSC (long-dashed/green), as well as IC scattering off of the reprocessed UV disk emission from the broad line region (dash-dotted/blue), dusty torus (dashed/pink), and host galaxy (dash-dot-dotted/gray); the black curve indicates the total of these components. As in Fig. 4.10, the dashed/pink, dash-dot-dotted/gray, and dash-dotted/blue blackbody-type peaks represent the dusty torus, starlight, and the UV disk emission components, respectively, along with their corresponding inverse-Compton components as required by the model. 108
4.12 The $\tau_{\gamma\gamma}$ opacity versus energy for several EBL models at $z = 0.896$. The highest-energy photon of 145 GeV (rest frame energy = 275 GeV) within the 95% containment radius of the 4C +55.17 position is also indicated (vertical dashed line). The horizontal line simply denotes $\tau_{\gamma\gamma} = 1$. At the observed energy, attenuation from the EBL is expected even for those models which predict low levels of EBL. 110
4.13 The observed LAT spectrum fit to a log parabola with attenuation from 9 different EBL models. The spectra are extrapolated beyond the observed energy of 145 GeV and compared against the upper limits from a $\sim$ 45 hour VERITAS observation, along with the differential flux sensitivity curve of MAGIC II for a 50 hour, 5σ detection of a source characterized by an exponentially decreasing spectrum (see Appendix C). For several EBL models, the 4C +55.17 spectrum is found to intercept the MAGIC II sensitivity, making 4C +55.17 a possible candidate for a future ground-based VHE detection. 112
4.14 VLA λ=90cm radio image from [233] with the 10-month initial LAT γ-ray localization error circles indicated: $r_{95\%} = 5.2'$ and $r_{68\%} = 3.2'$ (statistical only). The M87 core is the faint feature near the center of the few kpc-scale double-lobed radio structure (in white). At the adopted distance $D = 16$ Mpc, $1' = 4.7$ kpc (From [11]). 115

4.15 The LAT 4 year spectrum (red circles), compared against the previous 10-month extrapolation (gray) into the VHE range [11], with representative TeV measurements of M87 in a low state from the 2004 observing season (black triangles) and during a high state in 2005 (blue squares), both by HESS [25]. The LAT 4-year measured spectrum extends smoothly into the VHE range, consistent with the 10 month extrapolation. 118
4.16 SED of M87 with the 10 month LAT spectrum and the Jan. 7, 2009 MOJAVE VLBA 15 GHz and *Chandra* X-ray measurements of the core indicated in red. The non-simultaneous 2004 TeV spectrum described in Figure 4.15 and *Swift*/BAT hard X-ray limits (§ 4.4) of the integrated emission are shown in light brown. Historical measurements of the core from VLA 1.5, 5, 15 GHz [54], IRAM 89 GHz [98], SMA 230 GHz [291], *Spitzer* 70, 24 μm [269], Gemini 10.8 μm [238], *HST* optical/UV [278], and *Chandra* 1 keV from [208](hidden behind the new measurements) are plotted as black circles. The VLBA 15 GHz flux is systematically lower than the historical arcsec-resolution radio to infrared measurements due to the presence of intermediate scale emission (see e.g., [183]). The blue line shows the one-zone SSC model fit for the core described in § 4.4. 120
4.17 Multi-wavelength light curve of M87 from 2001 to 2011. The *Fermi*-LAT flux and weighted average (dashed line, second panel from top) is plotted against the VHE γ-ray flux from H.E.S.S., MAGIC, and VERITAS (top). Light curves for the emission cites at the core and at HST-1 are plotted separately for Chandra (third and fourth from top), along with optical and radio data of both core and HST-1 (panels 5-8) Adapted from [15]. 122

5.1 The operation $r^T C^{-1} r$ yields the number of sigma n_σ away from the ellipse along the direction of r. 126
5.2 The LAT gnomonic projection. Events are reconstructed in the downward ($-\hat{z}$) direction, and projected onto the s_1, s_2 plane (located at $z = 1$), where $s_1 = \frac{x}{z}$ and $s_2 = \frac{y}{z}$. 129
5.3 Comparison of covariance-smoothed counts map (left) of the FSRQ 3c454.3, against a standard counts map smoothed with a gaussian kernel of radius 6 pixels (right). The covariance-smoothed map shows greater symmetry, along with a sharper peak about the source position. 131

5.4 Comparison of covariance-smoothed counts maps using 2 years of preliminary pass 7 event data for AGN sources of similar 2FGL spectral index and > 100 MeV flux. Starting from upper left to bottom right: Fornax A, PKS_0010-401, PKS_0346-27, PKS_0359-264, PKS_0403-13, PKS_2035-714, PKS_2329-16, PKS_2351-309, and PMN_J0157-4614. With the exception of PKS_2329-16, all point sources are peaked around their true source position. The extended emission around Fornax A holds significant promise for future analysis using event-by-event errors with the Pass 8 data. Note that the number scale does not represent source photon counts, but rather a counts density per unit area over the chosen pixel size. 133
5.5 CAL crystal geometry. Errors in the positional measurements along the crystal length will increase with larger values of θ. 137
5.6 Event distribution of the pull (number of sigma) for each of the methods: 5 mm error plus angular correction (top), geometry-based error (middle), and 5 mm with no angular correction (bottom). Events are binned in intervals of 0.5 sigma. 139

A.1 Before (left) and after (right) images of the 20 cm VLA map for use as an extended source template in the LAT analysis. Indicated in green are the point sources removed from the map. 143

B.1 Event display for the 145 GeV photon. Green "x"s denote hits in the tracker, while red squares indicate an energy deposit in a calorimeter crystal. The white and yellow lines indicate the track candidates and the best track for the event, respectively. 145

List of Abbreviations

ACD	Anti-Coincidence Detector
ACT	Atmospheric Čerenkov Telescope
AEM	ACD Electronics Module
AGN	Active Galactic Nuclei
ASIC	Application Specific Integrated Circuit
ATEL	Astronomer's Telegram
ASP	Automated Science Processing
BLR	Broad-Line Region
BLRG	Broad-Line Radio Galaxy
BSPR	Blind Search Pattern Recognition
CSO	Compact Symmetric Object
CSS	Compact Steep Spectrum
CSPR	Calorimeter Seeded Pattern Recognition
CAL	Calorimeter
CDE	Crystal-Diode Element
CMB	Cosmic Microwave Background
CIB	Cosmic Infrared Background
COB	Cosmic Optical/UV Background
CT	Classification Tree
EAS	Extensive Air-Shower
EBL	Extragalactic Background Light
EED	Electron Energy Distribution
FFA	Free-Free Absorption
FITS	Flexible Image Transport System
FR (I/II)	Fanaroff-Riley type I/II
FREE	Front End Electronics
FSRQ	Flat Spectrum Radio Quasar
GASU	Global Trigger/ACD Electronics Module Signal Distribution Unit
GCN	Gamma-ray Coordinates Network
GPS	Gigahertz-Peaked Spectrum
GRB	Gamma-ray Burst
GTFE	GLAST Tracker Front End Electronics
GTI	Good Time Interval
GTRC	GLAST Tracker Readout Controller
GEM	LAT Global Trigger and ACD Electronics Module
GLEAM	Glast LAT Event Analysis Machine
HSP	High Synchrotron Peaked
HE	High Energy
HVBS	High Voltage Bias Supply
IACT	Imaging Atmospheric Čerenkov Telescope
IC	Inverse Compton
IRF	Instrument Response Function
ISOC	LAT Instrument Science Operations Center
ISP	Intermediate Synchrotron Peaked

L1 Proc	Level One Processing
LR	Likelihood Ratio
LSP	Low Synchrotron Peaked
MCM	Multi-Chip Module
MET	Mission Elapsed Time
MIP	Minimum Ionizing Particle
MMS	Micrometeoroid Shield
MSO	Medium Symmetric Object
NELG	Narrow-Emission-Line X-ray Galaxies
NLR	Narrow-Line Region
NLSy1	Narrow-Line Seyfert 1
PIC	Proton Induced Cascade
PMT	Photomultiplier Tube
PSF	Point Spread Function
QSO	Quasi-Stellar Object
ROI	Region Of Interest
SAA	South Atlantic Anomoly
SED	Spectral Energy Distribution
SFR	Star Formation Rate
SSA	Synchrotron Self-Absorption
SSD	Silicon Strip Detector
SSRQ	Steep Spectrum Radio Quasar
TEM	Tower Electronics Module
TKR	Tracker
TS	Test Statistic
VHE	Very High Energy
VLBI	Very Long Baseline Interferometry
WLS	Wavelength Shifting

Chapter 1
Introduction
1.1 History of γ-ray Astronomy

In the timeline of history in astronomy and astophysics, the field of observational γ-ray astronomy is relatively young. Prior to 1958, when Morrison [216] first outlined the prospect of studying γ-ray emission from astrophysical phenomenon such as cosmic ray interactions, pair annihilation, solar flares, supernova remnants, and synchrotron processes such as those postulated to exist within extragalactic radio sources, the field of γ-ray astronomy had not yet been established.

One of the primary challenges that faced many of the earliest attempts to study γ-rays in astronomy lie in the fact that the Earth's atmosphere (and indeed matter in general) is opaque to γ-rays (see Section 1.2.0.5), thus rendering many of the ground-based detection methods that had been used in astronomy at other wavelengths (i.e. radio and optical, see Figure 1.1) ineffective. Ultimately, the first instruments to observe astronomical γ-ray sources were space-based, with Explorer XI [184] being the first instrument of its kind to detect γ-rays of astrophysical origin. A decade later, SAS-2 became the first instrument to detect γ-ray point sources and a diffuse background [94], which was followed a decade later by COS-B [290], which provided the first complete map of the galaxy in γ-rays, along with a comprehensive point source catalog of 25 sources with 4 known associations.

With the launch of the Compton Gamma-Ray Observatory (CGRO) in 1991, the field of observational γ-ray astronomy had become firmly established, with CGRO's primary instrument, the Energetic Gamma-Ray Experiment Telescope (EGRET; [301]), detecting 271 high energy point sources with well-constrained γ-ray spectra. Among these sources, the largest number were associated with Active Galactic Nuclei (AGN), particularly blazars (see Section 2.2.2.4), along with a population of 6 γ-ray loud pulsars.

Developing in tandem with the space-based instruments, a number of techniques were also pioneered in ground-based observation of astonomical γ-ray sources through the detection of Čerenkov light that is created by energetic particles of γ-induced air showers as they pass through dielectric material [161]. These include water Čerenkov radiation telescopes such as Milagro [36] and HAWC [14], and the Imaging Atmospheric Čerenkov Telescopes (IACTs) such as HEGRA [26], the Whipple 10 meter reflector [107], and the newer generation instruments such as H.E.S.S., MAGIC, and VERITAS that are still operational today. These ground-based detectors probe an energy range much higher than space-based instruments (VHE; $> 100\,\mathrm{GeV}$), and have proven to be quite valuable for studies of the highest energy processes in the universe, while also complimenting the broadband coverage of space-based experiments to allow for coordinated multiwavelength observations.

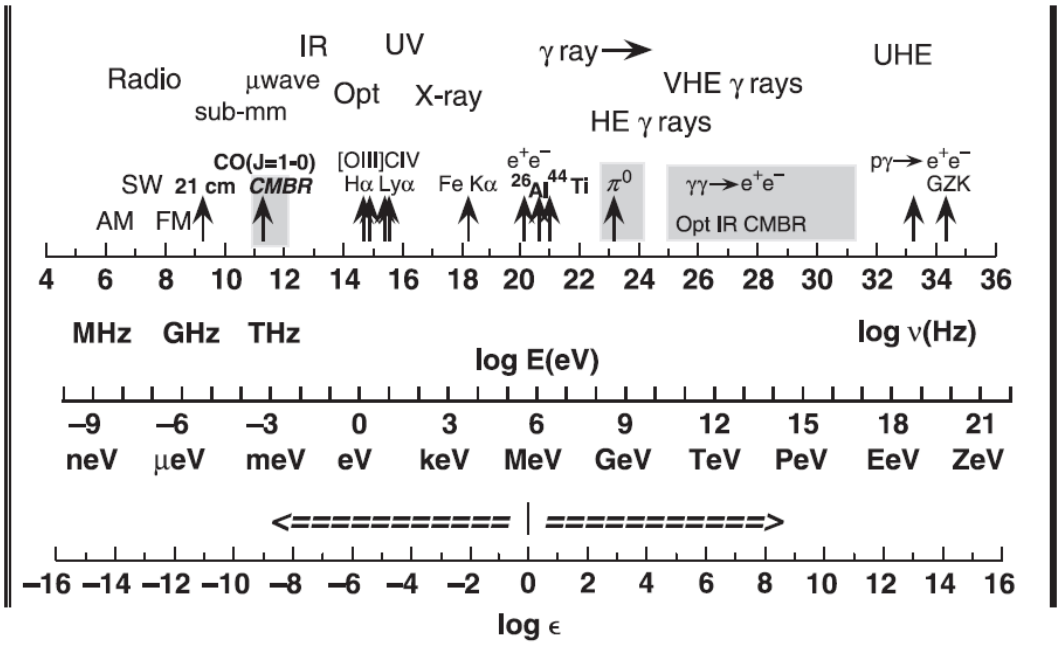

Figure 1.1: The electromagnetic spectrum as a function of frequency (top), energy (middle), and electron rest mass ($\epsilon = h\nu/m_e c^2$; top), along with some important astronomical lines and features (adapted from [95]).

1.2 Physical & Radiative Processes in γ-ray Astronomy

The highest-energy photons are known as γ-rays, with energies from $\sim 100\,\mathrm{keV}$ upwards [261](see Figure 1.1). γ-radiation is produced through several different processes that span a wide range of spectral energies, thus it is important to characterize γ-rays both in terms of their energy, as well as in terms of the physical processes that produce them. This leads to some ambiguity in the 100 keV lower bound, which exists primarily as a soft limit on γ-rays produced from nuclear decay of radioisotopes, and which makes up relatively little of the radiative output from astronomical sources. High energy γ-ray astronomy, on the other hand, primarily focuses on energies greater than $\sim 20\,\mathrm{MeV}$, where the concept of temperature begins to break down due to catastrophic cooling from pair creation and bremsstrahlung processes [95] (see also Section 1.2.0.3 and 1.2.0.5). It is above this range that γ-rays serve as the most efficient probes of the non-thermal universe. I will therefore focus on γ-rays above the non-thermal limit in this work, where I will discuss the physical and radiative mechanisms that are most relevant to the production of $> 100\,\mathrm{MeV}$ high energy (HE) γ-ray emission in astrophysical sources, either directly or indirectly (see Section 2.3 for a discussion of γ-ray emission models in AGN).

An understanding of the physical processes that can give rise to γ-ray emission in AGN is essential for understanding their nature. Such processes include synchrotron emission and inverse Compton (IC) scattering (Sections 1.2.0.1 & 1.2.0.2), which are most commonly used in the leptonic modeling of AGN spectra (see Sec-

tion 2.3), as well as hadronic processes such as photopair and photopion production (Section 1.2.0.6), which can also give rise to high energy γ-rays (Section 2.3.3). In addition, it is equally important to have an understanding of the mechanisms that are responsible for creating the underlying particle energy distributions that produce the types of γ-ray spectra that are seen in AGN (Section 1.2.0.4). Finally, a knowledge of the interaction mechanisms involving γ-rays such as $\gamma\gamma$ pair production is also essential (Section 1.2.0.5). In the following sections, I will review these processes and others in order to establish the necessary framework for understanding many of the concepts that will be discussed in later chapters.

1.2.0.1 Synchrotron Radiation

Synchrotron radiation is radiation produced from the acceleration of a relativistic charged particle in the presence of a magnetic field. It is the relativistic version of cyclotron radation, for which the frequency of emission is equal to the frequency of gyration [159]. Synchrotron emission differs from its nonrelativistic counterpart, however, in that the spectrum of emission is broadened due to relativistic beaming effects [159, 261]. The electron energy loss rate due to synchrotron radiation is given by [261]

$$-\left(\frac{dE}{dt}\right)_{syn} = \frac{4}{3}\sigma_{\rm T} c\beta^2\gamma^2 U_B \tag{1.1}$$

where $U_B = B^2/8\pi$ is the magnetic energy density. This is also commonly expressed in terms of the rate of change of the electron Lorentz factor [95]

$$-\dot{\gamma}_{\rm syn} = \frac{4}{3}\sigma_{\rm T} c\beta_{\rm par}^2\gamma^2 u_B \tag{1.2}$$

where

$$u_B \equiv \frac{U_B}{m_e c^2} \tag{1.3}$$

The peak observed frequency is given by

$$\nu_{pk}^{syn} \approx \frac{qB}{2\pi mc}\gamma^2 \tag{1.4}$$

For electrons, this yields

$$\nu_{pk}^{syn} \approx 2.79 B\gamma^2 {\rm MHz} \tag{1.5}$$

where B is measured in Gauss. The equation for the emitted synchrotron spectral power for a particle with pitch angle α is given by:

$$P(\omega) = \frac{\sqrt{3}q^3 B\sin\alpha}{2\pi mc^2}F(x) \tag{1.6}$$

where

$$F(x) = x \int_x^\infty K_{\frac{5}{3}}(\xi) d\xi \tag{1.7}$$

and $x \equiv \omega/\omega_c$. Here $K_{\frac{5}{3}}$ is a modified Bessel function of order 5/3.

Synchrotron Spectrum from a Power Law Distribution

It is often the case in astrophysical processes that the number density of particles within a limited range of energy can be approximately expressed as a power law [261]:

$$N(E)dE = \mathrm{C}E^{-p}dE \tag{1.8}$$

For such a distribution, it is possible to show that the resulting synchrotron spectrum will also take the form of a power law, with spectral index $s = (p-1)/2$. This result is obtained by integrating the particle distribution from Equation 1.8 times the radiation formula for a single particle, given by Equation 1.6, over a sufficiently wide range of energies or γ [261]:

$$P_{\mathrm{tot}}(\omega) = \mathrm{C} \int_{\gamma_1}^{\gamma_2} P(\omega)\gamma^{-p} d\gamma \tag{1.9}$$

$$\propto \int_{\gamma_1}^{\gamma_2} F\left(\frac{\omega}{\omega_c}\right) \gamma^{-p} d\gamma \tag{1.10}$$

$$= \omega^{-(p-1)/2} \int_{x_1}^{x_2} F(x) x^{(p-3)/2} dx \tag{1.11}$$

where the final form is obtained using the change of variables $x \equiv \omega/\omega_c$, noting that $\omega_c \propto \gamma^2$. From here, the integral over x must be solved explicitly over the bounds x_1 and x_2 in order to obtain an exact solution. However, in the limit of a sufficiently wide range of energy, the approximation $x_1 \approx 0, x_2 \approx \infty$ can be used, such that the integral in 1.9-1.11 is approximately constant, yielding the proportionality:

$$P_{\mathrm{tot}}(\omega) \propto \omega^{-(p-1)/2} \tag{1.12}$$

Synchrotron Self-Absorption

It is useful to express the spectral intensity of a radio source in terms of its brightness temperature, given by [95]:

$$T_B = \frac{c^2 I_\nu}{2 k_B \nu^2} \tag{1.13}$$

where k_B is Boltzmann's constant. The brightness temperature is the temperature at which a blackbody radiates at the intensity I_ν using the classical Rayleigh-Jeans equation for spectral radiance. It is a useful measure of the maximum intensity that

a population of radiating particles can emit before becoming self-absorbed. That is, if the brightness temperature exceeds the effective temperature of the radiating particles, the emission region will become optically thick, and only the outer surface of the emission will be visible.

For relativistic electrons, the limit on the brightness temperature is obtained from effective temperature:

$$T_B < \frac{\gamma m_e c^2}{3k_B} \tag{1.14}$$

which may be expressed in terms of the frequency as

$$T_B < \left(\frac{2\pi m_e c\nu}{qB}\right)^{1/2} \frac{m_e c^2}{3k_B} \tag{1.15}$$

The limit on the brightness temperature will influence the spectrum of compact sources by suppressing the lower frequency emission up to a frequency ν_1 where the emission is no longer optically thick ($\tau \lesssim 1$). For isotropic emission at sufficiently low energy, the spectrum of emission will approximately follow the brightness temperature according to:

$$I_\nu \simeq \frac{2k_B T_B \nu^2}{c^2} \tag{1.16}$$

but from Equation 1.15 we see that $T_B \propto \nu^{1/2} B^{-1/2}$, thus the spectrum below the optically thick frequency ν_1 will follow

$$S(\nu) \propto \nu^{5/2} \tag{1.17}$$

Above this energy, the spectrum for a power law distribution of electrons follows the standard relationship given by Equation 1.12 (see Figure 1.2).

Polarization

Synchrotron emission is polarized, with the degree of polarization depending on the orientation of the magnetic field with respect to the line of sight of the observer. For a uniform magnetic field as discussed above, the single point charge will be elliptically polarized, with the right- or left-handedness depending on the position of the observer's line of sight with respect to the pitch angle α [261]. Specifically, for viewing angles less than α, the polarization will be right handed, while for angles greater than α, the polarization will be left handed. However, because the emission is confined within a relatively small solid angle $\Delta\theta$ (of order $1/\gamma$) about α due to relativistic beaming effects, the distribution of a population of relativistic particles in most astrophysical processes will tend to cancel the elliptical polarization on either side. The result is that the emission will be partially linearly polarized, with the degree of polarization determined by the components of the emitted power $P_\perp(\omega)$ and $P_\parallel(\omega)$ in the directions perpendicular and parallel to the direction of the magnetic field [261]:

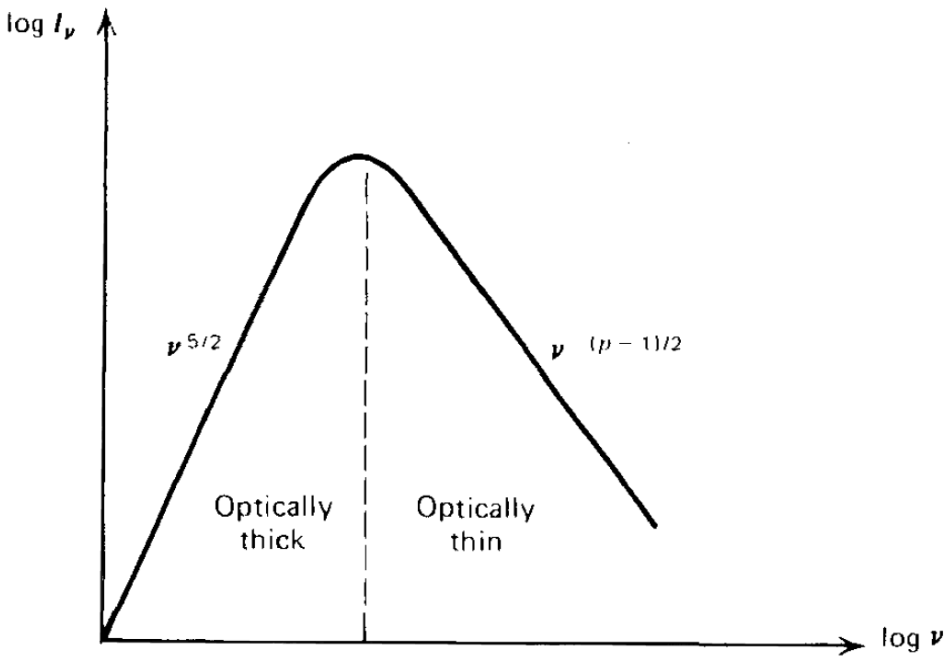

Figure 1.2: Synchrotron spectrum (in log-log representation), from a powerlaw distrubution of electrons (From [261]).

$$\Pi = \frac{P_\perp(\omega) - P_\parallel(\omega)}{P_\perp(\omega) + P_\parallel(\omega)} \tag{1.18}$$

1.2.0.2 Compton Scattering

Compton Scattering is the process in which a photon of energy E_γ interacts with a charged particle (in most cases, an electron or positron) by transferring a portion of its energy to the particle. The inverse process, in which a charged particle transfers a portion of its energy to the photon, is referred to as inverse Compton (IC) scattering. It is often convenient to refer to the photon energy in the dimensionless form $\epsilon = E_\gamma / m_e c^2$, where m_e is the electron mass. The behavior of these interactions is thus determined by the photon energy in the electron rest frame, given by the invariant $\bar{\epsilon} = \gamma\epsilon(1 - \beta_{\rm par}\mu)$, where $\mu = \cos\theta$, and θ is the angle between the incoming photon direction and the positive $\hat{x}$-axis of the boosted frame (for a boost that is taken in the $\hat{x}$ direction). Compton scattering is said to take place in the Thompson regime in the non-relativistic limit ($\bar{\epsilon} \lesssim 1$), while relativistic interactions ($\bar{\epsilon} >> 1$) are said to take place in the Klein-Nishina regime [95].

Consider an incoming photon with dimensionless energy ϵ in the frame of an electron at rest, which interacts and scatters at an angle χ with respect to its initial direction, resulting in a scattered photon energy of ϵ_s (see Figure 1.3). The solution for the angle of the scattered electron θ_e, along with its Lorentz factor γ_e, is obtained by conserving both energy and momentum of the system in the initial

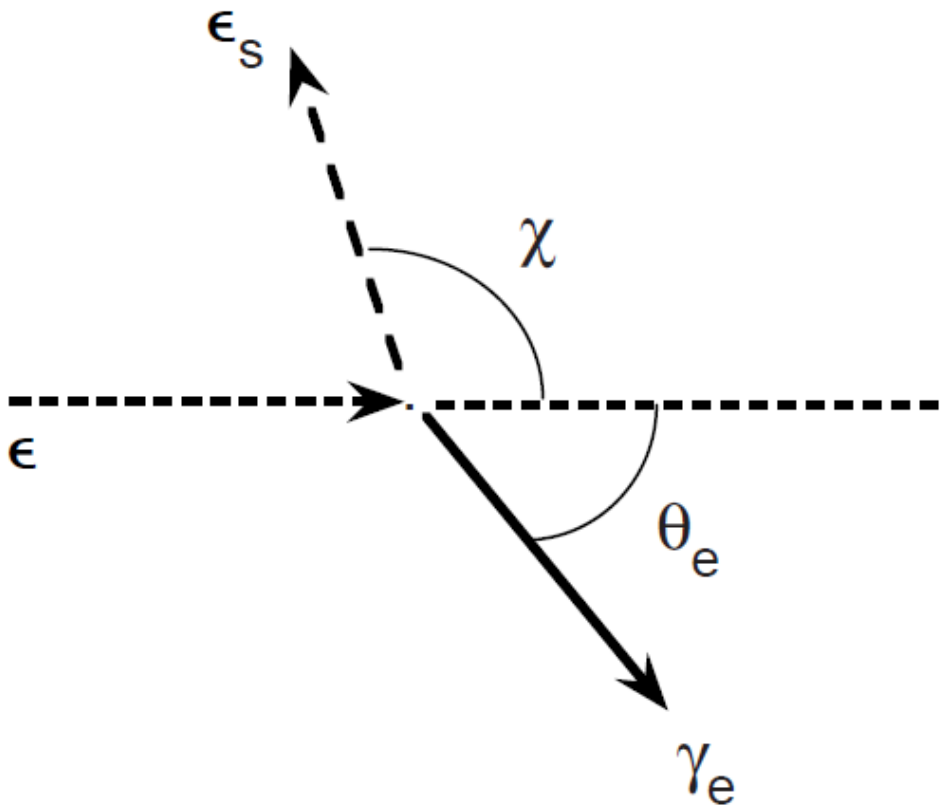

Figure 1.3: Compton scattering of an incident photon ϵ in the electron rest frame. The photon scatters with energy ϵ_s at angle χ, while the electron is scattered at angle θ_e with lorentz factor γ_e [95].

frame of reference to yield the following relationship[95]:

$$\epsilon_s = \frac{\epsilon}{1 + \epsilon(1 - \cos\chi)} \tag{1.19}$$

which can be written in terms of the wavelength as [261]:

$$\lambda_s - \lambda = \lambda_c(1 - \cos\chi) \tag{1.20}$$

where $\lambda_c \equiv h/mc$ is the Compton wavelength.

In the extreme cases, the photon is scattered with energy $\epsilon/(1 + 2\epsilon)$ for backwards scattering, while in the forward scattering case, the photon retains its original energy ϵ. Using the form of Equation 1.19 the Thompson and Klein-Nishina regimes may be distinguished by noting that the Thompson regime is defined in the $\epsilon \lesssim 1$ case, where $\epsilon_s \approx \epsilon$ for all directions, whereas the Klein-Nishina regime is defined for $\epsilon >> 1$, where ϵ_s is highly dependent on χ.

It is also worthwhile to look at the transition from Thomson to Klein-Nishina regimes through an examination of the cross section. The equation for the differential cross section for unpolarized radiation in the Thomson regime is given by [261]:

$$\frac{d\sigma_{\rm T}}{d\Omega} = \frac{1}{2} r_0^2 (1 + \cos^2\theta) \tag{1.21}$$

$$\sigma_{\rm T} = \frac{8\pi}{3} r_0^2 \tag{1.22}$$

In quantum electrodynamics, the differential cross section is instead given by the Klein-Nishina formula:

$$\frac{d\sigma_{\rm T}}{d\Omega} = \frac{r_0^2}{2}\frac{\epsilon_s^2}{\epsilon^2}\left(\frac{\epsilon}{\epsilon_s} + \frac{\epsilon_s}{\epsilon} - \sin^2\theta\right) \tag{1.23}$$

In this case, when the scattering is elastic ($\epsilon_s \sim \epsilon$), Equation 1.23 reduces to Equation 1.21. However, for inelastic scattering, the net effect is to reduce the cross section as the photon energy becomes increasingly larger. We thus see that in the extreme case of $h\nu >> mc^2$, the cross section for Compton scattering becomes increasingly negligible, thus making this process extremely inefficient at high energies.

Inverse Compton Scattering

The simple case of an incoming photon of energy ϵ scattering an electron at rest can be expanded to the case of an electron in motion via a transformation from the electron rest frame K' to an observer or lab frame K. Such a transformation allows not only the standard Compton scattering process to take place, but also can give rise to the IC scattering process when the interaction results in a net loss of energy by the scattered electron in the lab frame. In this case, the effects of relativistic

Doppler boosting must be taken into account, such that the original photon energy ϵ is seen in the electron rest frame as

$$\epsilon' = \epsilon\gamma(1 - \beta\cos\theta) \tag{1.24}$$

whereas the scattered electron's final energy, as seen in the *lab* frame, must also be Doppler shifted:

$$\epsilon_s = \epsilon'_s\gamma(1 + \beta\cos\theta'_s) \tag{1.25}$$

The net result is a conversion of a low-energy photon to a high energy one of order γ^2. It is worth noting that even at relatively high photon energies of order $\sim 100\,\mathrm{keV}$, the condition for Thomson scattering in the rest frame ($\gamma\epsilon << mc^2$) can still be achieved. Thus, with an additional boosting of order γ to these intermediate energies, the spectra of sources undergoing this process can reach several orders of magnitude higher than their initial photon energies, and are seen in nature to extend well into the hundreds of GeV in some cases (see Section 2.3).

The energy loss rate of electrons undergoing IC scattering in the electron rest frame is given by [193]:

$$-\left(\frac{dE}{dt}\right)' = \sigma_{\mathrm{T}} c U'_{rad} \tag{1.26}$$

where U'_{rad} is the energy density of photons in the electron frame. In the lab frame, this is given by:

$$-\left(\frac{dE}{dt}\right)_{IC} = \frac{4}{3}\sigma_{\mathrm{T}} c\beta^2\gamma^2 U_{rad} \tag{1.27}$$

where U_{rad} is the energy density of photons in the non-boosted frame, and the factor of γ^2 arises from Doppler boosting both the frequency and time of arrival of the photons. It is interesting to note the similarity of the energy loss rate from IC scattering to that of the synchrotron energy loss rate, given by Equation 1.1. The remarkable likeness of these two equations illustrates that the energy loss of the electrons is more closely tied the energy density of the field through which they pass than to the radiation process itself. In the case of synchrotron losses, electrons are accelerated by the perturbations of the electric field that are created as it passes through $\vec{B}$, whereas for IC scattering, the energy losses are due to the acceleration of the charge from its interaction with the scattered photon, but the net result is the same in either case.

1.2.0.3 Bremsstrahlung Radiation

Bremsstrahlung radiation (also referred to as breaking radiation or free-free radiation), results from the change in velocity of a charged particle in the Coulomb field of another nearby charged particle. For small angle scatterings, the emission from a single collision of an electron with a charged ion is [261]

$$\frac{dW(b)}{d\omega} = \frac{8Z^2e^6}{3\pi c^3 m^2 v^2 b^2} \tag{1.28}$$

where Z is the ion charge, b is the impact parameter satisfying the condition $b \ll \omega$. The total emission per unit time per unit volume per unit frequency range is given by:

$$\frac{dW}{d\omega dV dt} = \frac{16e^6}{3c^3 m^2 v} n_e n_i Z^2 \ln\left(\frac{b_{\max}}{b_{\min}}\right) \tag{1.29}$$

where n_e and n_i are the electron and ion densities, and $b_{\max}$ and $b_{\min}$ are the maximum and minimum allowed values of the impact parameter, given by $b_{\max} \equiv v/\omega$ and $b_{\min} = h/mv$. From the above equation, we find that the energy losses due to bremsstrahlung will be significantly greater for electrons than for protons, due to the m^{-2} dependence on the emission spectrum, which is important for example when considering the propagation and energy losses of particles within electromagnetic cascades.

1.2.0.4 Particle Acceleration

Particle acceleration mechanisms that occur at the vicinity of shock fronts are responsible for generating the observed power law spectra that are commonly found in particle distributions of astrophysical objects such as AGN jets [45, 46]. The primary mechanism responsible for this is attributed to first-order Fermi acceleration.

In first-order Fermi acceleration, particles are accelerated in the vicinity a shock front with magnetic field parallel to the direction of travel of the shock. Charged particles from within the shock can freely travel in and out of the shock provided that their gyroradii are larger than that of the thickness of the shock. The particles that are located upstream from the shock front will experience a turbulence in the form of Alfvén waves generated by particles passing through the shock front. Alfvén waves produce an oscillation of the charged particles within the magnetized plasma of the shock as a result of a restoring force provided by an effective tension of the magnetic field lines. These Alfvén waves will inevitably scatter the energetic particles, reducing their streaming to roughly the Alfvén speed, thus making it inevitable that the particles will be overtaken by the shock.

Unlike the upstream particles, those that are located downstream from the shock have will some probability η of escaping the shock front, or recrossing the shock front to the upstream region with probability (1-η), where these probabilities are determined by applying the diffusion equation to particles within the downstream region and finding the proportion of them that will diffuse back across the shock. Ultimately, this scenario can result in particles crossing from downstream to upstream and back over multiple iterations, each time causing the particle to gain energy. More specifically, a particle with energy E_k, which has performed k cycles passing from upstream to downstream and back to upstream, performs a further cycle and has its energy increased to [45]

$$E_{k+1} = E_k \left(\frac{1 + v_{k1}(u_1 - u_2)\cos\theta_{k1}/c^2}{1 + v_{k2}(u_1 - u_2)\cos\theta_{k2}/c^2} \right) \tag{1.30}$$

where v_{k1} is the velocity at which the particle crosses from upstream to downstream, θ_{k1} is the angle with respect to the shock normal, and u_1 is the mean velocity of the scattering center in the upstream region, with index 2 corresponding to the opposite regions. The resulting differential energy spectrum is given by

$$N(E)dE = \frac{\mu - 1}{E_0} \left(\frac{E}{E_0} \right)^{-\mu} dE \tag{1.31}$$

where

$$\mu = \frac{2u_2 + u_1}{u_1 - u_2} + 0 \left(\frac{u_1 - u_2}{c} \right) \tag{1.32}$$

1.2.0.5 Pair Production

Pair production is the mechanism whereby two photons interact with each other to produce an electron-positron pair:

$$\gamma + \gamma \longrightarrow e^+ + e^- \tag{1.33}$$

In quantum electrodynamics, the cross section for $\gamma\gamma$ pair production is given by[307]:

$$\sigma(q) = \frac{3}{8}\sigma_{\mathrm{T}} f(q) \tag{1.34}$$

where

$$f(q) = q \left[\left(1 + q - \frac{q^2}{2} \right) \ln \frac{1 + \sqrt{1-q}}{1 - \sqrt{1-q}} - (1+q)\sqrt{1-q} \right] \tag{1.35}$$

and

$$q = \frac{2m_e^2}{E\epsilon(1 - \cos\theta)} \tag{1.36}$$

where E and ϵ are the energies of the high and low energy photons, respectively, and θ is the collision angle. Figure 1.4 illustrates the behavior of $f(q)$ as a function of the collision angle theta for γ-ray photons at $E = 100\,\mathrm{GeV}$. It is clear that for any particular photon energy E, there will be an ideal range of energies ϵ of the incident photon for which the cross section is maximized. Thus we find that although the pair production cross section will be non-zero as far down as the threshold energy of $2m_e c^2$, it is far more likely that attenuation will take place for photon energies where $f(q)$ is maximized, namely at values of $q \simeq 0.5$. This means that the photon fields that are most important for attenuating γ-rays at a particular energy will have energies close to the value

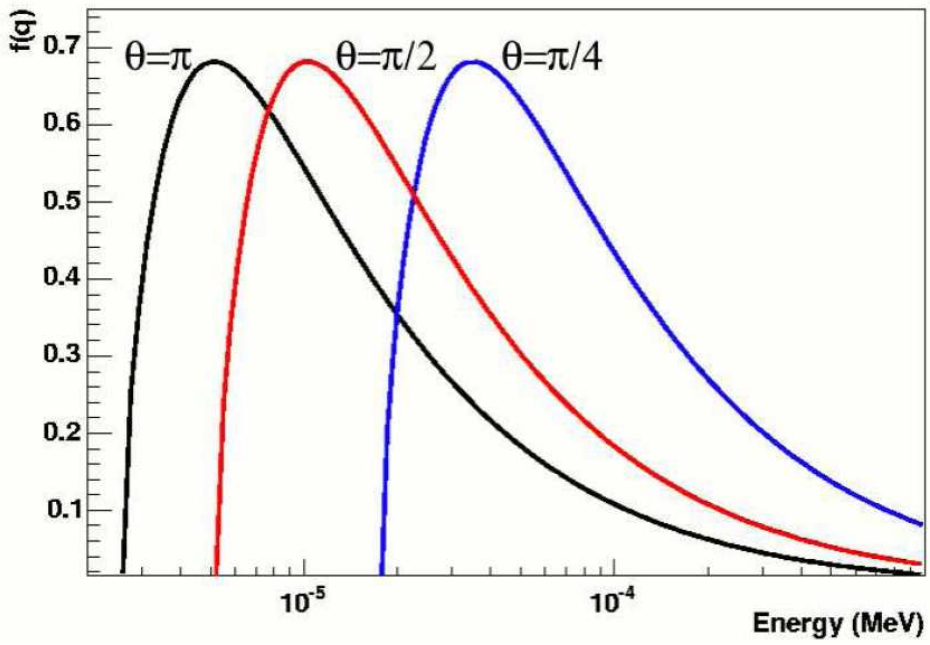

Figure 1.4: The behavior of $f(q)$ as a function of the lower energy photon, for an incident γ-ray with energy 100 GeV at collision angles $\theta = \pi, \pi/2, \pi/4$ (adapted from [254]).

$$\epsilon \sim \frac{1\mathrm{k}eV}{\left(\frac{E}{1\mathrm{G}eV}\right)(1-\cos\theta)} \tag{1.37}$$

For an isotropic photon field, the peak attenuation will occur at

$$\lambda(\mathrm{n}m) = 1.33\frac{E}{1\ GeV} \tag{1.38}$$

The effect of pair production on γ-ray spectra is ultimately described by an optical depth $\tau_{\gamma\gamma}(E)$, which is an integral quantity defined along a specific path. The opacity reduces the source flux by a factor of $\exp(-\tau_{\gamma\gamma})$. For an isotropic photon field, the absorption probability per unit pathlength is given by [95]

$$\frac{d\tau_{\gamma\gamma}(E)}{dx} = \frac{1}{2}\int_0^\infty d\epsilon n_{\mathrm{ph}}(\epsilon,\Omega)\sigma_{\gamma\gamma} \tag{1.39}$$

where $n_{\mathrm{ph}}(\epsilon,\Omega)$ is the photon density over the solid angle $d\Omega$ and $\mu = \cos\theta$. As expected, the optical depth will thus depend on both the energy spectrum and the number density of the photon field. These relationships play an important role in the attenuation of γ-ray spectra by photon fields that are both internal and external to the AGN, as will be discussed in Section 2.3.4.

1.2.0.6 Electromagnetic Cascades

When a very high energy electron or photon interacts with a dense material such as the Earth's atmosphere, an electromagnetic shower will be induced through the pair production and bremsstrahlung interactions, along with subsequent interactions of secondary particles. In high energy sources, a range of cascades can form depending on the target matter and radiation, the compactness, and the magnetic field strength [95]. In addition to $\gamma\gamma$ pair production, important processes involved in the propagation of the shower include photopair production

$$p\gamma \longrightarrow p + e^+ + e^- \tag{1.40}$$

and photopion processes

$$p\gamma \longrightarrow p\pi^0 \tag{1.41}$$

$$p\gamma \longrightarrow n\pi^+ \tag{1.42}$$

Further propogation of the particle shower will be induced through secondary interactions resulting in γ-ray production through pion decay, synchrotron radiation, and IC scattering. These secondary interactions will continue until the mean energy of the electrons falls below $\sim 20\,\mathrm{MeV}$, at which point the energy losses by ionization exceed those due to bremsstrahlung.

1.2.0.7 Čerenkov Radiation

When charged particles pass through a dielectric medium such as water or the Earth's atmosphere at a speed that is greater than the phase velocity of light in that medium, electromagnetic radiation will be produced. This radiation is referred to as Čerenkov Radiation, named after the scientist Pavel Alekseyevich Čerenkov, who first detected it experimentally. Under this process, the charged particle (e.g. an electron) passing through the material with velocity β will electrically polarize the atoms in the immediate vicinity of the moving particle due to the presence of its electric field. As the particle moves away, the polarized material will return to its unpolarized state, resulting in a radiation shockwave in the blue/violet portion of the optical spectrum that will propagate along the particle's trajectory with a beaming angle given by

$$\cos\theta = \frac{1}{n\beta} \tag{1.43}$$

where n is the refractive index of the medium. From the above equation, it follows that the threshold velocity for Čerenkov Radiation to be emitted is $\beta = 1/n$.

1.3 Detecting γ-rays

One of the challenges that must be overcome in the detection of astrophysical γ-rays is the fact that, above a threshold energy of $\sim 10\,\mathrm{MeV}$, γ-rays interact with matter primarily through the pair cration process, meaning that any interaction that a detecting instrument would make with γ-ray photons will inevitably result in the production of a particle shower. Furthermore, the Earth's atmosphere is opaque to γ-rays, which will significantly attenuate through the pair creation process before reaching the ground, thus requiring that any ground-based instruments for directly detecting γ-rays operate at extremely high altitudes and with extremely large effective areas. Despite these challenges, several methods have been developed for detecting astrophysical γ-rays using both ground-based as well as space-based instruments. A summary of the methods used in the current generation of instruments is described below.

1.3.1 Space-based

The primary type of instrument for space-based detection of γ-rays is the pair conversion telescope (see Figure 1.5). These instruments detect high energy γ-rays ($\gtrsim 20\,\mathrm{MeV}$) by tracking the resulting particles created after the conversion of a γ-ray photon into $e^+\,e^-$ pairs. In addition to determining the direction and energy of γ-ray photons, pair-conversion telescopes must also have a means of separating the photon-initiated events from those that arise from charged cosmic rays that pervade above the Earth's atmosphere.

Pair conversion telescopes share a number of common design features that allow the measurement of γ-rays to take place. The essential components include the converter-tracker, calorimeter, and anti-coincidence detector (ACD). The measurement of gamma-rays begins in the tracker, where incoming γ-rays are converted into $e^+\,e^-$ pairs. The tracker also measures the path traversed by each of the particles through positional measurements obtained as they pass through the instrument. Measurement of the energy of each γ-ray is performed by the calorimeter, which is located directly below the tracker. The calorimeter does this by directly absorbing the energy deposited by the resulting particle shower that is created after pair conversion. Finally, the entire detector is surrounded by the ACD, whose purpose is to detect incident charged particles that would otherwise be indistinguishable from γ-ray photons, thus providing an important means of background rejection.

The converter consists of high-Z material (typically tungsten or lead), while the tracker is made up of position-sensitive charged particle detectors. The converter-tracker is layered into multiple conversion/tracking planes, because the converting material itself causes multiple scattering, which must be minimized in order to achieve the best angular resolution. In considering the distribution and thickness of the converting material in the instrument, a balance must be achieved between maximizing the total amount of converting material (which maximizes the radiation lengths through which the photon passes, thus allowing for the greatest conversion efficiency) and minimizing the loss of angular resolution via multiple scattering

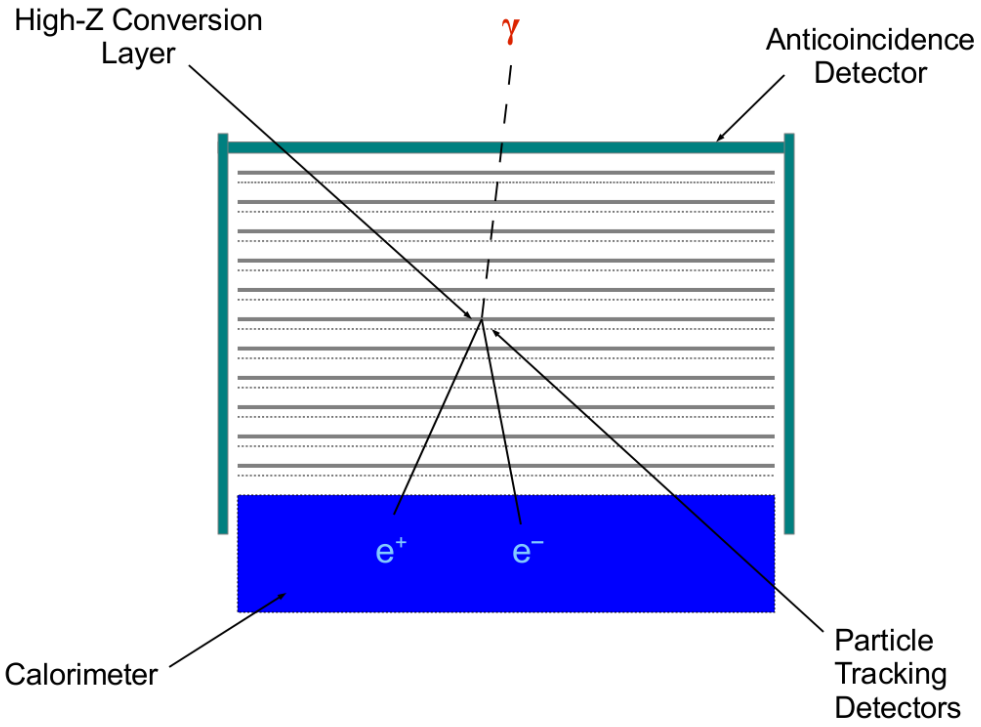

Figure 1.5: Diagram of a pair-conversion telescope.

through the material. To achieve this balance, alternating thin layers of converting material are stacked as closely as possible to the top of the planes of the tracker. After the initial $e^+ e^-$ pair is created in the converting material, the original direction can therefore be determined before the effects from multiple scattering become significant.

The calorimeter measures the energy of the event by directly absorbing the kinetic energy of the electromagnetic shower that is induced by the event. The most common type of calorimeter is made up of scintillating material whose light output is measured through light-sensing detectors such as photomultiplier tubes (PMTs) or photodiodes. A significant amount of scintillating material is often necessary to contain the full shower, thus making the calorimeter the heaviest component of pair-conversion telescopes. To compensate for this, a calorimeter may also be hodoscopic in design, meaning that it is able to track and image the particle shower, which in turn allows the energy to be estimated even if the shower is only partially absorbed by the calorimeter.

The final component of pair-conversion telescopes is the anti-coincidence detector (ACD). The purpose of the ACD is to provide a means of distinguishing the incoming γ-rays from cosmic rays. An ACD is made up of scintillating material, which is a material that produces light whenever a charged particle passes through it. The scintillating material in the ACD is coupled either to photomultiplier tubes (PMTs) or photodiodes that detect the light that is created from this interaction. The ACD itself encapsulates the entire detector, thereby providing a veto signal for any cosmic ray-initiated events that take place within the detector region. When neutral particles such as γ-ray photons pass through the ACD, they do so undetected, thus the scintillating material provides a filter for the γ-ray emission to pass through, while providing a signal for charged particles. By vetoing events that are coincident with a signal in the ACD, the instrument can discard the majority of charged particle background with minimal rejection of γ-ray events.

1.3.2 Ground-based

There are currently two classifications for ground-based instruments that are designed to detect astrophysical γ-rays. The first class is the Atmospheric Čerenkov Telescopes, which are designed to detect the Čerenkov radiation that is created by the particle showers that are induced when a γ-ray interacts with the Earth's atmosphere. The second group of instruments are the Extensive Air-Shower (EAS) arrays, which are designed to measure the particles of the showers themselves (see Figure 1.6). Each of these classes is described below.

1.3.2.1 Atmospheric Čerenkov Telescopes

At energies above $\sim 100\,\mathrm{GeV}$, individual cosmic photons may be detected on the ground by means of the resulting Čerenkov radiation that is produced as the electromagnetic cascade propogates through the Earth's atmosphere. To distinguish between the Čerenkov light produced from electromagnetic cascades and those pro-

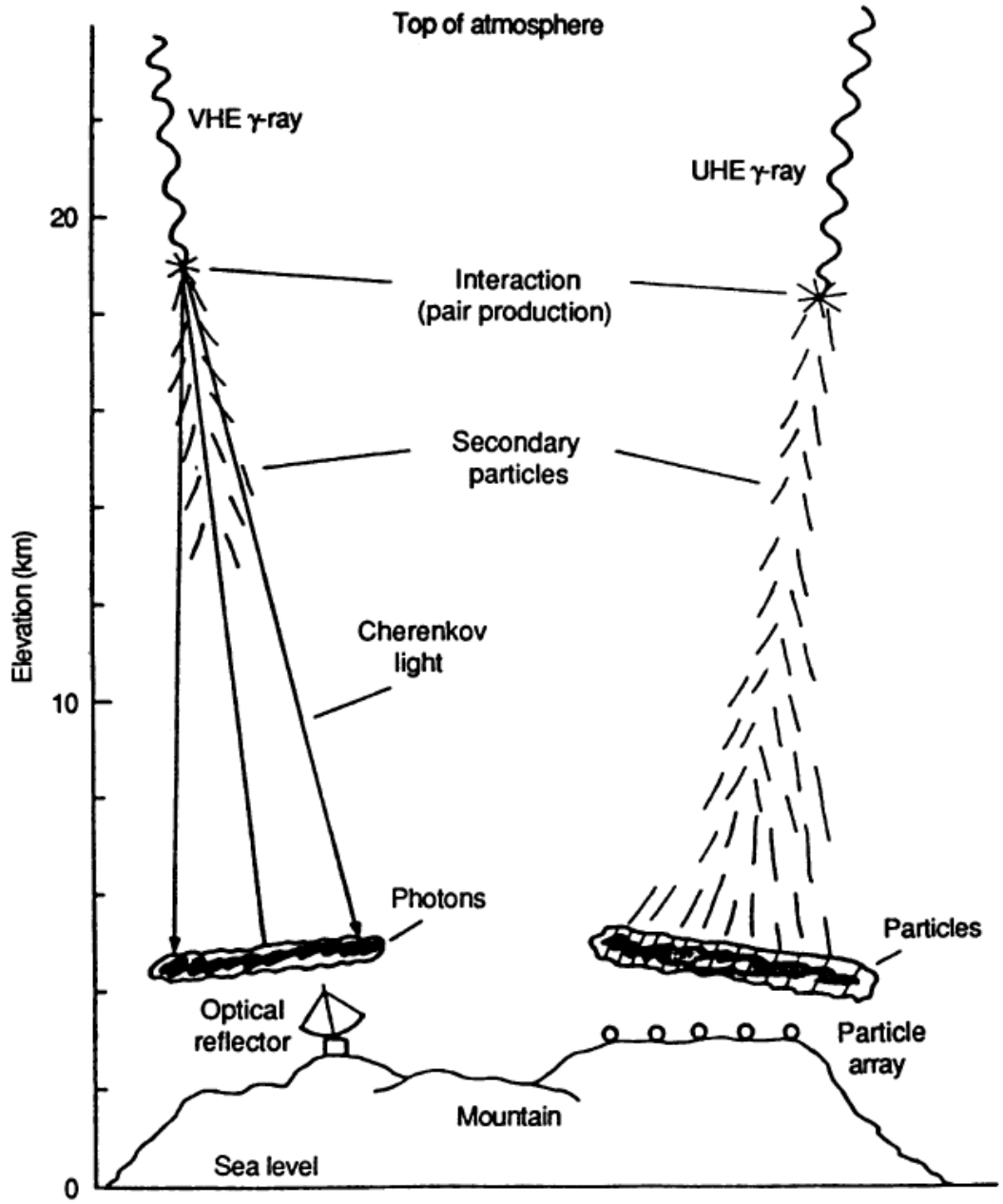

Figure 1.6: Schematic diagram of the two methods for ground-based detection of astrophysical γ-rays. Atmospheric Čerenkov Telescopes (ACTs; left) measure the Čerenkov radiation produced in the electromagnetic cascade, while Extensive Air-Shower (EAS; right) arrays directly detect the secondary particles from showers of sufficient energy to reach the ground. Adapted from [187].

duced from hadron-induced cascades, two techniques have been developed. The first is a non-imaging method that samples the shock front at different places in order to measure the timing and intensity properties of the cascade. This method has been used in the past by such telescopes as STACEE [146] and CELESTE [89]. The second and more conventional technique is that of imaging, which is utilized by the current generation of Imaging Atmospheric Čerenkov Telescopes (IACTs) including H.E.S.S. [48, 83], VERITAS[154], and MAGIC[194]. These telescopes determine the energy and location of the γ-rays by imaging the profile of the Čerenkov radiation created by the cascade, which is then compared to the expected profiles for electromagnetic versus cosmic-ray induced events. Ultimately, IACTs have a relatively poor duty cycle, due to their having to operate during clear, moonless nights. This is made up for by the superior angular resolution and large collection areas of the instruments, allowing them to have much greater precision in localization and variability studies than any other type of γ-ray telescope.

1.3.2.2 Extensive Air Shower Arrays

EAS arrays such as MILAGRO [36] and the HAWC array [14] directly detect the particle showers created by γ-ray induced electromagnetic cascades that are of sufficient energy to be able to reach the ground. The current generation of experiments utilizes what is known as the water Čerenkov technique. Under this method, an artificial body of water or array of water tanks are placed at high altitude, such that when charged particles pass through the water, Čerenkov radiation will be produced. The radiation is then measured by photomultipliers located inside the body of water, allowing the profile and timing of the shower to be reconstructed. Due to the nature of this method, the energy threshold observable by these telescopes is typically higher than that of the IACTs [1]. On the other hand, unlike the IACTs, EAS arrays can operate both day and night and have a very large field of view, allowing them to perform large all-sky surveys.

1.4 Organization of the Thesis

The objective of the research that is presented in this thesis is to examine a sample of Fermi-LAT non-blazar AGN whose multiwavelength properties provide evidence for an origin to the γ-ray emission outside of the subparsec-scale jet. In chapter 1, I reviewed the physical processes that are relevant in γ-ray astronomy. In chapter 2, I will introduce Active Galactic Nuclei, where I will discuss the classifications and properties of AGN in the context of the Fermi-LAT observations as of the second LAT AGN catalog [18]. I will also review the standard models that are used to explain the γ-ray emission seen in blazar sources, as well as to discuss the mechanisms that can give rise to γ-ray emission outside of the standard blazar zone.

[1] The HAWC experiment, however, is estimated to have an operational sensitivity down to $\sim 100\,\mathrm{GeV}$, although the sensitivity will improve significantly at energies above 1 TeV

In chapter 3, I will present an overview of the Fermi Large Area Telescope, where I will detail the LAT design and operational performance and discuss the methods used for event processing and reconstruction. In addition, I will review the concepts behind the LAT source analysis, including a description of the statistical likelihood and its use in obtaining data products such as a spectrum, light curve, and localization.

In chapter 4, I will present my work involving the analysis of three LAT sources: Fornax A, 4C +55.17, and M87. In the case of Fornax A, I perform a temporal and spatial analysis of the source, which I then use to obtain an upper limit to the γ-ray spectrum of the giant radio lobes. The upper limit obtained from the lobe spectrum in turn places an upper limit to the Extragalactic Background Light at the corresponding distance of Fornax A. I then move on to analyze 4C +55.17, where I examine the Very Long Baseline Array (VLBA) morphology of the source as well as its variability in order to demonstrate its nature as a compact symmetric object. I then go on to show that the source can be modeled as a γ-ray emitting CSO, which I then compare against a standard blazar modeling. Finally, I will move on to an analysis of M87, where I will discuss the source in the context of its historic flares at very high energy (VHE; $> 100\,\mathrm{GeV}$), and where I will demonstrate its non-variable nature in the LAT energy range and discuss the possible sites of γ-ray emission that are implied from this analysis.

In chapter 5 I review the work that I contributed for the improvement of the LAT angular resolution, as well as work that I conducted for obtaining error values of event directions that are obtained from the shower profile measured by the calorimeter. I also discuss the methods involved for performing a LAT analysis using event-by-event errors, rather than the current method which involves the use of a point spread function (PSF) defined as a function of log(energy) and cosine theta. I also present a method of making counts maps that are smoothed using the event-by-event errors, as opposed to a standard gaussian kernel smoothing.

Chapter 2
The Astrophysics of Active Galactic Nuclei
2.1 AGN Paradigm

Active Galactic Nuclei (AGN) are defined as galaxies with an "active" center. That is, the central nucleus is considerably more luminous than that of normal galaxies. Historically, AGN have been classified both in terms of their intrinsic properties, as well as in terms of their observational properties, which can vary significantly depending upon their orientation with respect to the observer's line of sight [305]. These differences arise primarily from the the asymmetry of the AGN, such that many of the observed differences can in fact be tied to processes that are intrinsically identical among the different classifications. One of the objectives of AGN astrophysics is therefore to identify the shared intrinsic properties of AGN among the numerous observed classifications in order to unify the classifications into physically distinct objects. An understanding of the structure of AGN along with the underlying physics that describes their emission properties is one of the primary goals of AGN astrophysics.

2.1.1 Black Hole & Accretion Disk

AGN are powered by a supermassive ($\sim 10^6 - 10^{10}\,\mathrm{M}_\odot$) black hole that lies at the galaxy's center, which is enveloped by an accretion disk of hot dense plasma that is actively accreting matter onto the black hole, whose gravitational potential energy acts as the primary source of the AGN luminosity. The accretion disk, which is located $\sim 10^{12} - 10^{14}\,\mathrm{cm}$ from the black hole [49, 305], emits strongly at UV/X-ray wavelengths, losing angular momentum through internal viscous processes, which causes matter to fall further into the black hole potential, acting as the source of fuel for the acceleration of matter along the relativistic jets (see 2.1.3). Outside of the accretion disk is a region of gas and dust that moves at high velocity, emitting broad optical and UV emission lines. This region is aptly referred to as the broad-line region, and can often be obscured depending upon the orientation with respect to the observer's line of sight (see 2.1.2).

2.1.2 Torus & Broad / Narrow Line Regions

Located approximately $\sim 1\,\mathrm{parsec}$ from the black hole is a dusty torus of parsec-scale size [185], which encircles the accretion disk and broad-line region (BLR), thereby obscuring their emission at transverse lines of sight. The postulated toroidal shape is based off of observations of polarized broad lines which have been attributed to rescattered emission from the BLR (thus requiring an asymmetry to account for the polarization[35]), which, along with the observation of hard X-ray spectra in the obscured nuclear regions (e.g. [41]), have led to a consensus that the

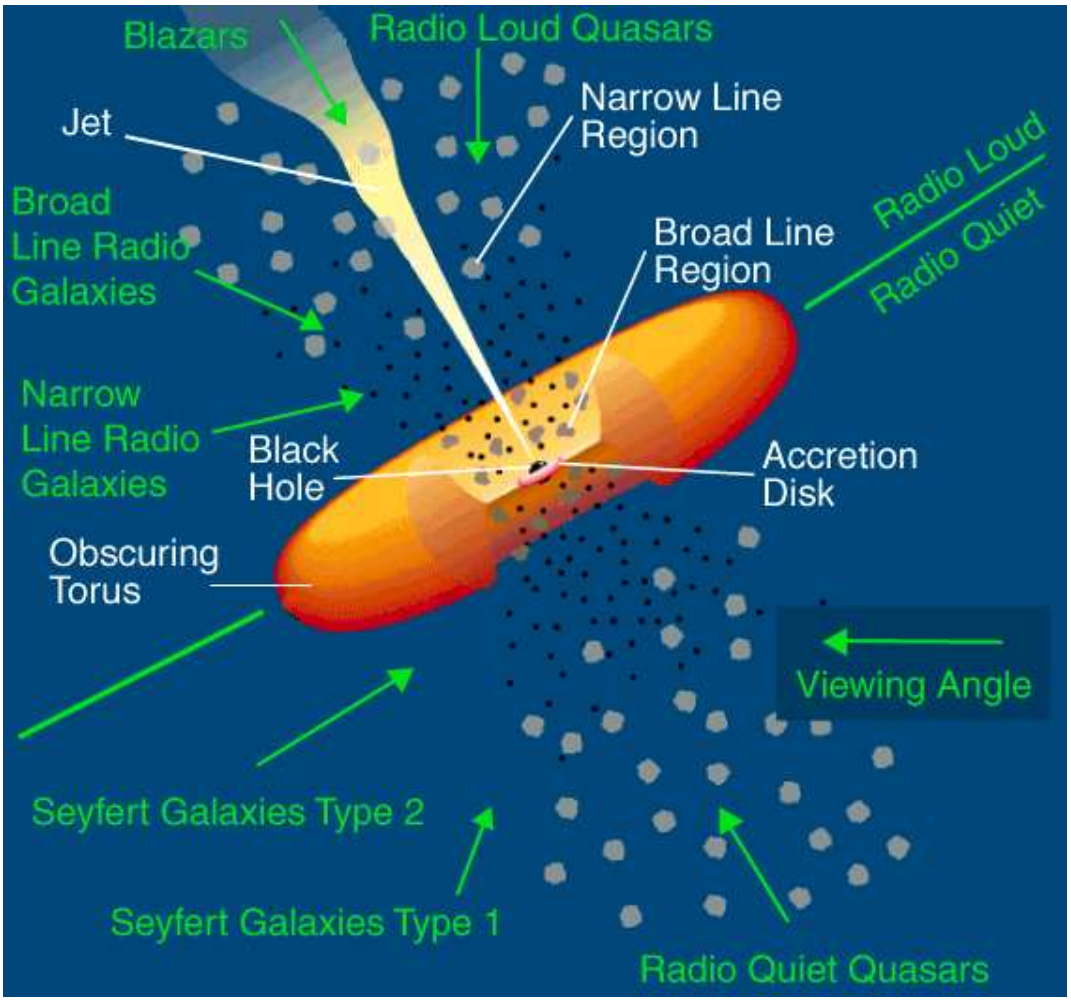

Figure 2.1: Anatomy of an Active Galactic Nucleus. Observed properties and behavior of AGN can vary considerably depending upon the observer's line of sight, despite many objects sharing the same intrinsic characteristics (from [186]).

orientation with respect to the observer's line of sight has a significant influence in terms of the obscuration effects. The precise shape of the torus is however still widely debated, and may vary among different AGN, appearing as a warped disk or other similar configurations, which may or may not be aligned along the same orientation as the accretion disk[189].

Located outside of the obsured regions of the dusty torus ($\sim 10 - 100\,\mathrm{pc}$ [49]) is a region of slower moving clouds of gas that produce emission lines with narrower widths, giving it the name the Narrow Line Region (NLR). Because the NLR is located further out from the torus, the narrow line is not hidden by toroidal obscuration effects, although the presense of narrow lines is not a universal feature among AGN, particularly among the BL lac objects (see 2.2.2.4).

2.1.3 Jets

AGN are typically divided into radio quiet and radio loud objects (see Section 2.2). One of the most prominent features among radio loud AGN is the presense of relativistic jets, which originate from the black hole and extend out in many cases to kiloparsec scale distances [305]. The relativistic speeds and highly beamed emission from the ejected plasma in jets has profound effects on the observed properties of AGN as a function of observer viewing angle (see 2.1.4). The AGN jet also serves as one of the primary sites of γ-ray production in the standard emission models of γ-ray loud sources (e.g. 2.3.1 & 2.3.2). Indeed, radio loud AGN with prominent jets is a key defining feature of γ-ray AGN, with nearly all such objects containing a relativistic jet of some kind.

2.1.4 Relativistic Doppler Boosting

The ejection of relativistic outflows along the jet has some important implications to the observational properties of AGN in terms of the intensity, variability, and apparent velocity of jetted material that is highly dependent on the angle of observation. In particular, the kinematic Doppler factor for a source in relativistic motion is given by:

$$\delta = \left[\gamma\left(1 - \beta\cos\theta\right)\right]^{-1} \tag{2.1}$$

where β is the source velocity in units where $c = 1$, the Lorentz factor $\gamma = (1-\beta^2)^{-1/2}$, and θ is the angle between the direction of motion and the observer's line of sight. Figure 2.2 illustrates the change in δ as a function of θ for several different values of γ.

One of the consequences of the Doppler effect for a relativistically beamed source is the ability for transverse motion to appear to take place at superluminal speeds for sources that are moving at small angles θ with respect to the observer's line of sight. This effect takes place due to the fact that the light originating at some earlier time must travel a longer distance than the light arriving at later times, when the emitting source is closer to the observer. In particular, the observed transverse

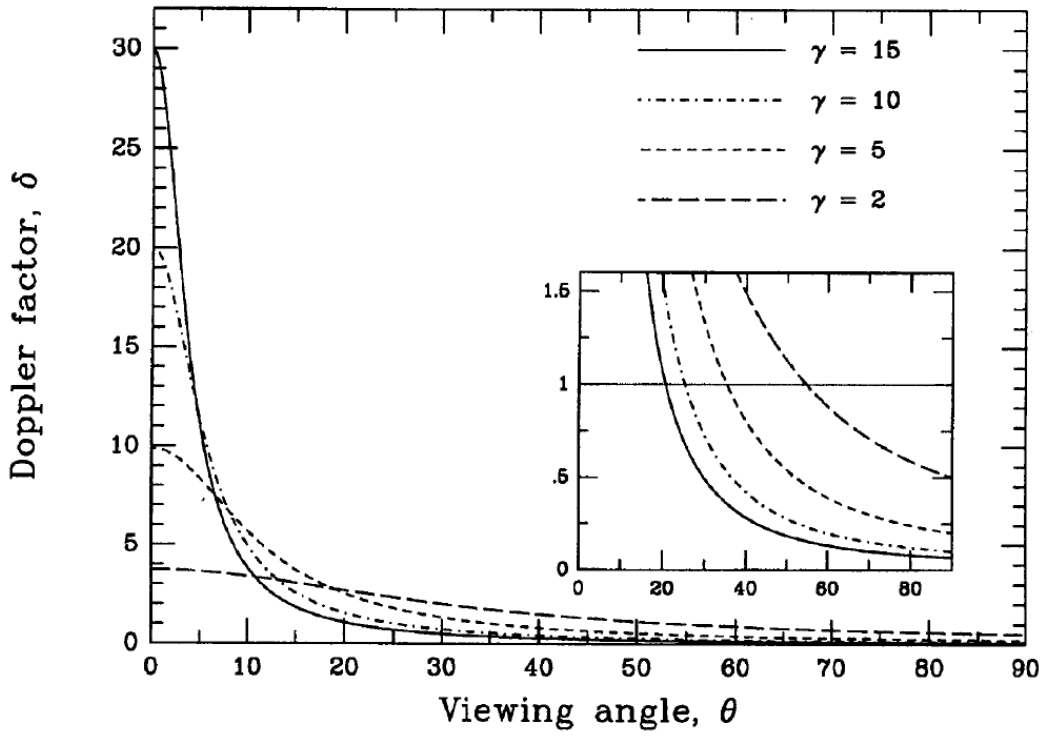

Figure 2.2: Illustration of the Doppler factor δ as a function of viewing angle θ for various values of the Lorentz factor γ (From [305]).

velocity β is related to the true velocity by the formula:

$$\beta_{\rm obs} = \frac{\beta \sin\theta}{1 - \beta\cos\theta} \tag{2.2}$$

Thus, for values of $\beta > 1/\sqrt{2}$, it is possible to achieve values of $\beta_{\rm obs} > 1$ for some values of θ. Apparent superluminal motion of Very Long Baseline Interferometry (VLBI) scale radio emissions that are ejected close to the black hole are commonly observed among relativistically beamed blazars (see Section 2.2.2.4), particularly during periods of high activity.

Another important consequence of the Doppler effect for relativistically beamed sources is the shortening of time intervals between events as measured in the *observer* frame, even in the context of time dilation. Again, this phenomenon arises due to the difference in distance that the light emitted at earlier times must travel compared to the light emitted at later times. The relationship between time intervals in the observer and emitter frame is given by

$$t = \frac{t'}{\delta} \tag{2.3}$$

where the primed quantity refers to the rest frame of the emitting source. One example of how this effect is important is when considering the implied causailty length scales required when looking at the duration of flaring events in AGN that take place over a given measured time. In the case of relativistically beamed sources, with large Doppler factors and small angles to the observer's line of sight, the characteristic time scales of flaring events can be orders of magnitude shorter in time when compared to the same time scales of events when measured at larger angles with respect to the observer's line of sight. Thus, events that might take place over several months for a source that is observed off-angle, can be contracted to day-to-week timescales for blazars.

The last important consequence of relativistic Doppler boosting is the effect that the Doppler factor has on the overall frequency and intensity of a source. When an emitting source is moving toward the observer, it will experience a blue shift

$$\nu = \delta\nu' \tag{2.4}$$

which can shift the Spectral Energy Distribution (SED; see Section 2.2.3) by an order of magnitude or more in wavelength. Furthermore, the specific intensity of the emission will be adjusted by the following formula:

$$I_\nu(\nu) = \delta^3 I'_{\nu'}(\nu') \tag{2.5}$$

This occurs due to the quantity I_ν/ν^3 being a relativistic invariant, and has a profound effect on the observational properties of a relativistically beamed source as compared to a source viewed off-angle. One example of this is that the VLBI imaging of blazars will exhibit unresolved radio cores that dominate the total emission, with brightness temperatures that exceed $T_B > 10^{10}$ K. The intensity of the Doppler boosted core emission is so bright in these cases, that it saturates the non-Doppler

boosted emission from the image, resulting in a core or core-jet morphology when viewed at milli-arcsecond scales (see Figure 2.3). This is one of the characteristic features of blazars in radio astronomy.

2.1.5 Giant Radio Bubbles

The last key feature among the radio loud AGN that contain relativistic jets is the presence of giant, kiloparsec-scale radio bubbles, that can extend out in some cases over an order of magnitude farther than the size scale of the host galaxy itself. Indeed, giant radio bubbles go hand in hand with jetted emission, and depending upon the source age and jet power, radio bubbles on various size scales can be seen, and have even shown evidence of multiple such features over several orders of magnitude in distance among objects which demonstrate recurrant jet activity (e.g. [171]).

One of the more significant discoveries related to the giant radio bubbles that has taken place in recent years is the detection of γ-ray emission from the radio lobes of the nearby galaxy Centaurus A by the Fermi-LAT ([110]; see also figure 2.4), which placed Centaurus A as the first radio galaxy to be spatially resolved with a γ-ray instrument. The γ-ray emission from the lobes in Centaurus A, which makes up over half of the total observed flux from the object, opens up the question of whether this is a defining feature among γ-ray AGN in general, or whether it is a unique feature among a select number of sources.

2.2 Taxonomy of AGN

AGN have historically been classified both in terms of their intrinsic properties, as well as their observational properties. AGN unification seeks to provide a road map between the two, relating objects of different observed classifications in terms of their inherent similarities. One of the major distinguishing characteristics between different AGN classifications is whether or not the AGN are radio quiet or radio loud, with the primary intrinsic difference between the two being the presence of relativistic jets in the latter case, and the absense of jets in the former. In terms of their observational properties, one commonly used criterion to distinguish between the radio loud and radio quiet AGN is based on the ratio of their 5 GHz radio to optical B-band flux, which lies at a ratio of $0.1-1$ for radio quiet objects, whereas the radio loud AGN typically show ratios of $10-1000$ [172]. Within this sub-category, the objects are further classified according to their optical spectra, with objects that exhibit broad optical emission lines being classified as Type 1, while those objects with only narrow lines or weak or unusual line emission being classified as Type 2. Lastly, a special categorization of Type 0 is set aside for the objects with a near-zero angle with respect to the observer's line of sight, which in the case of the radio loud objects make up the objects classified as blazars.

Table 2.1 illustrates the taxonomy of AGN, grouping the observed classifications in terms of their optical emission line properties, increasing or decreasing angle

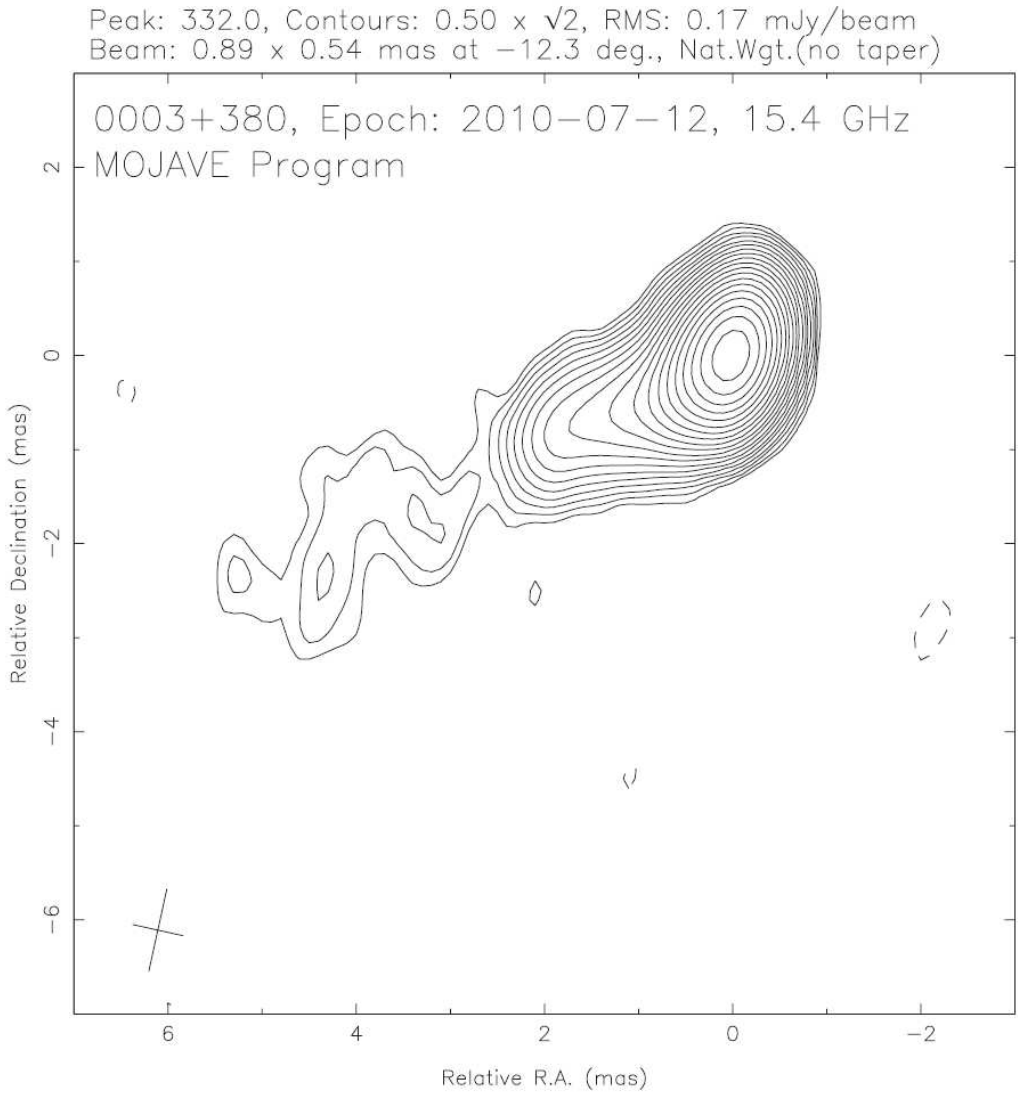

Figure 2.3: Archetypal core jet morphology of a 15 GHz VLBI image of the blazar 0003+380. The unresolved Doppler boosted core dominates the total emission (from [192]).

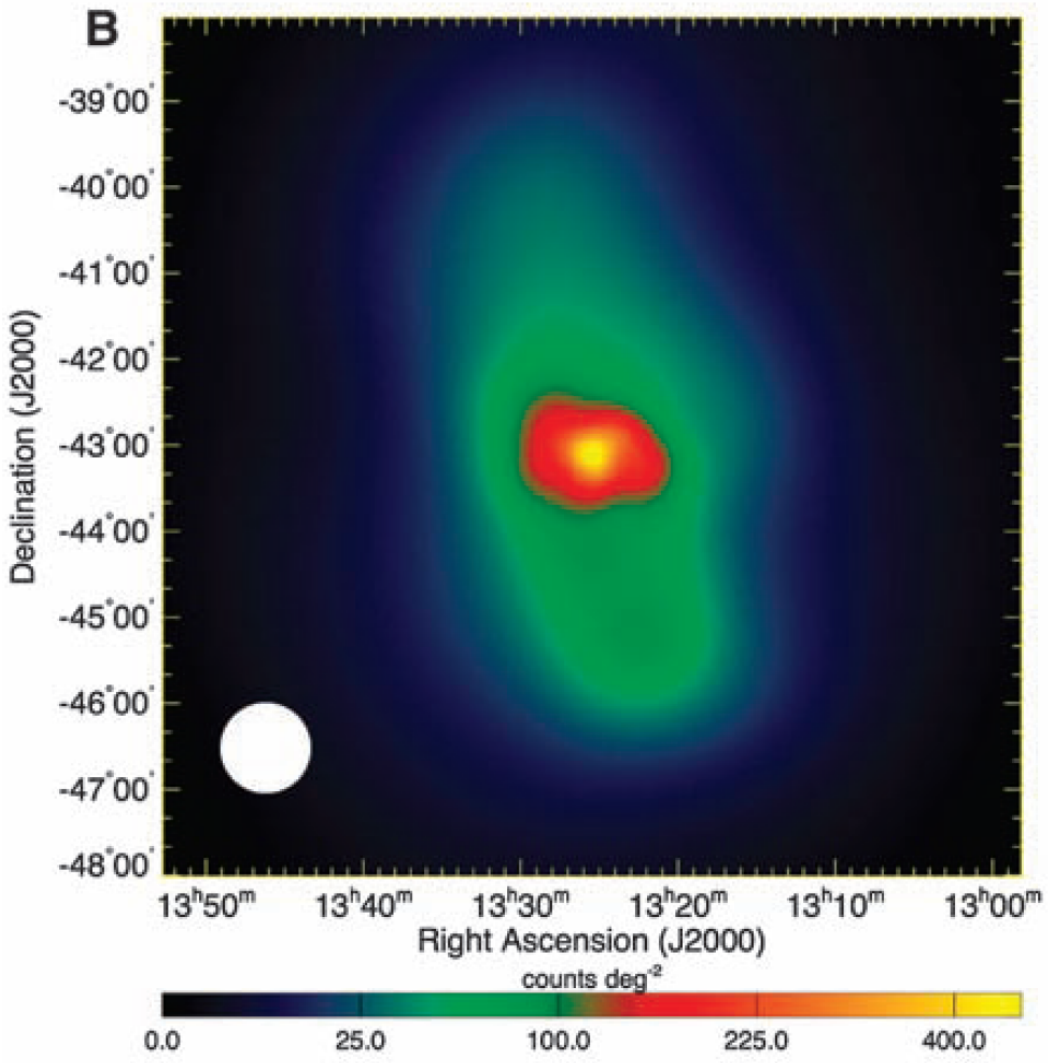

Figure 2.4: Fermi-LAT observation of γ-ray emission from the giant radio lobes of the nearby radio galaxy Centaurus A. The white circle with diameter 1° represents approximately the scale of the LAT point spread function (PSF). Adapted from [110].

	Type 2 (Narrow Line)	Type 1 (Broad Line)	Type 0 (Unusual)
Radio Quiet	Seyfert 2 NELG	Seyfert 1 QSO	Unknown
Radio Loud	FR I FR II	BLRG SSRQ FSRQ	BL Lac FSRQ

Table 2.1: Taxonomy of AGN according to their radio luminosity and optical emission line properties.

with respect to the observer's line of sight, and whether the objects are radio quiet or radio loud. The following sections summarize the basic taxonomy of AGN, as viewed under the paradigm of AGN unification illustrated in Table 2.1.

2.2.1 Radio Quiet AGN: Seyferts & QSO's

Comprising approximately 80% of the AGN population are the radio quiet objects, which include the Seyfert 1 and 2 galaxies, narrow-emission-line X-ray galaxies (NELG), and optically selected quasi-stellar objects (QSO)[305]. The Type 1 radio quiet group is characterized by the presence of broad emission lines, and is comprised of the Seyfert 1 and QSO's. The Seyfert 1 and QSO's are distinguished from each other by their intrinsic luminosities, with the Seyfert 1 galaxies being less luminous, closer objects with clearly resolved host galaxies, whereas the QSO's tend to be found at larger distances, exhibiting higher luminosity nuclei that tend to be unresolved at arcsecond-scale resolutions. Furthermore, an object is classified as a Seyfert 1 if the total energy emitted by the nuclear source is comparable to the total energy emitted by all of the stars in the galaxy (i.e., $\sim 10^{11}\,L_{\odot}$), whereas in a typical QSO the nuclear source is brighter than the host galaxy by a factor of 100 or more [241].

The Type 2 radio objects, which are characterized by their weak continua and only narrow line emission, are comprised of the Seyfert 2 objects, along with the NELGs. The primary difference between these classes lies in the characterization of their optical spectra, which in the case of Seyfert 2's is distinguished from normal galaxies by the emission line ratios of their collisionally-excited lines, which tend to be stronger with respect to the Balmer recombination lines in AGN, as compared to the weaker collisionally-excited lines of regular star-forming galaxies [246]. In the case of NELGs, however, the optical lines can become diluted due to a particularly strong host (e.g. [82, 304]), which can however be revealed as true Type 2 AGN spectra upon closer examination [246].

In terms of the AGN known to emit in the γ-rays, the radio quiet group has widely been found to also be γ-ray quiet [18]. This has important implications to the processes responsible for γ-ray emission in AGN, in that the γ-ray emission must be integrally tied to the presence of relativistic jets (see 2.3). The primary exception is the starburst galaxies (e.g. M82 and NGC 253 [12], and NGC 1068 and NCG 4945 [190]), whose γ-ray emission is instead attributed to cosmic ray electrons and ions formed from supernova remnants in galaxies with high star formation rates.

2.2.2 Radio Loud AGN

The radio loud AGN, which comprise the vast majority of γ-ray loud extragalactic objects, are characterized by the presence of powerful radio jets, which act as the primary site of γ-ray production in AGN (see 2.3). As in the case with their radio quiet counterparts, the radio loud sources are further divided into Type 2, Type 1, and Type 0 objects, with the primary distinction between each type being the angle at which the observer's line of sight is pointed with respect to the object's orientation.

2.2.2.1 Radio Galaxies

Making up the Type 2 radio loud sources are the Narrow-Line Radio Galaxies (NLRG), which have jets that are pointed at nearly perpendicular angles with respect to the observer's line of sight. The NLRGs are further divided into the Fanaroff-Riley type I and II (FR I & FR II; [104]) radio galaxies, which further distinguishes them based upon their radio morphologies and luminosities (see Figure 2.5), although this morphological distinciton is often made between the Type 1 objects as well (see 2.2.2.2). In particular, the FR I type radio galaxies are typically lower luminosity ($L_\nu(1.4\,\mathrm{GHz}) \lesssim 10^{32}\,\mathrm{erg\,s^{-1}\,Hz^{-1}}$) objects [63], characterized by jets and lobes that are brightest in the center, with decreasing surface brightness toward the outer edges. FR II sources, on the other hand, are typically high luminosity sources ($L_\nu(1.4\,\mathrm{GHz}) \gtrsim 10^{32}\,\mathrm{erg\,s^{-1}\,Hz^{-1}}$) that are limb-brightened, with enhanced "hot spots" at the outer edges of the giant radio lobes. The luminosity distinction, however, is only approximate, and there exists some degree of overlap between the two classes[305].

While radio galaxies make up one of the larger populations of misaligned AGN in the Fermi-LAT catalog, these sources predominantly belong to the FR I type morphology [18, 13]. To date, no high confidence associations of LAT sources with NLRGs of FR II type morphology have been reported. The only γ-ray sources of FR II type morphology are intermediately beamed steep spectrum radio quasars (SSRQ), broad-line radio galaxies (BLRG), and compact steep spectrum (CSS) sources ([18, 13, 66], see also 2.2.2.2 and 2.2.2.5) [1]. The lack of γ-ray emission from the FR II type NLRGs may have important implications in the modeling of γ-rays in jetted emission, with the degree of deceleration and collimation within the jets appearing to play an important role [132, 294] (see also 2.3.3).

2.2.2.2 Broad Line Radio Galaxies & Radio Loud Quasars

The Type 1 radio loud objects consist of the broad-line radio galaxies (BLRG), steep spectrum radio quasars (SSRQ), and flat spectrum radio quasars (FSRQ). The distinguishing feature that sets these objects apart from the Type 2 objects, as with the radio quiet Seyferts, is the presence of broad optical emission lines, which are

[1] [13] noted the low confidence association with PKS 0943-76, listing the object as a misaligned FR II galaxy, although this classification remains unconfirmed in the literature

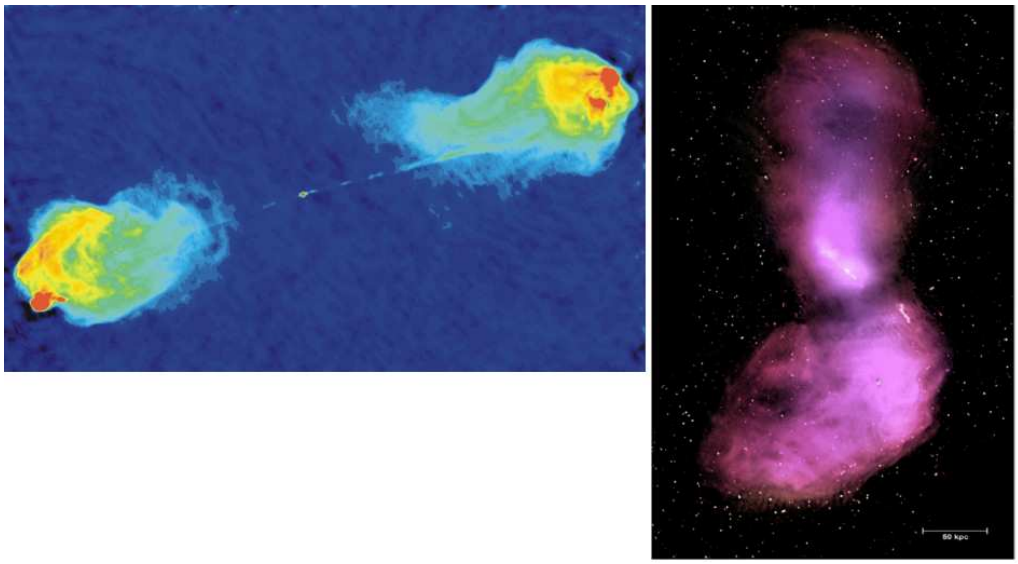

Figure 2.5: VLA radio morphology of the FR II radio galaxy Cygnus A at 6 cm (left) [237], compared to the 1.4 GHz ATCA enhanced image of the nearby FR I radio galaxy Centaurus A (right) [108].

seen in Type 1 objects but are absent in the Type 2 objects. The BLRGs and radio loud quasars are distinguished by their luminosities, with the BLRGs being the lower luminosity objects that are typically found at closer proximity, as compared to the more luminous radio loud quasars, which tend to be found at farther distances[305]. Within the radio loud quasars, sources are distinguished as either SSRQ or FSRQ based upon the shape of their radio spectra, where the broad-band SED of a quasar continuum is often discribed using a power law:

$$F_\nu = C\nu^{-\alpha} \tag{2.6}$$

Sources that are said to exhibit flat spectra are those sources with spectral index $\alpha_r < 0.5$, whereas steep spectrum radio sources have $\alpha_r > 0.5$. This division is related to the intrinsic properties of the source in that the extended, spatially resolved radio components tend to exhibit steep spectra, while compact, unresolved components tend to exhibit flat spectra. Thus, FSRQ spectra are considered to be dominated by compact emission, while SSRQ's are believed to be dominated by extended emission.

Although less predominant than the NLRGs, Type 1 AGN are a confirmed class of γ-ray emitting objects, with sources demonstrating both FR I and FR II type morphologies. Interestingly, among the Type 1 objects, the FR II morphology is the more common, making up 4 of the 5 such sources being reported thus far, including the BLRGs 3C 111 and Pictor A[2] [13, 66], the SSRQ 3C 207 [13], and the CSS/SSRQ 3C 380 [13].

[2]Pictor A should be considered a low confidence association due to possible source confusion in the region [168].

2.2.2.3 Radio Loud Narrow-Line Seyfert 1 Galaxies

Making up one of the more unusual classes of γ-ray emitting objects are the Radio Loud Narrow-Line Seyfert 1 galaxies (NLSy1). NLSy1's are similar to classic Seyfert 1 galaxies in that they demonstrate the typical permitted lines seen among the Seyfert 1 sources, but these lines are unusually narrow (FWHM (Hβ)$< 2000\mathrm{km\,s^{-1}}$), [OIII]/H$\beta$ < 3, and an FeII bump [243]. Among the NLSy1 population, a very small fraction of these objects ($< 7\%$) have been found to be radio loud [180]. Among these radio loud NLSy1's, five objects to date have been reported to be γ-ray emitters [19, 88], with strong flaring on day-to-week timescales being observed in several of the objects, thus revealing that the radio loud NLSy1's contain relativistic jets similar to those of the radio galaxies, quasars, and blazars. Also surprising is that the NLSy1's are predominantly found with spiral host galaxies [93], making them an important population for studying the formation of jets in spiral hosts.

To date, the exact relationship between the beaming angle in NLSy1's as compared to normal Seyfert 1 and 2 galaxies has not been firmly established, although it has been suggested that the flat spectrum NLSy1's, of which the γ-ray loud NLSy1's are comprised, may make up the population of spiral-hosted AGN with relativistic jets pointed toward the observer's line of sight [122]. In particular, the calculated jet power for NLSy1 objects ($10^{42.6} - 10^{45.6}\,\mathrm{erg\,s^{-1}}$) is in general lower than that of the FSRQs or BL Lacs, although the spectral and variability characteristics seem to suggest that a similar central engine is at work [121].

2.2.2.4 Blazars

By far the most common γ-ray emitting AGN are the Type 0 class, most widely known as blazars. Blazars are radio loud AGN whose jets are pointed at very small angles ($\lesssim 10^{\circ}$) with respect to the observer's line of sight. They are characterized by highly Doppler boosted emission that is believed to originate from the innermost regions ($< 1\,\mathrm{pc}$) of the relativistic jet, thus giving rise to unresolved, compact radio cores with high brightness temperatures ($T_b \gtrsim 10^{10}\,\mathrm{K}$), high polarization ($\gtrsim 1\%$), and extreme variability on day to week timescales [305]. Because of their extremely small beaming angles, these sources are most commonly seen to eject radio emission with apparent superluminal motion (see 2.1.4), and demonstrate core and core-jet radio morphologies at VLBI scales [191, 192]. These characteristics are in some sense inherent to the blazar class, and are therefore used to positively identify objects of unknown classification as blazars (e.g. [122]).

Within the blazar population, there are two firmly established classes of objects that are distinguished based upon their optical spectra[3]. These are the blazar FSRQ and BL Lac objects. As with their intermediately beamed counterparts, the blazar FSRQs are identified by the presence of broad lines in their optical spectra, of which the hydrogen Balmer-series lines (Hα λ6563, Hβ λ4861,Hγ λ4340) and promi-

[3]The radio loud NLSy1's, or some subset therein, are most likely a third class of blazar objects that has recently begun to emerge (see 2.2.2.3.)

nent lines of abundant ions (Mg II λ2798, C III λ1909 and C IV λ1549) are typically the strongest [241]. In contrast to the FSRQs, the BL Lac objects typically demonstrate no features in their optical spectra, although they share the other distinct characteristics that make up the blazar class.

2.2.2.5 Young Radio Sources (CSO / MSO / CSS / GPS Sources)

Typically, AGN taxonomy has delt with the grouping of sources based upon observed or intrinsic properties such as jet orientation, source luminosity, optical emission features, central black hole mass, etc. However, one aspect that has often been overlooked, particularly in earlier studies of AGN unification (e.g. [305, 241]), is the role that the age of the source has played in bringing about such a diverse class of AGN that exists today. Evolving nearly in parallel with the modern foundational studies of AGN unification (e.g. [313, 105, 249, 227]), the study of Compact/Medium Symmetric Objects (CSO/MSO), Compact Steep Spectrum (CSS) sources, and the Gigahertz Peaked Spectrum (GPS) sources began to consider some of the most pertinent questions regarding the evolution of AGN, such as how the source's properties may change over the course of its lifetime, and the consequences that such evolution would have to determining its future classification.

In general, the collective group of CSO / MSO / CSS / GPS sources is widely considered to be the young counterparts to fully evolved FR I and II radio galaxies and quasars[105, 249, 227, 39]. The study of young AGN began with the GPS sources, named as such due to their convex radio spectrum that peaks between $\sim 500\,\mathrm{MHz}$ and $10\,\mathrm{GHz}$, and the CSS sources, which were found to have convex spectra that peaked below $500\,\mathrm{MHz}$. The GPS and CSS sources make up $\sim 10\%$ and $\sim 30\%$ of radio surveys, respectively, and are extremely powerful ($logP_{1.4} \gtrsim 25\,\mathrm{W}$) and compact ($< 1\,\mathrm{kpc}$) objects [227]. A third source of high frequency peaked (HFP) sources, which show inverted spectra through the entire frequency range of the GPS sources, has also been discussed [87, 230].

In addition to their spectral identification, young radio sources are commonly identified by their radio morphology. The two common classifications of young radio sources in this regard are the compact symmetric objects (CSO) and Medium Symmetric Objects (MSO). Formally, CSOs are defined as having symmetric VLBI morphologies with total extent of ($< 1\,\mathrm{kpc}$), while MSOs are of size scale $1 - 15\,\mathrm{kpc}$. The sources demonstrate double-sided symmetric morphologies, similar to that of the FR I and FR II radio galaxies, but on much smaller scales (see Figure 2.6). In addition to their typical high power and symmetric VLBI radio structures, CSO/MSO objects are characterized by their extremely low variability, with many sources being non-variable over decade timescales, and typically weak polarization of $\lesssim 0.5\%$ [249]. The ages of a number of these objects have also been calculated through observations of the proper motions of the minature lobes as they advance from the central core, and these have been found to demonstrate kinematic ages of a few thousand years or less [249, 234, 219, 244, 141].

Prior to the launch of Fermi, it was predicted that the class of young radio sources could be γ-ray emitting objects, given their possible evolution into the FR I

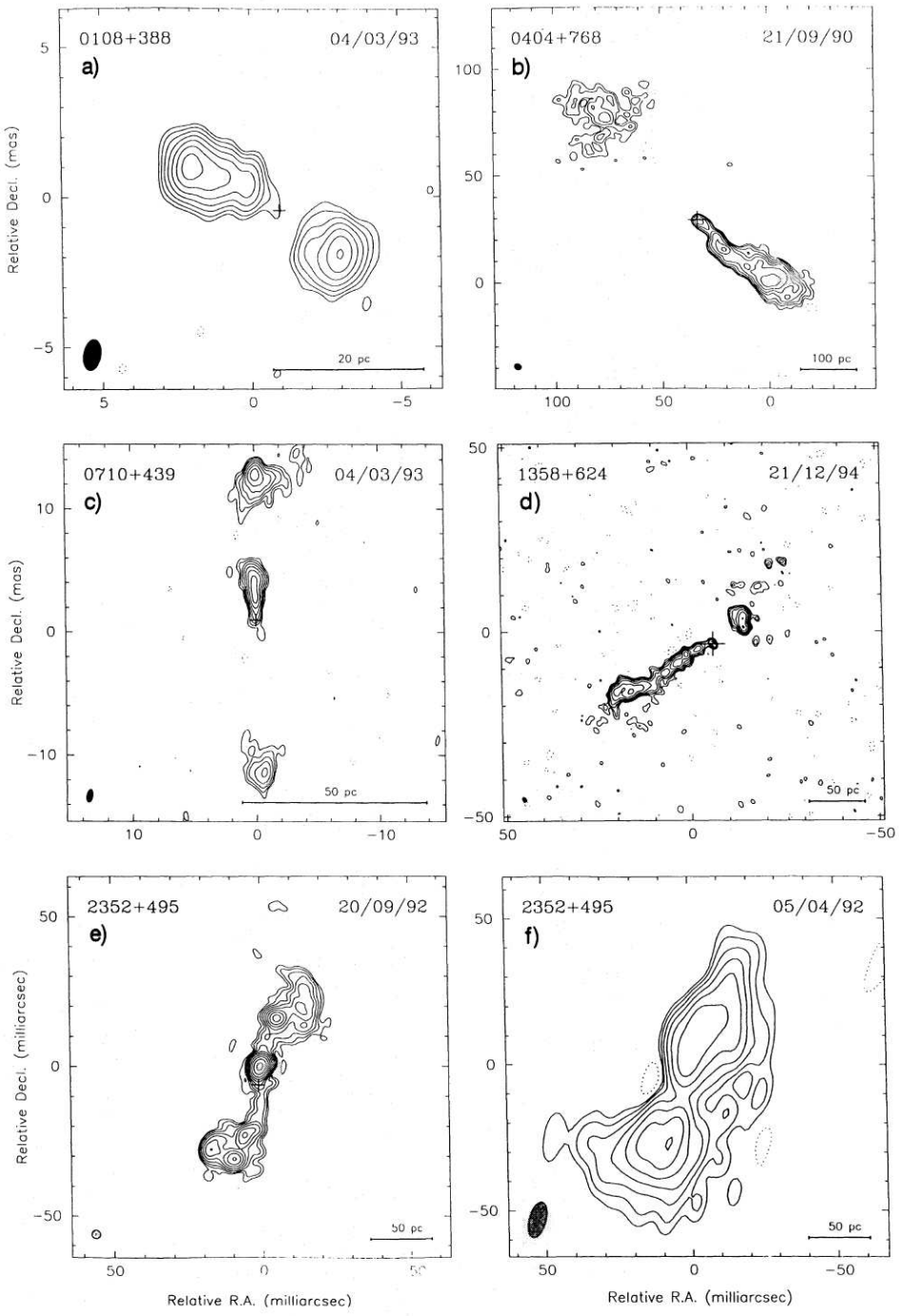

Figure 2.6: Characteristic morphologies of the Compact Symmetric Objects. a) 0108+388 at 8.4 GHz [316], b) 0404+768 at 1.6 GHz [245], c) 0710+439 at 8.4 GHz [316], d) 1358+624 at 8.4 GHz [297], e) 2352+495 at 1.6 GHz [249], f) 2352+495 at 0.610 GHz [249] (Adapted from [249]).

and II objects, coupled with their unusually high radio luminosities (e.g. [177, 281, 176, 175]). To date, however, young radio sources remain an unconfirmed class of γ-ray emitting objects, although a sample of objects with compact symmetric VLBI morphologies that are associated with Fermi-LAT sources has been found [211, 218] (see also 4.2). Thus, the role that young radio AGN may play in non-thermal emission processes at their earliest stages, and how their evolution into γ-ray loud objects takes place, is still unresolved.

2.2.3 SED Classification & The Blazar Sequence

One of the defining characteristics among radio loud AGN, and in particular among the γ-ray blazars, are the broad, double-peaked spectral energy distributions (SEDs) in the $\log \nu - \log \nu F_\nu$ representation of their broadband emission. The nature of this feature is most widely attributed to the synchrotron and IC processes, with the first peak arising from synchrotron emission of relativistic electrons that are accelerated through the magnetic field of the jet, while the second is most commonly attributed to IC emission (see 2.3). Within the blazar subclass of AGN, Fossati et al. (1998) [123] found that there existed a negative correlation between the peak position of the synchrotron component and the intrinsic synchrotron peak luminosity, which Donato et al. (2001) [101] found could be described fully using a single parameter, namely the bolometric luminosity (see Figure 2.7). In addition, it was found that the dominance of the γ-ray peak became more pronounced with decreasing synchrotron peak frequency. These correlations were referred to as the "blazar sequence", and led Ghisellini et al. (1998) [134] to suggest that the correlation was intrinsically tied to the blazars, due to the decreasing intrinsic power of the source being coupled with decreasing cooling effects from a reduced external radiation field as the peak frequency moved from low to high frequency.

Following these initial results of the blazar sequence, evidence against the blazar sequence has been mounting, as the number of known blazars has increased, and it has been found that the previously observed correlation does not fully describe the newer data sets (e.g. [223, 137]). Furthermore, Nieppola et al. (2008) [224] argued that the negative correlation between synchrotron peak frequency and bolometric luminosity could in fact be due to an observational effect that arises from a negative correlation that they measured between the source luminosity and the Doppler factor, which had been ignored in previous work.

While the diversity among blazars may not allow such a simple description as the blazar sequence implies, much of the terminology in terms of the SED classification remains a useful tool, as there nevertheless remains a number of observational properties that can be correlated with the location of the synchrotron peak among the FSRQ blazars and BL Lacs. In particular, the SED classification of low synchrotron peaked (LSP), intermediate synchrotron peaked (ISP), and high synchrotron peaked (HSP) blazars originally established by [235] to classify BL Lac objects is still used within the literature, and has also been carried over in some cases to the blazar population as a whole (e.g. [5, 18, 191]). In particular, sources are classified as LSP if their synchrotron peak $\nu^S_{peak} < 10^{14}\,\mathrm{Hz}$, while ISP

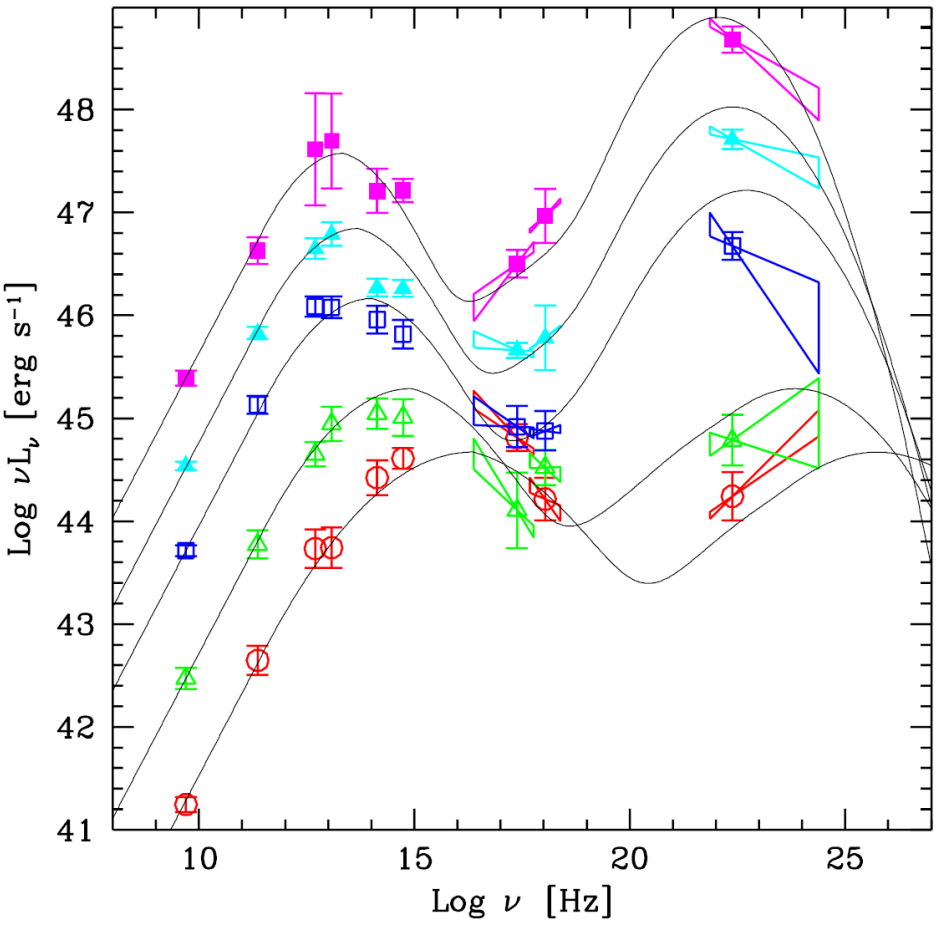

Figure 2.7: The average SED of blazars studied by [123], which shows a distinct double peak for all sources, widely attributed to the synchrotron and inverse Compton processes [101]. The apparent anti-correlation between the low energy synchrotron peak and the bolometric luminosity has historically been referred to as the blazar sequence [249]. Adapted from [101].

sources have $10^{14}\,\mathrm{Hz} < \nu^S_{peak} < 10^{15}\,\mathrm{Hz}$, and HSP sources have $\nu^S_{peak} > 10^{15}\,\mathrm{Hz}$. Among the γ-ray blazars, the diversity in ν^S_{peak} is most widely noted within the BL Lac population, with a relatively even distribution of sources across the frequency range $10^{13}\,\mathrm{Hz} < \nu^S_{peak} < 10^{15}\,\mathrm{Hz}$, while the FSRQ blazars are almost exclusively LSP sources, although some ISP FSRQs have been found [18].

Another important relationship that still holds for the vast majority of blazar sources is that of the ratio between the synchrotron and IC peaks for each of the subclasses. In particular, the FSRQ and LSP BL Lac populations are characterized by soft γ-ray photon indices, with their IC peaks occurring at or near $\sim 100\,\mathrm{MeV}$ [18, 3]. HSP sources, on the other hand, are characterized by much harder spectral indices (and, in general, lower bolometric luminosities, in agreement with the blazar sequence), with IC components that peak at or above $\sim 10\,\mathrm{GeV}$. This is in some sense not surprising, given the underlying synchrotron self-Compton (SSC) and external Compton (EC) processes that appear to be at work in the vast majority of these objects, as will be demonstrated in the following sections.

2.3 Models of Gamma-ray Emission from AGN

The observed double peak in the spectra of radio loud AGN as discussed in 2.2.3 is most widely attributed to the synchrotron and IC processes. While the precise location of the γ-ray emission with respect to the central engine may differ among particular objects, the synchrotron/IC process appears to be at work in the vast majority of cases. The following sections review the most fundamental processes involved in the modeling of the continuum emission from γ-ray AGN.

2.3.1 Synchrotron Self-Compton Radiation

Synchrotron self-Compton (SSC) is the process in which synchrotron radiation is produced by relativistic electrons that are accelerated in the presense of a magnetic field along the jet direction, which is then IC scattered to the high energy range by the same electron population that produced it. In the case of γ-ray loud AGN, this process is one of the primary mechanisms attributed to the IC peak that is so commonly seen in their SED. The simplest representation of this process is the one-zone SSC model, in which a single population of relativistic electrons is responsible for producing both the synchrotron and IC emission [140, 181, 206, 136].

The classical application of the one-zone SSC model (e.g. [55, 181, 206]) uses a conical jet with constant opening half-angle ϕ, and with relativistic electrons and magnetic field injected at a point which lies an axial distance R_0 from the vertex of the cone (see Figure 2.8). The electron population, which is often treated as a spherical or cylindrical homogeneous "blob" traveling with bulk Lorentz factor Γ and an angle to the observer's line of site θ (e.g. [135, 61, 117]), such that the comoving volume may be given by $V'_b = 4\pi R'^3_b/3$, where primed quantities denote the comoving frame. The electron energy distribution (EED) is then allowed to evolve through radiative and adiabatic cooling to produce both the synchrotron and IC

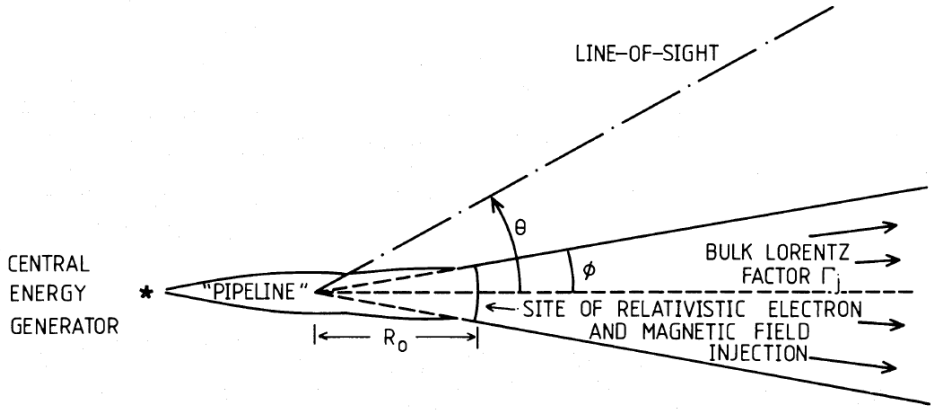

Figure 2.8: Diagram of the synchrotron self-Compton process in a conical jet, as originally proposed by [206]. Relativistic electrons are injected at an axial distance R_0 from the vertex of the cone, resulting in the formation of a shock. Accelerated electrons from within the shock produce synchrotron emission, which is then reprocessed into X-ray / γ-ray energies through inverse Compton scattering of the same electron population off of the synchrotron photons.

peaks. Ultimately, if the EED is known (for example, if it is retroactively obtained from the fit of the synchrotron spectrum, as in [117]), along with the observables of the source redshift, the observed synchrotron specrum, and the variability timescale $t_{v,min}$ (which places constraints on the size of the emitting region), the comoving magnetic field B and Doppler factor δ can be derived using the δ-approximation for the synchrotron flux (see [117] for a detailed review).

It is important to note the relationships that the synchrotron and self-Compton spectra have with respect to the intrinsic source properties such as the magnetic field, source size, electron density, and electron energies. Following the formalism of [57], we find that if the magnetic field B changes, then both the synchrotron and IC flux densities will be affected by roughly the same factor. An increase in the magnetic field will result in a higher synchrotron cutoff frequency (see Equation 1.4), and consequentially a higher flux density at all frequencies between the original cutoff and the new one. However, if the cutoff reaches the Klein-Nishina limit (see Section 1.2.0.2), then the effect of the magnetic field will be suppressed. Furthermore, changes in the doppler factor δ will have the same effect as with the magnetic field, while variations in the electron density (expressed as the normalization) will have a more substantial effect on the scattered emission, due to the additional multiplicative factors of the electron density (see, e.g. Equations 1.8 & 1.9).

In terms of the source size, an increase in the radius of the emitting region (and hence in the volume) will increase the flux densities for the synchrotron and scattered flux densities by a factor of R^3 and R^4, respectively (see expression 2.2.5 in [57]). Reducing the density while increasing the radius R in such a manner as to keep the product of the two constant will result in an effect similar to changing the magnetic field, but will leave the cutoff frequency unchanged, while a softening of

the synchrotron spectrum will result in a sharp dropoff in the scattered spectrum.

2.3.2 External Compton Process

While the one-zone SSC model often does a sufficient job of modelling the IC peak for a large number of blazar spectra, it is commonly found that the high energy peak requires an additional source of seed photons, with higher energy density than that produced from the synchrotron emission of the comoving blob, in order to properly fit the observed X-ray / γ-ray data. An alternative hypothesis to the SSC model proposes that the rescattered emission from ambient photon fields produced from the broad-line region [274], dusty torus [56], and / or from the accretion disk [97, 96] can dominate over the SSC component (see Figure 2.9).

In order to simultaneously achieve the necessary energy densities to exceed that of the synchrotron energy density produced by the jet, while avoiding the inevitable absorption of γ-rays by soft photons that would occur if the production mechanism were to take place at distances close to the jet ($< 10^{17}$ cm), the central source photons must be rescattered at regions farther from the jet, rather than from direct radiation of the central source [274]. Measured in the comoving frame, this radiation will be strongly blueshifted, as compared to the strongly redshifted emission that would otherwise arrive from direct emission from the central source (as was proposed originally by [97]), allowing for much more relaxed constraints on the magnetic field.

While the original EC models for AGN take place within the inner parsec of the jet (typically denoted the "blazar zone"), it is worth noting that these models were largely motivated by the day-to-week timescale flaring that was seen among the EGRET era blazars. EC models involving relativistic electrons much farther from the blazar zone (> 100 kpc scale) [147, 133] have also been necessary to consider in light of recent observations [110]. In particular, the giant radio lobes of radio galaxies such as Centaurus A are filled with magnetized plasma containing ultra-relativistic electrons that are well known to emit synchrotron radiation, and have been observed previously to exhibit IC spectra that extend into the X-ray range (e.g. [109, 84, 167]). At the observed distances from the galaxy, the dominant ambient photon fields are that of the cosmic microwave background (CMB; [148]) and extragalactic background light (EBL; [152, 133], see also 2.3.4.2). When relativistic electrons interact with these fields, the IC processes will result in a shift in the frequency of the scattered photon by a factor of γ^2, similar to what occurs in the comoving frame of electrons in blazar jets. However, a fundamental difference of this process from that of blazars lies in the fact that the electrons within the giant radio lobes are not traveling at a bulk velocity away from the central engine. The emission in this case is truly isotropic, and no Doppler enhancement is expected to take place.

Following the standard one-zone models, a number of additional leptonic models have been proposed to account for various observations that may not be sufficiently described by the simple one-zone SSC or EC interpretations. Such models have featured the addition of multiple emission components [205], decelerating jet flows of downstream components[132], and inhomogeneous flows within the struc-

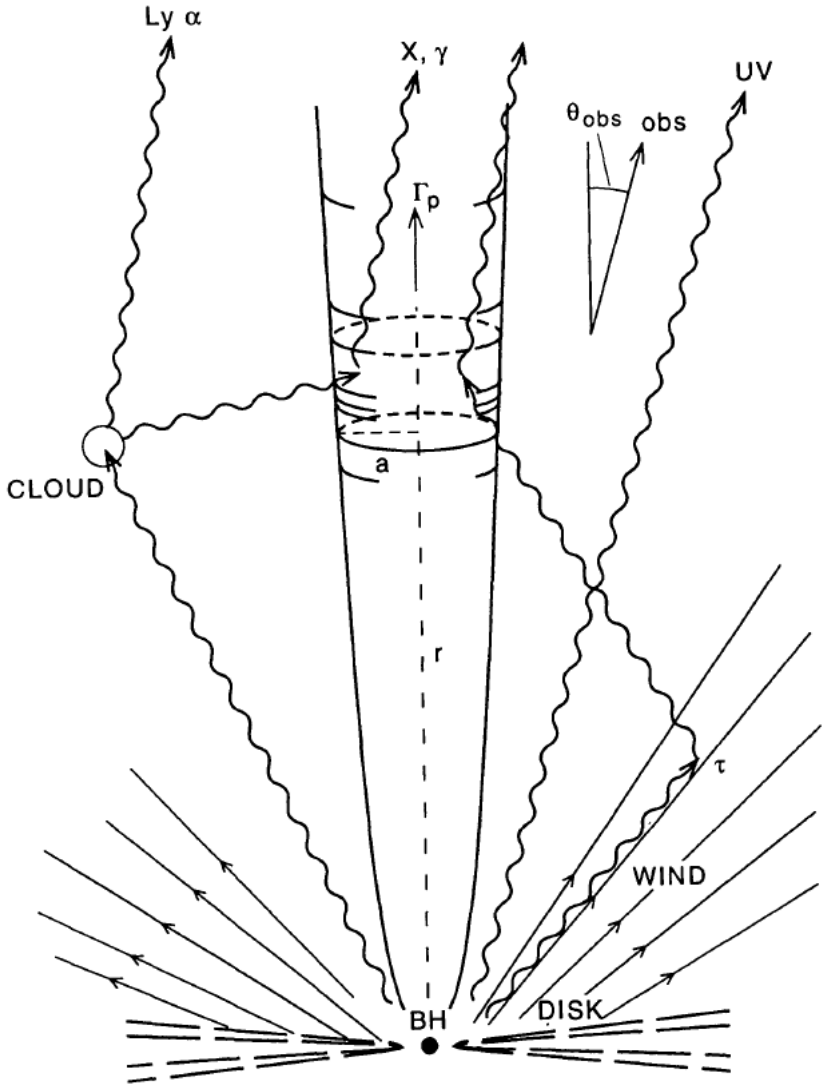

Figure 2.9: Diagram of the external Compton process. Relativistic electrons are accelerated along the jet direction away from the black hole, with the radiating region (short cylinder of dimension a) moving with pattern Lorentz factor Γ_p. Rescattered emission from the surrounding UV disk, broad line region, and dusty torus act as the primary source of seed photons, and dominate over the self-Compton emission if the energy density of the rescattered emission exceeds that of the internally produced synchrotron radiation in the comoving frame [274].

ture of the jet itself [294], to name just a few. While the details of such models may differ between such variants, ultimately the synchrotron and IC processes are still at work.

2.3.3 Proton Based Models

In proton-based models (e.g. [203, 248, 217, 252]), it is assumed that the acceleration mechanism that is responsible for the leptonic emission will inevitably accelerate protons in the same fashion. In this case, the lower energy peak is still attributed to synchrotron emission from leptons, but the γ-ray emission is instead attributed primarily to pion and pair photoproduction and subsequent synchrotron cascade reprocessing, in which protons are shock accelerated to energies of 10^{11} GeV, where they then undergo proton-photon collisions, resulting in cascade emission in the X-ray to γ-ray range which can dominate over the IC component (commonly referred to as a Proton Induced Cascade, or PIC). The primary cooling channel of the protons is photomeson (mainly pion) decay, yielding neutrinos, pairs, and γ-rays.

The ultimate energy source in proton based models is the kinetic energy of the jet, with some fraction of the kinetic energy being converted to non-thermal particle distributions through shock acceleration. Equipartition of the relativistic particles and the magnetic field is also often assumed. The cosmic ray ratio η, defined as a fraction of the proton energy density u_p with respect to the electron energy density u_e, is assumed to be much greater than 1, consistent with observations of cosmic ray energy densities in interstellar space. [204] have argued that the luminosity of the proton-induced shower to the SSC luminosity can be given by:

$$\frac{L_{\rm PIC}}{L_{\rm SSC}} \simeq \frac{\eta}{30} a^{-1/4}(1+240a)^{-1/2} \tag{2.7}$$

where a is the ratio of the photon to magnetic energy densities. Thus, with sufficiently small a and large η, the PIC contribution is expected to dominate over that of the SSC-induced IC component.

2.3.4 Spectral Attenuation in AGN

One of the important considerations to take into account in the modeling and fitting of AGN spectra at γ-ray energies is the effect that photon-photon pair production (see 1.2.0.5) will have on the attenuation of γ-ray spectra at energies greater than that of the combined electron-positron pair $\gtrsim 1\,\mathrm{MeV}$. As shown in Section 1.2.0.5, the cross section to $\gamma\gamma$ pair production is dependent upon the energy of both the incident and target photons, as governed by Equation 1.37. Ultimately, this means that for γ-rays incident upon a target photon field, the γ-rays at $\sim 1\,\mathrm{GeV}$ energies will be most attenuated by soft X-ray ($\sim$keV) photons, while γ-rays in the range of $\gtrsim 1\,\mathrm{TeV}$ will be most attenuated by photons in the IR range and below. Within about an order of magnitude on either side of these peak frequencies, attenuation can still take place, but is suppressed. This effect is important to

consider both for attenuation processes within the AGN itself, as well as those that take place far from the AGN due to the passage of γ-rays through the background radiation that permeates the Universe.

2.3.4.1 Internal $\gamma\gamma$ Absorption

For γ-ray blazars that demonstrate rapid day-to-week timescale variability, tight constraints on the size of the emitting region can be set via the causality lengthscales of light travel times [150], implying in many cases extremely confined emission regions on the order of $< 1\,\mathrm{mpc}$. Confinement to such lengthscales has important implications when considering the attenuation that would be expected at the implied number densities, as discussed in Section 1.2.0.5. In particular, if one were to naively calculate the attenuation due to $\gamma\gamma$ pair production at the observed luminosities and lengthscales for a source that is at rest, one would find that the γ-ray spectra would be highly attenuated above $\approx$ a few hundred keV.

If we consider a spherical emission region of radius R that is *at rest* in the stationary frame, and that emits at a luminosity $L_\gamma \approx 500\,\mathrm{keV}$, the number density of $\approx 1/2\,\mathrm{MeV}$ photons in the source is given by [95]

$$n_\gamma \approx \frac{L_\gamma}{4\pi R^2 m_e c^3} \tag{2.8}$$

A source is said to become *compact* to $\gamma\gamma$ pair production if

$$\tau_{\gamma\gamma} \approx n_\gamma \sigma_{\gamma\gamma} R \gtrsim 1 \tag{2.9}$$

Defining the compactness parameter

$$\ell_\bullet \equiv \left(\frac{L_\gamma}{R}\right) / \left(\frac{4\pi m_e c^3}{\sigma_{\gamma\gamma}}\right) \gtrsim 1 \tag{2.10}$$

where we take $\sigma_{\gamma\gamma} \approx \sigma_\mathrm{T}$ (see [95], Figure 10.2), a source becomes compact to $\gamma\gamma$ pair production when $\ell_\bullet \gtrsim 1$, or if L_γ/R exceeds the electron compactness value

$$\frac{4\pi m_e c^3}{\sigma_\mathrm{T}} = 4.64 \times 10^{29}\ \mathrm{erg\ s^{-1}\ cm^{-1}} \tag{2.11}$$

From the above equation, the implied compactness for a typical emitting region $R \approx 10^{15}\,\mathrm{cm}$ and luminosity $L_\gamma \approx 10^{48}\,\mathrm{erg\,s^{-1}}$ would be $\ell_\bullet \gtrsim 1000$. However, the implied attenuation at energies as low as a few hundred keV is inconsistent with the observed spectra of γ-ray blazar sources that have been found to extend well into the GeV range and beyond. In order for the source to be transparent to its own spectral emission, the assumption that the source is at rest in the stationary frame must be discarded. Rather, γ-ray transparency can be guaranteed if the source is in relativistic motion, such that the luminosity in the comoving frame remains at a value that does not exceed the threshold defined in Equation 2.10 (see section 2.1.4). The minimum Doppler factor is commonly calculated when fitting variable blazar spectra (e.g. [7, 2]), and this is a direct result of the constraints placed by the opacity due to $\gamma\gamma$ pair production.

2.3.4.2 External Absorption and the Extragalactic Background Light

As γ-rays travel from their source of origin to Earth, transversing distances that span up to thousands of megaparsecs, they will attenuate with the isotropic background photon fields that pervade the universe, with the most important contribution coming from background photons that fall in the Infrared to soft X-ray range. As it turns out, the Extragalactic Background Light (EBL), which falls within the UV to far-infrared (FIR) range of the electromagnetic spectrum, is of sufficient energy density to contribute to the spectral attenuation of γ-rays at redshifts beyond $(z \gtrsim 0.1)$[4].

The EBL is the electromagnetic radiation attributed primarily to starlight that has accumulated over the course of the lifetime of the universe since the decoupling of matter and radiation following the big bang [152]. The EBL consists of two spectral components. The first occurs in the UV-Optical-NIR (near-infrared) frequency range, and is referred to as the Cosmic Optical Background (COB). The COB is attributed to the cumulative output of direct emission from stars, while the second component, referred to as the Cosmic Infrared Background (CIB), spans the MIR (mid-infrared) to FIR (far-infrared) range and is attributed to dust emission resulting from the absorption and re-emission of starlight by the interstellar medium.

Because of the nature of its formation, the EBL is not a static quantity. The level of EBL that permeates the nearby regions of space in present time is not equivalent to that of the EBL at higher redshifts when the universe was at an earlier stage of its evolution. Furthermore, the EBL represents only a small fraction of the local background radiation at its respective energy range, with the dominant source of background light being the zodiacal light produced from within our own solar system. Thus, precise measurements of the EBL are difficult to obtain, with most methods providing only lower or upper limits [199, 170, 131, 33, 231].

The attenuation due to $\gamma\gamma$ pair production is represented by an opacity $\tau(z, E)$ that is both redshift and energy dependent. This is due to the fact that the EBL spectrum is evolving over time. The opacity manisfests itself in the typical exponential decay in the power law spectrum above the observed energies at which pair production can take place. Several models have been proposed which seek to estimate values for $\tau(z, E)$, and in general, these models can be classified according four basic methods. The first method is a backward evolution approach, which uses IR data from local galaxies and extrapolates their evolution backward to higher redshifts and shorter wavelengths (e.g. [201, 202, 285, 124]). A second method is a forward-evolution based calculation that models galaxy formation to determine the stellar emission (e.g. [247, 138, 139]). The third approach derives the EBL by inferring the galaxy evolution through observed quantities such as the star formation rate (SFR) density of the universe (e.g. [262, 178, 118]), while the fourth approach uses models of galaxy formation that are based off of direct observation of galaxy populations over the range of redshifts that contribute significantly to the EBL (e.g.

[4]The cosmic X-ray background, which is the primary contributor of soft X-ray photons that would contribute to the attenuation of γ-ray photons at $\sim$GeV energies, is not of sufficient photon density to be a significant source of attenuation in AGN spectra.

[100]).

Through measurements of spectral attenuation of large populations of blazars, the Fermi-LAT has served as a useful tool for placing upper limits on the opacity due to the contribution from the COB [6, 20]. Similar methods have also been performed at TeV energies to place constraints on the CIB (e.g. [284, 279, 24]), while methods using combined LAT and IACT data have also recently been considered [131, 231]. The basic premise of these methods is to either assume a minimum threshold value to the hardness[5] of the intrinsic source spectrum at the attenuated energy range [25], or to measure the spectrum of a blazar source or population at an energy range where EBL attenuation is not yet significant, then assume an intrinsic extrapolation that is consistent with the measured lower energy spectrum. Provided that the redshift of the source(s) is known and that the assumptions regarding the spectral hardness are valid [6], one can then place an upper limit on the opacity as a function of energy at the given redshift by measuring the deviation of the observed spectrum from the extrapolated value as a function of energy. These methods are especially useful for studying the evolution of the EBL over time, due to the fact that the attenuation can be measured in this manner for a large population of sources over a significant range in redshift. On the other hand, this method can only be used to acquire an upper limit.

A more recent method that has been proposed by Geoganopoulos et al. (2008) [133] would use the broadband modeling of the γ-ray emission from the giant lobes of radio galaxies to obtain a measurement of the EBL. By modeling the HE emission that is produced when EBL photons IC-scatter off of the relativistic electrons within the giant lobes (see 2.3.2), a measurement of the EBL can be obtained provided that the lobe magnetic field B and the EED normalization are known. The B field and EED normalization are obtained by modeling the IC emission from the well-measured CMB, which will manifest itself at an energy range that is ~ 10 and 1000 times lower than that of the CIB and COB, respectively. As discussed in Section 1.2.0.2, the IC spectrum will be shifted in frequency by $\gamma_{\rm max}$, where $\gamma_{\rm max}$ is the maximum Lorentz factor of the EED. Thus, for observations with the Fermi-LAT, a very narrow range of $\gamma_{\rm max} \sim 10^5$ serves as the ideal value for measuring the IC component due to the EBL.

[5] a hard spectrum is one with small values of the photon index Γ

[6] Some authors have pointed out ways to circumvent these assumptions (e.g. [283, 60, 27]), which has led to a lack of consensus on the meaning of these upper limits

Chapter 3
The Fermi Gamma-ray Space Telescope Large Area Telescope
3.1 Fermi Large Area Telescope Design

3.1.1 LAT Modular Design

The LAT is built upon a 4×4 array of 16 tower modules supported by a low-mass aluminum grid [37]. Each of the 16 modules functions as an independent unit from the other 15 towers, with each module housing its own precision converter-tracker and calorimeter. Communication within each of these subsystems (i.e. trigger and event readout) is performed by the Tower Electronics Module (TEM), which is located at the base of each tower. The TEM is also responsible for relaying the information from the tracker and calorimeter subsystems to the LAT GASU (Global Trigger/ACD Electronics Module (AEM) Signal Distribution Unit), which is responsible for formatting and transmitting the information to the LAT on board computer.

The primary advantage of the LAT modular design is that of redundancy. Both within the tower electronics themselves as well as within the LAT GASU, a single failure in any of the subsystems will not result in a critical failure overall, due to each subsystem being independent, as well as having a secondary backup at each stage. In the event that there is a critical failure in any one of the towers (due, e.g., to micrometeoroid penetration or impact with space debris), the remaining towers can still function, allowing for the continued use of the instrument at a reduced efficiency.

3.1.2 Tracker

The LAT tracker uses silicon strip detectors (SSDs) for the track reconstruction and primary trigger mechanism, interleaved between thin planes of tungsten that serve as the converting material. The use of silicon strip technology provides a number of advantages that make it ideal for a space-based mission [38]. In particular, the LAT tracker is self-triggering, requiring no external trigger mechanism for the active elements, nor the use of any consumables such as gas [37]. In addition, silicon detectors require a relatively low voltage to operate, are robust and reliable enough to endure a space environment, and provide high signal to noise and low dead time, all while being implemented upon a relatively compact design. These features naturally allow for significant improvements over tracker designs of previous generations that did not utilize silicon detector technology, including a much higher efficiency and a significantly improved angular resolution of individual events.

The LAT tracker geometry is divided into 18 separate layers arranged from top to bottom (Figure 3.1). A layer consists of two separate planes of SSDs oriented at 90° with respect to each other, and which are located immediately below a layer of

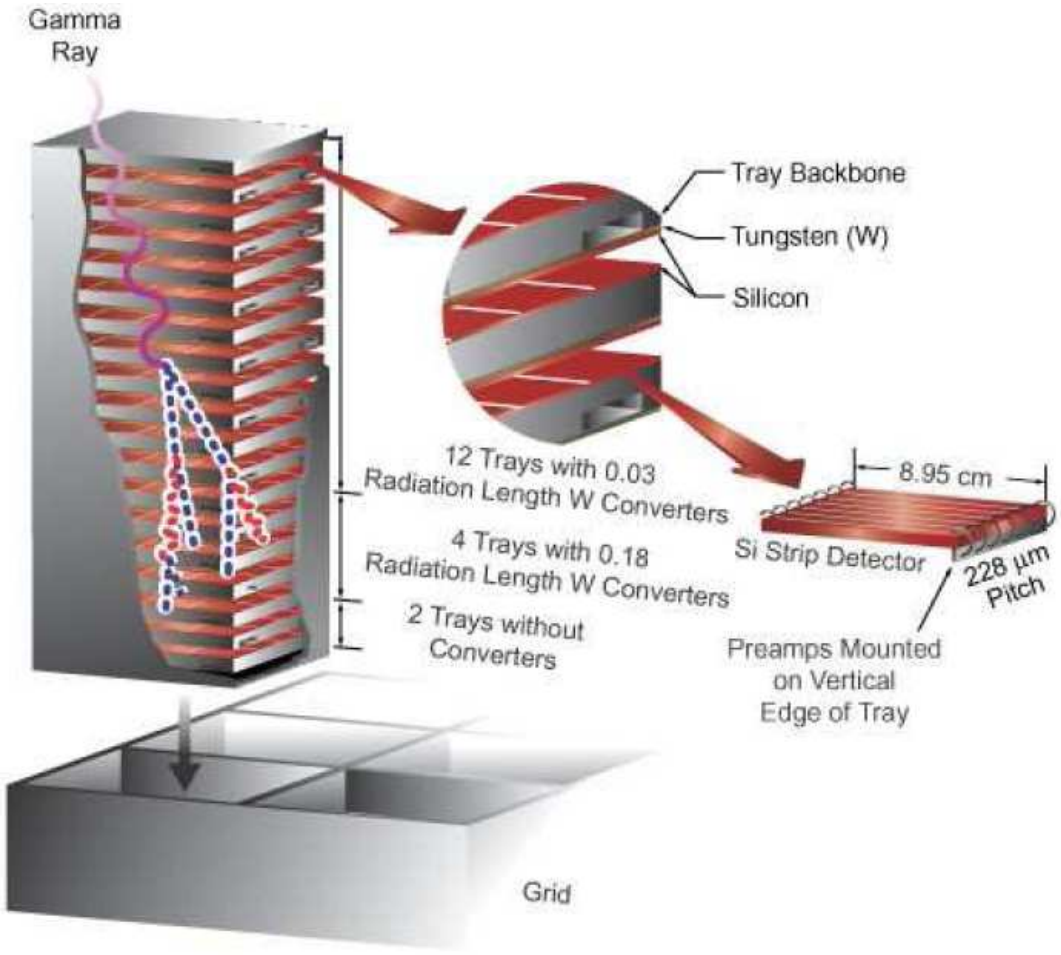

Figure 3.1: Modular design of the LAT tracker [47].

tungsten converting material. There are three different types of layers that vary in the amount of tungsten converting material that is included. The top 12, or "front" layers, contain 3% converting length material. These are designed to minimize the amount of multiple scattering through the tungsten in order to improve detection of γ-rays near the lower energy threshold of the LAT, where a loss of angular resolution due to multiple scattering is significant. The next 4 layers, referred to as the "back" layers, contain 18% radiation length converters and serve to increase the effective area while sacrificing angular resolution due to multiple scattering. These layers are important for the highest energy response in the LAT, where effects of multiple scattering are less important, and where the statistics instead become the limiting factor. Finally, the last two layers contain no tungsten due to the nature of the onboard trigger, which requires three layers in a row to be be triggered in order for the event to be read out (see Section 3.2.1 for further details).

The tracker electronics work through the TEM, which provides the interface between the LAT GASU (see Section 3.1.1), and the tracker and calorimeter front-end electronics [40]. The TEM communicates to the tracker through 36 front-end

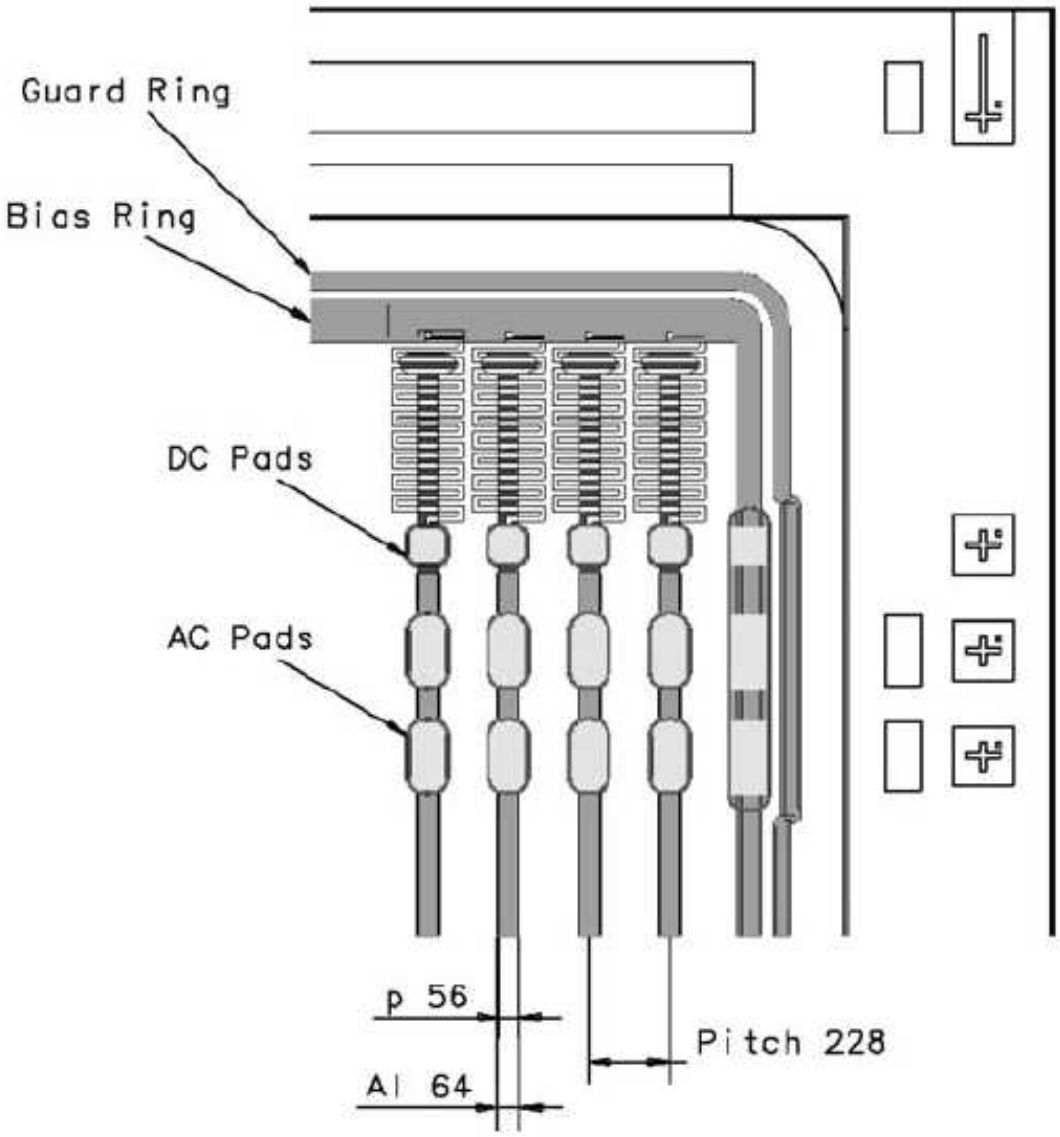

Figure 3.2: Schematic of one corner of the silicon detector. Each strip is biased through a polysilicon resistor and extends underneath the resistor itself in order maximize the active area. The Al readout electrodes include two AC pads for wire bonding to the front end electronics and one DC pad for testing purposes. The guard ring serves to minimize the insensitive area at the detector edge. [47].

electronics multi-chip modules (MCMs) 3.3. Each MCM supports the readout of 1536 silicon strips and is made up of a single printed wiring board upon which are mounted 24 64-channel amplifier-discriminator Application Specific Integrated Circuits (ASICs/GTFE) and two digital readout-controller ASICs (GTRC), the latter of which provide communication to and from the TEM. The MCM architecture is designed such that when a strip initially fires, the only signal sent to the TEM by either of its two GTRC's is the combined OR of all GTFEs located within a single layer. The GTFEs are arranged such that any information passing to or from either of the GTRCs must first pass through all subsequent GTFE chips en route to the GTRC. To prevent a critical failure, the GTFEs are programmed to send data or trigger signals from one or the other of the GTRC's, and to receive commands from only one or the other as well. Thus if one GTFE fails, the GTFEs on either side can be programmed to communicate only through the channels that avoid passage through the failed GTFE. Once a trigger is sent to the GTRC, it is then passed to the TEM as a "trigger request" for trigger processing (See Section 3.2.1).

3.1.3 Calorimeter

The LAT uses a hodoscopic, or imaging, calorimeter (CAL) which serves the dual purpose of measuring the energy of the resulting particle shower after pair conversion of an incoming γ-ray, as well as to assist in distinguishing electromagnetic showers from hadronic showers through imaging of the shower profile. Like the precision silicon tracker (Section 3.1.2), the calorimeter is modular in design, with each of the 16 towers housing its own independent calorimeter subsystem and corresponding electronics. Each subsystem consists of 96 thalium-doped CsI scintillation crystals of size $2.7 \times 2.0 \times 32.6\,\text{cm}$ with PIN photodiode readouts attached at either end [37] to form a crystal-diode element (CDE). The CDE's are individually wrapped in reflecting material to prevent optical leakage and are arranged into 8 layers of 12 crystals each (Figure 3.4), with each layer oriented at 90° with respect to its adjacent layers, thus forming an $x - y$ array to aid in shower reconstruction. The calorimeter makes up the bulk of the mass in the LAT, reaching approximately 2000 kg over all 16 modules, with total radiation lengths at normal incidence of $X_0 = 8.6$ [114, 37].

The photodiodes used in the LAT calorimeter were custom designed to meet the dynamic energy range and mechanical specifications required by the LAT. This range is measured using two separate photodiodes that are mounted over a single ceramic carrier, forming a dual PIN photodiode at either end. The first diode is of larger surface area ($10.5 \times 14.0\,\text{mm}$) and covers a lower energy range from 2 to 800 MeV, while the second smaller surface area ($10.5 \times 2.4\,\text{mm}$) diode covers the range of 40 MeV to 100 GeV, thus providing significant overlap for cross-calibration of the electronics. The asymmetry of the light that is read by the photodiodes also provides an excellent measure of the position along the crystal where the energy was deposited. For a given CsI crystal, calibration tests using cosmic ray muons could successfully produce positional resolutions of a few millimeters for low energy depositions ($\sim 10\,\text{MeV}$) to a fraction of a millimeter for larger energy depositions

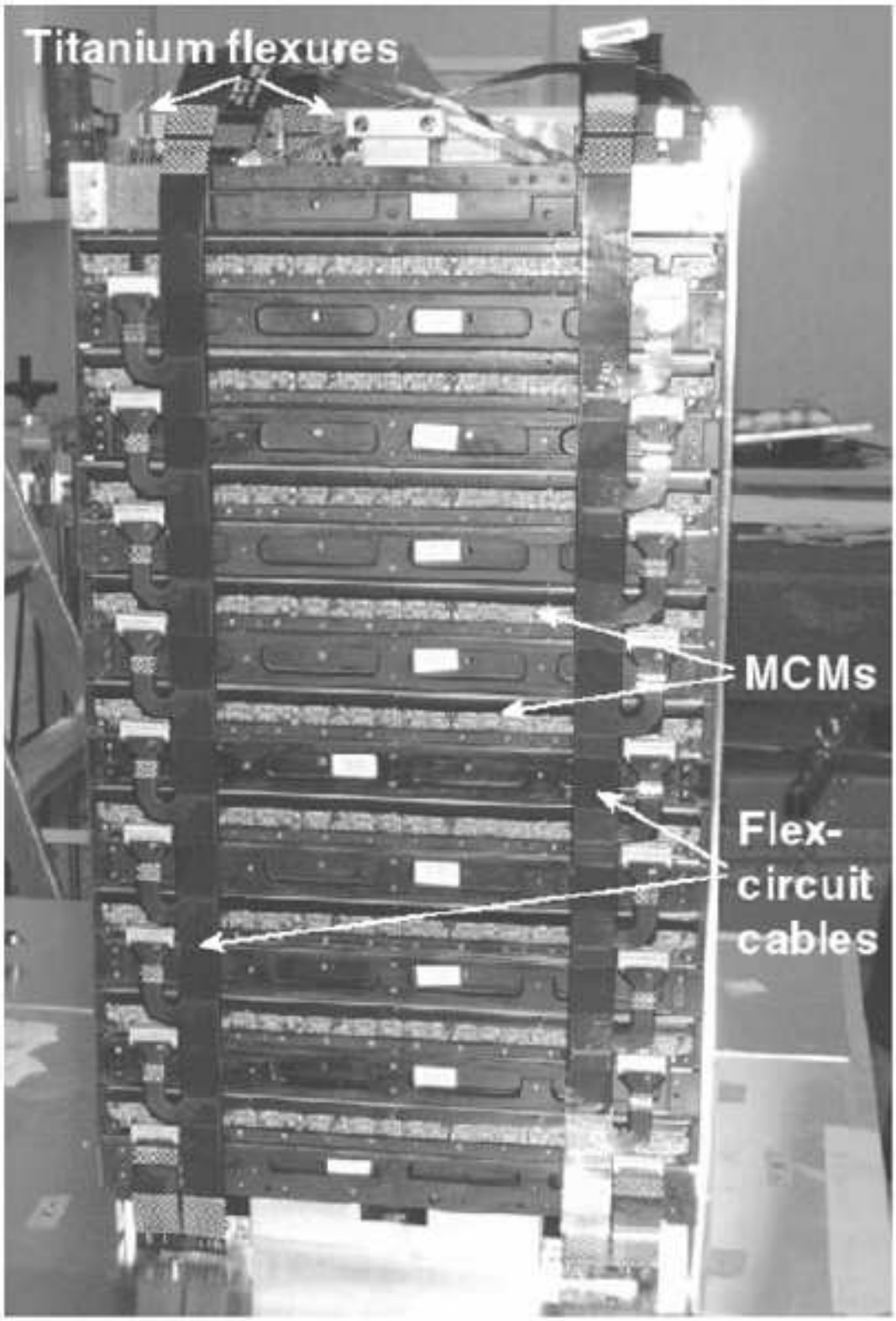

Figure 3.3: Inverted side view of one tracker module. Each side houses nine MCMs and 2 flex-circuit cables which extend to the tower electronics located below the calorimeter (not shown) [40].

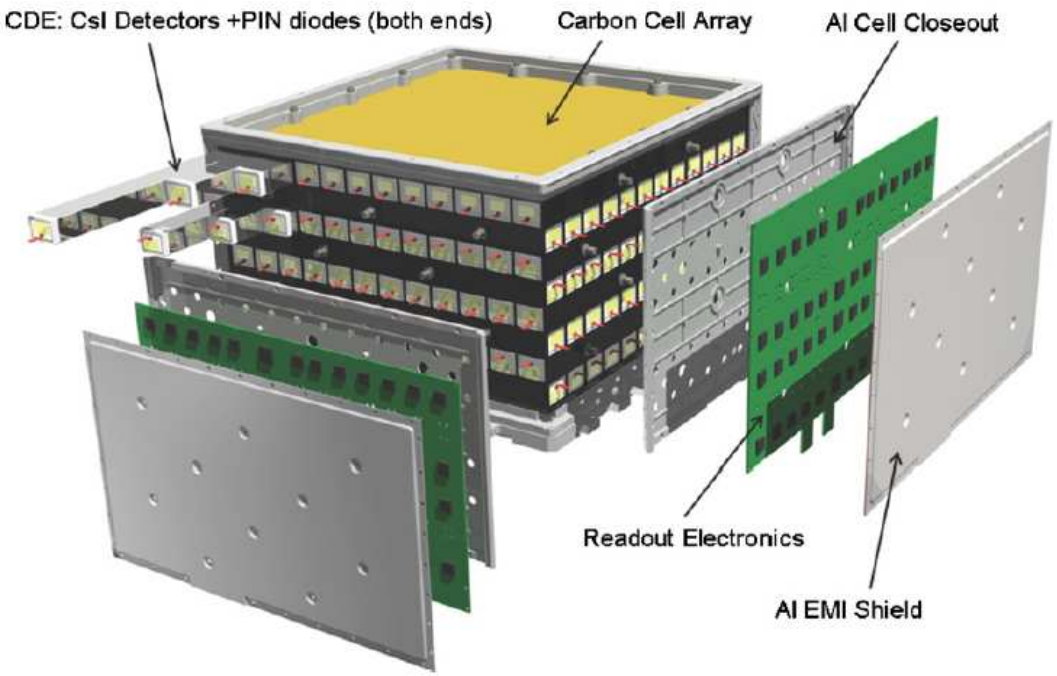

Figure 3.4: The LAT hodoscopic calorimeter design [37].

($\sim 1\,\mathrm{GeV}$) [163].

In addition to the energy range and deposition requirements, the calorimeter electronics were designed to meet a processing deadtime of $< 20\mu$s per event in order to achieve an optimal readout of a trigger acknowledge (Section 3.2.1). This was possible through commercial off-the-shelf successive approximation analog-to-digital converters (ADCs) for each CDE, which allow all digital conversions to be performed simultaneously, thus mimimizing the amount of deadtime after trigger [163].

The organization of the CAL front-end electronics is illustrated in Figure 3.5. The calorimeter electronics are designed to work in parallel with the tracker, with each subsystem communicating independently at the tower level with the TEM (Section 3.1.2). After the initial passage of a charged particle through one of the CDEs, each of the PIN diodes injects charge into a separate charge-sensitive preamp, which then passes through two shaping amps with 3.5μs peaking time. The two shaping amps have different gains in order to select an optimal range in energy for each of the diodes. These include a full range amp for each diode, as well as a 1/4 range and 1/8 range amp for the low- and high-energy diodes, respectively. Together this provides four separate readouts for a single crystal end. In most of the events read out by the LAT, only one of the four signals is selected for readout (see Section 3.2.1). This is carried out by a multiplexer which selects the optimal energy range to be digitized. In addition to the 3.5μs shaping amps, a faster shaping amp with a peak time of 0.5μs and corresponding discriminator is also used to provide for the triggering of events using the calorimeter, which is an alternative to the standard three-in-a-row tracker layer trigger and is used for calibration purposes and for

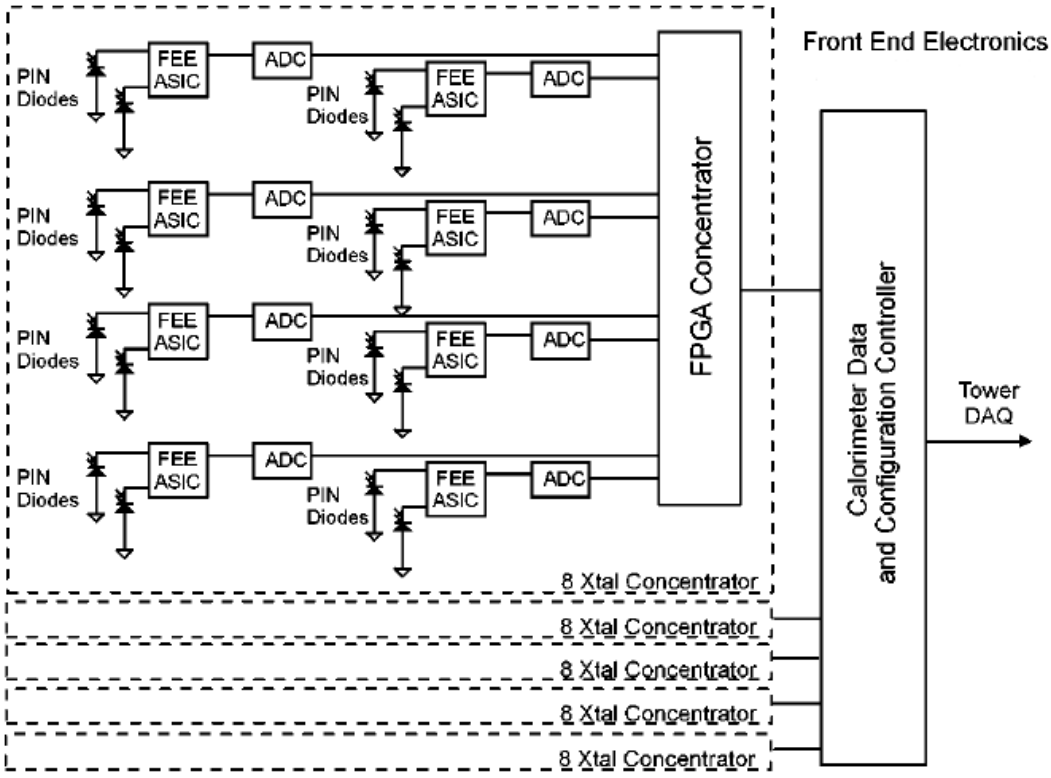

Figure 3.5: Diagram of one calorimeter FREE board [163].

readout of high energy events that did not convert in the tracker (see Sections 3.2.1 and 5.3. After passage through the shapers/discriminators, each signal is then sent to its respective ADC for digitization, where it is subsequently sent to the tower data acquisition system (DAQ) for processing.

3.1.4 Anti-coincidence Detector & Micrometeriod Shield

The LAT ACD serves as a shield that allows the passage of γ-ray photons into the LAT, while rejecting charged particle background. The most notable feature in the LAT ACD design over previous instruments lies in the segmentation of the ACD into multiple segments, or tiles, rather than a single ACD shield covering the entire detector. The purpose of this design feature is to minimize the effect known as "backsplash" [37]. Backsplash can occur when particle showers from high energy events (typically $\gtrsim 1\,\mathrm{GeV}$) deposit their energy into the instrument, resulting in $\sim 100 - 1000\,\mathrm{keV}$ photons from secondary particles to be emitted isotropically and subsequently Compton scatter within the ACD. The resulting scintillation can thereby trigger a veto signal even in the case of a valid γ-ray event. This effect is especially problematic for instruments that utilize a single ACD shield that encompasses the entire detector [52, 116, 301]. Minimizing the effects of backsplash is therefore an important consideration in the design of current-generation pair-

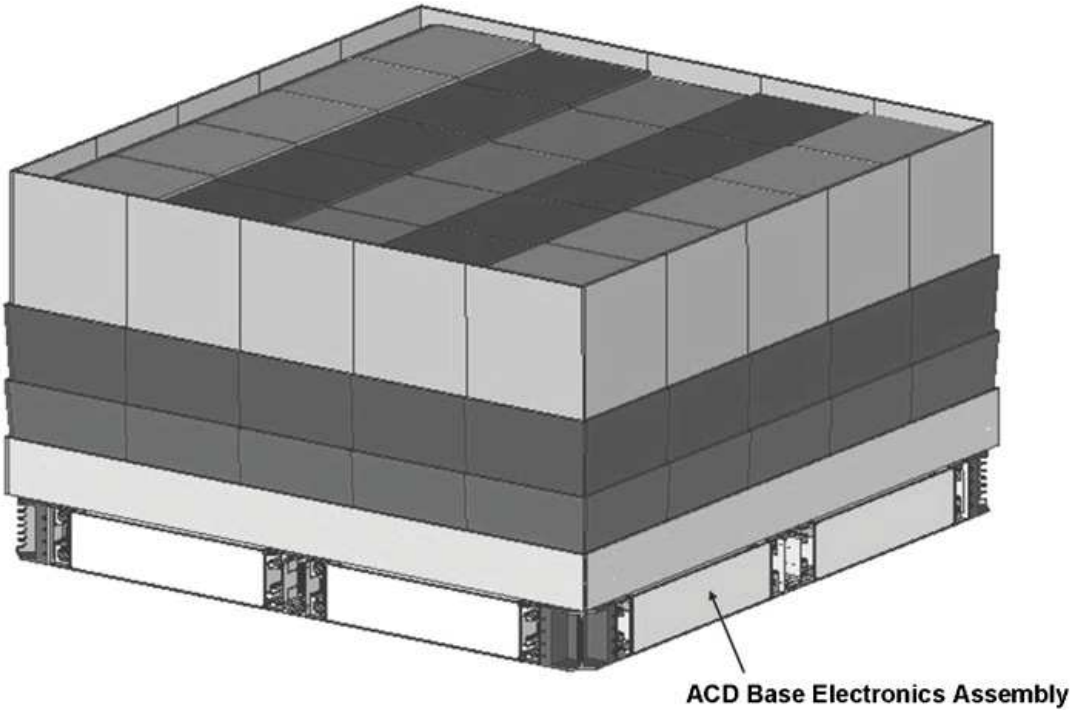

Figure 3.6: LAT ACD tile layout, taken from [37].

conversion telescopes, and the LAT is the first pair creation telescope to implement such a design [215], thus significantly reducing the effects of backsplash compared to previous instruments.

The LAT ACD design is comprised of 89 segments of ElJen-200 polyvinyltoluene (PVT) plastic scintillator produced by ElJen Technology, which is arranged in a 1.7 m×1.7 m×0.9 m encasing that covers the top (z) and four sides (x & y) of the detector [214]. Figure 3.6 shows the arrangement of tiles within the LAT ACD. The top face is made up of a 5×5 array of tiles, while the side faces consist of 3 rows of 5 tiles each, plus one additional large tile spanning the bottom row. The tiles have a thickness of 10 mm, with the exception of the top center row tiles, which are 12 mm thick[1]. Tiles range in size from 15 cm×32 cm to 32 cm×32 cm in addition to the larger tiles with dimension 17 cm×170 cm. Tile size and thickness was chosen in order to optimize particle detection, reaching an overall balance between reduction of backsplash through multiple tiles while maintaining an orbital power consumption of less than 12 W.

In order to maximize the light readout in each tile of the ACD, as well as to shield each tile from external light contamination, the tiles are individually wrapped in two layers of highly reflective white Tetratec, then by two layers of light-shielding black Tedlar. As a consequence of this, the existence of small mechanical gaps $2 - 3$ mm in size between the separate tiles was necessary. These gaps are covered,

[1]Due to their location with respect to the ACD readout electronics, the thicker center tiles were required in order to provide sufficient light yield to compensate for the attenuation of light through the readout fibers

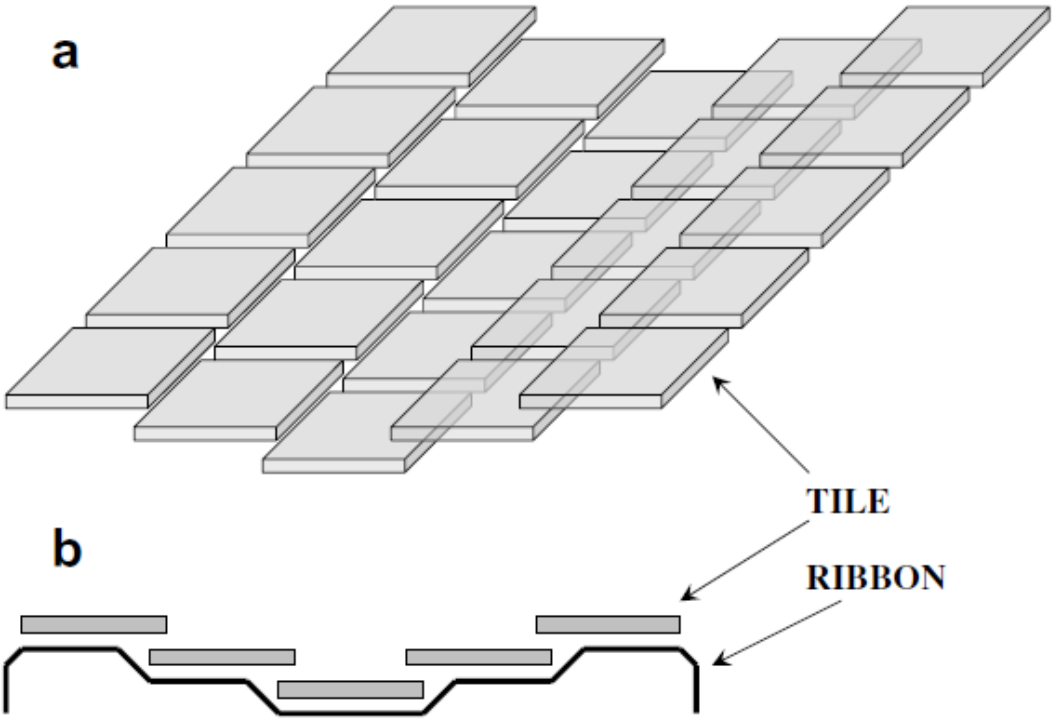

Figure 3.7: (a) Stacking of tiles along a single dimension on the top of the LAT ACD. (b) Cross section of ribbon placement for gaps in the remaining dimension [215].

however, in order to maintain the 0.9997 particle detection efficiency requirement set forth prior to launch [215]. Gaps along one of the dimensions could be avoided by stacking the tiles such that they overlap by 20 mm in a single direction (see Figure 3.7). In the remaining dimension, the gaps are covered using flexible scintillating "ribbons." The ribbons themselves consist of twenty-five 1.5 mm square fibers arranged into three layers approximately 3 m in total length, which are shaped to conform to the profile of each gap. As confirmed by detailed monte carlo simulations, the addition of ribbons in this manner was sufficient in maintaining the overall desired efficiency of > 0.9997 [215].

In addition to its function as a charged particle detector, the ACD also serves the secondary purpose of housing the LAT micrometeoroid shield (MMS) and thermal blanket. The MMS mitigates damage to the instrument from micrometeoroid penetration and high velocity space debris, while the thermal blanket maintains the necessary thermal stability for the LAT hardware to function. Both the MMS and thermal blanket were designed using the minimal amount of inert material possible to meet the specified performance goal of no more than 1 particle penetration in five years at a probability of 95%. Minimization of the material was necessary in order to achieve the lowest degree of irriducible background introduced through cosmic ray interactions (See Section 3.3.4). The MMS was therefore constructed using four layers of Nextel^{TM} fabric located between four layers of 6 mm thick Solimide^{TM}

foam, and reinforced by 6-8 layers of Kevlar^{TM} fabric. This resulted in a total area density of 0.39 g/cm^3, which is roughly 10% above the original design goal, and can withstand penetration from a 2mm diameter aluminum particles traveling at speeds of up to 7 km/s.

ACD tile readout is another important factor in the LAT ACD design. Considerations include the uniformity of light collection (with a pre-launch requirement of $\sim \pm 10\%$ uniformity for each tile), redundancy of light readout for each tile, and minimization of inert material in the LAT field of view. ACD readout is implemented through the use of wavelength shifting (WLS) fibers that are embedded into the tiles and routed to photomultiplier tubes (PMTs) located at the base of the detector. Each tile is threaded with 1 mm diameter WLS fibers BCF-91A, made by Saint-Gobain. This material was chosen to match the 425 nm wavelength peak of the ElJen-200 emission spectrum, thus maximizing the collection of light by the WLS fibers. Due to the nature of the design, some WLS fibers (such as those belonging to the top center tiles) must be longer in order to reach the PMT location, which results in a higher attenuation of light through the material. All fibers of length > 40 cm are therefore rerouted to clear, 1.2 mm diameter BC-98 fibers, also by Saint-Gobain, with measured attenuation lengths of ~ 6 m (as compared to the 1.6 mm of the BCF-91A fibers) [214]. Alternating fibers are then bundled into two groups and sent to two separate PMTs for redundancy.

The ACD electronics processes the light output generated by tiles and ribbons as charged particles pass through. All electronics are located at the base of the ACD in order to minimize the intert material in the LAT FoV (see Figure 3.6). Signal processing begins at the front-end electronics (FREE) boards. The FREE boards are responsible for reading the input signal from the PMTs and sending this information to the LAT GASU (see Section 3.1.1. Two opposite sides of the ACD house 4 FREE boards each for a total of 144 channels, while the remaining two sides house two boards each for a total of 72 channels, thus totaling 216 channels in all. Of these, 194 channels are utilized (one for each PMT). In addition, each of the 2 PMTs belonging to a single tile or ribbon is sent to a different FREE board in order to retain functionality in the event of a failure. Each PMT is also powered by two separate high voltage bias supplies (HVBSs) for redundancy, which are then attached to one of the channels of the FREE board.

The FREE boards include 18 analog ASICs and 18 ADCs, as well as one digital ASIC which connects to the LAT GASU. The analog ASICs function by splitting the analog signal from each PMT into two separate signals, each of which is separately amplified, shaped, and discriminated. The first discriminator is the VETO discriminator, which is used to signal the passage of any charged particle. The second is the high-level discriminator, which signals the passage of heavy nuclei (i.e. Carbon, Nitrogen, & Oxygen) that produce a higher amplitude signal and are used for calibration of the LAT calorimeter. A third discriminator is used to control the choice between the two gains, either high or low, that is then passed to the ADC to be used for processing of the signal in the digital ASIC, which performs the digital logic from the 18 input analog signals given by the analog ASICs and provides the interface for event readout and communication to and from the LAT

GASU.

3.2 Data Aquisition and Event Processing

3.2.1 Trigger Filter & Data Aquisition

Data aquisition by the LAT begins with the onboard trigger, which can be initiated by each of the three major subsystems (tracker, calorimeter, or ACD) via a trigger primitive [260]. The input signals from each of the trigger primitives are combined via an algorithm in the LAT Global Trigger and ACD electronics module (GEM) to form a named trigger specific to the type of primitives that are sent (referred to as the trigger engine [143]), which may or may not initiate a Level One Trigger (L1T) request. The primitives themselves include those originating from one of the 16 towers, those originating from the ACD, as well as primitives that exist solely for calibration and testing purposes. Thus, not all primitives initiate a trigger request. Instead, primitives can be used to veto a particular event or may be set to only be read over a specific prescaled count rate, depending upon the trigger engine that the combined set of primitives belongs to.

A total of 8 different trigger primitives exist, allowing for 256 possible combinations. The eight primitives are the three-in-a-row (TKR), three-in-a-row with ACD veto (ROI), CAL LO, CAL HI, heavy nuclei (CNO), periodic, solicited, and external trigger. From these, a total of 16 trigger engines exist, each of which is initiated under a specific set of primitives (Table 3.1). For example, the primary trigger utilized during nominal science operations that indicates the passage of a possible *gamma*-ray occurs with engine 7, which is initiated when a TKR primitive is received without an ROI. Trigger engines utilizing the CAL LO and CAL HI primitives also exist, where CAL LO and CAL HI correspond to the low and high discriminator signals from each of the calorimeter PIN photodiodes (Section 3.1.3). The primary primitive contributed by the ACD is the ROI. This primitive often acts as a fast discriminator to reduce the number of triggers that must be processed by the onboard filter [215]. An ROI occurs when a signal from an ACD tile shadows one of the 16 towers, and in most cases these events are rejected by the onboard filter, though some are also prescaled for acceptance at a certain rate for calibration purposes.

Upon receipt of a trigger primitive, the GEM opens a trigger window of duration $\sim 600\,\mathrm{ns}$ in order to receive any additional primitives [156]. After the window closes, each primitive that was received is assigned to a corresponding bit in the Condition Summary Word, which is used by the trigger scheduler to determine whether and in what manner to read out the event. In the case of a trigger acknowledge, the GEM sends a trigger message back to the each of the detector front ends (TEM and AEM) with a delay that matches with the signal peak in each of the subsystems [64, 163, 215]. The trigger acknowledge results in the full instrument readout, including tracker hit strip addresses and time over threshold, and pulse heights for the calorimeter and ACD channels [37]. The average dead time for event readout

Engine	Ext	Solicited	Periodic	CNO	CAL-HI	CAL-LO	TKR	ROI	Zero-supp	Ranges	Prescale Count	Marker	Inhibit	Avg Rate (Hz)
0	1	x	x	x	x	x	x	x	Yes	1-rng	0	0	no	0
1	0	x	x	x	x	x	0	1	Yes	1-rng	0	0	no	0
2	0	1	x	x	x	x	x	x	Yes	1-rng	0	0	no	0
3	0	0	1	x	x	x	x	x	No	4-rng	0	0	no	2
4	0	0	0	1	x	1	1	1	Yes	4-rng	0	0	no	2
5	0	0	0	1	x	x	x	x	Yes	1-rng	249	0	no	100
6	0	0	0	0	1	x	x	x	Yes	1-rng	0	0	no	2
7	0	0	0	0	0	x	1	0	Yes	1-rng	0	0	no	150
8	0	0	0	0	0	1	0	0	Yes	1-rng	0	0	no	1800
9	0	0	0	0	0	1	1	1	Yes	1-rng	0	0	no	700
10	0	0	0	0	0	0	1	1	Yes	1-rng	49	0	no	110
11	0	0	0	0	0	0	0	0	Yes	1-rng	0	0	no	0
12-14												0	yes	
15												5	no	

Table 3.1: Table of trigger engines and their respective primitives. Listed are the conditions of the trigger primitives belonging to each trigger engine: 1 = asserted, 0 = not asserted, and x = don't care, along with the readout instructions for each engine (zero-suppression enable/disable, CAL 4-range/1-range), and whether the event readout has been prescaled to a particular value. Table taken from [143].

is 26.5μs[2]. It is essential that the readout of the each detector element takes place before falling below threshold, otherwise the signal is lost. Figure 3.8 illustrates an example trigger timing for a simulated 6-fold coincidence of three consecutive x-y planes of the tracker for a typical TKR trigger acknowledge. If T_1 and T_2 are the times where a particular strip falls above and below threshold, respectively, and if T_{ack} represents the time of the initial trigger request, then the difference of (T_2-T_{ack}) for each strip must exceed the trigger acknowledgement time ΔT_d, in order for the strip to be captured. Each GTFE (Section 3.1.2) must then relay its information of the fired channels back to the GTRC and through to the TEM where it is sent to the GASU for processing. Simulated data have shown that event readout of individual strips is successful with roughly 96% efficiency [64].

The rate of triggered events on board the LAT ranges from approximately 2 to 4 kHz. The available daily downlink volume for ground processing is limited to ~ 104 Gb, which amounts to an average event rate typically between $\sim 400 - 600$ Hz (see Figure 3.9). Consequently, the LAT electronics must facilitate onboard processing to reduce the rate of events being sent to the ground. Thus the LAT GASU also features an instrument-level Event Builder Module consisting of two Event Processor Units (EPUs) that identify charged particle background after event readout from a trigger acknowledge. After onboard processing by the EBM, events are then sent to the ground through the spacecraft interface unit, where they then undergo higher level ground-based processing (Section 3.2.2).

[2]Full 4-range CAL readout and non zero-suppression increase the dead time to $\sim 65\mu$s [143]

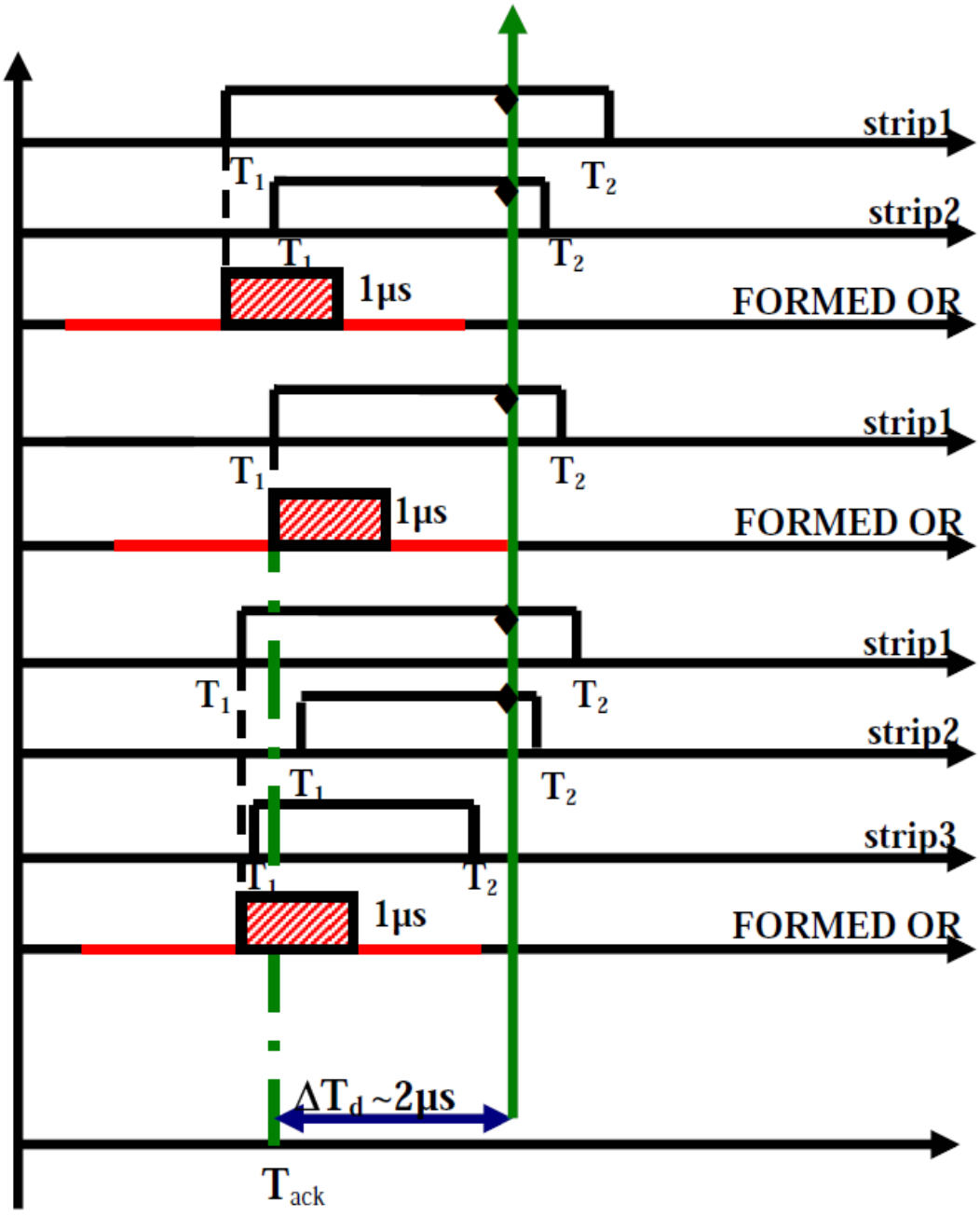

Figure 3.8: Illustration of the trigger timing for a 6-fold coincidence of three adjacent tracker planes. Only the strips that remain above threshold after event readout (T_2 to the right of the vertical green line) are successfully captured [64].

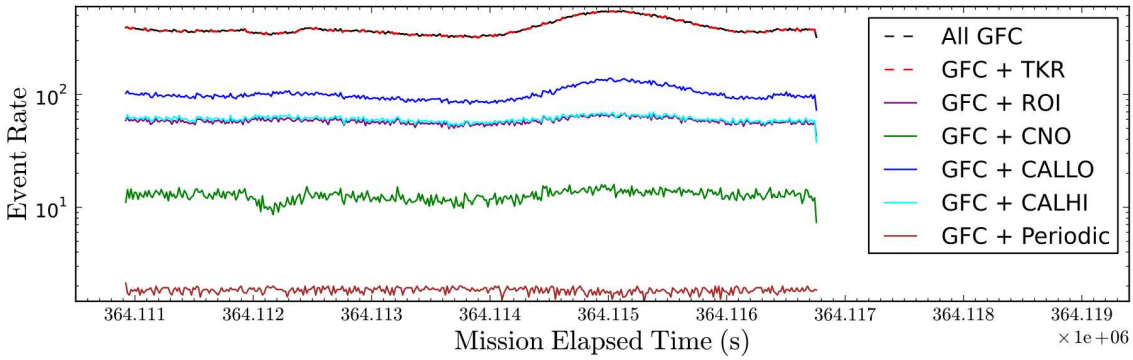

Figure 3.9: Average rate of primitives received after passage of the onboard gamma filter during nominal science operations. Individual primitives for each event are subsequently categorized into trigger engines, which encode the trigger context information and trigger accept message (see Table 3.1)

3.2.2 Data Quality & Instrument Operations

3.2.2.1 Onboard Filter

The processing of LAT data takes place both on the instrument itself via the onboard science processing, as well as on the ground via the pipeline and automated science processing. The first step in the processing of LAT data takes place on board the instrument itself and is referred to as the onboard filter. The primary purpose of the onboard filter is to reduce the rate of events being downlinked from their initial $2-4\,\mathrm{kHz}$ to the required $\sim 400-600\,\mathrm{Hz}$ (Section 3.2.1), as well as to minimize the instrument dead time, which is driven primarily by the readout of the calorimeter during a trigger acknowledge (Section 3.1.3).

The flight software onboard the LAT allows for several different operational modes of the onboard filter in order to facilitate both the nominal science operations as well as instrument calibration and diagnostics. Currently implemented are the Pass-through filter (PFC), track-alignment filter (MFC), Heavy ion filter (HFC), Gamma filter (GFC), and Diagnostic filter (DFC). Each of these is configured with specific sets of parameters that control how events are filtered and sampled, as well as to define which statistics on the filtered events are to be acquired. The primary filter configuration is the GFC configuration, which is designed to accept γ-rays and reject charged particles. This filter configuration is applied during nominal science ops along with the DFC and HFC configurations, which provide monitoring of on-orbit backgrounds and handle the sampling of minimum ionizing particles (MIP) and heavy ion events. The remaining filters operate during calibration runs and are not part of the nominal science operations. These include the PFC configuration, which is designed to accept prescaled events regardless of their trigger type, as well as the MFC configuration (also referred to as the MIP configuration), which is designed to accept off-axis MIPs for alignment of tracker towers.

3.2.2.2 Downlink & Event Processing

After processing of the raw instrument data onboard the LAT, those events that pass the onboard filter are downlinked to the LAT Instrument Science Operations Center (ISOC) for further processing. The pipeline, known as the "Level One Processing" (L1 Proc), begins immediately after downlink of the raw data to the LAT ISOC, which occurs approximately every three hours. The L1 Proc implements the reconstruction of these data using sophisticated track-finding algorithms in order to determine each event's direction, energy, and classification (Section 3.3). The pipeline processes this data at a rate of $\sim 300\,\mathrm{Hz}$ every $1 - 2\,\mathrm{hr}$, thus allowing for the continuous processing of data as it is received from the spacecraft. After the L1 Proc, the data is then passed to the Automated Science Processing, where several higher-level analysis tasks are performed, including refined GRB localization, searching for flaring sources, and individual source monitoring.

The processing of LAT data via the L1 Proc is divided into deliveries and runs. A delivery is the total amount of data received by the ground from a single contact with the downlink satellite, and each delivery consists of approximately $3 - 4$ runs, with each run containing the data obtained over a single orbit[3]. Each of these is assigned a unique id number and processed individually. In addition to the processing of the individual runs and deliveries, detailed information on the LAT operation for each run is monitored for data quality assurance. This includes all information on the instrument status, as well as information about the events themselves, including arrival times, trigger & filter rates, GPS & navigational information, hardware occupancies (e.g. Tkr, CAL, and ACD hit maps), and reconstruction information. Many of these quantities are flagged with expected ranges that provide warnings or errors when a quantity falls above or below its nominal value. It is therefore necessary to continually monitor this information and to address any errors or warnings that may have occurred during a particular run in order to ensure that the LAT is operating as expected.

Monitoring of LAT during each run requires an understanding of the LAT nominal operations in order to determine the significance and proper handling of any alarms that may be triggered. The standard mode of operation performed by the LAT is an all-sky survey mode, where it observes the full sky approximately every 3 hours. This is performed over two 1.5-hour orbits, and between each orbit the LAT alternates its pointing direction at 50° above and below the Earth's zenith. In addition, the LAT remains inactive during certain times, particularly during periods when it is located within the South Atlantic Anomaly (SAA), a region of the sky characterized by abnormally high cosmic ray activity. Occasionally, the observatory will also change its mode of operation to preferentially point to a particular location in the sky. During these pointed mode observations, many of the nominal event rate alarms may be triggered due to the Earth's limb being in the LAT field of view, thus it is important that such effects also be considered.

The final step in the event processing is to analyze the higher level data prod-

[3]individual runs may be divided over multiple deliveries and are not necessarily processed on the ground in the order that the data is received

ucts via the Automated Science Processing (ASP) pipeline. The primary purpose of the ASP is to provide a refined analysis of incoming data and to acquire immediate information on transient events such as GRBs and flaring AGN as quickly as possible. The ASP uses source-finding algorithms to search for candidate flaring sources and any GRB's detected within the given time frame. In addition, routine analysis is performed on individual sources being monitored from a preselected list.

After the ASP processing is complete, any relevant information that is of immediate interest regarding transient sources is released to the community via the Gamma-ray Coordinates Network (GCN). In the case of flaring AGN, sources whose $> 100\,\mathrm{MeV}$ flux is found to exceed a threshold of $1 \times 10^{-6}\,\mathrm{ph\,cm^{-2}\,s^{-1}}$ are reported via Astronomer's Telegram (ATEL) as well.

3.3 LAT Event Reconstruction

The LAT is a particle detector by design, and it follows that the reconstruction of events in the LAT make use of the same track and vertex-finding algorithms used in present-day particle detectors. The following sections describe the methodology used for track and vertex reconstruction for particle detectors in general as well as in the LAT. A more in-depth discussion of the general methods described here can be found in [126] and [286].

3.3.1 Track and Vertex Reconstruction: A General Overview

The primary task of any high-energy particle physics experiment is to recover the kinetic parameters, such as the energy, direction, and starting position, of the particles that are being measured (i.e. after a collision, or in the case of the LAT, after a particle shower is initiated within the detector). The methodology in this case can be divided into three primary objectives: track finding, track fitting, and vertex reconstruction. The purpose of track finding is to establish an initial set of track "candidates" that are believed to originate from a given particle. Each set of track candidates belonging to a single particle is determined through pattern recognition and classification using the sets of position measurements (hits) that are obtained from the detector elements of the experiment. The algorithms for track finding are intended to be conservative, in the sense that none of the potential track candidates are discarded during this stage.

After a list of candidate tracks is established, the task of track fitting is performed. Track fitting uses statistical procedures in order to determine the set of parameters $\boldsymbol{q}_k$ that make up the state vector $\boldsymbol{q}$ that describes the total kinetic state of the original particle, as well as to determine the errors and covariances of each of these parameters in the form of an error covariance matrix $\mathbf{C}$. Examples of track parameters include the position of the particle along the track, its direction at a given position, and its energy. A classification belonging to each of the track candidates (e.g. particle tracks, detector noise, or other forms of background), is also established in order to most accurately reconstruct the original physics of the

interaction.

In addition to track finding and track fitting, the task of vertex reconstruction is also an important step in reproducing the physics of a particular set of events. After the list of tracks is established via track fitting, vertex reconstruction uses the track directions to determine the positions where particles were originally produced. Establishing the set of vertices for a given interaction is important, as it provides information about the energy and momentum of the collision or interaction, as well as to determine the nature of the particles being produced by tracing back the secondary particles to a common vertex. This also allows the decay lengths of short-lived particles to be determined by calculating the distance between two vertices, and in the case of the LAT, provides crucial information about the possible sites of pair production within the tracker, and ultimately determines the final direction of incoming events.

3.3.2 LAT Directional Reconstruction

3.3.2.1 Track Finding

Track finding in the LAT begins by establishing the set of clusters, or pairs of adjacent x-y tracker strips, that may be associated with potential track candidates. Referred to as cluster finding, this step is achieved by separating the unwanted signal, usually in the form of detector noise or so-called "ghost signals" (signatures from particles unrelated to the primary event), from the set of cluster candidates that may be associated with potential tracks. Track finding thus becomes a task of searching via pattern recognition for signatures among cluster candidates that point along possible track directions. In general, the algorithms used to search for track candidates can be divided into global and local methods, where global methods search for all tracks simultaneously, and local methods search for tracks on an individual basis.

In the case of the LAT, track finding is performed through a *combinatoric* local cluster analysis, combining information from the activated detector elements in both the tracker and calorimeter in order to establish a set of track candidates [37]. The primary method of track selections occurs when a some or all of the energy from the induced particle shower is deposited into the calorimeter (as opposed to those that miss the calorimeter altogether or whose energy is deposited exclusively in the tracker). This method is referred to as Calorimeter-Seeded Pattern Recognition (CSPR). Under this method, both the energy centroid and principal axis of the shower deposited within the calorimeter are first determined by performing a moments analysis on the individual CAL crystals[4]. This is done by calculating the center of mass, along with the moment of inertia tensor $\mathbb{I}$, using the measured crystal energy as the weight in place of the mass (for further details, see Section 5.3). Once the CAL energy centroid is established, the individual clusters are found by

[4]as of the most recent pass 7 event reconstruction, individual cluster analysis within the calorimeter is not performed, and the calorimeter is treated as a single cluster. However, see Section 5.3 for recent developments in this area.

assuming that the centroid lies on the trajectory. Track candidates are selected by searching for trajectories within the activated tracker elements that point toward the energy centroid, beginning with those hits in the tracker that are furthest from the centroid and moving inward.

A second method for track finding known as Blind Search Pattern Recognition (BSPR), is performed when the majority of the shower energy is deposited outside the calorimeter. This most often occurs in low-energy showers ($\lesssim 100MeV$), for which a large fraction ($\gtrsim 50\%$) of the total energy is often dissipated in the tracker before reaching the calorimeter. In addition, some showers can take place near the tower edges, such that the majority of the energy escapes through the side of the LAT, rather than being captured in the calorimeter below. For the blind search events, track candidates are selected by randomly searching for trajectories that are consistent with a straight path traveling through adjacent tracker layers and pointed toward the direction of the calorimeter. Any trajectory that lies along three subsequent hits in the tracker is considered in the track fitting algorithms (Section 3.3.2.2).

3.3.2.2 Track Fitting & The Kalman Filter

Once all clusters and their constituent track candidates have been selected, the next task is to find which of these candidates represents the "best track", which in the case of the LAT is the track (or tracks) with the highest probability of pointing back to the site of initial pair creation. In general this step involves fitting each of the track candidates with a track fitting algorithm using a specified track model that describes precisely how the track parameters at a given surface k depend on the state of the parameters at another surface i:

$$\boldsymbol{q}_k = \boldsymbol{f}_{k|i}(\boldsymbol{q}_i) \tag{3.1}$$

where $\boldsymbol{f}_{k|i}$ represents the track propagator from surface i to surface k and $\boldsymbol{q}$ is the state vector containing the full set of state parameters. Propagation of the track requires detailed knowledge of the composition and geometry of the detector in order to accurately predict the multiple scattering of particles through each of the detector layers and to correctly model the energy losses due to ionization and Bremsstrahlung. In addition, the covariance error matrix elements $\mathbf{C}_i$ must also be propagated using the similarity transformation:

$$\mathbf{C}_k = \mathbf{F}_{k|i}\mathbf{C}_i\mathbf{F}_{k|i}^{\mathrm{T}} \tag{3.2}$$

where $\mathbf{F}_{k|i}$ is the Jacobian matrix for the propagation from layer i to layer k:

$$\mathbf{F}_{k|i} = \frac{\partial \boldsymbol{q}_k}{\partial \boldsymbol{q}_i} \tag{3.3}$$

Finally, a relationship between the measured quantities $\boldsymbol{m}_k$ (i.e. the hit strips in the tracker), and the state vector $\boldsymbol{q}$, along with the associated Jacobian of this transformation, must also be established:

$$\boldsymbol{m}_k = \boldsymbol{h}_k(\boldsymbol{q}_k) \tag{3.4}$$

$$\mathbf{H}_k = \frac{\partial \boldsymbol{m}_k}{\partial \boldsymbol{q}_k} \tag{3.5}$$

With this information, the track fitting algorithm can then be performed. The most common type of algorithm used for track fitting in particle physics uses a linear least squares approach, in which the track propagator at any particular layer is a linear function of the state vector at that layer. In the case of the LAT, the algorithm used for track fitting is an adaptation of the Kalman Filter process [126]. The Kalman Filter begins with the first hit belonging to a particular track, then propagates the state vector $\boldsymbol{q}_0$ forward, making a prediction of the state vector $\boldsymbol{q}_1$ and its associated covariance in the layer where the next measured hit is available (Equations 3.1 & 3.2, for $i = 0$, $k = 1$). After propagation, an update step is then applied which corrects the prediction made in the previous step using the information from the measurement in layer k:

$$\boldsymbol{q}_{k|k} = \boldsymbol{q}_{k|k-1}\mathbf{K}_k[\boldsymbol{m}_k - \boldsymbol{h}_k(\boldsymbol{q}_{k|k-1})] \tag{3.6}$$

Here $\mathbf{K}_k$ represents the gain matrix, which is derived using the covariance matrix of the state vector $\mathbf{C}$, the covariance matrix of the measured quantities $\mathbf{V}$, and the Jacobian of the measurements $\mathbf{H}$:

$$\mathbf{K}_k = \mathbf{C}_{k|k-1}\mathbf{H}_k^{\mathrm{T}}(\mathbf{V}_k + \mathbf{H}_k\mathbf{C}_{k|k-1}\mathbf{H}_k^{\mathrm{T}})^{-1} \tag{3.7}$$

The covariance matrix $\mathbf{C}$ is then updated by

$$\mathbf{C}_{k|k} = (\mathbf{1}_{k|k-1} - \mathbf{K}_k\mathbf{H}_k)\mathbf{C}_{k|k-1} \tag{3.8}$$

After filtering, a final smoothing step is applied which propagates the track backwards, opposite the direction of the original track. Figure 3.10 illustrates the basic steps of the Kalman Filter process as the track is propagated from surface $k-1$ to surface k. Starting with the pairs located farthest from the calorimeter, the procedure is iterated over subsequent tracker layers starting with the initial hit, while also allowing for missing hits in dead regions. The procedure is terminated when the track passes through two planes without a hit, barring any dead regions. Once a track has been successfully found and at least two tracker layers have been fully iterated with the Kalman fit, the process is terminated. From here the χ^2 fit, the total number of hits, the total gaps, and other relevant quantities pertaining to the track fit are also obtained.

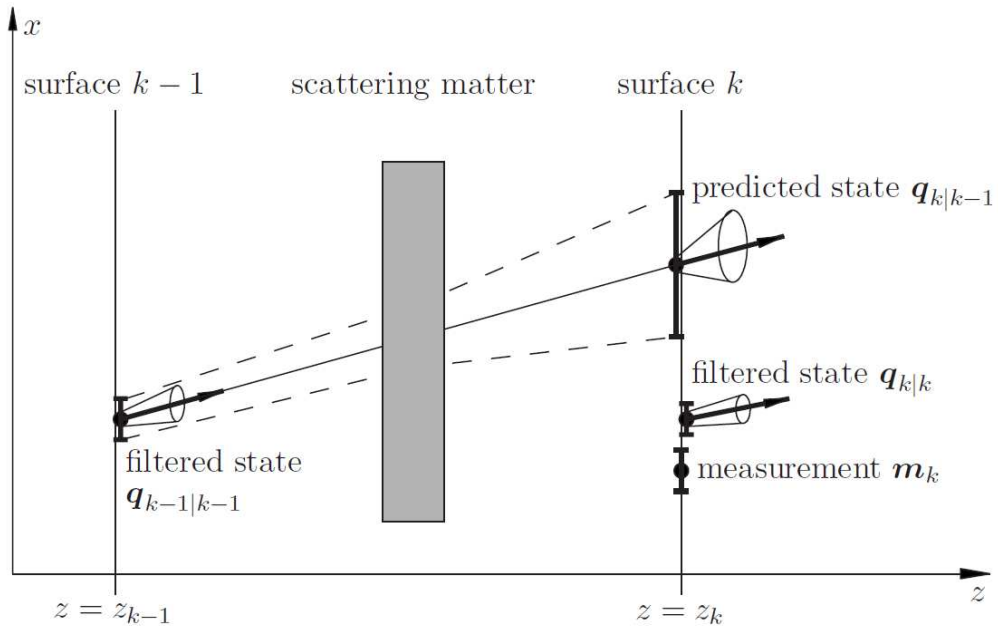

Figure 3.10: Illustration of the Kalman Filter Process [286]. The state vector $\boldsymbol{q}$ is propagated from layer $k-1$ to layer k, taking into account the multiple scattering through the detector material. The measured position $\boldsymbol{m}_k$ is then used as a correction to the predicted state $\boldsymbol{q}_{k|k-1}$ to obtain the final filtered state $\boldsymbol{q}_{k|k}$.

3.3.2.3 Vertex Reconstruction

The final stage of the LAT track reconstruction is the combination of tracks into vertices. A vertex corresponds to the original incoming direction of the reconstructed event. Vertex finding begins with the best track among those fit with the Kalman filter. Vertices are selected by searching for additional tracks that form within a pre-specified distance of closest approach from the the best track (the default is 6 mm). The search is performed by looping over all other candidate tracks for the given event. The highest quality track within the accepted distance (if such a track exists) is chosen as the second track and is combined with the best track to form a vertex solution, which is found by covariantly combining the parameters of both tracks. The vertex position is then chosen to match as closely as possible with the intersection of the two tracks.

3.3.3 Energy Reconstruction

The energy reconstruction in the LAT begins with the measured signal from each of the individual calorimeter crystals, which provides both the measured energy as well as an estimate of the position along the crystal where the energy was deposited (see Section 3.1.3). The energy moment of inertia tensor is first calculated using the measured values of energy and position in instrument coordinates of all of the crystals (for full mathematical description, see Section 5.3). A diagonalization

of the inertia tensor then yields the principal axis of the shower, which is used in subsequent steps of the reconstruction such as the vertex and track fitting. Because the principal moment is needed prior to applying the initial track fitting algorithm, this means that an initial pass of the energy reconstruction must be performed prior to obtaining any information about the event from the other subsystems. Thus, at this stage only the raw energy measured from the calorimeter is known.

Once the information available from the calorimeter is incorporated into the reconstruction and a vertex solution is obtained, further corrections to the energy estimate become possible. At this stage, the vertex solutions are used to estimate the amount of energy leakage that occurred through the sides of the instrument, as well as energy lost due to passage through the tracker material. A number of algorithms are used to determine this depending upon the energy of the shower that is measured from the calorimeter. The default method is a parametric correction, which is based on the barycenter of the shower. This method is also used for iteration of the Kalman fit (Section 3.3.2.2), as it can be applied over the entire energy range of the LAT, which is not true for the remaining method.

The second method, which is used primarily for high energy events, is the shower profile method. This method examines the longitudinal and transverse development of the shower within the instrument and compares against the expected behavior for showers at different energies. The profile method depends on a sufficient deposit of energy to take place within the calorimeter in order for the hodoscopic design to be utilized. In particular, the profile method starts to work with events beyond $\sim 1\,\mathrm{GeV}$, and remains effective for energies up to several TeV.

It is also necessary to apply a correction to the energy losses due to direct deposition of energy into the tracker, particularly for events below 100 MeV. This is done by considering the entire tracker as a sampling calorimeter. The energy that is deposited in each tracker layer is estimated by counting the number of hits that fall within a cone of radius $E^{-1/2}$, where E is the calorimeter raw energy. This energy is then added directly to the corrected energy after reconstruction.

3.3.4 Background Rejection

At the reconstruction level, the background refers to any event in the LAT that is due to the local environment surrounding the instrument, rather than from actual γ-ray sources on the sky. The background is further divided into two categories: reducible background, which is background that in principle can be removed at the reconstruction level (i.e. cosmic ray-induced particle showers), and irreducible background, which is background that is completely indistinguishable from normal γ-ray events (i.e. secondary γ-rays resulting from cosmic ray interactions that take place directly outside the vicinity of the LAT). Background rejection is thus one of the most important tasks of the LAT. This is true for both the onboard and ground-based processing. For example, a necessary requirement of the onboard trigger is to reject a sufficient level of background to compensate for the instrument deadtime that results from the event readout following a trigger acknowledge (Section 3.2.1). Without a sufficient understanding of the background event rates, as well as a means

of reducing this rate to a level that can meet the downlink requirements of the instrument, science with the LAT would not be possible. Furthermore, a reduction of the background using the ground-based processing is equally important, as this ultimately determines the LAT performance (Section 3.4).

Background rejection onboard the LAT lies primarily with the rejection of events with an "ROI" tag (Section 3.2.1). However, rather than to maximize the background rejection at this stage, the primary function of the onboard filter is to meet the LAT downlink requirement of 1.2 Mbps while avoiding the rejection of as many γ-ray event candidates as possible. Therefore, the ROI primitive is designed only to reject those events with the highest probability of being due to charged particle background. Namely, only those regions which directly shadow the tower where the three-in-a-row was called can trigger an ROI. The result is that prior to the ground-based background rejection, only approximately 1 in 300 events are γ-rays, with the remainder being made up of reducible background.

The ground-based rejection of charged-particle background is achieved using a classification tree (CT) based approach [37]. The primary task at this stage is to use the best reconstructed track information in conjunction with the ACD in order to reject the majority of the remaining background events that passed the previous set of cuts. Because the track direction and energy are well constrained at this stage, CT's can be trained to eliminate events with much higher precision than in the previous stages. For example, at the highest energies, only the ACD tile that intersects with the reconstructed track direction is considered, unless the track points at one of the vertical edge corners or at one of the screw holes used to mount the particular tile, in which case the event is automatically rejected. The acceptance or rejection of events also takes into account the event topology, in which case the event is rejected if the shower profile shows an abundance of hits or unassociated tracks indicative of a charged particle, as well as to use the signals within the tracker strips as a means of distinguishing electrons or positrons from hadrons. Ultimately, however, the rejection of charged particle background cannot be achieved without risking rejection of possible γ-ray events as well. Thus the amount of background that is rejected at this stage must take into account the loss of effective area that takes place with more stringent cuts.

3.3.5 Event Classification

As mentioned in Section 3.3.4, a complete rejection of charged particle background can never be fully achieved. Instead, the set of cuts must strike a balance between background rejection and instrument effective area, with no single set of cuts being optimal under all circumstances. Events in the LAT are therefore assigned a classification based on which type of analysis being performed, taking into account the quality of reconstruction within the instrument that is determined using the CT-based approach. For example, bright transient sources such as GRBs are classified under the "transient" event class, which is designated for short-lived, bright sources that demonstrate high statistics with respect to the background. For such events the primary focus is to maintain the highest effective area possible in

order to maximize the photon statistics while still maintaining an appropriate minimum level of background rejection. For much more faint point sources such as low-luminosity AGN, the background rejection plays a much more important role, particularly at high energies where insufficient rejection of a single charged-particle event can significantly affect a source's spectrum. In this case, events are classified as "source" class events, which contain more stringent cuts to reject possible charged particle background than is applied for the transient class, at the cost of lower effective area.

In the latest iteration of the LAT Instrument Response Functions (IRFs), four event classes are used in the standard analysis: transient, source, clean, and ultraclean. Each event class is a subset of the previous class, with ultraclean being a subset of clean, which is a subset of source, and so on. As discussed above, the transient class is used primarily for GRBs, while the source class is used for fainter point sources such as AGN and pulsars. The clean class is used when an even higher level of background rejection than source class photons is desired, as would be the case for diffuse analyses that cover large areas of the sky. Finally, the ultraclean class represents the highest level of background rejection, as well as the lowest effective area of all event classes. The ultraclean class is useful as a consistency check for some types of analysis, particularly in the case when individual events have a significant impact on the science. Events that pass the ultraclean cuts offer the highest level of confidence of being a photon that the LAT reconstruction can provide.

3.4 LAT Instrument Performance

3.4.1 GLEAM Simulation Software

An integral part of determining the LAT instrument performance lies in the use of monte carlo simulation software used by present day particle detectors. The GLEAM (Glast LAT Event Analysis Machine) simulation software package [59], based off of the Geant4 & 5 toolkits, was developed in order to perform the detailed monte carlo simulations necessary for characterization of the LAT instrument response. The GLEAM package hosts all the necessary tools for generating events and simulating their interactions within the LAT, including a full detailed description of the LAT geometry and its materials, as well as proper handling of charged particle interactions with these materials. This offers the important advatange of allowing much of the calibration to be handled through the monte carlo, where reconstructed data can be compared with monte carlo truth without the statistical limitations imposed by on-orbit calibrations.

3.4.2 Effective Area

The LAT effective area ($A_{\rm eff}$) is determined using GLEAM monte carlo simulations. γ-ray events are generated in a $6\,{\rm m}^2$ area in uniform bins of ϕ, $\cos(\theta)$, and $\log(E_{\rm generated})$, with 0.1 steps in $\cos(\theta)$ and 4 bins per decade in energy. A value for

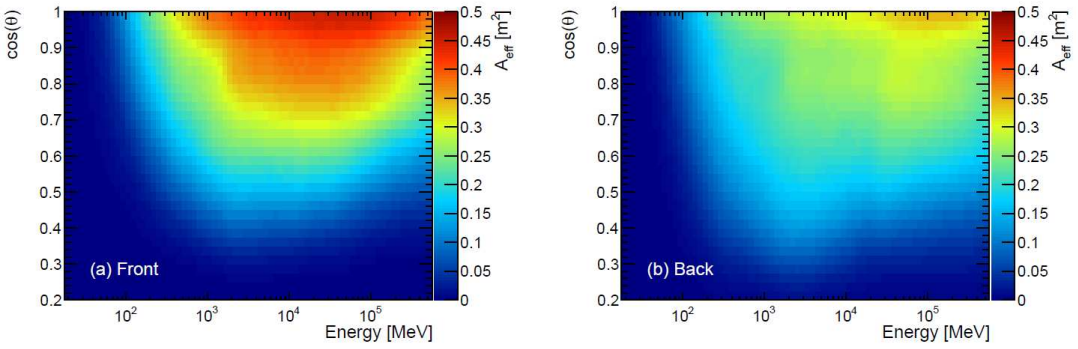

Figure 3.11: LAT effective area for front (left) and back (right) events, as a function of monte carlo energy and $\cos(\theta)$ [113].

$A_{\rm eff}$ is then determined within each bin of (E, θ) by multiplying the $6\,\mathrm{m}^2$ area by the ratio of events detected to events generated within the bin:

$$A_{\rm eff}(E_i, \theta_j, \phi_k) = (6\mathrm{m}^2)\left(\frac{n_{i,j,k}}{N_{\rm gen}}\right)\left(\frac{2\pi}{\Delta\Omega_{j,k}}\right)\left(\frac{\log_{10} E_{\rm max} - \log_{10} E_{\rm min}}{\log_{10} E_{\rm max,i} - \log_{10} E_{\rm min,i}}\right) \tag{3.9}$$

where $\Delta\Omega_{j,k}$ is the solid angle subtended by bin j, k, $E_{\rm min}$ and $E_{\rm max}$ are the minimum and maximum energy range of the monte carlo simulation, and $E_{\rm min,i}$ and $E_{\rm max,i}$ are the boundaries of the $i^{\rm th}$ energy bin [113]. For non-transient analyses, the ϕ-dependence becomes negligible and it is sufficient to use a ϕ-averaged value in these cases. Thus equation 3.9 reduces to:

$$A_{\rm eff}(E_i, \theta_j, \phi_k) = (6\mathrm{m}^2)\left(\frac{n_{i,j}}{N_{\rm gen}}\right)\left(\frac{2\pi}{\Delta\Omega_{j}}\right)\left(\frac{\log_{10} E_{\rm max} - \log_{10} E_{\rm min}}{\log_{10} E_{\rm max,i} - \log_{10} E_{\rm min,i}}\right) \times R(E_i, \theta_j, \phi_k) \tag{3.10}$$

where $R(E_i, \theta_j, \phi_k)$ is a correction factor on the order of 10% to account for the ϕ averaging. Finally, in addition to the (E, θ) binning, the effective area is also binned in terms of front and back tracker conversion layers due to their different expected performance (see Section 3.1.2).

Figure 3.11 shows the LAT effective area as a function of energy and solid angle. The primary factors that determine $A_{\rm eff}$ are the geometrical cross section of the LAT, as well as the efficiency for converting and identifying γ-ray events. As a general rule, the LAT effective area improves with increasing energy and decreasing angle of incidence with respect to the LAT boresight, with the greatest effective area being achieved for front events between $10 - 100\,\mathrm{GeV}$ at normal incidence. Below this energy range, the quality of event reconstruction begins to deteriorate due to the effects of multiple scattering, which becomes increasingly more pronounced off-axis. Above this range, the LAT geometry becomes the primary driver of $A_{\rm eff}$, with losses due to backsplash effects (see Section 3.1.4) also playing an increasingly important role at higher energies.

3.4.3 Point Spread Function

Due to the nature of the event reconstruction, the PSF of the LAT is uniquely described for each event. For this reason, the LAT PSF would ideally be quantified on an event-by-event basis, using for example the covariance information from the Kalman fit that is implemented at the track fitting step during reconstruction (Section 3.3.2.2). Indeed, much of the work of this thesis focuses on the development of the event-by-event covariance information in order to utilize this information as part of the standard likelihood analysis. However, because the covariance-based analysis is still in development, a simpler characterization of the LAT PSF is used. In earlier versions of the instrument response (namely, all irfs prior to and including pass 6 version 3) the PSF was obtained using GLEAM monte carlo simulations, and was characterized as a function of both the energy and solid angle. This was later replaced with an on-orbit derived PSF after a discrepancy between the monte carlo and on-orbit data was discovered [113]. The following section discusses the LAT PSF in the context of these latter two characterizations.

3.4.3.1 Monte Carlo Derived PSF

The two most significant limiting factors in the LAT PSF are the effects of multiple scattering and the inherent geometry of the LAT, including the $228\,\mu$m strip pitch, the number and spacing of the tracker planes, and the overall height of the tracker. The energy of the event weighs heavily on which of these is the primary contributor to the angular uncertainty, with the effects of multiple scattering being dominant in the energy range below $\sim 3\,\mathrm{GeV}$ to $\sim 20\,\mathrm{GeV}$, while above these energies the LAT geometry becomes the limiting factor [113]. Thus, as with the effective area, the LAT PSF is dependent on both the energy and the incoming angle of the event, and its characterization using the monte carlo takes both of these factors into account.

The GLEAM *allGamma* monte carlo simulation used to determine the LAT PSF is the same as that used for the derivation of the effective area (Section 3.4.2). The simulation is run with an even distribution of events in energy and solid angle, and the PSF is characterized according to this binning. The energy dependence of the monte-carlo derived PSF is determined using a scaling factor given by the formula:

$$S(E) = \sqrt{\left[c_0 \cdot \left(\frac{E}{100\ \mathrm{MeV}}\right)^{-\beta}\right]^2 + c_1^2} \tag{3.11}$$

where the values of the fitting parameters c_0, c_1, and β are determined analytically through the *allGamma* simulation. The pass 7 monte carlo-derived parameter values are listed in Table 3.2.

To determine the θ-dependence, events are first scaled by their respective energy scaling factors then binned in terms of their scaled angular deviation in equal intervals of Monte Carlo energy and $\cos(\theta_{\mathrm{MC}})$ (Figure 3.12). The next step

Conversion Type	$c_0[^\circ]$	$c_1[^\circ]$	β
Front	3.32	0.022	0.80
Back	5.50	0.074	0.80

Table 3.2: Table of analytic parameters for the energy scaling function $S(E)$ (See Equation 3.11)[113].

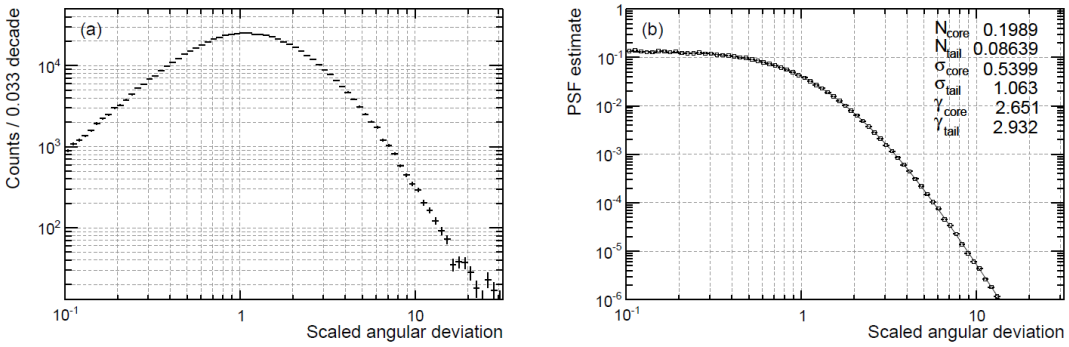

Figure 3.12: (a) Histogram of scaled angular deviation. (b) Angular density histogram fit to LAT psf using events from from `P7SOURCE_V6` event class, $5.6 < E < 10\,\text{GeV}$, and $26^\circ < \theta < 37^\circ$ [113].

is to convert the histogram to a density histogram by dividing by the bin width, thus removing an additional factor of r from the solid angle integral. The resulting density histogram is then fit to the sum of two King Functions [174], where the King Function is given by:

$$K(x,\sigma,\gamma) = \frac{1}{2\pi\sigma^2}\left(1-\frac{1}{\gamma}\right)\cdot\left[1+\frac{1}{2\gamma}\cdot\frac{x^2}{\sigma^2}\right]^{-\gamma} \tag{3.12}$$

and is defined to satisfy the normalization condition:

$$\int_0^\infty K(x,\sigma,\gamma)2\pi x dx = 1 \tag{3.13}$$

Here the factor of $2\pi x$ arises from the integration of the solid angle $d\Omega = \sin(x)dxd\phi$ using the small angle approximation $\sin(x) \approx x$.
The full probability density is therefore given by:

$$P(x) = f_{\text{core}}K(x,\sigma_{\text{core}},\gamma_{\text{core}}) + (1-f_{\text{core}})K(x,\sigma_{\text{tail}},\gamma_{\text{tail}}) \tag{3.14}$$

where f_{core} is the modified normalization of the core King Function given by:

$$f_{\text{core}} = \frac{1}{1+\text{N}_{\text{tail}}\cdot\sigma_{\text{tail}}^2/\sigma_{\text{core}}^2} \tag{3.15}$$

where N_{tail} is the initial normalization of the tail distribution.

3.4.3.2 In-flight Derived PSF

Shortly after launch it was discovered that the distribution of events around sources with known location was wider than predicted from the Monte Carlo above energies of a few GeV. Thus it became necessary to derive the PSF using on-orbit data. The in-flight derived PSF is determined in a similar manner as the Monte Carlo-derived PSF, but uses point sources with high detection signficance in order to determine the distribution of photons around known positions in space. This is achieved through a stacking analysis of high significance LAT sources. In the $1 - 10\,\mathrm{GeV}$ range, pulsars are the ideal candidates for such calibration, as phase selection of their γ-ray emission can be used to significantly reduce the γ-ray background. Above these energies, pulsar spectra exhibit an exponential decay thus reducing the available statistics, at which point AGN located outside of the galactic plane become the more viable candidates.

To fit the on-orbit PSF, events are divided into front and back converting subsamples and energy bins of 4 per decade. Due to lack of statistics, the θ-dependence is not taken into account, and an acceptance-weighted average over all incidence angles is used instead. In the case of the pulsar stacking analysis, the background is taken into account by normalizing both the on- and off-pulse emission by the relative phase then subtracting the off-pulse emission from the on-pulse emission. In the case of AGN, the background is modeled to a flat distribution in each energy band using an annulus around the stacked sources, with inner radius that safely exceeds the distribution around the point source. Each distribution is then fit to a single King Function (Equation 3.12) in each of the energy bands, for both front- and back-converting events.

3.5 Likelihood Analysis Technique

3.5.1 Statistical Likelihood

The LAT is a particle detector by design, thus the analysis of LAT data must be performed with this in mind. A primary limition of space-based γ-ray instruments is the point spread function (PSF), which in the case of the LAT can reach as large as several degrees (Section 3.4.3). Because of the significant overlap of sources over these distances, common techniques such as aperture photometry are often insufficient for obtaining an accurate spectrum of individual sources. This is further complicated by the energy dependence of the PSF, which varies over orders of magnitude across the LAT energy range, as well as by the dependence on the LAT geometry itself, which affects the PSF as a function of the location of the initial pair creation in the instrument. Proper analysis of a source therefore requires modeling both the source itself as well as any other nearby sources that could effect the region.

The standard LAT analysis utilizes a technique based off of the statistical method of maximum likelihood [119]. The likelihood is defined as the probability that a set of data fits a specified hypothesis or model. More specifically, the LAT

data are the list of photons/events extracted from a particular region of interest (ROI), along with their relevant quantities such as the energy E, incident angle θ, and incoming direction in galactic or J2000 equatorial coordinates. The model is comprised of a list of sources and their associated spectra, which are described by a set of spectral parameters. The model is then fit to the data, and the likelihood determines the probability that the model and data are in agreement.

Two standard methods exist for the analysis of LAT data using likelihood: a binned method and an unbinned method [209]. In the binned method, events are binned into three-dimensional counts maps, with two dimensions representing the spatial coordinates and the third being an even binning in logarithmic energy. The likelihood is calculated as the product of probabilities

$$L = \prod_{ij} p_{ij} \tag{3.16}$$

where

$$p_{ij} = \frac{\theta_{ij}^{n_{ij}} e^{-\theta_{ij}}}{n_{ij}!} \tag{3.17}$$

is the Poisson probability of observing n_{ij} counts in pixel ij, and θ_{ij} is the number of counts predicted by the model. The logarithm of the likelihood is often a useful quantity, and is given by

$$\ln L = \sum_{ij} n_{ij} \ln(\theta_{ij}) - \sum_{ij} \theta_{ij} - \sum \ln(n_{ij}!) \tag{3.18}$$

Because the last term is model independent, it can be neglected, leaving

$$\ln L = \sum_{ij} n_{ij} \ln(\theta_{ij}) - \sum_{ij} \theta_{ij} \tag{3.19}$$

In the unbinned case, each photon is counted independently, thus the value of n_{ij} in equation 3.16 is simply 1. Thus equation 3.16 reduces to

$$p_{ij} = \theta_{ij} e^{-\theta_{ij}} \tag{3.20}$$

where i, j now represent the exact spatial coordinates of the photon. Note that the probability is always maximized when the number of predicted counts θ_{ij} approaches the observed counts n_{ij}. To calculate the individual θ_{ij}, a model predicted counts density $S(\varepsilon, \hat{p}_{kl})$ for given true energy ε and position $\hat{p}_{kl}$ must first be calculated by multiplying an event rate r_{kl} (obtained from the model predicted spectrum at position kl) by the time integrated LAT exposure ϵ_{kl} at position kl. The predicted counts density is then convolved with the instrument response $R(\varepsilon', \hat{p}_{ij}; \varepsilon, \hat{p}_{kl})$ in order to form a map of the expected counts:

$$\theta_{ij}(\varepsilon', \hat{p}_{ij}) = \int_{ROI} d\varepsilon \, d\hat{p}_{kl} \, S(\varepsilon, \hat{p}_{kl}) \, R(\varepsilon', \hat{p}_{ij}; \varepsilon, \hat{p}_{kl}) \tag{3.21}$$

For standard LAT analysis it is safe to ignore the effects of energy dispersion, such that we assume $\varepsilon' = \varepsilon$. With this in mind, a more careful examination of Equation 3.21 reveals that in the special case where $S(\varepsilon, \hat{p}_{kl})$ may described by:

$$S(\varepsilon, \hat{p}_{kl}) = \sum_{sources} n(\varepsilon) s(\hat{p}_{kl}) \tag{3.22}$$

where $n(\varepsilon)$ is the number of counts predicted at the given energy ε and $s(\hat{p}_{kl})$ is an overall spatial function normalized to 1, then this allows $n(\varepsilon)$ to be carried outside of the spatial integral in equation 3.21, such that the spatial convolution can be pre-computed prior to spectral fitting. This computational trick is used in the LAT unbinned analyses software to pre-compute the diffuse response in the tool `gtdiffrsp`. This is a noteworthy property of the convolution step, as it saves computational time with likelihood fitting of diffuse sources such as the galactic and extragalactic diffuse emission, as well as to play an important role in the implementation of event-by-event errors in LAT likelihood analysis (see Section 5.2.2.

The primary task of likelihood analysis with the LAT is therefore to calculate the predicted counts θ_{ij} for different models and to determine which model best fits the data by comparing their relative likelihood values. An important limitation to the likelihood method is that one can only calculate the relative significance between two hypotheses in order to determine which model better fits to the data, which means that knowledge of the data is limited only to the specific hypotheses being tested. The method used to compare hypotheses using the Fermi-LAT data is known as the likelihood ratio test (LRT; [222]). The likelihood ratio is simply the likelihood of the null hypothesis divided by the likelihood of the alternative hypothesis. An important theorem related to the LRT is Wilks' theorem [312]. If we define the test statistic (TS) as

$$\mathrm{TS} \equiv -2(\ln(L_0) - \ln(L_1)) \tag{3.23}$$

then Wilks' Theorem states that the TS is distributed as χ^2 in the null hypothesis (i.e. when the null hypothesis is true) with $h - m$ degrees of freedom, where $h - m$ are the number of additional parameters that are optimized in the alternative hypothesis. The LRT thus provides an analytical expression that can be used to test the significance of detection of a source, with the caveat that the null hypothesis (e.g. the model of the diffuse background and surrounding point sources within a region) be adequately described. An additional caveat to this method is that the comparison between hypotheses must be made between nested models. In other words, in order for Wilks' theorem to hold, the alternative hypothesis must be given as the original model plus one or more additional parameters.

Due to the nature of Wilks' Theorem, both the detection of LAT sources and the analysis of their spectra go hand in hand. For example, in the case of a source whose spectrum is described by a power law function

$$\frac{dN}{dE} = N_0 \left(\frac{E}{E_0} \right)^{\gamma} \tag{3.24}$$

it is common to allow both the normalization N_0 and the photon index γ to remain as free parameters. In this case, the significance of detection of the source with respect to the null hypothesis would be distributed as χ^2_2.

It is important to note that Wilks' Theorem may be applied for a particular parameter only in the regime where the number of counts that carry information about that parameter are significant. The deviation from χ^2 is expected to be of order $N_\Lambda^{-\frac{1}{2}}$, where N_Λ are the number of counts carrying information about parameter Λ. This cannot be determined explicitly from the likelihood fit itself, therefore discretion should be made when determining whether or not Wilks' Theorem can be applied. This is particularly important when considering upper limits for sources whose predicted counts are fewer than ~ 20, where the deviation from χ^2 becomes significant (see Section for further discussion).

The fitting of the individual parameters is achieved using Newton-Raphson iteration [102] in order to reach the maximum value of the likelihood, which occurs when the derivative of the likelihood with respect to all fitting parameters is zero. More specifically, if the vector of model parameters is $\mathbf{\Lambda}$ and its vector of derivatives is $\mathbf{D}$, where

$$D_i \equiv \frac{\partial \ln L}{\partial \Lambda_i} \tag{3.25}$$

then the maximum likelihood ($\mathbf{D} = 0$) is achieved though successive model estimates using the formula $\mathbf{\Lambda_{n+1}} = \mathbf{\Lambda_n} + H^{-1}\mathbf{D}$ where H is the Hessian matrix

$$H_{ij} \equiv -\frac{\partial^2 \ln L}{\partial \Lambda_i \partial \Lambda_j} \tag{3.26}$$

and n is the nth iteration of the estimation of $\mathbf{\Lambda}$.

The Hessian matrix also provides the information needed to determine the errors and covariances between all parameters. Combining Wilks' Theorem with Equation 3.23, we note that the χ^2 distribution pertains for each parameter. As noted by [288], the log-likelihood ratio can be expanded about its maximum in terms of each of the parameters by means of a Taylor expansion

$$\begin{aligned} \ln(L) &= \ln(L_0) + \frac{1}{2}\sum_{ij} \frac{\partial^2 \ln L}{\partial \Lambda_i \partial \Lambda_j}(\Lambda_i - \Lambda_i^*)(\Lambda_j - \Lambda_j^*) \\ &= \ln(L_0) + \frac{1}{2}\sum_{ij} H_{ij}(\Lambda_i - \Lambda_i^*)(\Lambda_j - \Lambda_j^*) \\ &= \ln(L_0) + \frac{1}{2}(\mathbf{\Lambda} - \mathbf{\Lambda}^*)^T \mathbf{H} (\mathbf{\Lambda} - \mathbf{\Lambda}^*) \end{aligned} \tag{3.27}$$

In the linear approximation, it can be shown that the distribution function of the parameter space $\mathbf{\Lambda}$ (that is, the probability of obtaining particular values Λ_l within the allowed range of each parameter), is described by a multivariate normal distribution given by

$$p(\mathbf{\Lambda}) = (2\pi)^{-\frac{N_\Lambda}{2}} |\mathbf{\Sigma_\Lambda}|^{-\frac{1}{2}} \exp\left[-\frac{1}{2}(\mathbf{\Lambda} - \mathbf{\Lambda}^*)^T \mathbf{\Sigma_\Lambda^{-1}} (\mathbf{\Lambda} - \mathbf{\Lambda}^*)\right] \tag{3.28}$$

where $\mathbf{\Sigma_\Lambda}$ is the covariance matrix of the parameter space $\mathbf{\Lambda}$ and $p(\mathbf{\Lambda})$ has been normalized to 1 for generality. This is seen by noting that the objective function can be defined as the negative logarithm of the probability

$$J(\mathbf{\Lambda}) \equiv -\ln p(\Lambda) = \frac{N_\Lambda}{2}\ln(2\pi) + \frac{N_\Lambda}{2}\ln|\mathbf{\Sigma_\Lambda}| + \frac{1}{2}(\mathbf{\Lambda} - \mathbf{\Lambda}^*)^T \mathbf{\Sigma_\Lambda^{-1}} (\mathbf{\Lambda} - \mathbf{\Lambda}^*) \tag{3.29}$$

Ignoring the normalization terms, equations 3.29 and 3.27 take the same form. Thus in the linear approximation $\mathbf{H}$ is equivalent to Σ_Λ^{-1}. This can be further seen by taking the second derivative of equation 3.29 explicitly with respect to each of the fit parameters:

$$H_{ij}(\Lambda^*) = \left.\frac{\partial^2 J(\mathbf{\Lambda})}{\partial\Lambda_i\Lambda_j}\right|_{\Lambda=\Lambda^*} = (\mathbf{\Sigma_\Lambda^{-1}})_{ij} \tag{3.30}$$

and noting that the objective function $J(\mathbf{\Lambda})$ is simply the log likelihood of the model in question. Thus in the linear approximation, $\mathbf{H}^{-1}$ fully describes the errors and their covariances for all model parameters wherever Wilks' Theorem is valid.

3.5.2 Modeling γ-ray emission using the LAT data

3.5.2.1 Event Selection and Exposure

Proper modeling of the γ-ray emission from a particular region requires both an appropriate selection of events as well as an accurate calculation of the exposure over the ROI. In the standard LAT analysis events are selected based off of their classification, which is determined by a set of selection cuts that are applied to the data in order to optimize the type of analysis that is to be performed (Section 3.3.5). For example, a standard analysis of point sources requires a selection of cuts that achieves significant background rejection while maintaining maximum effective area. In the case of transients such as γ-ray bursts, the background cuts may be relaxed due to the high signal to noise. The set of cuts applied for each type of analysis is specified by their event class, and each of these is assigned a separate integer value.

In addition to selecting on event class, cuts are also made on the incoming zenith angle of each event[5] in order to avoid contamination due to the Earth's limb, which is known to be a significant source of γ-rays. The data is also selected based off of a series of "good time intervals" (GTI's) that determine which times the LAT is taking data suitable for science analysis. For example, a standard set of cuts would be to reject time intervals where the LAT is inside the SAA, is at a rocking angle larger than its nominal maximum of 52 degrees, or is taking data over a period of time where the data quality itself is marked as poor. In addition, cuts

[5]the recommended zenith angle cut as of the time of this writing is $< 100^\circ$

could be applied to remove time intervals where the sun may be in the field of view, or intervals where a nearby bright γ-ray burst could be contaminating the region in order to obtain a more accurate spectral fit. The science itself could also be a motivating factor behind specific time interval selection (for example, to compare spectra during flaring versus non-flaring states in AGN, or to obtain a spectrum of on- versus off-pulse emission in pulsars).

After the events are selected, the exposure (effective area times time) over the given region must be calculated. Due to the geometric dependence of the LAT effective area, the first step in the exposure calculation is to determine as a function of $\cos(\theta)$ (where θ is the angle of incidence with respect to the LAT boresight) how much time the LAT was exposed to each region of the sky over the good time intervals. This step produces a livetime cube in FITS (Flexible Image Transport System) format. Once the livetime cube has been produced, an exposure map over the region can then be calculated. This requires a description of the instrument response functions, which includes the LAT effective area as a function of Log(energy) and $\cos(\theta)$. Because the effective area is energy-dependent, the exposure map is additionally binned as a function of energy (usually Log(Energy), to match with the binning of effective area) such that for any event (or bin) with given energy and position on the sky, an appropriate exposure can be determined for that event/bin. With the exposure properly calculated, the likelihood is then maximized as discussed in Section 3.5.1.

3.5.2.2 Spectral & Temporal Analysis

While the standard likelihood method is successful in fitting source spectra, the most common data products in multiwavelength astronomy such as spectral energy distributions (SEDs) and light curves, are not a direct product of the method. These higher-level data products must therefore be constructed using likelihood as a framework. For example, the construction of a SED, with points in flux density $\nu\ F_\nu$ as a function of energy is the primary means to model a source's multiwavelength spectrum, yet these points cannot be directly obtained from a single likelhood fit of the data. Obtaining a model-independent spectrum would be preferred, because the LAT energy range spans several orders of magnitude, thus the shape of the spectrum over such a large range is difficult to know *apriori*. While a truly model-independent fit of the observed data would be ideal, this is not easily accomodated using the LAT likelihood method.

A solution to obtaining an SED that is quasi-model-independent is to note that the shape of any smooth spectrum over the interval ΔE, where $\lim \Delta E \rightarrow 0$ reduces to a single power law. It is therefore possible to approach a model-independent spectrum by dividing the data into separate bins in Log(Energy) and performing a separate likelihood fit over each bin to a single power law. This differs from the standard "binned likelihood" method in that each energy bin is fit independently from the others, rather than the total spectrum being fit to a single function. This ensures that with a proper binning (such that each point is detected with non-marginal significance), the spectral shape is obtained without resorting to *apriori*

assumptions concerning the functional form. While this approach may not be mathematically rigorous in regions where there is a spectral break, it is often the case that the statistical errors around such features are larger than the loss of precision that arises by fitting these features using a single power law.

Temporal analysis of LAT data may also be performed using a maximum likelihood approach. Light curves of particular sources are computed by dividing a dataset into shorter time intervals then refitting the parameters of the sources within the given region. The choice of time binning is driven by the underlying science and by the statistics available to obtain a significant detection in each bin. The latter of these depends largely on the exposure and the flux of the source. For the brightest sources, the LAT can probe variability in as little as second timescales, while for faint sources, a light curve may not be possible simply due to lack of statistics.

A standard method for probing the variability of a source follows that of [4] and [225]. In each time bin, all known γ-ray sources that fall within the ROI are fit with their spectral indices fixed to their best fit values over the full time period, while the normalization parameters remain free. Ideally, one would choose to keep all parameters free and quote the flux above the pivot energy, however the value is unique for each bin thus a single value cannot be chosen without introducing some covariance between the flux and spectral parameters. In this case, the errors will not be quoted at their relative minimum with respect to the flux. Fixing the spectral index instead allows the flux to be quoted above any energy, the tradeoff being that the variability is examined as an average change over the LAT energy range and is no longer sensitive to changes that occur only within specific regions of the observed spectrum.

Variability in LAT sources may be examined in a number of ways. The most common of these methods involve testing for general variability over the entire observed time range. This can be done by directly comparing the flux points against the weighted mean by means of a χ^2 test:

$$\begin{aligned} w_i &= \frac{1}{\Delta F_i^2 + (f_{\rm rel} F_i)^2} \\ F_{\rm wt} &= \frac{\sum_i w_i F_i}{\sum_i w_i} \\ V &= \sum_i w_i (F_i - F_{\rm wt})^2 \end{aligned} \tag{3.31}$$

Here w_i represents the weight of the ith flux point, which is determined as a function of the statistical uncertainty ΔF_i and the systematic error $f_{\rm rel}$, which is assigned a fractional value of the measured flux F_i, on the order of $\sim 3\%$. The weighted average $F_{\rm wt}$ is not known *a priori*, therefore V is expected, in the absense of variability, to follow a χ^2 distribution with degrees of freedom equal to the number of flux points minus 1. Thus, for any given light curve, a χ^2 value can be calculated using the weighted average as the tested hypothesis, which can in turn be used to calculate a P-value, $P(\chi^2 \geq \chi^2_{\rm obs})$, which represents the theoretical probability that one would

obtain a χ^2 value greater than the measured value in the case where the tested hypothesis is true.

Upper limits may be included in this calculation as well. This is done by calculating two values for all points with TS below a chosen significance, the first being the best fit value, and the second being the 95% confidence upper limit. In the calculation of the weighted mean, the best fit flux value is used for F_i. For the statistical error ΔF_i, one half the difference between the upper limit and best fit values are used. This allows all points to be included in the calculation of the weighted mean and the corresponding calculation of χ^2, regardless of the significance of detection of the individual flux points.

3.5.2.3 Localization & Source Association

Localization of point sources using LAT data follows the same principles of maximum likelihood fitting as with spectral analysis. The best-fit position of a source is found by performing a maximum likelihood fit of the source over several positions, with the maximum likelihood value (smallest value of $-\log(\text{likelihood})$) representing the best-fit position. Such a fit also introduces two additional degrees of freedom (the longitude and latitude), which must be taken into account when determining the overall detection significance of a source. Therefore, an increase in the TS from the true source position is expected to be distributed as χ^2_2, with localization contours around the best-fit position of $2.3, 6.0$, and 9.1 for confidence intervals of $68\%, 95\%$, and 99%, respectively [209].

Because of the relatively large positional uncertainties of LAT sources ranging from a few arcminutes to over 1 degree, it is often insufficient to claim a detection using the simple criterion that a known point source overlaps with a LAT error circle. It is often the case that more than one association may exist for a single LAT source, and in some cases, two γ-ray emitting sources may be appear as a single source if they are positioned closely enough that the LAT PSF significantly overlaps between the two across their spectra (usually within $\sim 0.5^\circ$ of each other). In order to claim a detection of a source it is therefore necessary to establish additional criterion such as correlated variability, pulsed emission, or extended structure, which can then be used to rule out other spurious associations.

In the majority of cases where a clear detection cannot be established, a measure of the confidence of an association with a particular source or sources using statistical methods must be performed. A number of such methods have been used to establish associations with LAT sources [6]. Examples include the Bayesian, $\log(N) - \log(S)$, and Likelihood Ratio methods. The Bayesian method calculates the posterior probability that a source from a pre-defined catalog of sources C is associated with a particular LAT source S, taking into account all other candidate sources in the vacinity of S and assuming an equal probability among all sources in C of being γ-ray emitters. The probability of γ-ray emission in this case is not known, but may be tuned in order to reach a specified number of false positive associations

[6] For an in-depth description of these methods, see e.g. [4, 225, 18]

for a given threshold of the posterior probability.

Similar to the Bayesian method is the $\log(N) - \log(S)$ method, which also uses Bayes' Theorem, but differs from the former method in that the density of candidate sources is estimated by using the radio $\log(N) - \log(S)$ of the candidate population. That is, only sources with $S > S_k$ and $\alpha < \alpha_k$ are included in the candidate source density. This method is useful in that the list of candidate sources can be extended to include non-uniform surveys falling below the formal flux-limit of a particular catalog without the loss of statistical validity.

Another method is the Likelihood Ratio (LR) method, which makes use of uniform surveys in the radio and X-rays in order to establish a probability based off of a likelihood ratio calculation. For the LR method, the probability density of sources uses the $\log(N) - \log(S)$ of the particular sky survey, as well as to assume a uniform density in $\log(N) - \log(S)$ over the full sky. To determine the significance, a normalized distance r_{ij} between each candidate i and γ-ray source j is calculated using the following:

$$r_{ij} = \frac{\Delta}{(\sigma_{\rm a}^2 + \sigma_{\rm b}^2)} \tag{3.32}$$

where Δ is the angular separation between candidate i and γ-ray source j, and $\sigma_{\rm a}$ and $\sigma_{\rm b}$ represent the errors on the γ-ray and candidate source positions, respectively. From here, a likelihood ratio $\mathrm{LR_{ij}}$ can be calculated using the following formula:

$$\mathrm{LR_{ij}} = \frac{\mathrm{e}^{-\mathrm{r_{ij}^2}/2}}{\mathrm{N}(>\mathrm{S_i})\mathrm{A}} \tag{3.33}$$

where $N(> S_i)$ is the surface density of objects greater than S_i. A significance can then be determined by comparing the distribution of $\mathrm{LR_{ij}}$ from the given γ-ray population against the average distribution obtained for a randomly distributed set of γ-ray positions with equivalent σ_i. From here a cutoff value of $\mathrm{LR_{ij}}$ can be established to determine the threshold for a reliable association.

3.5.2.4 Pointlike Method

The `pointlike` software package is a collection of routines for performing maximum likelihood analysis of LAT data[173]. It utilizes an energy-dependent HEALpix (see Section 5.2.3 for further description of HEALpix) binning scheme to match the angular resolution of the LAT, and a sparse binning algorithm to optimize the computational efficiency, such that only pixels with event counts greater than 0 are considered when performing likelihood analysis. Aside from the computational efficiencies introduced through HEALpix, `pointlike` introduces further computational efficiencies in the calculation of Equation 3.21 by using an exposure-weighted PSF. That is, the PSF is averaged over all angles $\cos\theta$, and the livetime and exposure calculations are then pre-computed for a particular binning scheme prior to the spectral fitting of the source. For source analysis, this ultimately means that the `pointlike` method optimizes the calculation of the likelihood, allowing for

much faster computation of complex calculations, at the expense of introducing a theta-averaged PSF.

One particular area that pointlike becomes useful is in the detection of extended γ-ray emission from sources [188]. In the standard `gtlike` analysis, extension is detected by producing a spatial map template of the hypothesized spatial distribution of the γ-rays, typically using a radio image of the source, as in e.g. [110], or a more general shape such as a gaussian, disk, or hollow disk, that represents a closest approximation of the spatial extent of the source (e.g. [111, 112]). In the latter case, application of Wilks' theorem is used to determine the significance of the detection using the best fit values for the parameters that determine the shape and size of the map template (e.g. σ in the case of a gaussian or disk). However, use of this method is burdensome for the standard likelihood, as it requires application of a "profile likelihood", in which the fit is run multiple times using a fixed value of the parameter, and incrementing the parameter by some small amount over each fit, thus obtaining a "profile" of the likelihood as a function of the change in the parameter. This is necessary in the case of spatial map template fitting, in that each adjustment of the spatial parameters requires creating a new map template and running a separate instance of the likelihood for each map.

Using the pointlike tool, however, allows for the spatial parameters to be adjusted internally within a single fit, as well as to allow an adjustment of the localization parameters of the map itself. This in turn allows for the most efficient method for searching for a general spatial profile, in the case where the location and spatial distribution of the γ-ray emission is not known *a priori*. Lande et al. (2012) [188] demonstrated the use of this method for use within the second Fermi-LAT catalog (2FGL), where they reported the detection of 7 spatially extended sources whose extension had previously gone undetected.

Chapter 4
Observations of non-blazar emission in Fermi-LAT AGN

The Fermi-LAT has provided a wealth of groundbreaking information on the nature of the high-energy sky. Our understanding of the nature of extragalactic sources has been enhanced, with over 1017 confirmed associations with known AGN achieved thus far [18]. The vast majority of γ-ray AGN are found to be associated with FSRQ or BL Lac blazars (see Section 2.2.2.4). It is well established that the jet emission close to the central engine in these objects is significantly Doppler enhanced (see Section 2.1.4), which leads to the broad, double peaked continuum emission that dominates the broadband spectrum of the source (see Section 2.2.3), variability on day-to-week timescales, compact / unresolved radio cores with high polarization and brightness temperatures exceeding $T_b > 10^{10}$ K, and apparent superluminal motions of radio components at VLBI scales.

While the significant Doppler enhancement of the cores of blazar sources may allow for detailed studies of the emission at sub-parsec scales (presumably within a region lying close to the black hole central engine; see 2.3), it is precisely for this reason that blazars are among the poorest objects to consider for studying emission mechanisms that may occur at farther distances from the parsec-scale jet (up to 100's of kpc). Rather, it is in the unbeamed (type 2; see Sections 2.2.2.1 & 2.2.2.5) sources that such studies are most appropriate. In these sources, the core emission is suppressed (see Figure 2.2), thereby offering the greatest promise for observing extended emission components that might otherwise be hidden by the Doppler enhanced core of blazar sources. With such a small sample ($\lesssim$ 25) of confirmed γ-ray AGN that are non-blazar sources[18, 13], dedicated multiwavelength studies of these objects are essential, as they can lead to a number of important discoveries that would otherwise not be possible in blazar studies.

In the following chapter, we examine the multiwavelength properties of three objects that challenge the standard (i.e. "blazar-zone") models of γ-ray emission in AGN. Two of these objects, Fornax A and M87, are well established radio galaxies, while the third, 4C +55.17, is classified in the literature as an FSRQ blazar, but demonstrates none of the hallmark properties such as variability or Doppler enhanced radio emission that are inherent to an FSRQ blazar classification. The origin of the γ-ray emission is discussed for each of these objects. Furthermore, we demonstrate how the unique spectral and physical properties of two of the objects, Fornax A and 4C +55.17, are particularly useful in placing constraints on the extragalactic background light (EBL; see Section 2.3.4.2).

4.1 A Search for Extended γ-ray Emission from the Radio Galaxy Fornax A

4.1.1 Introduction

The radio galaxy NGC 1316 (Fornax A), famous for its radio lobes spanning $\sim 50'$, with a lobe-to-lobe separation of $\sim 33'$ [103, 120], is one of the closest and brightest radio galaxies, located at a distance of only 17.8 ± 0.3 (random) $\pm$ 0.3 (systematic) Mpc [287]. Located within the Fornax cluster, the source is hosted by the giant elliptical NGC 1316 which features a LINER core [158], and is believed to have undergone several merger events over the course of its history [265, 198, 142]. The inner radio structure of the source has been imaged to arcsecond resolution, and consists of a flat spectrum ($\alpha = 0.4$) core and dual-opposing "s"-shaped jets that extend out to ~ 5 kpc before abruptly terminating[130]. The giant radio lobes are characterized by a complex polarized filamentary structure with no observable hotspots [120] and have been well studied in the X-rays [109, 165, 293], with the observed X-ray emission being attributed to both thermal and IC processes [267].

The recent association of Fornax A with the Fermi-LAT source 2FGL J0322.4-3717 [225] raises an important question regarding the origin of its γ-ray emission. In particular, Georganopoulos et al. (2008) [133] demonstrated that high energy γ-ray emission could be produced when extragalactic background light (EBL) photons inverse-Compton (IC) scatter off of the relativistic electrons in the giant lobes of radio galaxies such as Fornax A (see Section 2.3.4.2). A proper measurement of the γ-ray spectrum could in turn be used to obtain a direct measurement of the cosmic infrared background (CIB) and cosmic optical background (COB) components of the EBL, provided an independent measurement of the electron energy distribution (EED) and magnetic field B are accurately obtained. As pointed out by Georganopoulos et al. (2008), this can be achieved by modeling the IC component at lower energies (in this case, in the X-ray band) due to IC scattering off of the well-measured cosmic microwave background (CMB).

The mechanism put forth by Georganopoulos et al (2008) is believed to be the same one responsible for producing the γ-ray emission that is observed in the lobes of Centaurus A [110]. However, in the case of Centaurus A, the measured EED and B field make the source a poor candidate for EBL measurement, because they place the IC component due to EBL scattering at much higher energies ($\gtrsim 10$ GeV), whereas the primary contributor of seed photons for IC scattering into the 100 MeV-10 GeV range is the CMB light (see [110] for further discussion on the modeling of the lobes of Centaurus A). Because the CMB dominates over the EBL in terms of overall magnitude, this makes the contribution from EBL photons difficult to constrain in the spectral modeling of Centaurus A at LAT energies.

One of the significant challenges in obtaining a measurement of the EBL via the γ-ray spectrum of a radio galaxy such as Fornax A is the separation of possible γ-ray emission arising in the vicinity of the central black hole engine from that arising within the giant radio lobes. For this reason Fornax A is a unique candidate for measuring the EBL using the LAT data, as its total angular extent ($\sim 50'$) makes

it one of the few radio galaxies to approach the detectable threshold of resolution by the LAT. Indeed, the LAT has observed extended emission in a number of supernova remnants whose total angular extent is comparable to that of Fornax A [111, 112], although such sources have been detected at notably higher significance.

In the following sections, an investigation into the origin of the high-energy γ-ray ($> 100\,\mathrm{MeV}$) emission in Fornax A is performed through detailed spatial and spectral analysis using 44 months of LAT all-sky survey data. In Section 4.1.2, the details of the LAT observations, including localization, spectral, and spatial analysis are described. In Section 4.1.4 the results are discussed in the context of both the core and extended components, along with a discussion of potential future observations with the NuSTAR telescope. Final conclusions are presented in section 4.1.5.

4.1.2 Observations

The following analysis is comprised of 44 months of nominal all-sky survey data extracted from a $15^\circ \times 15^\circ$ square region of interest (ROI) around the J2000.0 radio position of Fornax A (R.A.$= 03^\mathrm{h}22^\mathrm{m}41.718^\mathrm{s}$, Decl.$= -37^\circ12'29.62''$;[268]) and covers the mission elapsed time (MET) 239557417 to 356197417 (August 4, 2008 through April 15, 2012). Event selections include the "source" event class [37] recommended for point source analysis, a zenith angle cut of $< 100^\circ$ to avoid contamination from the earth limb, and rocking angle cuts at 43° and 52°, respectively, for times corresponding to a change in the instrument's rocking angle from 39° to 50° that occured on September 3, 2009 (MET 273628805). An energy cut of $100\,\mathrm{MeV} < \mathrm{E} < 300\,\mathrm{GeV}$ was also applied. Science Tools `v9r27p1` and instrument response functions (IRFs) `P7_SOURCE_V6` were used for this analysis[1].

In order to properly model the γ-ray emission, all point sources from the 2FGL catalog [225] within 15° of the source were initially included. Catalog sources falling within the square ROI around Fornax A were modeled with their flux and spectral parameters set free, while those sources that fell outside the 10° ROI were fixed at their catalog values. The diffuse background was modeled using the recommended[2] Galactic diffuse `gal_2yearp7v6_v0` along with the corresponding isotropic spectral template `iso_p7v6source.txt` for the pass 7 version 6 irfs. Because the 44 month data set covered a longer time period than the 2FGL, there was a possibility that new point sources (e.g. variable blazars) could have emerged within the field of view (FOV) after 2 years. To account for these additional sources, a test statistic map of the full region was created prior to the formal fit, and all peaks exceeding a test statistic (TS; see Section 3.5.1, Equation 3.23) value of 25 were modeled as point sources using a simple power law spectrum. This resulted in the inclusion of one additional point source not seen in the 2FGL catalog.

Prior to the spectral fit, a 44 month localization of the source was conducted

[1] Identical analyses were conducted using P7_CLEAN_V6 irfs, along with higher threshold cuts at low energy, but which resulted in systematically lower test statistics in all subsequent fits, and are therefore not included.

[2] `http://fermi.gsfc.nasa.gov/ssc/data/access/lat/BackgroundModels.html`

by creating a TS map of a $4^\circ \times 4^\circ$ square region (0.05° pixel separation) around the Fornax A position. The TS map was created by running a binned analysis at each of the pixel locations using a point source fit to a power law with index and normalization parameters left free. The 68%, 95%, and 99% confidence contours were then determined by decrements of 2.3, 6.0, and 9.1 from the maximum TS, as described in [209].

The spatial and spectral analysis of Fornax A was performed using two methods. The first method used a standard binned `gtlike` fit comparing three test cases. The first case used a single point source located at the central Fornax A core position. In the second case, a spatial map template of the 20 cm VLA image obtained from [120] was constructed to represent the extended radio emission (see Appendix A for details of the spatial map template preparation). In the third case, both the point source and the template were fit simultaneously. In each of the three cases, a single power law function was used to model the spectrum. A maximum energy of 35 GeV for the source spectrum was chosen to agree with the highest energy photon associated with the source, which was obtained using the `gtsrcprob` tool (see Section B for a description of the `gtsrcprob` tool).

The second method, which was used for quantifying the significance of the spatial extension of the source, was a `pointlike` fit (see Section 3.5.2.4) comparing four distinct spatial models: disk, elliptical disk, gaussian, and elliptical gaussian. Using this method, we obtained a simultaneous best-fit of the position, spectrum, and spatial extension of the source, as well as a significance of detection of the source extension.

The γ-ray variability (> 100 MeV) over the 44-month period was tested via a light curve divided into time bins of 225 days. Due to the limited statistics over each interval, Fornax A was fit to a single power-law point source in each bin, with index fixed to the best-fit value from the point source fit and the prefactor parameter left free. To improve the fit convergence, point sources in the ROI were included only if they were detected with a TS greater than 1 ($\sim 1\sigma$). The source variability was analyzed by means of a χ^2 test following the procedure outlined in Section 3.5.2.2. Here we assume the model describing the data to be a constant straight line with intercept equal to the weighted mean of all data. For points whose detections surpassed the threshold of $> 2\sigma$ (TS > 4), the statistical errors obtained from the fit were used in determining the weighted average. For those points which did not reach the 2σ threshold, the prescription described in Section 3.5.2.2 was followed. That is, the best-fit flux values were used for the F_i terms, and one-half the difference between the 95% upper limit and the best-fit value F_i was used for the statistical error ΔF_i. This allowed both upper limits and non-upper limits to be used in the calculation of the weighted average. From here, a χ^2 probability ($P(\chi^2 \geq \chi^2_{\rm obs})$; see Section 3.5.2.2) could be used to determine the significance of variability from the source.

4.1.3 Monte Carlo Simulations

In order to obtain a better understanding of the instrument response for a γ-ray source of similar size and spectrum to Fornax A, we ran three monte carlo simulations using the LAT `gtobssim` software. Each of these simulations was designed to mimic the possible emission scenarios that could take place within the source. For each of the simulations the on-orbit spacecraft file was used as a template for reproducing the flight path and directional pointing of the LAT over the 44-month simulated time period. In each scenario, the total emission from Fornax A was chosen to match the observed γ-ray spectrum and flux obtained from the `gtlike` point source of the 44-month on-orbit data.

In the first scenario, Fornax A was modeled as a point source located at the core position. In the second scenario, the γ-ray emission was modeled using only the spatial map template described in Section 4.1.2. In the third scenario, the point source and the spatial map template were both modeled together, with the flux evenly distributed between the two. For each of the scenarios described above, a spectral analysis was performed using `gtlike` and compared against the results obtained from the in-flight data. In particular, an investigation of the fit convergence in each of the three scenarios was compared to the in-flight results in order to search for any similarities between the in-flight and simulated data, as well as to determine if a spatial resolution of the lobes could in theory be achieved using the LAT 44 month data set.

4.1.4 Discussion

4.1.4.1 LAT Results

As noted in 4.1.1, the greatest challenge in modeling the γ-ray emission from the lobes of radio galaxies is the ability to differentiate between the contribution from the extended lobe emission, and that which originates from the core. Perhaps most challenging is that even in the case where an extended HE component from Fornax A is detected within the LAT, the resolution of the instrument in no way guarantees that a spatial and spectral distinction between the lobe and core components will be achievable. An examination of the LAT data can nevertheless offer important insights into the nature of the emission, provided a full understanding of the instrument response is demonstrated. In particular, a number of important insights can be ascertained by comparing the behavior of simulated emission from the lobes and core as discussed in 4.1.3 that lead to a better understanding of the nature of the γ-ray emission in Fornax A.

Figure 4.1 compares the localization that is obtained from an analysis of the real data, compared to the those obtained from the monte carlo simulations discussed in 4.1.2. From the resulting comparison, it is evident that the overall abilty of the LAT to differentiate between the localizations in each of the cases using the pass 7 reprocessed IRFs is close to the resolution threshold of the instrument. While a distinction can be made in terms of the localization contours in the different cases

(the widest originating from the pure lobe emission, the most circular from the point source, and the smaller ellipse from the combined distribution), the size scale of the 68%, 95%, and 99% confidence contours in each of the cases lies within a factor of 2, which indicates that future improvements on the LAT PSF may not be sufficient in differentiating between the spectra of the two regions.

In order to examine this question in more detail, we compare the results from the spectral fits of the different test cases using `gtlike`. Table 4.1 lists the spectral parameters in each of the test cases, along with the source TS and overall value of $-\log$ likelihood. To understand these results, we first note that in order for there to be a confirmed detection of γ-ray emission from the lobes, certain conditions must be met. According to Wilks' Theorem [209], the log(likelihood) values between two models obeys a χ^2 distribution only if the alternative hypothesis can be described through an addition of one or more parameters onto the null hypothesis (see Equation 3.23 and surrounding discussion). Therefore, a direct comparison of the -log(likelihood) values between the lobe template and point source spectral fits cannot be quantified in terms of a significance. Instead, a detection of the extended lobes using this method can only be achieved by fitting both the point source and lobe template together, then determining if the improvement in the combined fit is statistically significant compared to the single point source or pure lobe emission cases. If the source is emitting pure lobe emission, a detection would require that the combined fit was a statistically significant improvement over the single point source fit, while not being a statistically significant improvement over the pure lobe fit.

From the results of Table 4.1, we can see that the fit of the real data does not improve the statistical significance over the point source fit to be considered a detection of extension in either case. However, a comparison of the behavior of the fit convergence does in fact provide an indication regarding the possible contribution from an extended component. More specifically, an attempt to fit the combined point source + lobes template to the monte carlo truth exhibits different behavior in each of the three cases. In the case where pure point source emission was simulated, an attempt to fit both the lobe and core spectra simultaneously resulted in a non-convergence on the fit of the lobe emission spectral parameters. Similarly, in the case where pure lobe emission was simulated, an attempt to fit both lobe and point source emission resulted in a non-convergence of the point source spectral parameters. In each of these cases, the index parameter was placed at an extremum of the allowed bounds, rather than converging on a value that lay between them. Conversely, in the case where both the core and lobes were simulated, the fit was able to reach a convergence on both sources, albeit at a low detection significance. A comparison of these trends to the analysis of the real data indicates that the fit of the real data behaves most similarly to the lobes plus point source simulation, in that the fit was able to reach a convergence for both sources, albeit at a low detection significance for the point source.

The second test of extension that was conducted on the source attempted to fit the emission to a general profile shape using the `pointlike` analysis tool. The results from this approach are summarized in table 4.2, where we see that only a marginal

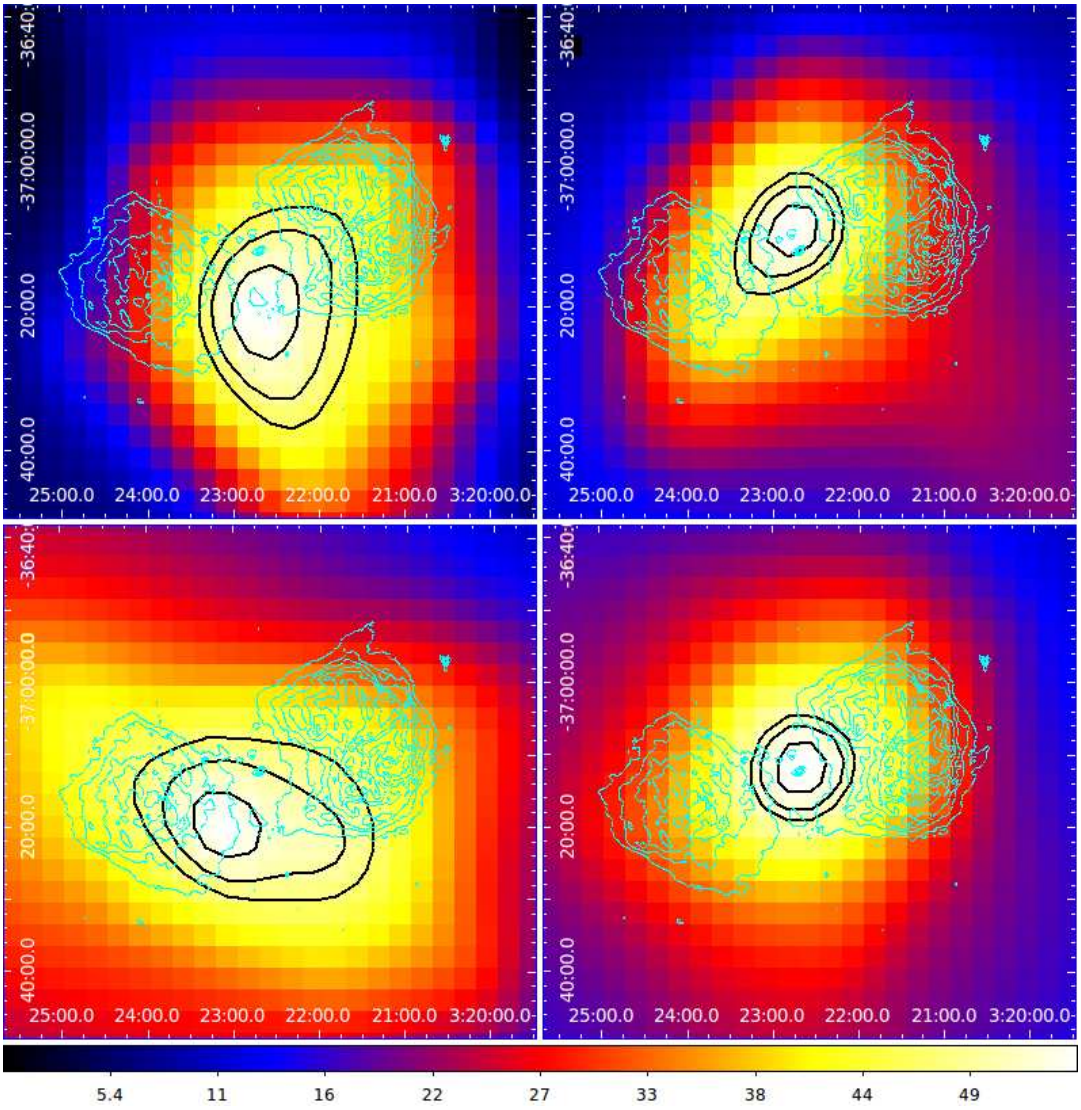

Figure 4.1: Test Statistic maps and associated localization contours (black) representing the 68%, 95%, and 99% confidence regions for the observed data (upper left), compared against the simulated confidence regions from an even distribution between lobes and core (upper right), pure lobe emission (lower left), and pure point source emission (lower right). Contours from the 20 cm image from [120] are included for reference (cyan).

Observed Data				
Spatial Model	Γ	Integral Flux[a]	TS	-log(likelihood)
point source only	2.25 ± 0.13	7.7 ± 2.0	54.9	329669.44
lobes only	2.19 ± 0.12	7.7 ± 1.9	58.9	329667.51
combined (point)	2.21 ± 0.46	1.3 ± 3.4[b]	1.4	329667.40
combined (lobes)	2.19 ± 0.15	6.4 ± 3.8	37.1	329667.40
Monte Carlo, Point Source Truth				
Spatial Model	Γ	Integral Flux[a]	TS	-log(likelihood)
point source only	2.39 ± 0.11	14.5 ± 2.8	121.0	333954.16
lobes only	2.34 ± 0.11	14.3 ± 2.7	113.4	333957.90
combined (point)	2.20 ± 0.12	9.5 ± 2.5	100.3	333949.48
combined (lobes)	NC	NC	NC	333949.48
Monte Carlo, Lobe Truth				
Spatial Model	Γ	Integral Flux[a]	TS	-log(likelihood)
point source only	2.51 ± 0.18	12.9 ± 3.0	60.8	332583.78
lobes only	2.41 ± 0.13	12.4 ± 2.8	67.0	332580.60
combined (point)	NC	NC	NC	332575.90
combined (lobes)	2.20 ± 0.14	7.6 ± 2.3	50.1	332575.90
Monte Carlo, Lobe and Point Source Truth				
Spatial Model	Γ	Integral Flux[a]	TS	-log(likelihood)
point source only	2.14 ± 0.13	7.3 ± 2.1	76.1	333642.00
lobes only	2.11 ± 0.12	7.8 ± 2.0	77.0	333641.77
combined (point)	1.86 ± 0.34	1.4 ± 1.9[b]	10.1	333639.98
combined (lobes)	2.26 ± 0.22	6.9 ± 3.3	29.0	333639.98

Table 4.1: Spectral parameters for the `gtlike` analysis of Fornax A using 44 months of data for both the observed source as well as the monte carlo simulations of a point source emission, extended lobe emission, and an even distribution between lobe and point source. A value of "NC" indicates a failure of the fit parameters to converge within the allowed bounds. [a]Flux is given above 100 MeV in units of $[10^{-9}\,\mathrm{cm}^{-2}\,\mathrm{s}^{-1}]$. [b]A larger statistical error in the integral flux than the value itself is a consequence of the low detection significance combined with a large covariance between the index and prefactor parameters. In this case, the parameters are not well constrained and should be considered largely uncertain.

indication of extension at the $\sim 2\sigma$ level was seen in each of the tested cases. As applied to searching for spatial extention in a LAT-detected source, the pointlike method has a distinct advantage over `gtlike` in that it allows a simultaneous fitting of source extension together with the spectrum and position of the source. Most advantageous is the ability to quantify a test statistic for the source extension, due to the parameterization of the spatial templates, which allows for the direct application of Wilks' Theorem. On the other hand, the `pointlike` tool compromises on the PSF used to convolve the estimated counts in the spectral fitting procedure by averaging the PSF over all angles θ, ϕ for a given band in measured energy (see Sections 3.4.3 & 3.5, in particular Equation 3.21). Therefore, while a $\mathrm{TS}_{extension} > 25$ would constitute a detection, a significance below this value does not necessarily rule out an extended component, nor does it imply that the possibility of future detection cannot be achieved through a more accurate description of the instrument PSF (see Section 5.2.2).

The last test was an examination of the variability of the γ-ray source. The light curve of Fornax A over the 44 month period is shown in Figure 4.2. The χ^2 test against the 44-month weighted average yielded a χ^2 probability $P(\chi^2 \geq \chi^2_{\mathrm{obs}})$ of 0.6761, in agreement with the tested hypothesis. From these results, we can see that while the relatively low statistics in the γ-rays is undoubtedly a contributing factor to the lack of variability seen in the source, a significant contribution of the total γ-ray emission originating from the extended lobes certainly cannot be

Spatial Model	Γ	Integral Flux[a]	$\sigma^{b}_{\rm semimajor}$	$\sigma^{b}_{\rm semiminor}$	$\mathrm{TS}_{extension}$
circular disk	2.22 ± 0.11	9.1 ± 2.0	0.40 ± 0.07		7.7
elliptical disk	2.23 ± 0.11	9.3 ± 2.0	0.42 ± 0.05	0.39 ± 0.04	7.7
circular gaussian	2.23 ± 0.11	9.1 ± 2.0	0.20 ± 0.05		6.4
elliptical gaussian	2.24 ± 0.11	9.4 ± 2.1	0.24 ± 0.11	0.15 ± 0.07	6.4

Table 4.2: Spectral parameters for the `pointlike` analysis of Fornax A comparing the spatial models of a circular disk, elliptical disk, circular gaussian, and elliptical gaussian. [a]Flux is given above 100 MeV in units of $[10^{-9}\,\mathrm{cm}^{-2}\,\mathrm{s}^{-1}]$. [b]Semimajor and semiminor axes are given in units of degrees.

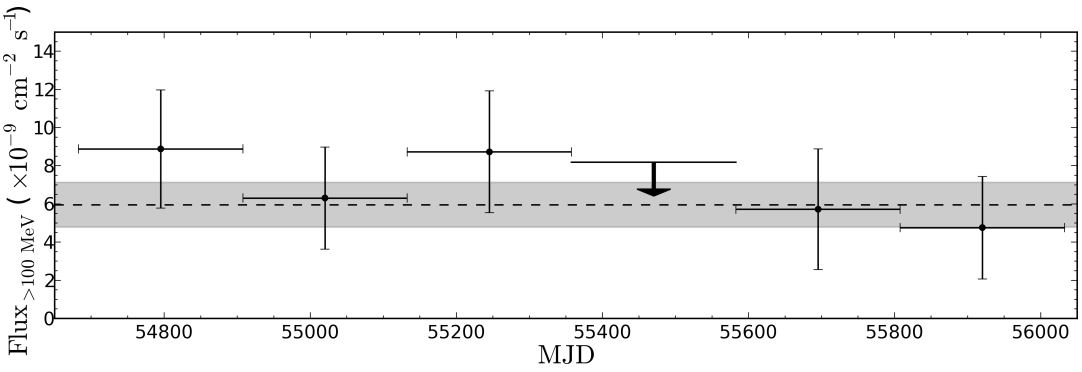

Figure 4.2: 44-month light curve of Fornax A, modeled as a point source to a power law spectrum with photon index $\Gamma = 2.25$. The points were divided into 225 day bins, with the dashed horizontal line and dark gray region representing the weighted mean and corresponding error over the period of observation. Each point falling below a 2σ detection was plotted as an upper limit.

ruled out, and would indeed be supported by these results. Furthermore, with the lower limits included in the weighted average, no significant deviation below the weighted average was found to occur, which otherwise might be expected in the case of variable emission originating from the core. Continued monitoring of the source variability from *Fermi*-LAT will be helpful, as longer-timescale variability can be tested, allowing for improved statistics, as well as the ability to detect any potential flaring activity that might occur in the coming years.

4.1.4.2 Future Outlook: High Resolution Imaging with the NuSTAR Telescope

In the likely case where a spatial and spectral distinction between the HE lobe and core spectra in the LAT range cannot be achieved, there is still a significant potential in being able to model the two components using multiwavelength data. This can be done via high resolution measurements of the non-thermal spectra from both the lobes and core at a high enough energy that the two spectral components can be extrapolated into the LAT energy range and compared against the total γ-ray spectrum. The NuSTAR telescope [149] is perhaps the most promising instrument in the current generation of telescopes for achieving this. The NuSTAR telescope is a hard X-ray telescope operating in the energy range of $3 - 78.4\,\mathrm{keV}$, with an angular

resolution of 18″ full width at half-maximum, with a half-power diameter of 58″, and an energy-dependent FOV, defined by the radius at which the off-axis effective area falls to 50% of its on-axis value, of 10′ at 10 keV and 6′ at 68 keV. Figure 4.3 illustrates the NuSTAR FOV compared to the angular size of the western lobe of Fornax A, where we find that NuSTAR is capable of detailed structural imaging of the non-thermal emission, while simultaneously allowing a nearly complete view of the western lobe from within the defined FOV.

Equally important to the angular resolution offered by the NuSTAR telescope is the range of energy that it covers. Figure 4.4 illustrates the preliminary modeling of the combined lobe and core SED, where we find that the extrapolation of the IC emission from the core component into the LAT range is currently unknown, due to a lack of constraint in the spectrum below the LAT energy range. The NuSTAR telescope is ideal for obtaining the spectral shape of both the core and lobe components, which will significantly aid in modeling the total LAT emission. For example, if the core spectrum follows the extrapolation into the LAT range as illustrated in Figure 4.4, the modeling would place a larger component to the core, thus reducing the total contribution to γ-rays of the lobes. If, on the other hand, NuSTAR measures a soft spectrum from the core, then the bulk of the LAT emission would be attributed to the lobes, thus constituting a higher level of EBL.

4.1.5 Conclusions

We have demonstrated that the LAT emission is consistent with a non-variable source, with marginal evidence of extension. While further improvements on the LAT angular resolution could potentially lead to a detection of extension from Fornax A, the most promising method for spatially and spectrally resolving the non-thermal lobe and core emission, and consequentially obtaining a measurement of the EBL, lies in the vastly improved angular resolution of hard X-ray instruments such as NuSTAR. Indeed, Fornax A may be one of multiple radio galaxies where such spectral constraints could be performed, with other promising candidates such as Centaurus B and NGC 6251 also offering potential. A measurement of the EBL on multiple galaxies within the resolution of NuSTAR would bring a higher level of confidence to the EBL measurement using this method, as well as to provide separate measurements as a function of redshift.

4.2 Nonblazar properties of the gamma-ray AGN 4C+55.17

4.2.1 Introduction

The radio-loud active galaxy 4C +55.17 (0954+556), formally classified as a flat spectrum radio quasar (FSRQ), has a history of γ-ray observations dating back to the EGRET era, as 3EG J0952+5501 [151, 210] and EGR J0957+5513 [74]. Due to a relatively poor localization of the EGRET source, however, the association of the γ-ray emitter with 4C +55.17 remained tentative at that time. This association was on the other hand quickly confirmed by the LAT [37], initially as 0FGL J0957.6+5522

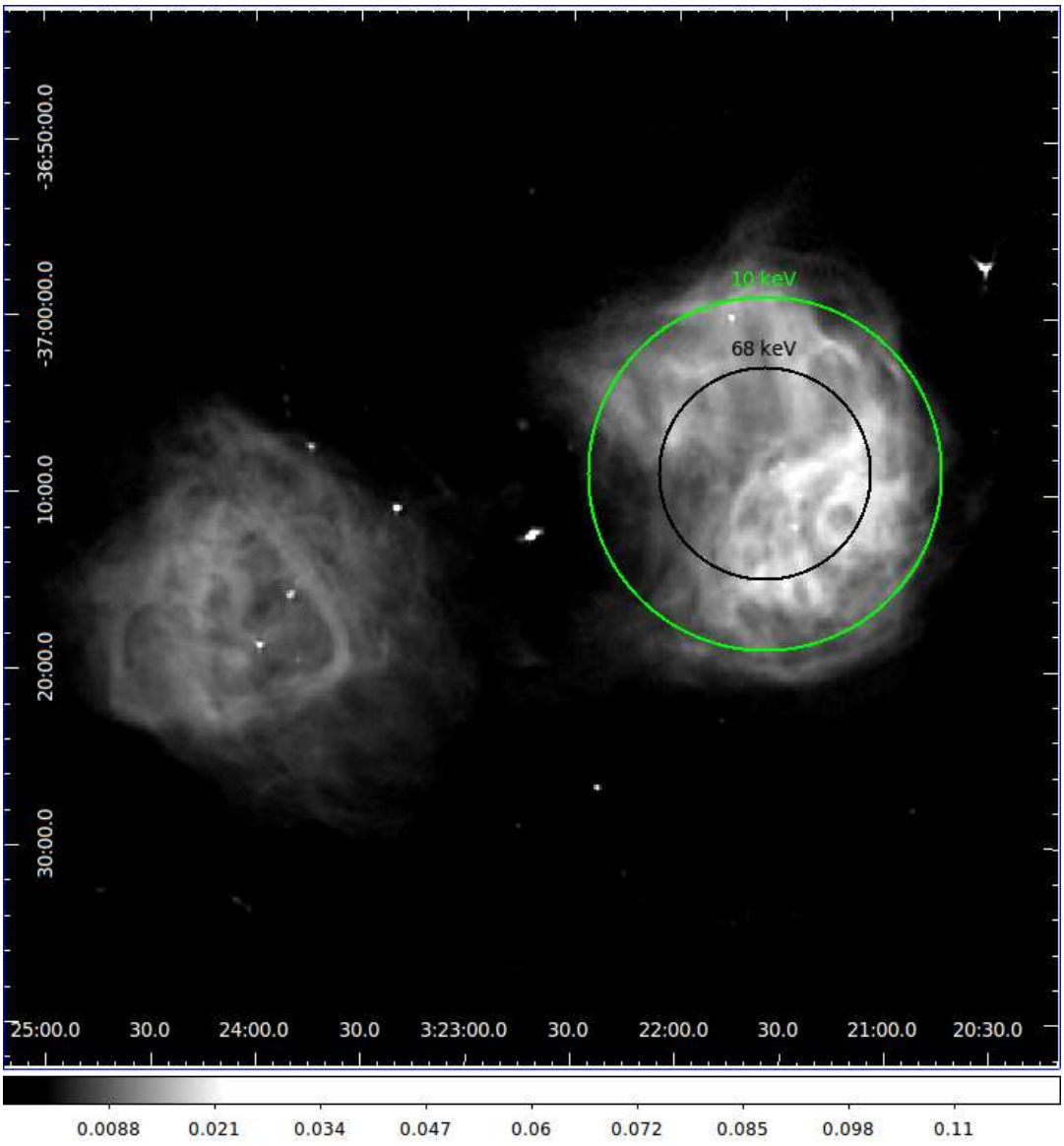

Figure 4.3: NuSTAR Field of View (FOV) at 68 keV (black) and 10 keV (blue), compared to the total size scale of the lobes of Fornax A. The FOV is defined by the radius at which the off-axis effective area falls to 50% of its on-axis value.

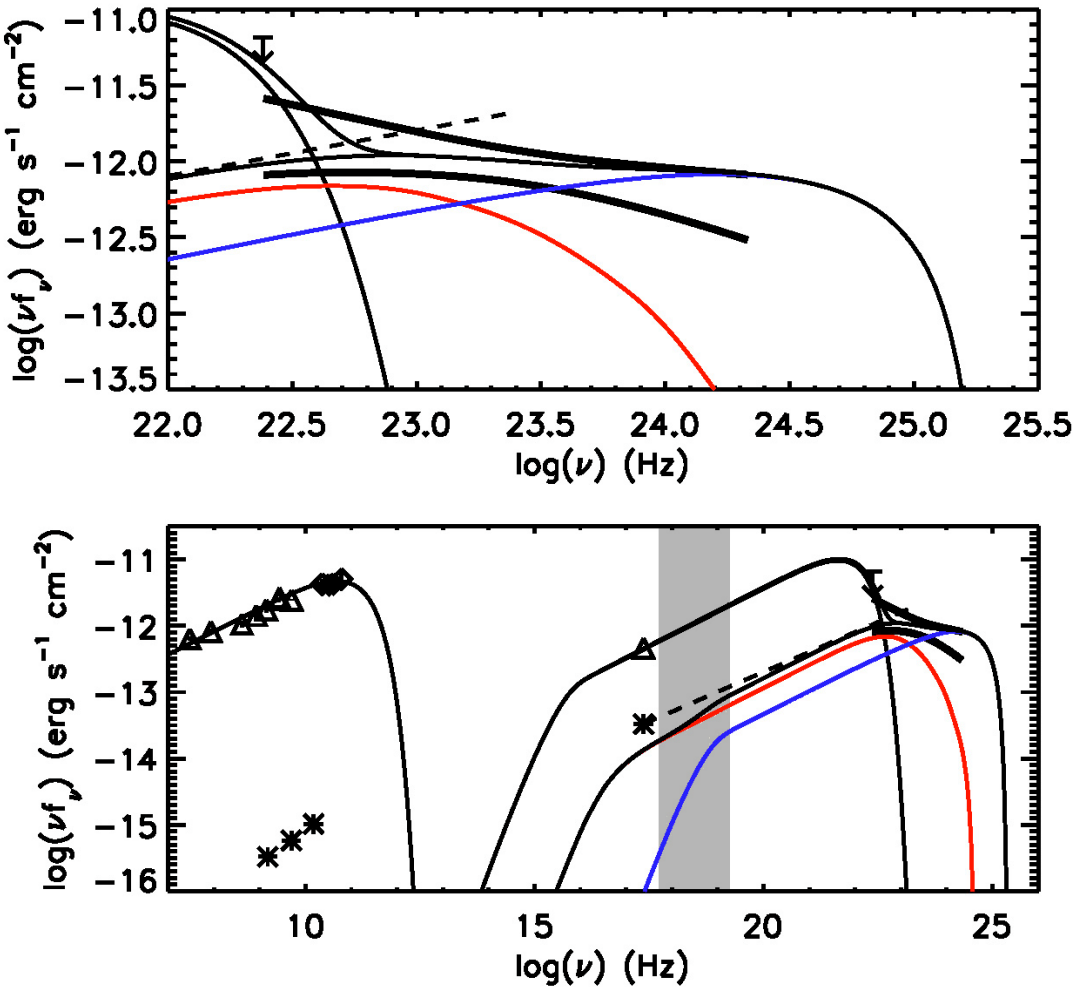

Figure 4.4: Preliminary modeling of the extended γ-ray emission from Fornax A, along with archival data of the lobe (triangle) and LINER core (square) emission. The historical EGRET upper limit is also plotted. The blue line is the IC emission due to the COB and the host galaxy optical photons, the red line is the IC emission due to the CIB, and the black line is the total SED due to CMB (left IC peak), and EBL and host galaxy seed photons (right IC peak). The dashed black like represents the extrapolation of the core flux through the NuSTAR energy range (gray shaded area) and into the LAT spectrum (thick black lines). A well measured spectrum of the Fornax A lobe and core emission in the NuSTAR energy range would provide important constraints to the spectral modeling of each source.

[9, 10], and most recently as 1FGL J0957.7+5523 [4], with a significantly improved localization of 0°.017 [211].

The quasar classification of 4C +55.17 may be attributed to the presence of broad optical emission lines in its spectrum [314] and high optical/UV core luminosity (absolute B-band magnitude, $M_{\rm B} < -23$;[308]). Its redshift[3], $z = 0.896$, is based on the detection of Lyα and C_{IV} lines with the *Hubble Space Telescope*-Faint Object Spectrograph (HST-FOS;[314]) and Mg_{II} in the SDSS spectrum [264]. The optical-UV properties of the source, together with its high γ-ray luminosity of the order $L_\gamma \simeq 10^{47}\,{\rm erg\,s^{-1}}$, have in turn led to the common classification of 4C +55.17 as a blazar/FSRQ.

However, 4C +55.17 also exhibits a number of morphological and spectral properties that have placed its exact blazar/FSRQ classification into question [207, 259]. FSRQs are uniquely characterized by the presence of a central compact radio core exhibiting a highly variable flat-spectrum continuum, high brightness temperatures ($T_{\rm b}$), and, typically, superluminal motions on Very Long Baseline Interferometry (VLBI) scales [305]. Indeed, all of the aforementioned radio properties are shared by the luminous blazars detected in γ-rays: these are exclusively observed to possess compact, highly polarized jets a few milliarcseconds (mas) in angular size, and unresolved radio cores with brightness temperatures in the range $T_{\rm b} = 10^{10}$–$10^{14}\,{\rm K}$ when observed at 5 GHz [296] and 15 GHz [182, 191]. In comparison, 4C +55.17 demonstrates none of these characteristics. To date, the source shows no evidence of blazar flaring at any wavelength, nor any evidence of long-term variability, with the exception of a $\sim$ 30% optical flux-density change noted over a period of 7 years between recent *Swift*/Ultraviolet/Optical Telescope (UVOT) measurements and archival SDSS data (see Sections 4.2.3 and 4.2.4 for discussion). Furthermore, the VLBI radio morphology of the source is extended over $\sim 400\,{\rm pc}$ (projected). The peak surface brightness in a VLBA 15 GHz image taken from [259] is found in the northernmost component and is clearly resolved, with a corresponding brightness temperature $T_{\rm b} < 3 \times 10^8$ K ([191], also consistent with a measurement at 5 GHz;[296]), which is uncharacteristic of all the other known quasar-hosted γ-ray blazars (see in particular Figure 4.5).

Based on the radio morphology of 4C +55.17, [259] first suggested that the source may in fact belong to the family of young radio sources (for a review, see[227]), rather than blazars. Such sources are characterized by a very low radio variability (if any) and symmetric double radio structures resembling "classical doubles" on much smaller scales: linear sizes (LSs) $\lesssim 1\,{\rm kpc}$ for compact symmetric objects (CSOs) and $\sim$ 1–15 kpc for medium symmetric objects (MSOs;[39]), to be compared with the typical LSs of "regular" Fanaroff–Riley type-II radio galaxies of $\sim 100\,{\rm kpc}$. In many cases, CSO sources are found to exhibit a turnover in their radio spectra in the range of 0.5–10 GHz, as the so-called Gigahertz Peaked Spectrum (GPS) objects do [90]; similarly, MSOs often display turnover frequencies below 0.5 GHz, typical of the Compact Steep Spectrum (CSS) class of sources [106]. The overlap between

[3]Assuming a ΛCDM cosmology with $H_0 = 71\,{\rm km\,s^{-1}\,Mpc^{-1}}$, $\Omega_{\rm M} = 0.27$, and $\Omega_\Lambda = 0.73$, the luminosity distance $d_{\rm L} = 5785\,{\rm Mpc}$, and the conversion scale is $1\,{\rm mas} = 7.8\,{\rm pc}$.

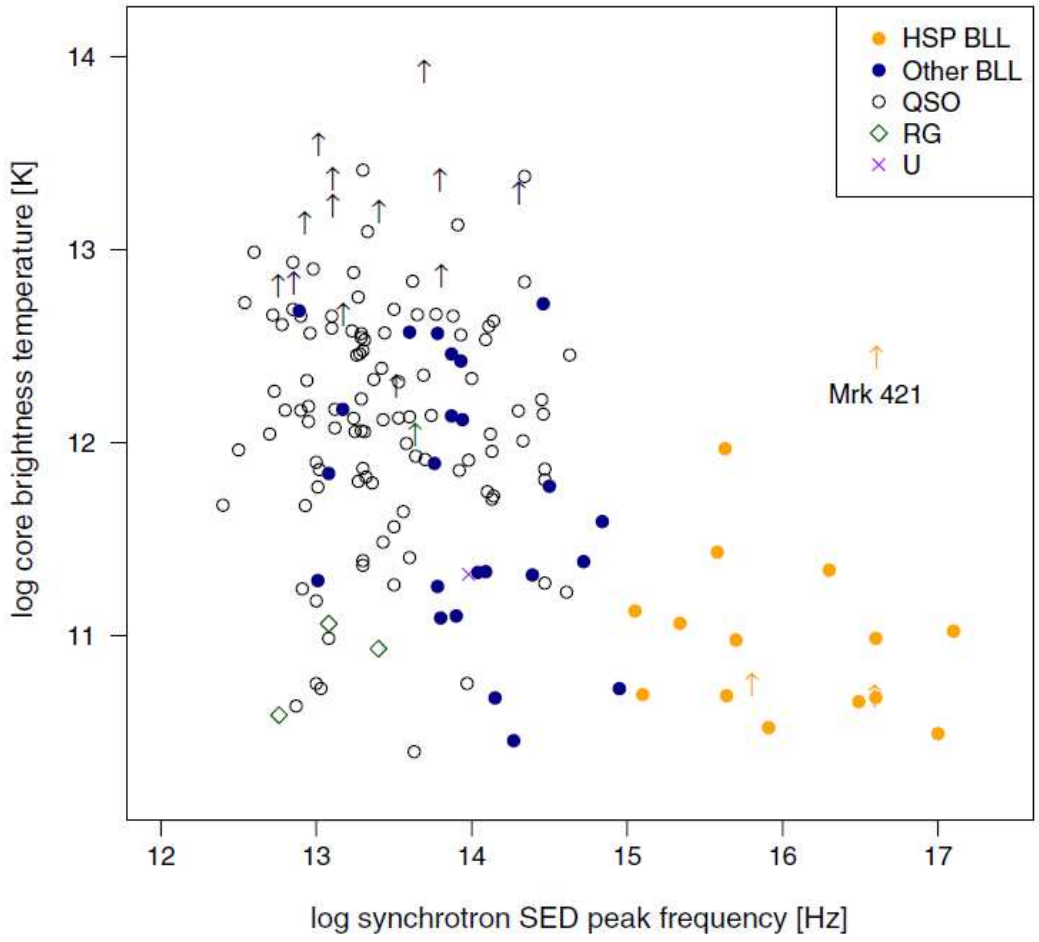

Figure 4.5: Radio core brightness temperature of the 15 GHz MOJAVE northern hemisphere VLBA blazar monitoring program, plotted against γ-ray SED peak frequency(from [191]). The filled circles represent BL Lac objects, divided into high synchrotron peaked (orange), and low synchrotron peaked (blue). Open circles represent quasars, the green diamonds radio galaxies, and purple crosses optically unidentified objects. The plot includes all sources from the MOJAVE sample detailed in [191], with the single exception of 4C +55.17. At a synchrotron peak frequency of $10^{13.77}$ Hz, with brightness temperature $T_b = 10^{8.46}$ K, 4C +55.14 falls several orders of magnitute below the sample population.

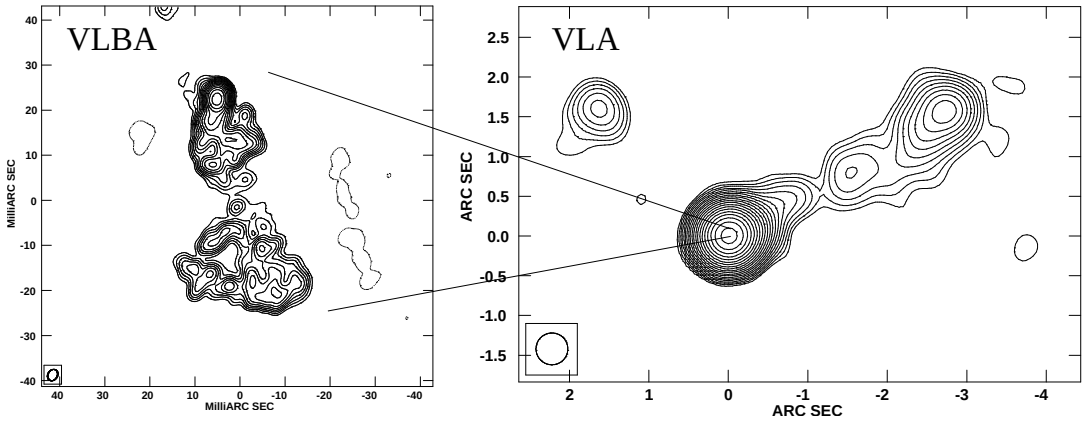

Figure 4.6: VLBA 5 GHz map (left) featuring the inner parsec-scale radio structure of 4C +55.17, reimaged using data from [153]. The beam size is 2.0 mas × 1.6 mas (position angle = −29.6°), and the contour levels increase by factors of $\sqrt{2}$ beginning at 1 mJy/beam. The resolved morphology has a total angular size of 53 mas (413 pc). The VLA 5 GHz map (right) with a 0.4″ beam (lowest contour is 2 mJy/beam increasing by factors of $\sqrt{2}$) shows the large scale radio structure (from[295]).

CSO and GPS samples, as well as between samples of MSOs and CSS sources, is however not complete [276, 39]. In the case of 4C +55.17, the VLBI morphology at 5 GHz reveals two distinct emission regions, to the north and south ([259]; see also Figure 4.6), covering a total angular extent of 53 mas (= 413 pc, projected). On the kpc scale, the source reaches 4″.5 (∼ 35 kpc, projected), and it is resolved with the Very Large Array (VLA) in three components, the central one hosting the VLBI structure. The northern component of the pc-scale emission features a compact region with a relatively flat spectrum ($\alpha = 0.4, F_\nu \propto \nu^{-\alpha}$;[259]), which can be attributed to a core or a hot spot region, while the southern component features a more diffuse and slightly steeper-spectrum ($\alpha = 0.49$) region. [259] have pointed out that these two components resemble more compact hot spots and lobes, suggesting a CSO/MSO classification for this object. The kpc-scale emission might thus be interpreted as a remnant of previous jet activity, as this is a common feature among sources that show evidence of intermittent behavior (e.g.,[42, 195, 229]). Under the CSO/MSO framework, [259] found no core candidate between the VLBA-scale lobes at a level $\gtrsim 2$ mJy beam^{-1} in a 15 GHz map.

An 11 month comparison of the γ-ray variability and spectral properties of 4C +55.17 against the other LAT FSRQs highlights the atypical behavior of the source [4, 5]. Among all of the sources originally detected in the 3 month LAT Bright AGN Sample (LBAS;[10]) that were classified as FSRQs, 4C +55.17 is characterized by the lowest variability index [4]. In addition, the γ-ray continuum is found to have one of the hardest spectra among FSRQs in the 1st LAT AGN Catalog (1LAC;[5]). In fact, of those sources included in the 1LAC (FSRQ or otherwise) with > 1 GeV flux greater than or equal to that of 4C +55.17, only five — all of which are BL Lac objects (PKS 2155–304, Mkn 421, 3C 66A, PG 1553+113, and PKS 0447-439) — appear with a harder γ-ray spectrum.

In this work, we re-examine the high-energy γ-ray ($> 100\,\mathrm{MeV}$) properties of 4C +55.17 using 5 years of LAT all-sky survey data and discuss the implications of these results in two domains. First, we reconsider the underlying physical processes responsible for the γ-ray emission through detailed broadband modeling of the source in the context of two scenarios: "young radio source" and "blazar." In addition, we demonstrate that the observed properties of the source make it an ideal candidate for studying the high-redshift universe at very high energies (VHEs), in particular for placing constraints on the level of extragalactic background light (EBL). The section is organized as follows. Section 4.2.2 details the analysis of 5 years of LAT data and discusses the supporting multiwavelength observations. In particular, Section 4.2.2.1 focuses on the LAT data reduction, presenting new spectral, and variability analysis, including a detailed analysis of the 145 GeV photon detection associated with the source (see also Appendix B). Section 4.2.3 discusses the multiwavelength observations, including analysis of archival radio and *Swift* X-ray and optical data, as well as a new hard X-ray detection with the *Swift* Burst Alert Telescope (BAT). Spectral properties and classification of 4C +55.17 are discussed in Section 4.2.4. We follow with a detailed analysis of the high energy spectrum of 4C +55.17, where we place constraints on models of EBL and discuss the implications of the 145 GeV photon detection to future VHE observations of the source (Section 4.2.5). Our conclusions are presented in Section 4.2.6.

4.2.2 Observations

4.2.2.1 *Fermi*/LAT Observations

The following analysis is comprised of 5 years of nominal all-sky survey data extracted from a $14^\circ \times 14^\circ$ square region of interest (ROI) around the J2000.0 radio position of 4C +55.17 (R.A. = $09^\mathrm{h}57^\mathrm{m}38.1844^\mathrm{s}$, Decl. = $55^\circ22'57.769''$;[115]) and covers the mission elapsed time (MET) 239557417 to 397323817 (August 4, 2008 through August 4, 2013). Event selections include the "source" event class [37] recommended for point source analysis, a zenith angle cut of $< 100^\circ$ to avoid contamination from the earth limb, and rocking angle cuts at 43° and 52°, respectively, for times corresponding to a change in the instrument's rocking angle from 39° to 50° that occured on September 3, 2009 (MET 273628805). Science Tools `v9r27p1` and the pass 7 version 15 reprocessed instrument response functions (IRFs) `P7REP_SOURCE_V15` were used for this analysis.

In order to model the γ-ray emission, all point sources from the 1FGL catalog [4] within 15° of the source were included. Sources within 10° of the 4C +55.17 radio position were modeled with their flux and spectral parameters set free, while those sources that fell outside the 10° ROI were fixed at their catalog values. The diffuse background was modeled using the recommended[4] Galactic diffuse `gll_iem_v02.fit` along with the isotropic spectral template `isotropic_iem_v02.txt`.

Prior to fitting the spectrum, the high energy photons attributable to the

[4] `http://fermi.gsfc.nasa.gov/ssc/data/access/lat/BackgroundModels.html`

4C +55.17 position (both radio and γ-ray) were found by comparing the energy and incoming angle θ (defined with respect to the spacecraft zenith) of each photon within the ROI to the 95% containment radius of the point spread function defined by the `P7REP_SOURCE_V15` IRFs. Included among those photons was a 145 GeV event at an angular separation of 0.06° (R.A. = $09^{\rm h}58^{\rm m}03^{\rm s}$, Decl. =55°24′00″) from the 4C +55.17 position, falling well within the 95% containment radius for the given energy and angle of incidence, including an additional event at 146 GeV that fell just outside of the 95% containment radius at an angular separation of 0°.89, but which was attributed to the source at 56% probability in the analysis described in Appendix B). Through the analysis of the event diagnostics, the photon nature of the 145 GeV event was confirmed to high probaility (see Appendix B). In addition, several photons in the $\sim 30 - 85$ GeV range were also detected.

A spectral analysis of 4C +55.17 was performed with `gtlike` using the LAT data between 100 MeV and 300 GeV. Spectral data points were first obtained by fitting each of 9 equal logarithmically spaced energy bins to a separate power law with index and prefactor parameters set free. From the resulting data points, a significant spectral curvature over the range from 100 MeV to 20 GeV was found which could be fit to the data points using a log parabola function. The maximum energy of 20 GeV was chosen in order to avoid fitting any portion of the spectrum that may be significantly attenuated by the EBL. A likelihood ratio test [209] resulted in a 3.9σ improvement of the log parabola over the single power law, which we found sufficient in light of the agreement with the spectral data points at lower energy to warrant its use in modeling the intrinsic spectrum.

To test the γ-ray variability over the 5 year period, we made light curves in time bins of 14 days. Due to the limited statistics over each interval, the source was fit to a single power-law in each bin, with index and prefactor parameters free. To improve the fit convergence, point sources in the ROI were included only if they were detected with a test statistic (TS; see Equation 3.23) greater than 1 ($\sim 1\sigma$). The resulting light curve (> 1 GeV), divided into 14 day bins, is shown in Figure 4.7. The variability of 4C +55.17 was analyzed by means of a χ^2 test following the method outlined in Section 3.5.2.2, where we assumed the model describing the data to be a constant straight line with intercept equal to the weighted mean of all $> 3\sigma$ detections. This test yielded a weighted mean of $(9.49 \pm 0.20) \times 10^{-9}\,{\rm ph\,cm^{-2}s^{-1}}$, and yielded a χ^2 probability $P(\chi^2 \geq \chi^2_{\rm obs})$ of 0.96 and 0.87 for the 7 day and 28 day light curves, respectively, in agreement with the tested hypothesis. We therefore found no evidence of variability in γ-rays over the 5 year LAT observing period, consistent with the previous 11-month and 19-month lightcurve analysis ($\sim$ 30 day bins, and 7 day bins, respectively) from [4] and [211].

An second diagnostic in testing whether the non-variable emission in 4C +55.17 represents a significant deviation from the behavior of γ-ray loud blazar sources is to compare the observed variability index against the population of LAT AGN in a manner that differentiates between sources whose non-variability is statistically significant and sources whose variability is due instead to a lack of statistics from low detection significance. In order to carry out this test, we used the complete sample of LAT AGN that was obtained through an association of sources conducted

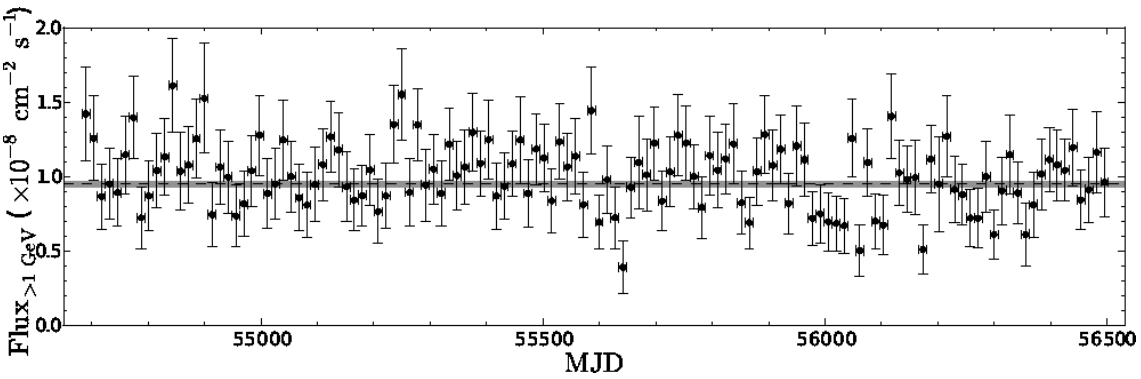

Figure 4.7: Fermi-LAT 5 year γ-ray light curve of 4C +55.17 divided into 14 day bins. All points represent $> 3\sigma$ detections and are plotted along with their statistical errors. The dashed horizontal line and gray region represent the weighted mean and corresponding error derived from all $> 3\sigma$ detections over the observing period.

on an internal four year catalog using the methods outlined in [18]. From the parent sample, we obtained energy flux measurements that were calculated by integrating the spectra times the energy of each source over the LAT energy range of 100 MeV to 300 GeV. This allowed a distinction to be made among different sources in terms of their signal over background as well as to remove any spectral bias that would favor sources that peaked at the lower energy threshold, which would occur in the case of using the standard flux above a given energy. The energy flux was then plotted against the variability indices that were obtained from the four year data set using the variability test described in [225].

The results from the aforementioned diagnostic are illustrated in Figure 4.8. The plot reveals 4C +55.17 as having the highest energy flux among all LAT AGN over the four year data set. A dedicated search of the non-variable objects whose energy flux was in the vicinity of 4C +55.17 (within a factor of ~ 2) yielded four objects: B3 0133+388, Centaurus A, AP Lib, and RGB J2243+203. Among those, two objects are classified as HSP BL Lac (B3 0133+388 and RGB J2243+203), one as a LSP BL Lac (AP Lib), and another is the nearby radio galaxy Centaurus A. It is worth noting that HSP BL Lac objects demonstrate typically lower core brightness temperatures than their LSP BL Lac or FSRQ counterparts, which has given rise to the so-called "Doppler factor crisis" [191], though in the present case, no such crisis is seen, due to the lack of variability in these sources. Also interesting to note is the prominance of Centaurus A, which has been confirmed to emit a significant fraction of its γ-ray flux as an extended isotropic emission [110], which would account for the lack of variability seen from the source. Perhaps the most unusual object to be found as non-variable over the four year data set is the LSP BL Lac object AP Librae, which historically has been distinguished by its large rapid flares in the optical band [71]. Interestingly, during the fifth year of LAT observation over the period MJD 56306-56376, AP Lib underwent a factor 3.5 flare at HE, coinciding with the discovery of VHE γ-ray emission up to the TeV range by H.E.S.S. [145], thus establishing its status as a variable object in the HE/VHE range.

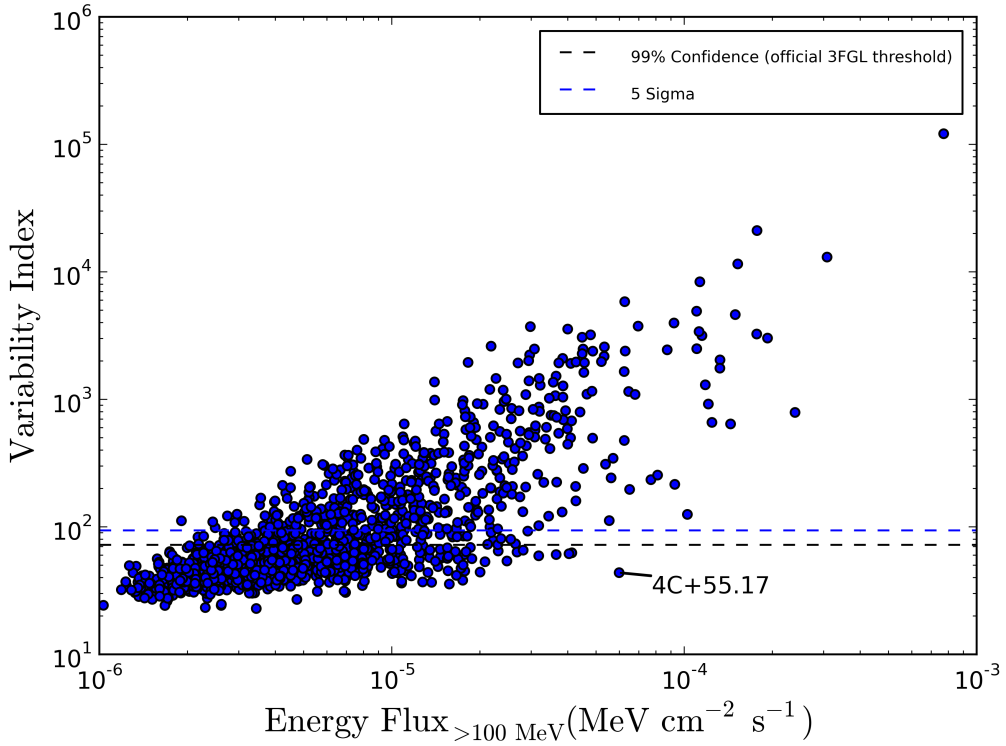

Figure 4.8: Energy Flux over the LAT energy range versus variability index for AGN associations using a four year internal LAT catalog. The dashed black line represents the 99% confidence threshold for variability, following the official 2FGL catalog. The dashed blue line represents a more conservative 5σ confidence level. 4C +55.17 currently stands as the most luminous non-variable AGN across the LAT energy range.

4.2.3 Multiwavelength Data

4.2.3.1 X-ray

We analyzed all *Swift* [129] data obtained over the 19-month LAT observing period, which consisted of three X-ray Telescope (XRT;[68]) snapshots (1.6-4.5 ks), in order to check the X-ray state of the source. We used the xrtgrblc script (available in the HEASoft package version 6.8) to analyze the XRT observations: we reprocessed the data stored in the HEASARC archive using the latest XRT calibration database (20091130), selecting the events with 0-12 grades in photon counting mode (PC). The scripts chose the optimal source and background extraction regions based on the source intensity: the X-ray photons were extracted using a $25''$ circle for the source and an annulus with $50'' - 150''$ inner-outer radius for the background. Adding all of the exposure and performing a C-statistic fit from $0.3 - 10\,\mathrm{keV}$ using XSpec12, we found the best fit obtained to be a power law with absorption fixed at the galactic value ($N_{\mathrm{H}} = 9 \times 10^{19}\,\mathrm{cm}^{-2}$), where we obtained the photon index $\Gamma = 1.84 \pm 0.19$, with an absorbed flux of $(8.3^{+1.7}_{-1.4}) \times 10^{-13}\,\mathrm{erg\,cm^{-2}\,s^{-1}}$ and an unabsorbed flux of $(8.5^{+1.7}_{-1.4}) \times 10^{-13}\,\mathrm{erg\,cm^{-2}\,s^{-1}}$. Comparing each of the individual observations, no X-ray variability was found, with all measurements falling within the joint errors. These results were also compared with previous *Chandra* data [295] obtained June 16, 2004, where the flux was found again to be non-variable within the statistical errors. Finally, historical X-ray data from ROSAT [81] obtained November 7, 1993 were included in the spectral energy distribution (SED) modeling to further constrain the soft X-ray portion of the spectrum.

In the hard X-rays, data from the *Swift*/BAT [29, 28] were analyzed using five years of cumulative exposure from November $2005 - 2010$. We detect the source for the first time in the hard X-ray band, with a $15 - 150\,\mathrm{keV}$ flux of $(6.75^{+0.38}_{-5.21}) \times 10^{-12}\,\mathrm{erg\,cm^{-2}\,s^{-1}}$ and a power-law photon index, $\Gamma = 1.79^{+1.17}_{-0.84}$.

4.2.3.2 Optical & Infrared

During each of the three *Swift* pointings in 2009, Ultra-Violet/Optical Telescope (UVOT;[258]) observations were also obtained. Data were obtained in all 6 filters in the first two epochs, and the last epoch with only the $W2$ filter. The data reduction and analysis was performed using the uvotgrblc script, which reprocesses the data stored in the HEASARC using the latest UVOT calibration database (20100129). The optimal source and background extraction regions were a $5''$ circle and a $27'' - 35''$ annulus, respectively. Table 4.3 summarizes these observations. A comparison of the results between each epoch shows the source to fall within the joint errors in flux in the optical to UV bands across all three epochs. These results were also compared with archival SDSS data from February 2, 2002 [21]. A comparison of the UVOT and SDSS U-band flux densities shows an increase from $(0.187 \pm 0.003)\,\mathrm{mJy}$ in the SDSS data to $(0.250 \pm 0.007)\,\mathrm{mJy}$ in the UVOT data, indicating a $\sim 30\%$ rise in flux over 7 years. In addition, the UVOT V- and B-band flux densities were averaged using a least-squares approach to a linear fit and com-

Band	λ [Å]	$F_{\rm ep1}$ [mJy]	$F_{\rm ep2}$ [mJy]	$F_{\rm ep3}$ [mJy]
V	5402	0.331 ± 0.061	0.337 ± 0.029	..
B	4329	0.262 ± 0.015	0.286 ± 0.015	..
U	3501	0.249 ± 0.010	0.251 ± 0.011	..
UVW1	2634	0.175 ± 0.007	0.174 ± 0.007	..
UVM2	2231	0.142 ± 0.029	0.167 ± 0.007	..
UVW2	2030	0.125 ± 0.009	0.127 ± 0.005	0.130 ± 0.005

Table 4.3: *Swift*/UVOT observation of 4C +55.17. The observations were obtained on 2009 March 5 (ep1), Nov 11 (ep2), and Nov 26 (ep3).

pared with the SDSS g-band, which fell between the two. The average of the UVOT V- and B-bands, measured at (0.305 ± 0.014) mJy, shows a similar $\sim 25\%$ increase from the SDSS measured value of (0.240 ± 0.011) mJy. A comparison of the *Swift* UVOT measurements to the continuum flux underlying the Lyα line obtained by HST-FOS in 1993 [314] shows the fluxes to be equal between these two periods.

In the near-infrared, we included historical data from the 2MASS Point Source Catalog [85], for which the absolute calibration was taken from [79]. All infrared, optical, and ultraviolet data were dereddened by means of the extinction laws given by [70], assuming a B-band Galactic extinction ($A_{\rm B} = 0.038$) as determined via [263], and a ratio of total to selective absorption at V equal to $R_{\rm V} = 3.09$ [257].

4.2.3.3 Radio

To model the γ-ray emission in 4C+55.17 (sec. 3.1), we compiled integrated radio to sub-mm measurements of the source [58, 155, 250, 162], including 5-year WMAP data [315], and other archival data from the NASA/IPAC Extragalactic Database (NED). In order to isolate the total radio flux from the inner ~ 400 pc scale structure[5], we re-analyzed several archival VLA data sets from 5 to 43 GHz (see Figures 4.10 and 4.11). The typical resolutions are $\sim 0.1''$ to $0.4''$, ensuring a total measurement of the ~ 50 mas scale structure without loss of flux as in the VLBI observations (e.g.,[259]). We also include similar measurements from previously published VLA 5 and 8.4 GHz [251, 220, 295] and MERLIN 0.4 and 1.7 GHz [251] maps.

The radio variability properties of 4C +55.17 are important for assessing its nature. We therefore searched the literature for various archival radio to sub-mm monitoring observations of the source (e.g.[34, 310, 266, 162]), including 22 and 37 GHz data from the Metsähovi monitoring program [298, 299, 300]. While the Wardle et al. (1981) [310] data was not publicly available, we note from the literature that the authors found the source to be non-variable. Variability in each of the remaining cases was measured by applying a statistical χ^2 test of the available data using the hypothesis of a constant source with flux equal to the weighted mean. The results were consistent with the tested hypothesis in each case, with the exception

[5]The kpc-scale radio emission is not expected to contribute significantly toward the modeling of the high energy portion of the spectrum (see §4.2.4.1 & §4.2.4.2).

of the Metsähovi data, which yielded probabilities $P(\chi^2 \geq \chi^2_{obs})$ of 6.44×10^{-56} and 8.56×10^{-24} at 22 GHz and 37 GHz, respectively. To quantify this variability, we compared fractional variability indices using the formula $Var_{\Delta S} = (S_{max} - S_{min})/S_{min}$ used in a variability study of GPS sources [303], where we obtained values of 3.5 and 1.43 at 22 and 37 GHz, respectively. The 22 GHz value fell slightly above the nominal variability threshold of 3.0 set by [303] as an upper limit for the bona fide GPS sources. This result, however, arose due to a single outlying flux measurement at 22 GHz of 0.32 ± 0.09 Jy which occurred ~ 40 minutes after a previous measurement of 1.12 ± 0.08 Jy at the same frequency[6]. Removing this questionable flux point and performing the test again resulted in a fractional variability index of 0.89, which fell well within the proposed threshold for genuine GPS galaxies. We therefore find the degree of variability in 4C +55.17 to be consistent with the behavior of confirmed young radio galaxies, rather than blazars.

4.2.4 Modeling & Classification

4.2.4.1 CSO Modeling

As noted in the introduction, there are several reasons to consider the possible nature of 4C +55.17 as an example of a luminous AGN exhibiting recurrent jet activity, with young and symmetric (CSO-type) inner radio structure instead of a "core-jet" morphology typical of blazars. While the physical nature and the origin of the CSOs is at some level still debated, the most likely and widely accepted hypothesis states that they are the young versions of present-day extended radio galaxies [242, 105]. In the alternative explanation, these sources are considered to be of a similar age to normal radio galaxies, but only confined/frustrated due to dramatic interactions with a surrounding dense gas in their host galaxies [306, 313]. The latter scenario is however inconsistent with the lack of observational evidence for the amount of ambient gas required to supply sufficient confinement [91, 72, 73, 271] (see, however, [127] for notable exceptions). More promising is therefore the "youth" scenario for CSOs, for which a number of evolutionary models were proposed [43, 92, 240, 169].

While many observational properties of 4C +55.17 make its classification as a young radio source compelling, it is also worth noting the characteristics that could make such a classification potentially difficult. For example, if 4C +55.17 is indeed a CSO, it is the only such object to be identified as a γ-ray emitter in 1FGL/1LAC, with a GeV flux nearly an order of magnitude higher than the lower limit of the complete flux-limited subsample within the 1LAC catalog [5]. This would immediately set the object apart as an outstanding member of its class. In addition, the relatively high radio polarization of the source ($\sim 3\%$ in a $\sim 0.2''$ resolution VLA 8.4 GHz image;[160]), is uncharacteristic of the typically low ($< 1\%$) radio polarization seen among CSOs [249], although polarized emission from CSOs has occasionally been found (e.g.,[144]). The low polarization of CSOs, which are entirely embedded within

[6]Variability within hour timescales is rare at the frequencies observed by Metsähovi (A. Lahteenmaki, T. Hovatta, & M. Tornikoski, private communication 2010)

the inner regions of the host galaxy, is often attributed to the large expected Faraday depths of the surrounding interstellar medium [67, 51, 144]. The surrounding medium may also play a key role in shaping the spectral turnover seen in the GPS class of young radio sources, through the free-free absorption (FFA) process (either internal or external to the emission region;[51, 44, 236]). The nature of the absorber is however still widely debated, and both the synchrotron self-absorption (SSA) and FFA processes are considered as viable options [228, 276].

If FFA effects are indeed responsible for the spectral turnover in GPS sources, then the relatively flat ($\alpha \simeq 0.4 - 0.5$) power-law radio continuum of 4C +55.17, which shows no indication of a low-energy turnover, may indicate an exceptionally small amount of ionized ambient gas in the vicinity of its young radio structure. More specifically, if the radio absorber may be identified with ionization-bounded hydrogen clouds of interstellar matter present at pc to kpc distances from the center and engulfed by the expanding lobes, as proposed by Begelman (1999) [44] and advocated by Stawarz et al. (2008) [281], and if a significant part of this gas has been evacuated prior the onset of new jet activity, then one would expect much less severe absorption of the low frequency radio emission, resulting in a higher turnover frequency compared to that of GPS galaxies. In this case, the relatively high polarization of 4C +55.17 (as for a young radio source) would find a natural and straightforward explanation as well.

In considering the hypothesis outlined above, and in order to investigate the γ-ray emission detected from 4C +55.17 in a framework that is more consistent with the observed properties of the source, we apply the dynamical model for the broadband emission of CSOs proposed by [281] and successfully tested against a sample of X-ray detected young radio galaxies of the CSO type by [232]. In this model, the newly born relativistic jets propagate across the inner region of the host galaxy and inject ultrarelativistic electrons into the compact lobes. These electrons, which provide the bulk of the internal lobes' pressure, cool radiatively and adiabatically within the sub-relativisticly expanding plasma, thus producing isotropic synchrotron (radio) and IC (X-ray to γ-ray) radiation. In the model, the broadband emission spectra are evaluated self-consistently for a given set of the initial parameters of the central engine and of the host galaxy, taking into account the time-dependent evolution of the radiating electrons. For a given linear size of the system, which is uniquely related to a particular age of the system, the observed broadband emission spectrum is given as a snapshot of the evolving multiwavelength radiation of the lobes. Based on this model, Stawarz et al. (2008) [281] suggested that, in fact, young radio galaxies should be detected by *Fermi*/LAT at GeV photon energies, albeit at low flux levels and after an exposure longer than one year. Other (physically distinct) scenarios for the production of soft, high energy, and VHE γ-rays in the lobes and hot spots of young radio galaxies have been proposed and investigated by [177, 176] and [175].

In the more detailed description of the model, the jets with total kinetic power ($L_{\rm j}$) propagate with the advance velocity ($v_{\rm h}$) in the interstellar medium, characterized by a given number density ($n_{\rm ext}$; see Figure 4.9). At a particular instant of the source evolution, the inflated lobes will have a corresponding linear size (LS). The

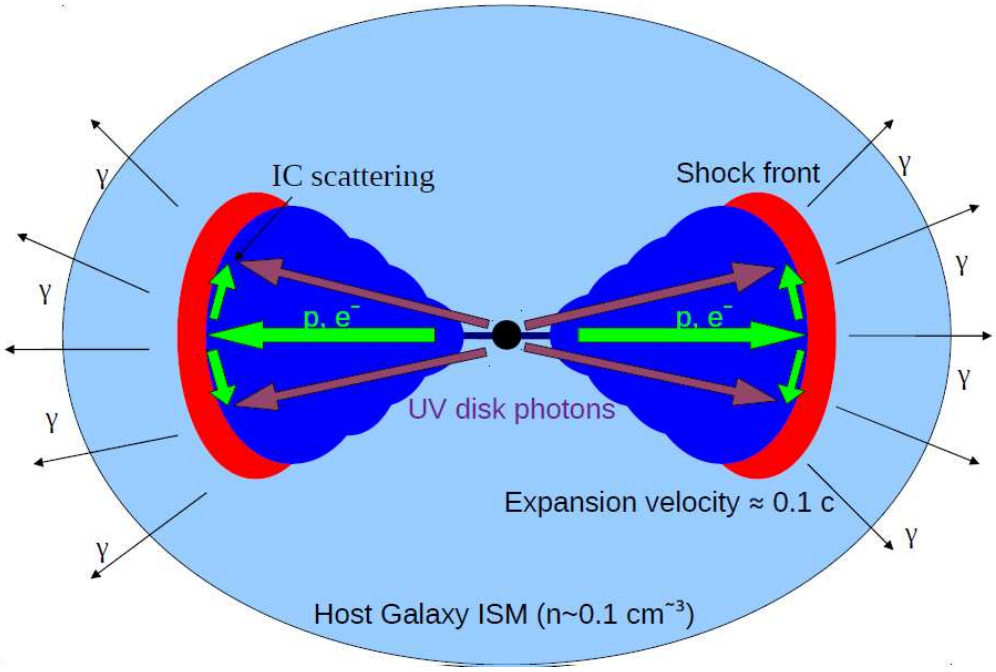

Figure 4.9: Conceptual diagram of the model proposed by Stawarz et al. (2008)[281]. A broken power law electron energy distribution is injected from the terminal jet shock into the expanding lobe. The electron population undergoes adiabatic and radiative cooling effects, producing synchrotron emission from the internal magnetic field, and IC emission from scattering off of the photon fields produced within the active center.

electrons injected through the termination shock into the lobes with the intrinsically broken power-law energy distribution cool due to the synchrotron and IC processes. The most relevant ambient photon fields for the IC scattering are the UV emission of the accretion disk (mean photon energy $\varepsilon_{\rm disk} = 10\,{\rm eV}$, disk luminosity $L_{\rm disk}$), the starlight ($\varepsilon_{\rm star} = 0.83\,{\rm eV}$, host luminosity $L_{\rm star}$), and the infrared emission of the obscuring nuclear torus ($\varepsilon_{\rm dust} = 0.02\,{\rm eV}$, dust luminosity $L_{\rm dust}$). The magnetic field intensity is expressed in terms of the ratio of energy densities stored in the radiating electrons and the magnetic field, $U_{\rm e}/U_{\rm B}$, which is constant during the expansion of the radiating plasma. Note, however, that $U_{\rm e}$ and $U_{\rm B}$, as well as the energy densities of the ambient photon fields (and hence the electron cooling conditions) do change with time, and therefore depend on LS (see [281] for more details).

The fit of the "young radio source" model to the collected broadband dataset for 4C +55.17 is illustrated in Figure 4.10. In fitting the SED, we assume that the projected source size of the inner radio structure ($LS \simeq 400\,{\rm pc}$) is equal to the actual source size (that is, we assume that the lobes are exactly perpendicular to the line of sight), though we note that this may be underestimated due to possible projection effects. Indeed, some amount of projection off the plane of the sky is required to account for the presence of the intense disk-related optical/UV continuum and the broad optical emission lines in the spectrum of 4C +55.17 (which might otherwise be

completely obscured), as well as to account for the asymmetry in brightness between the two lobes. In fitting the broadband SED, the following model free parameters were obtained: $L_{\rm j} \simeq 6.6 \times 10^{47}\,{\rm erg\,s^{-1}}$, $L_{\rm disk} \simeq 2 \times 10^{46}\,{\rm erg\,s^{-1}}$, $L_{\rm star} \simeq 10^{45}\,{\rm erg\,s^{-1}}$, $L_{\rm dust} \simeq 10^{45}\,{\rm erg\,s^{-1}}$, $U_{\rm e}/U_{\rm B} \simeq 160$, $v_{\rm h} \simeq 0.3c$, and $n_{\rm ext} \simeq 0.1\,{\rm cm^{-3}}$. The injection electron energy distribution is characterized by the minimum, break, and maximum electron Lorentz factors, $\gamma_{\rm min} \simeq 1$, $\gamma_{\rm br} \simeq 2 \times 10^4$, and $\gamma_{\rm max} \simeq 4 \times 10^5$, respectively, as well as by the low- and high-energy electron spectral indices, $s_1 \simeq 0.5$ and $s_2 \simeq 2.5$. The model successfully fits all the relevant data points within the low-frequency (radio) and high-frequency (hard X-ray to γ-ray IC component) ranges; it also reproduces nicely the spectral break within the *Fermi*/LAT photon energy range. We note that in our modeling here and below we do not consider γ-ray absorption effects related to the direct or reprocessed emission of the accretion disk, which may lead to the attenuation of the lobes' (or jets') emission at photon energies $> 100\,{\rm GeV}$ (see in this context [292]).

Looking closely at the UV part of the spectrum, we note an approximate factor of two difference between what is observed and what is required for producing the appropriate luminosity in IC-scattered γ rays. This can be resolved by recalling that in the framework of the model the optical/UV photon energy range is dominated by the thermal UV disk emission that may suffer from some non-neglible obscuration by the circumnuclear dust for moderate inclinations of the source to the line of sight. Also worth noting are the variation timescales of the disk, which are governed by the viscous motion within tens of gravitational radii from the black hole [80]. This can account for the $\sim 30\%$ variation over seven years seen between the optical measurements from UVOT and SDSS (see § 4.2.3). On the other hand, the CSO-related non-thermal IC emission is expected to be non-variable in accordance with the observations, because this emission is produced within the hundred-pc-scale and sub-relativistictically expanding lobes, and hence the UV photons seen by the lobes' electrons will be averaged over the entire spatial extent of the radio structure. Here we do not model the accretion-related emission in detail, but only roughly represent it as a blackbody component for the purpose of the evaluation of the IC radiation of the lobes. Likewise, the steep-spectrum soft X-ray continuum is not accounted for by the IC emission of compact lobes and instead may be attributed to the radiative output of the accretion disk and its corona (see [272, 270] for the X-ray properties of young radio sources). Yet it should be also noted that the particular CSO model presented here cannot account for the millimeter–to–near infrared emission of 4C +55.17. In the framework of the discussed scenario, this has to be attributed to the radiation of the underlying jet, and not of the compact lobes.

The physical parameters of 4C +55.17 emerging from the model fit presented above may be compared with the physical parameters of bona fide young radio galaxies derived in the framework of the same model by [232]. The most significant differences can be noted in the kinetic luminosity of the jet ($L_{\rm j}$), the UV luminosity of the accretion disk ($L_{\rm disk}$), and the electron–to–magnetic field energy density ratio ($U_{\rm e}/U_{\rm B}$). In particular, the jet and the disk luminosities of 4C +55.17 are higher (by one to two orders of magnitude, on average) than the analogous luminosities of GPS radio galaxies. This is in fact expected, since the analyzed source is much more

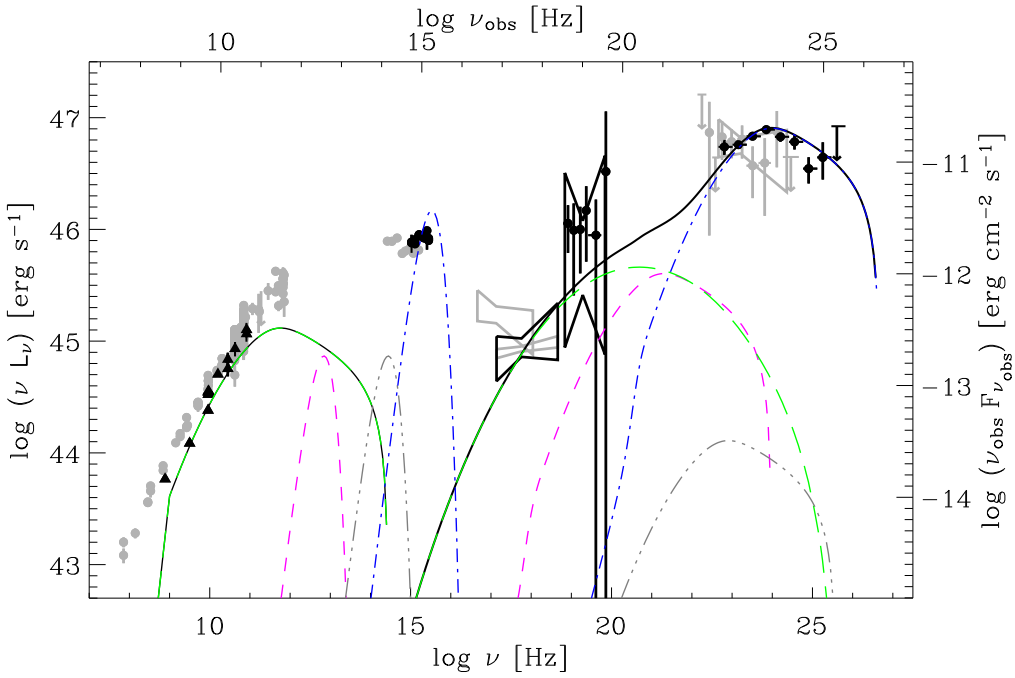

Figure 4.10: The CSO model of 4C +55.17 versus multiwavelength data, including the new LAT spectrum along with contemporaneous data with *Swift* XRT, BAT, and UVOT (black bullets). Archival detections (gray) with EGRET [151], ROSAT, Chandra, SDSS, 2MASS, 5-year integrated WMAP, and historic radio data are also included, as well as archival VLA measurements (black triangles) of the inner $\sim$ 400pc radio structure (see § 4.2.3). De-absorption of the observed *Fermi* spectral points using the [118] EBL model was applied in order to properly model the intrinsic γ-ray spectrum. Black curves indicate the total non-thermal emission of the lobes, with the long-dashed/green representing the contribution from synchrotron self-Compton (SSC). Dashed/pink, dash-dot-dotted/gray, and dash-dotted/blue blackbody-type peaks represent the dusty torus, starlight, and the UV disk emission components, respectively, along with their corresponding inverse-Compton components as required by the model.

powerful than the relatively low-power radio galaxies modeled by [232]. The disk luminosity obtained from the fit can also be compared with the expected value based on the total luminosity of emission in broad lines ($L_{\rm BLR}$). Using eq. (1) in [76], along with the line fluxes of 4C +55.17 obtained in [314] and the line ratios from [125], we estimate the value of $L_{\rm BLR}$ to be $1.2 \times 10^{45}\,{\rm erg\,s^{-1}}$. Using the approximation $L_{\rm disk} \simeq 10 \times L_{\rm BLR}$, we thus obtain $L_{\rm disk} \simeq 1.2 \times 10^{46}\,{\rm erg\,s^{-1}}$, which again falls within a factor of two of the value obtained through the model, consistent with the level of uncertainty expected using this method.

4.2.4.2 Blazar Modeling

As already noted in the introduction, the lack of pronounced variability and resolved VLBI structure in 4C +55.17 would make it a highly unusual case of a blazar/FSRQ. Still, it is a worthwhile exercise to consider the physical parameters implied from the blazar model. In the framework of the blazar scenario the observed non-thermal emission of this source, including the γ-ray flux detected by *Fermi*/LAT, is expected to originate in the innermost parts of a relativistic jet that is closely aligned with the line of sight (e.g.,[274]). In this case, the broadband emission of 4C +55.17 should be strongly Doppler boosted in the observer rest frame, and variable on short (days to weeks) timescales. The expected size of the blazar emission region (sub-pc), which is orders of magnitude smaller than the linear size of the resolved inner radio structure discussed previously ($\sim 400\,{\rm pc}$), as well as the presence of relativistic beaming effects, constitute the main differences between the "blazar" and "young radio source" scenarios.

In order to model the broadband spectrum of 4C +55.17 as a blazar emission, we apply the dynamical model BLAZAR developed by [212] and later updated by [213] for the correct treatment of the Klein-Nishina regime (for applications of the model, see e.g.[275, 166]). The model describes the production of the non-thermal emission by ultrarelativistic electrons, which are accelerated in situ within thin shells of plasma propagating along a conical relativistic jet (bulk Lorentz factor, $\Gamma_{\rm j} \gg 1$, jet opening angle $\theta_{\rm j} \sim 1/\Gamma_{\rm j}$) and which carry a fraction $L_{\rm e}/L_{\rm j}$ of the jet kinetic power. The acceleration process is attributed to the Fermi mechanism operating at strong shocks that are formed within the outflow as a result of the shells' collisions, which take place at distances greater than r_0 from the jet base, resulting in the injection of a broken power-law electron energy distribution into an emission region of linear size R and magnetic field intensity B. The non-thermal emission evaluated at $r \simeq R/\theta_{\rm j} \gtrsim r_0$ includes the synchrotron and IC components, with the target photons for the inverse-Compton scattering provided by the jet synchrotron radiation and the external photon fields (predominantly accretion disk emission reprocessed in the broad line region and within the dusty torus).

The BLAZAR fit to the broadband spectrum of 4C +55.17 is shown in Figure 4.11. The fit was obtained with the following free parameters of the model: $L_{\rm j} \geq L_{\rm e} \simeq 6 \times 10^{42}\,{\rm erg\,s^{-1}}$, $L_{\rm disk} \simeq 3 \times 10^{46}\,{\rm erg\,s^{-1}}$, $L_{\rm dust} \simeq 6 \times 10^{45}\,{\rm erg\,s^{-1}}$, $r_0 \simeq 4 \times 10^{18}\,{\rm cm}$, $r \simeq 8 \times 10^{18}\,{\rm cm}$, $\Gamma_{\rm j} \simeq 12$, and $B \simeq 0.2\,{\rm G}$. For the injection electron energy distribution, the electron Lorentz factors $\gamma_{\rm min} \simeq 1$, $\gamma_{\rm br} \simeq 1.5 \times 10^3$,

and $\gamma_{\rm max} \simeq 10^6$ were obtained, along with the spectral indices, $s_1 \simeq 0.5$ and $s_2 \simeq 2.8$. The blazar model fit to the collected dataset, and the implied physical parameters of the 4C +55.17 jet and its central engine, may be regarded as consistent with other γ-ray blazars. Notable differences with respect to the CSO model discussed previously can be however noted within the radio–to–X-ray frequency range. In particular, unlike the CSO fit, the blazar model fit does not account for the bulk of the observed radio fluxes. These emissions, in the framework of the blazar scenario, must therefore be produced further down the jet, at relatively large distances from the blazar emission zone. On the other hand, the high-energy tail of the synchrotron blazar emission dominates the radiative output of the system around the observed near-infrared and optical frequencies, and also at soft X-rays. The observed hard X-ray spectrum of 4C +55.17 cannot be fully attributed to the IC blazar emission and requires an additional spectral component. In general, the CSO and blazar fits differ the most within the near infrared and X-ray domains, hence future constraints on the hard X-ray and near infrared spectra, along with continued monitoring from the radio to the γ-ray band, should be considered as a potential way of discriminating between the two scenarios.

In comparing these two models, we also note the important difference between the blazar and CSO model for 4C +55.17 in the radiative efficiency of the emission zone. Compact emission zones of blazar sources are typically characterized by a very low (less than a few percent) radiative efficiency (e.g.,[274]). In this context, only a small fraction of the jet kinetic power is dissipated in the blazar emission zone and radiated away in the form of high-energy emission, which is strongly Doppler-boosted in the observer frame due to the relativistic bulk velocity of the emitting plasma. This is also the case for 4C +55.17 when modeled in the framework of the blazar scenario discussed above. On the other hand, the radiative efficiency of the sub-relativistically expanding lobes of young radio sources is known to be large, often exceeding 10% [91, 281], which naturally accounts for the particularly high intrinsic radio luminosity of these sources, being comparable to the most powerful radio galaxies and quasars [249]. Likewise, when modeling 4C +55.17 as a CSO, the radiative efficiency was similarly high. The improved radiative efficiency of CSO sources, together with the relatively high jet kinetic power implied by the young radio source scenario (higher than that implied by the blazar model), can thus account for the observed γ-ray luminosity even in the absence of relativistic beaming.

While the CSO-type and blazar modelings of the broadband spectrum of 4C +55.17 can both account for the γ-ray emission from the source, we find the implied value for the bulk Lorentz factor $\Gamma_{\rm j} \simeq 12$ under the blazar scenario difficult to reconcile with its observed VLBI properties. The physical mechanism responsible for the steady γ-ray emission is also not easily explained under this framework. Still, the unusual characteristics of 4C +55.17 as for a young radio source may be evidence for a combination of radiation produced in the sub-pc scale relativistic jet and the emission of the compact lobes. The modeling of this complex scenario, which might require a combination of the two models discussed above, is beyond the scope of the present work. A similar situation was recently considered by Migliori (in prep),

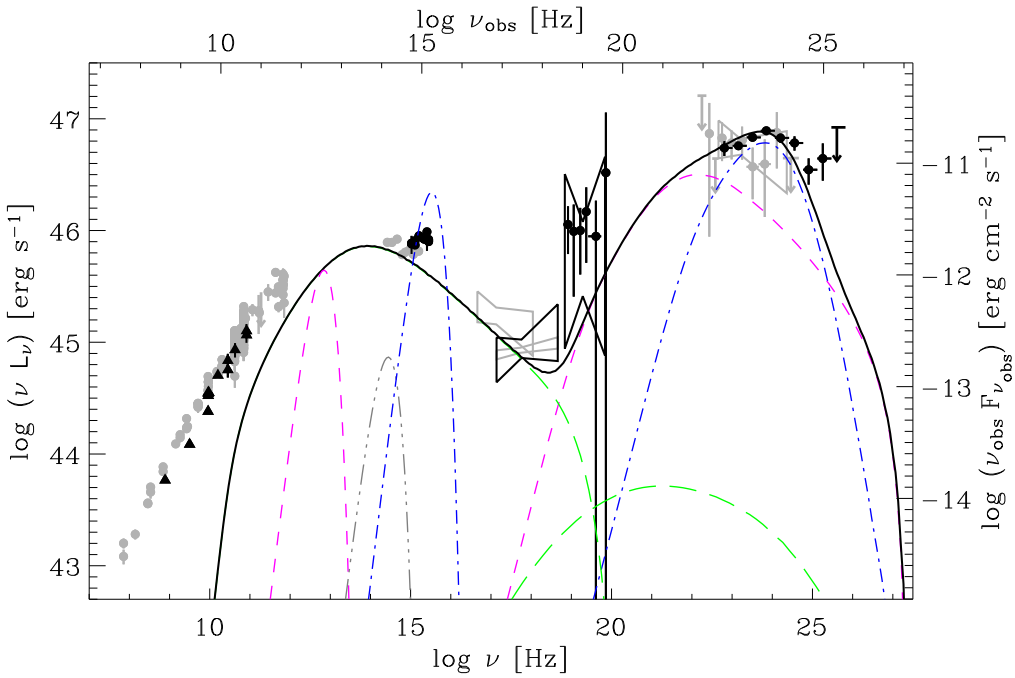

Figure 4.11: Blazar fit using multi-wavelength data for 4C +55.17. Indicated are the individual contributions from synchrotron and SSC (long-dashed/green), as well as IC scattering off of the reprocessed UV disk emission from the broad line region (dash-dotted/blue), dusty torus (dashed/pink), and host galaxy (dash-dot-dotted/gray); the black curve indicates the total of these components. As in Fig. 4.10, the dashed/pink, dash-dot-dotted/gray, and dash-dotted/blue blackbody-type peaks represent the dusty torus, starlight, and the UV disk emission components, respectively, along with their corresponding inverse-Compton components as required by the model.

who have studied the high-energy (X-ray to γ-ray) emission of radio-loud quasars with CSO-type inner radio morphology, such as, e.g., 3C 186. Objects of that type might be very common in scenarios of intermittent jet production in active galaxies, proposed to account for the evolution of radio-loud AGNs (e.g.,[255, 273, 86] and references therein). With its complex radio structure featuring inner and outer lobes, as well as jet-like features [259, 295], 4C +55.17 might thus be another example of AGN with intermittent jet production.

4.2.5 High Energy γ-ray Continuum of 4C +55.17

At energies $\gtrsim 10$ GeV the γ-ray continua of high-redshift sources begin to suffer from substantial attenuation by the still poorly known extragalactic background light (EBL; see Section 2.3.4.2) photon field due to the photon-photon pair creation process [152]. By attributing the attenuation of AGN γ-ray spectra to these interactions, it is thus possible to place significant upper limits to the EBL provided some estimate of the source's intrinsic spectrum [24]. In this respect, combined *Fermi* and VHE measurements by Cherenkov telescopes such as MAGIC, H.E.S.S., and VERITAS, continue to prove successful at providing these limits (e.g. [131, 33, 231]). Furthermore, with the VHE detection of the FSRQ 3C 279 ($z = 0.536$) by MAGIC [200], and the recently announced detections of others quasars – PKS 1510–089 ($z = 0.361$) by H.E.S.S. [309] and PKS 1222+216 ($z = 0.432$) by MAGIC [33] – the search for increasingly distant luminous sources in the observable range of ground-based Cherenkov Telescopes has become one of considerable interest to the TeV community.

The extension of the observed γ-ray spectrum of 4C +55.17 up to energies of 145 GeV, coupled with the source's relatively high redshift of $z = 0.896$, immediately places it among the most important high-z objects that can be used for constraining the widely debated EBL level even within LAT energies; for an overview of different methods for constraining the EBL with the *Fermi*/LAT, see [6]. Figure 4.12 illustrates the $\tau_{\gamma\gamma}$ opacity at the redshift $z = 0.896$ due to γ-ray absorption with the EBL intensity and spectral distribution for various models [118, 124, 138, 178, 285] considered as a function of photon energy. The highest-energy photon associated with 4C +55.17 is also indicated. As illustrated in the figure, attenuation due to the EBL-related absorption of γ-rays within the observed range is predicted in all the scenarios, including those close to the lower limits derived from galaxy counts (e.g.,[124, 118, 138]).

To test the validity of particular models of the EBL using the 4C +55.17 spectrum, we followed the likelihood ratio test method described in [6]. The full > 100 MeV observed spectrum was first fit to a log parabola with EBL attenuation from 9 separate EBL models [100, 118, 124, 138, 139, 179, 247] (see also [211] for a fit of the 19 month spectrum to additional models), with the normalization of the attenuation parameter $\tau_{\gamma\gamma}(E, z = 0.896)$ fixed to 1 at all energies. The indices from each of the spectral fits, as well as the integral flux values, are summarized in Table. 4.4. Allowing the normalization of the predicted opacity $\tau_{\gamma\gamma}$ to remain free, we then compared each result with the likelihood values obtained when the

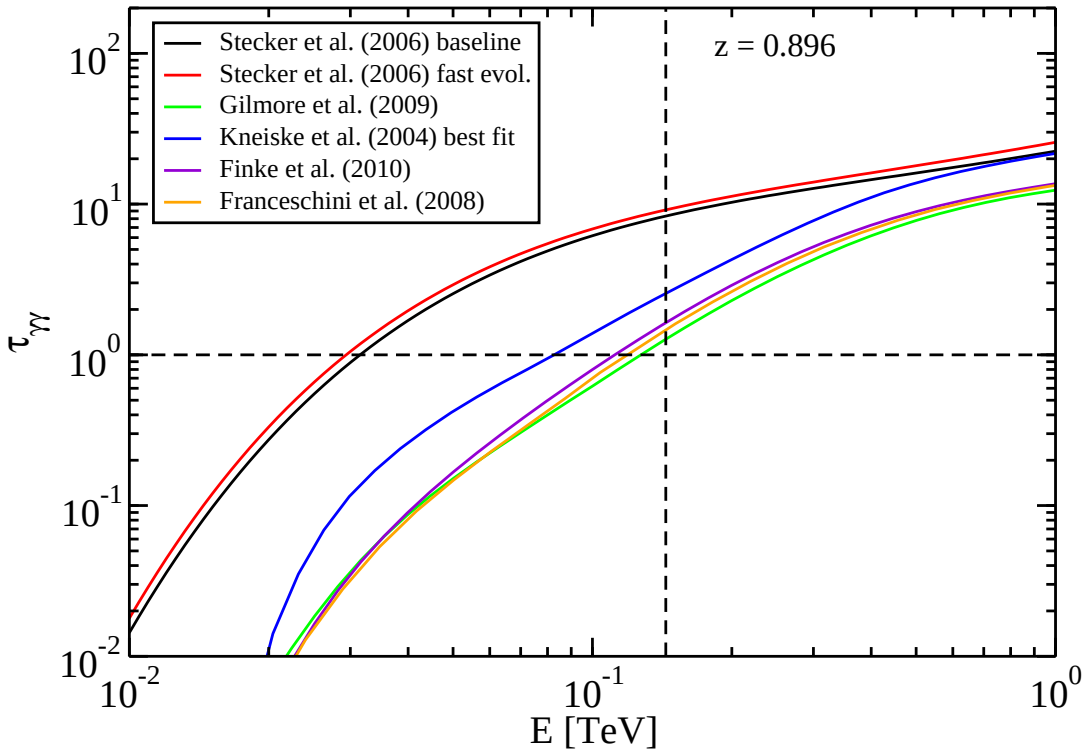

Figure 4.12: The $\tau_{\gamma\gamma}$ opacity versus energy for several EBL models at $z = 0.896$. The highest-energy photon of 145 GeV (rest frame energy = 275 GeV) within the 95% containment radius of the 4C +55.17 position is also indicated (vertical dashed line). The horizontal line simply denotes $\tau_{\gamma\gamma} = 1$. At the observed energy, attenuation from the EBL is expected even for those models which predict low levels of EBL.

EBL Model	α	β	Flux[a]	-log(likelihood)
Dominguez et al. (2011)	1.84 ± 0.02	0.082 ± 0.006	8.23 ± 0.21	454772.676
Finke et al. (2010)	1.84 ± 0.02	0.08 ± 0.01	8.24 ± 0.24	454772.837
Franceschini et al. (2008)	1.84 ± 0.02	0.08 ± 0.01	8.23 ± 0.24	454772.710
Gilmore et al. (2009)	1.84 ± 0.02	0.08 ± 0.01	8.23 ± 0.24	454772.673
Gilmore et al. (2012) fixed	1.84 ± 0.02	0.08 ± 0.01	8.23 ± 0.24	454772.661
Gilmore et al. (2012) fiducial	1.84 ± 0.02	0.08 ± 0.01	8.27 ± 0.25	454772.930
Kneiske & Dole (2010)	1.84 ± 0.02	0.08 ± 0.01	8.25 ± 0.24	454772.747
Kneiske & Dole (2010) CMB	1.84 ± 0.02	0.08 ± 0.01	8.25 ± 0.24	454772.747
Primack et al. (2005)	1.84 ± 0.02	0.08 ± 0.01	8.27 ± 0.25	454772.743

Table 4.4: De-absorption of γ-ray flux using different EBL models with fixed $\tau_{\gamma\gamma}$ normalization. [a]Flux is given above 100 MeV in units of $[10^{-8}\,\mathrm{cm}^{-2}\,\mathrm{s}^{-1}]$.

normalization parameter was fixed to 1. In cases where the $\tau_{\gamma\gamma}$ normalization was reduced, a rejection at the level of n standard deviations (σ) of the particular model could be established using the formula:

$$n = \sqrt{-2 \times \left[\log\left(L_{\mathrm{fixed}}\right) - \log\left(L_{\mathrm{free}}\right)\right]}\,, \tag{4.1}$$

where L_{fixed} and L_{free} are the likelihood values of the fits for fixed and free normalizations on $\tau_{\gamma\gamma}$, respectively. Using these results, we found that all the tested models were consistent with the attenuation seen in the 4C +55.17 spectrum.

With its excellent sensitivity in the high-energy range, the LAT instrument provides a unique opportunity to search for VHE candidates at high redshifts through detailed spectral analysis of the Fermi-LAT data. In the case of 4C +55.17, the attenuated high-energy spectrum obtained from fitting the nine tested EBL models is illustrated in Figure 4.13. Each spectrum is extrapolated beyond the highest observed photon energy of 145 GeV and compared against the upper limits from a $\sim$ 45 hour observation from the VERITAS telescope, along with the differential flux sensitivity curve of the MAGIC telescope. The observed 4C +55.17 spectrum is found to lie close to the observable threshold for ground-based observations. It is also worth noting that while intrinsic absorption from interactions with the UV disk and infrared torus may contribute to the spectral attenuation at energies > 100 GeV, this effect would be reduced in cases where the γ-ray emission takes place at hundreds-of-parsecs scale distances from the central black hole, for which there is compelling evidence in the case of 4C +55.17 (see § 4.2.4.1). In addition, with the present analysis we find no evidence of variability in 4C +55.17 over 5 years of LAT observing time, and furthermore we find its flux to be consistent with the EGRET measured value, thus showing no evidence of variability at γ-ray energies over decade timescales as well. The non-variable γ-ray continuum of the source thus promises the opportunity to observe the source over extended timescales, in contrast to other VHE-detected quasars, which were detected only during periods where the sources were in a flaring state. In this way 4C +55.17 stands apart from all of the EBL-constraining sources considered in [6], as it holds the greatest potential for providing future constraints.

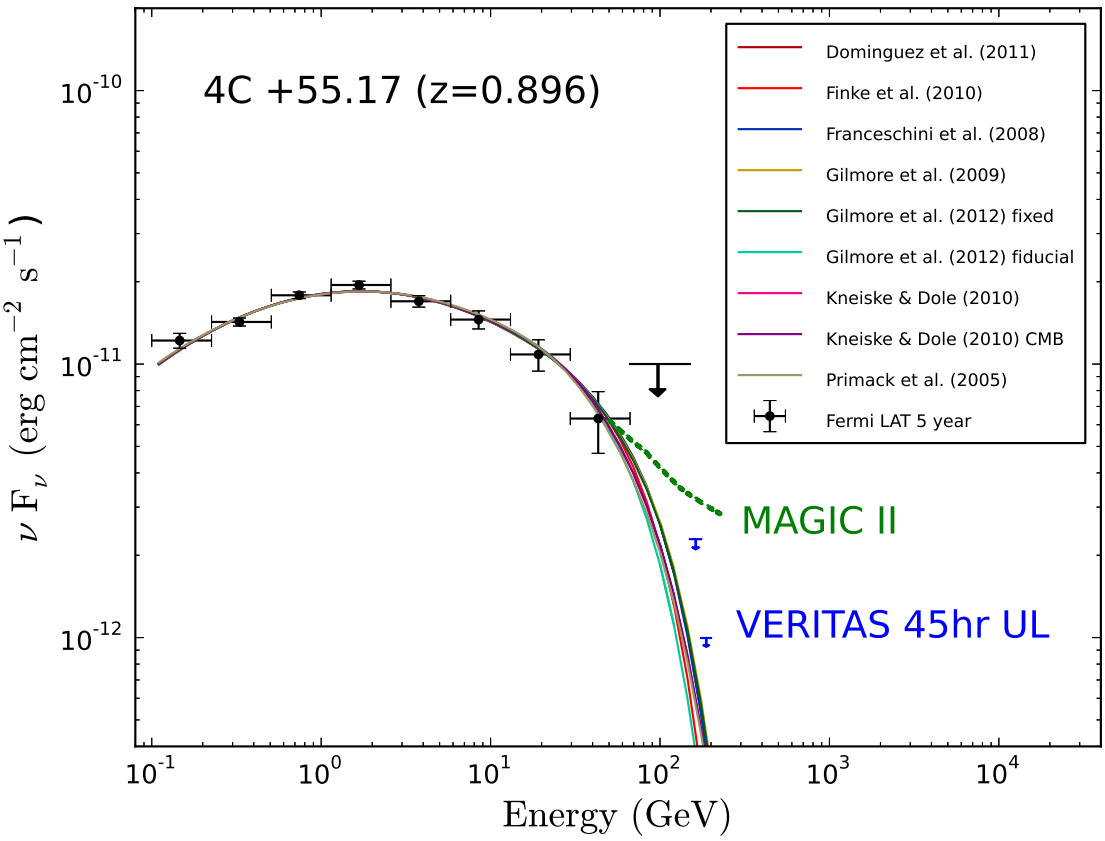

Figure 4.13: The observed LAT spectrum fit to a log parabola with attenuation from 9 different EBL models. The spectra are extrapolated beyond the observed energy of 145 GeV and compared against the upper limits from a $\sim$ 45 hour VERITAS observation, along with the differential flux sensitivity curve of MAGIC II for a 50 hour, 5σ detection of a source characterized by an exponentially decreasing spectrum (see Appendix C). For several EBL models, the 4C +55.17 spectrum is found to intercept the MAGIC II sensitivity, making 4C +55.17 a possible candidate for a future ground-based VHE detection.

4.2.6 Conclusions

The investigation of the multiwavelength properties of 4C +55.17, including its uncharacteristic γ-ray spectrum, lack of distinct variability, and CSO-like radio morphology, places into question the blazar nature of this γ-ray source. In light of these observations, we have modeled the radio to γ-ray emission of 4C +55.17 as a young radio source using a dynamic model that is consistent with the full extent of its observed properties. Furthermore, we anticipate that through continued monitoring of 4C +55.17 at high energies with the *Fermi* LAT, as well as in the radio through X-rays, the precise classification of 4C +55.17 will become increasingly more apparent. If, for example, rapid variability is found in the source, this would place constraints on the size of the γ-ray emitting region, which would provide strong evidence for a blazar classification. On the other hand, continued nonvariability would be inconsistent with such a classification, and would instead favor an extended emitting region. Thus we expect that 4C +55.17 will be an important target for future observations across all wavelengths.

4.3 The Origin of Gamma-ray Emission from the radio galaxy M87

4.3.1 Introduction

The radio galaxy M87 has an extensive history, being one of the most famously studied AGN due both to its relatively nearby proximity (D = 16 Mpc)[302], as well as its characteristically bright arcsecond-scale jet [226], which is powered by a $\sim (3-6) \times 10^9$ solar mass supermassive black hole [197, 128] that has been imaged down to $\sim$0.01 pc resolution ($\sim 15-30\times$ the Schwarzschild radius)[164, 196, 16]. While M87 has remained a source of study across the broadband spectrum [54, 278, 208, 239], its history as a γ-ray source has been one of increasing interest as well, being observed regularly by HESS, MAGIC, and VERITAS, with variable VHE emission on timescales of days to years being observed by all three telescopes [25, 30, 17, 16]. In addition, the source was one of the first three radio galaxies detected by the Fermi-LAT, with no significant HE γ-ray variations being reported to date [11, 15].

Perhaps one of the more significant questions that remains to be answered regarding M87 lies in the site of the high energy GeV and Very High Energy (VHE) TeV emission that is observed in the source. The very first evidence for VHE emission from M87 was reported by the HEGRA collaboration in 2003 [23], and was later confirmed by H.E.S.S., MAGIC, and VERITAS [25, 17, 30]. While the detection of TeV emission from a radio galaxy was in itself an important milestone, perhaps even more intriguing was the context of the initial H.E.S.S. detection of the γ-ray emission in light of contemporaneous multiwavelength measurements of the emission sites at the black hole central engine, as well as a secondary jet "knot" located ~ 60 pc from the core, referred to as HST-1[53]. In particular, Cheung et al. (2007) [77] reported detections of VLBA superluminal radio features, as well as an X-ray outburst of > 50 times observed by Chandra, both of which were found

to occur in the HST-1 knot, while simultaneous measurements of the core region were found to be quiescent. This led them to place into question the core region as the standard γ-ray emission site, arguing that the γ-ray emission site was instead located as far as 100 pc from the jet.

In the following sections, the high energy emission of M87 is investigated through detailed analysis of the *Fermi*-LAT data, and is compared against simultaneous and archival multiwavelength data. An origin of the LAT emission from the unresolved parsec scale jet (hereafter, denoted as the 'nucleus' or 'core') observed contemporaneously with *Chandra* and the VLBA[7] is compared against both historic and contemporaneous measurements of the emission site HST-1, located approximately ($\sim$ 0.1 kpc) from the cental engine. Section 4.3.2 contains the details of the LAT observations, including a description of the *Chandra* and VLBA data utilized, with the discussion of these results in section 4.4.

4.3.2 Observations

4.3.2.1 10 Month Initial Detection

The initial LAT detection of M87 reported in [11] and summarized here is comprised of 10 months of LAT all-sky data, (Aug. 4, 2008 - May 31, 2009) corresponding to a mission elapsed times (MET) 239557418 to 265420800, and followed the pass 6 standard selections of "Diffuse" class events [37] with energies $E > 200$ MeV, a zenith angle cut of $<105°$, an ROI cut of 15 degrees around the radio source position [69], and a rocking angle cut of 43° applied in order to avoid Earth albedo γ-rays. *Fermi* Science tools[8] version v9r10 and instrumental response functions (IRFs) version `P6_V3_DIFFUSE` were used for the analysis.

A localization analysis with `GTFINDSRC` resulted in a best-fit position, RA = 187°.722, Dec. = 12°.404 (J2000.0 equinox), with a 95% confidence error radius, $r_{95\%} = 0°.086 = 5.2'$ (statistical only; $r_{68\%} = 3.2'$), and a TS of 108.5, which is equivalent to a source significance $\sim \sqrt{TS} = 10.4\sigma$. To account for possible contamination from nearby sources, the model included all point sources detected at $> 5\sigma$ in an internal LAT 9-month source list within a region of interest (ROI) of r=15° centered on the γ-ray position. Galactic diffuse emission was modeled using GALPROP [289], updated to include recent gas maps and a more accurate decomposition into Galactocentric rings (galdef ID `54_59varh7S`). An additional isotropic diffuse component modeled as a power-law was included. Figure 4.14 shows the resultant γ-ray source localization on a VLA radio image from [233]. The γ-ray source is positionally coincident with the known radio position of the M87 core (RA = 187°.706, Dec. = 12°.391;)[115], with an offset ($0°.020 = 1.2'$) that is a small fraction of the localization circle. Currently, the best estimate of the systematic uncertainty in $r_{95\%}$ is $2.4'$ [9], which should be added in quadrature to the determined statistical one.

[7]The National Radio Astronomy Observatory is a facility of the National Science Foundation operated under cooperative agreement by Associated Universities, Inc.

[8]http://fermi.gsfc.nasa.gov/ssc/data/analysis/documentation/Cicerone/

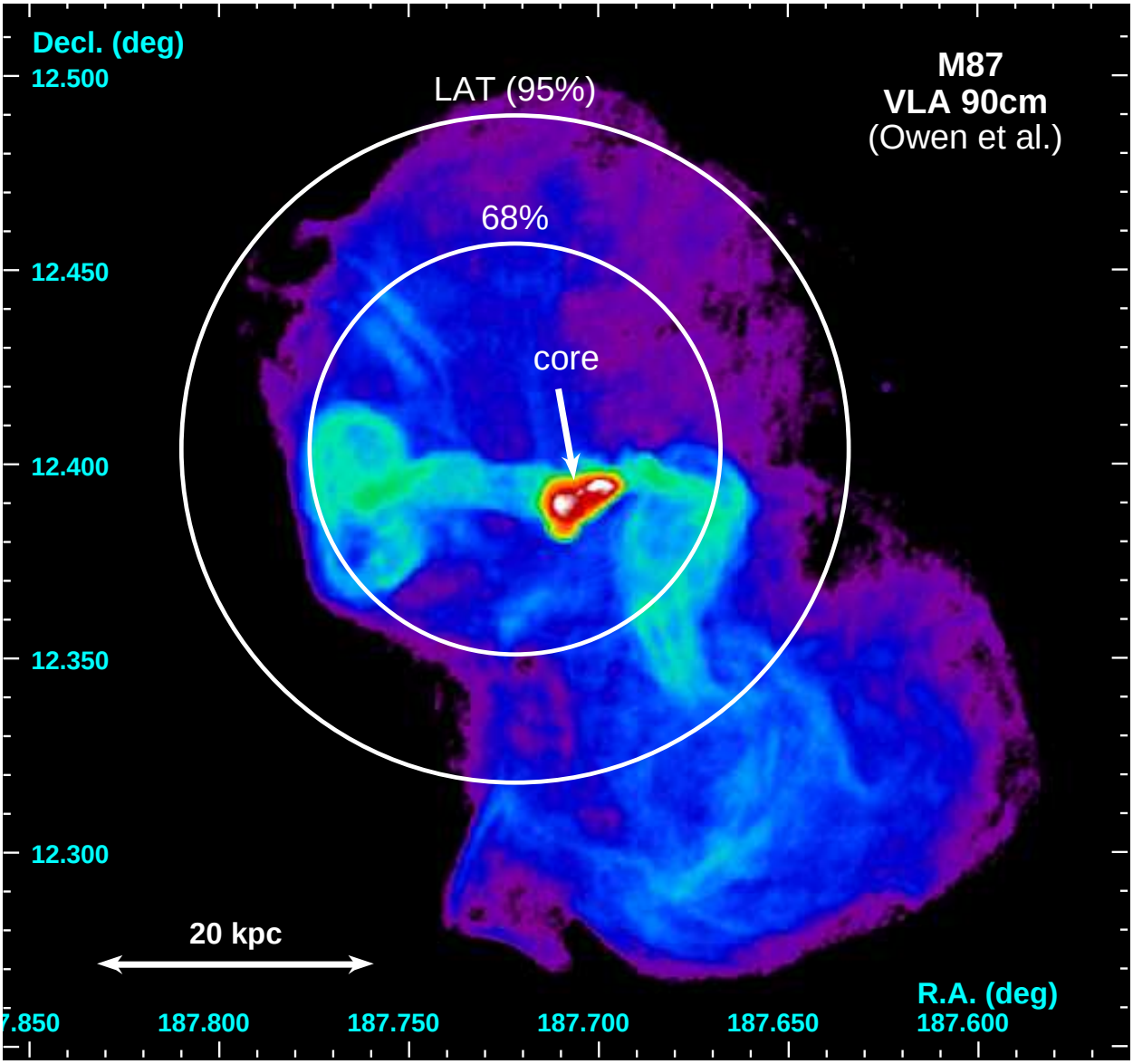

Figure 4.14: VLA λ=90cm radio image from [233] with the 10-month initial LAT γ-ray localization error circles indicated: $r_{95\%} = 5.2'$ and $r_{68\%} = 3.2'$ (statistical only). The M87 core is the faint feature near the center of the few kpc-scale double-lobed radio structure (in white). At the adopted distance $D = 16$ Mpc, $1' = 4.7$ kpc (From [11]).

A radial profile of the γ-ray source counts (not shown) was extracted for the total energy range (>200 MeV). The profile was consistent with that of a point source simulated at energies $0.2 - 200$ GeV using the fitted spectral parameters above with a reduced $\chi^2 = 1.04$ for 20 degrees of freedom. The total $\sim 0^\circ.2$ extent of the 10's kpc-scale radio lobes of M87 (Figure 4.14) [233] is comparable to the LAT angular resolution, $\theta_{68} \simeq 0^\circ.8\ E_{\rm GeV}^{-0.8}$ [37]. Given the small angular extent of M87, a possible contribution of the extended radio lobes to the total γ-ray flux could not be determined.

Spectral analysis was performed utilizing an unbinned likelihood fit of the >200 MeV data with a power-law ($dN/dE \propto E^{-\Gamma}$) implemented in the `gtlike` tool. This resulted in $F(>100\ {\rm MeV}) = 2.45\ (\pm 0.63) \times 10^{-8}$ ph cm^{-2} s^{-1} with a photon index, $\Gamma = 2.26 \pm 0.13$; errors are statistical only. The flux was extrapolated down to 100 MeV to facilitate comparison with the previous EGRET non-detection of $< 2.18 \times 10^{-8}$ ph cm^{-2} s^{-1} (2σ) from observations spanning the 1990's [253]. Thus, there were no apparent changes in the flux (i.e., a rise) in the decade since the EGRET observations. Systematic errors of $(+0.17/-0.15) \times 10^{-8}$ ph cm^{-2} s^{-1} on the flux and $+0.04/-0.11$ on the index were derived by bracketing the energy-dependent ROI of the IRFs to values of 10%, 5%, and 20% above and below their nominal values at $\log(E[{\rm MeV}]) = 2$, 2.75, and 4, respectively. The 10 month spectrum extends to just over 30 GeV where the highest energy photon is detected within the 95% containment radius.

4.3.2.2 MAGIC & VERITAS Multiwavelength Campaign

In order to facilitate contemporaneous spectra during a subsequent multi-wavelength campaign with MAGIC and VERITAS [15], an additional 2 year analysis was also conducted, consisting of nominal all-sky survey data between the energy range 100 MeV and 300 GeV, and spanning the mission elapsed time (MET) 239557417 to 302630530 (August 4, 2008 through August 4, 2010). Event selections include "diffuse" class events recommended for pass 6 point source analysis, a rocking angle cut of $< 52^\circ$, and a zenith angle cut of $< 100^\circ$ in order to avoid contamination from the Earth's limb. A 2 ks window beginning at MET 259459364 was also removed in order to avoid contamination from GRB 090323, which occurred nearby. The two year analysis was performed using instrument response functions (IRFs) `P6_V11_DIFFUSE` and science tools `v9r20p0`, along with the recommended[9] Galactic diffuse `gll_iem_v02.fit` and corresponding isotropic spectral template `isotropic_iem_v02.txt`, which have been appropriately scaled in order to account for the acceptance differences between the `P6_V11_DIFFUSE` and `P6_V3_DIFFUSE` IRFs.

An analysis of the 2-year LAT spectrum was also performed using the binned likelihood method [209], selecting all events that fell within a $20^\circ \times 20^\circ$ square region of interest (ROI) centered at the M87 radio position [69]. All point sources from an internal 2-year preliminary catalog that fell within 15° of the source were included

[9] `http://fermi.gsfc.nasa.gov/ssc/data/access/lat/BackgroundModels.html`

in the fit. All sources that fell within the square ROI were modeled with their normalization and index parameters set free, while those that fell outside of the ROI were fixed to their catalog values. The M87 spectrum was modeled to a power law with photon index and normalization parameters left free and using the radio position as the source location. A point source was detected with a test statistic (TS; Mattox et al. 1996) of 301, representing a detection of $\sqrt{301} \simeq 17\sigma$. From the resulting fit, the photon index and flux($> 100\,\mathrm{MeV}$) were found to be 2.16 ± 0.07 and $(2.66 \pm 0.36) \times 10^{-8}\,\mathrm{ph\,cm^{-2}\,s^{-1}}$, respectively. The largest systematic errors can be attributed to uncertainties in the modeling of the diffuse background emission. These were found by repeating the analysis with both binned and unbinned `gtlike` using a refined version of the diffuse background model that was under development by the LAT collaboration at the time of the analysis. Systematic errors on the index and flux were thus found to be $(+0.05/-0.01)$ and $(+0.40/-0.13)\times 10^{-8}\,\mathrm{ph\,cm^{-2}\,s^{-1}}$, respectively. Comparing these results with the initial 10-month spectrum reported in Abdo et al.(2009), we found no evidence of variability in the flux above 100 MeV between the first 10 months of data and the 14 months that followed. Comparing the $> 1\,\mathrm{GeV}$ flux between these two epochs, however, we note a marginal indication of a rise in the flux of the latter epoch at a significance of 2σ.

The LAT 3σ light curve ($> 1\,\mathrm{GeV}$, see Figure 4.17) was constructed using the events that fell within a 10° circular ROI centered at the M87 radio position. To generate the light curve, events were grouped into 56-day (8 weeks) time bins, and a separate likelihood analysis using `gtlike` was performed over each of the bins. All point sources from the 2-year fit were included in the model over each interval. Sources that fell within the 10° ROI were fit with their normalization parameters free, while the photon index of each source was fixed to the best-fit value obtained from the full 2-year analysis. Both the index and normalization parameters of M87 were left free, except in the case of upper limit calculations, in which case the spectral index was fixed to the nominal 2-year average of 2.16. In order to avoid modeling sources with a negative TS value, an initial fit over each interval was performed, and all sources found to have a TS< 1 were subsequently removed from the fit. Following precisely the method for variability detection outlined in [225], the weighted average was first calculated with a resulting value of $(1.62 \pm 0.18) \times 10^{-9}\,\mathrm{ph\,cm^{-2}\,s^{-1}}$. A χ^2 analysis was then performed by comparing the best-fit values of all points against the weighted average, and the resulting probability $P(\chi^2 \geq \chi^2_{\mathrm{obs}})$ was found to be 0.027, which represents a significance of 2.2σ and falls slightly below the threshold for variability defined in [225].

4.3.2.3 Four Year Very High Energy Detection

Following the multiwavelength campaign with MAGIC and VERITAS, a subsequent 4 year analysis revealed for the first time a detection of the M87 LAT spectrum at Very High Energy ($> 100\,\mathrm{GeV}$), which we include here for completeness. The four year analysis followed the same procedure discussed in 4.3.2.2, but covered the MET $239557417 - 365817600$ (August 4, 2008 to August 4, 2012) and used instrument response functions `P7_SOURCE_V6`, along with the corresponding

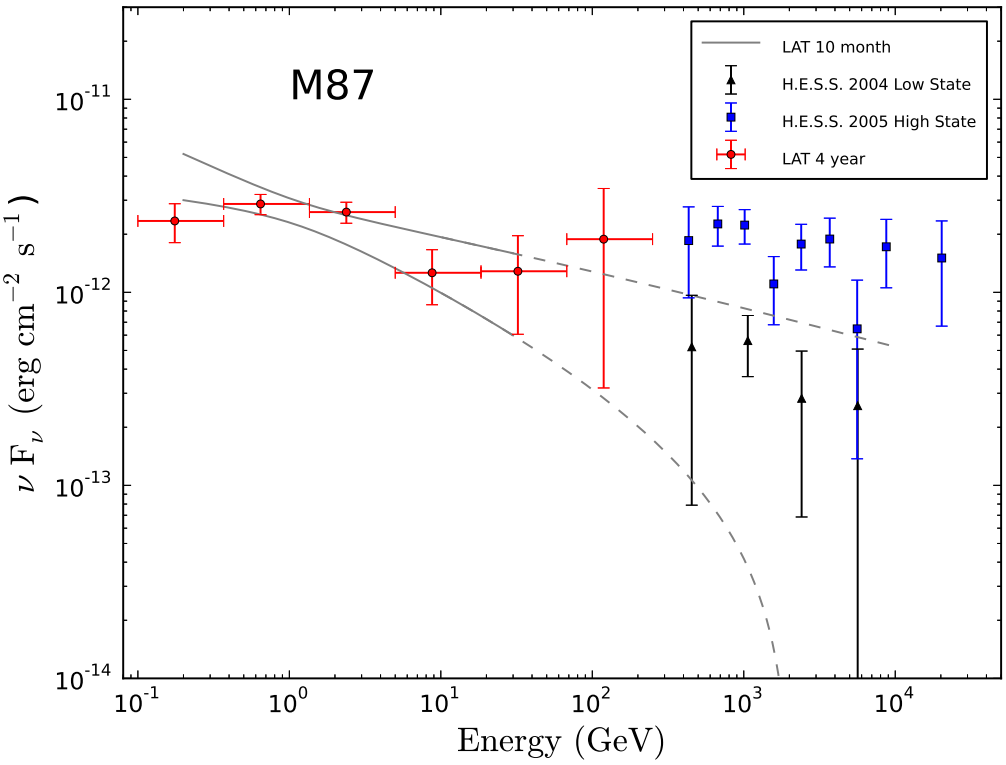

Figure 4.15: The LAT 4 year spectrum (red circles), compared against the previous 10-month extrapolation (gray) into the VHE range [11], with representative TeV measurements of M87 in a low state from the 2004 observing season (black triangles) and during a high state in 2005 (blue squares), both by HESS [25]. The LAT 4-year measured spectrum extends smoothly into the VHE range, consistent with the 10 month extrapolation.

recommended [10] Galactic diffuse `gal_2yearp7v6_v0.fits` background models and corresponding isotropic spectral template `iso_p7v6source.txt`.

The LAT spectral data points presented in Figure 4.15 were generated by performing a subsequent likelihood analysis in six equal logarithmically spaced energy bins from $0.1 - 250$ GeV, consistent with the highest measured photon energy of 246 GeV, and are plotted against the extrapolation of the 10-month LAT spectrum into the VHE range.

The variability test implemented under the 2-year multiwavelength campaign was extended to the 4-year data set using a time binning of 56 days. The resulting χ^2 fit resulted in a χ^2 probability $P(\chi^2 \geq \chi^2_{\rm obs})$ of 0.73, consistent with a non-variable source. Continued daily monitoring of M87 since this analysis has also shown no evidence of flaring from M87.

[10] `http://fermi.gsfc.nasa.gov/ssc/data/access/lat/BackgroundModels.html`

4.4 Discussion

In standard modeling of γ-ray blazars, the source of HE emission takes place within a few parsecs of the central black hole engine, where outflows are accelerated at relativistic bulk velocities, acting as the source of rapid variability that is a characteristic of such sources (see Section 2.2.2.4). It is therefore natural to use a similar mechanism in the case of misaligned galaxies to explain the origin of their γ-ray emission due to their intrinsic similarities to blazars [78], but with jets that are oriented at systematically larger angles to our line of sight, thus constituting their parent population. In this respect, radio galaxies can provide a more efficient laboratory for studying the emission zone than blazars, as the large angular orientation to the observers' line of sight allows for better spatial precision when measuring events as they take place along the jet. In the case of M87, a careful examination of the jet components during the three reported TeV flares in 2006, 2008, and 2010 can provide a number of insights into the complex nature of flaring activity that is seen from the source, as well as to challenge the standard models used in blazar emission.

In Figure 4.15, the four year LAT spectrum of M87 is plotted along with the TeV spectra from HESS [25] during its historical-minimum in 2004, and during its high state in 2005 (cf., Fig. 3 in [17]). Here we see that the M87 LAT spectrum transitions smoothly into the TeV range, consistent with the 10-month extrapolation. This allows the HE and TeV spectral components to be modeled using a single emission mechanism. Note however that because the HE emission is not well localized (See Figure 4.14), a distinction between relative contributions from the core, HST1, or other possible sites of emission along the kpc-scale jet or the giant radio lobes cannot be established using a comparison of the spectra alone.

In the modeling of the LAT initial detection as discussed in [11], M87 (Figure 4.16) was modeled using the LAT 10 month data and the overlapping Jan. 7, 2009 *Chandra* and VLBA measurements of the core [11]. The broad-band SED was fit with a homogeneous one-zone synchrotron self-Compton (SSC) jet model [117] assuming an angle to the line of sight, θ=10°, and bulk Lorentz factor, $\Gamma_{\rm b} = 2.3$ (Doppler factor, $\delta = 3.9$), consistent with observations of apparent motions of $\gtrsim 0.4c$ ($\Gamma_{\rm b} > 1.1$) in the parsec-scale radio jet [196]. A broken power-law electron energy distribution $N(\gamma) \propto \gamma^{-p}$ was assumed, and the indices, $p_1 = 1.6$ for $\gamma = [1, 4 \times 10^3]$ and $p_2 = 3.6$ for $\gamma = [4 \times 10^3,\ 10^7]$ were estimated based on the available core measurements. The normalization at low energies was constrained by the single contemporaneous VLBA 15 GHz flux which was measured with $\sim 10^2 - 10^3\times$ better resolution than the adjacent points. The source radius, $r = 1.4 \times 10^{16}$ cm = 4.5 mpc was chosen to be consistent with the best VLBA 43 GHz map resolution (r <7.8 mpc = 0.1 mas, [164, 196]) and was of order the size implied by the few day timescale TeV variability [16]. For the source size adopted, internal $\gamma - \gamma$ absorption was avoided so that the LAT spectrum extended relatively smoothly into the TeV band, consistent with the historical-minimum flux detected by HESS [25] and the upper limit of < 1.9% Crab from VERITAS observations [157] that were contemporaneous over the 10 month period.

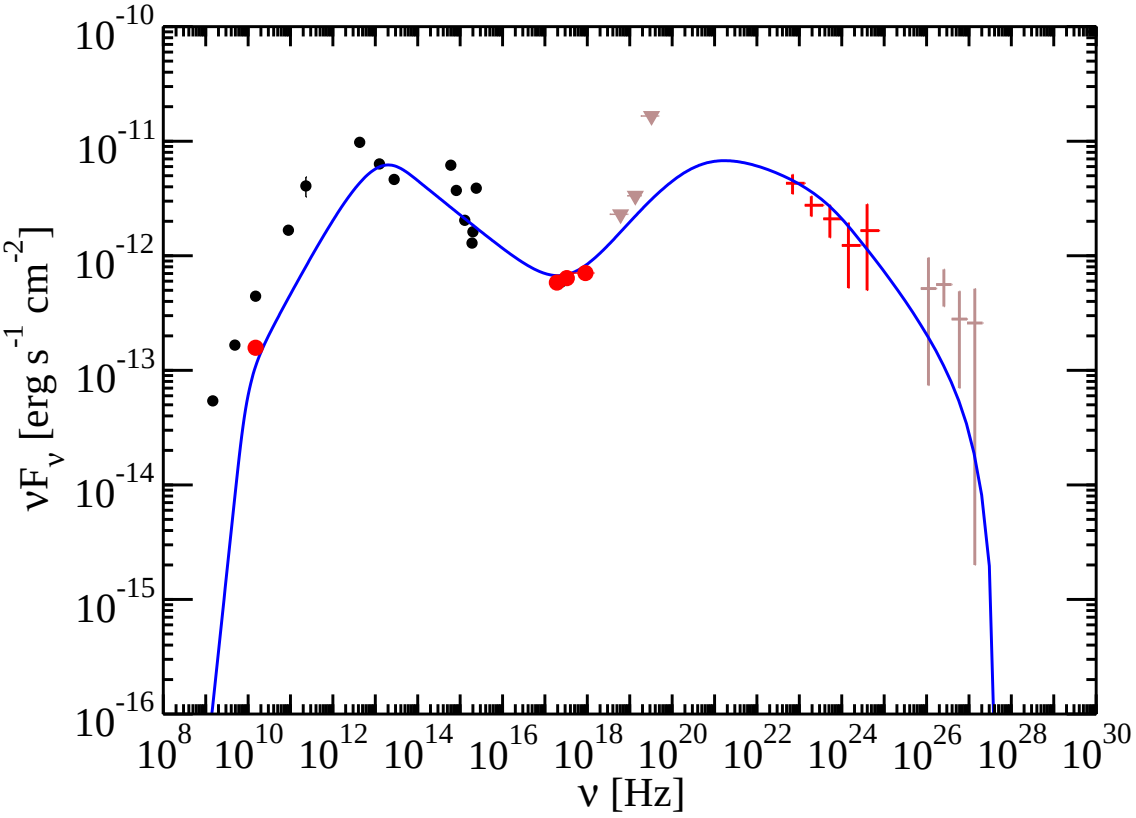

Figure 4.16: SED of M87 with the 10 month LAT spectrum and the Jan. 7, 2009 MOJAVE VLBA 15 GHz and *Chandra* X-ray measurements of the core indicated in red. The non-simultaneous 2004 TeV spectrum described in Figure 4.15 and *Swift*/BAT hard X-ray limits (§ 4.4) of the integrated emission are shown in light brown. Historical measurements of the core from VLA 1.5, 5, 15 GHz [54], IRAM 89 GHz [98], SMA 230 GHz [291], *Spitzer* 70, 24 μm [269], Gemini 10.8 μm [238], *HST* optical/UV [278], and *Chandra* 1 keV from [208](hidden behind the new measurements) are plotted as black circles. The VLBA 15 GHz flux is systematically lower than the historical arcsec-resolution radio to infrared measurements due to the presence of intermediate scale emission (see e.g., [183]). The blue line shows the one-zone SSC model fit for the core described in § 4.4.

In the SSC model, the magnetic field was $B = 55$ mG and assuming the proton energy density is $10\times$ greater than the electron energy density, the total jet power was $P_{\rm j} \sim 7.0 \times 10^{43}$ erg s^{-1}. The jet power is particle dominated, with only a small contribution from the magnetic field component ($P_{\rm B} \sim 2 \times 10^{40}$ erg s^{-1}). In comparison, the total kinetic power in the jet is $\sim$few $\times 10^{44}$ erg s^{-1} as determined from the energetics of the kpc-scale jet and lobes [50], and is consistent with the jet power available from accretion, $P_{\rm j} \lesssim 10^{45}$ erg s^{-1} [256, 99]. These power estimates are similar to those derived for BL Lacs from similarly modeling their broad-band SEDs (e.g.,[75]).

As demonstrated by the parameters of the fit, the one zone SSC model reproduced well the observed 10 month spectrum. However, as discussed above, the emission was confined to a source radius of $r = 1.4 \times 10^{16}$ cm = 4.5 mpc, which was applied to account for the day to week timescale variability seen in the TeV. Using this physical scenario, a similar level variability in the HE emission would also be expected, given the single population of leptons used to model both the HE and VHE portions of the spectra. An examination of the 4-year LAT light curve of M87, however, reveals a steady-state emission over the 4 year period, which is not readily explained by the one zone SSC model. One possibility for this discrepancy might be the existence of a steady component outside of the pc-scale core, such as the well-known arcsecond-scale jet (e.g.,[54, 208, 239]), for which the dominant seed photon source for IC is the host galaxy starlight. However, applying this model to one of the brightest resolved knots in the jet – knot A, $\sim$1 kpc projected distance from the core – results in a spectrum peaking at TeV energies [282], which would be expected to produce a harder spectrum than is observed by the LAT.

Another possible location for HE emission is the superluminal knot HST-1 ($v > 4c - 6c$;[53, 77]) located ~ 60 pc from the central black hole. The knot HST-1 is not a unique feature to M87, with a recollomation shock located ~ 140 pc from the core of the γ-ray loud radio galaxy 3C 120 also being reported [22]. In the case of HST-1, the surrounding circumnuclear and galactic photon fields are expected to be of sufficient energy density to allow for an IC component at HE/VHE energies [280], but could also account for a steady emission over 4 year timescales due to its less compact size of ~ 2 pc [77], although the exact timescales of variability for this feature remain largely unknown due to the lack of consensus regarding the origin of the TeV emission seen by H.E.S.S in 2005 [15].

Figure 4.17 illustrates the multiwavelength light curves of the M87 core, along with the superluminal knot HST-1, during the three major TeV flaring events in 2006, 2008, and 2010 as reported in [15]. During the 2010 multiwavelength campaign, the LAT reported a marginal indication of variability at the 2σ level using statistical errors only. However, a reexamination of this variability using the same binning with the updated pass 7 IRFs as discussed in 4.3.2.3 found the source to be consistent with a steady flux.

The lack of variability of M87 in the LAT range has been reported as a trend among the population of misaligned sources [13], although mounting evidence for variability in the γ-ray loud radio galaxies 3C 78 , 3C 111, and 3C 120 has begun to emerge [5, 18, 168]. Most notably, a similar misaligned TeV source Perseus A

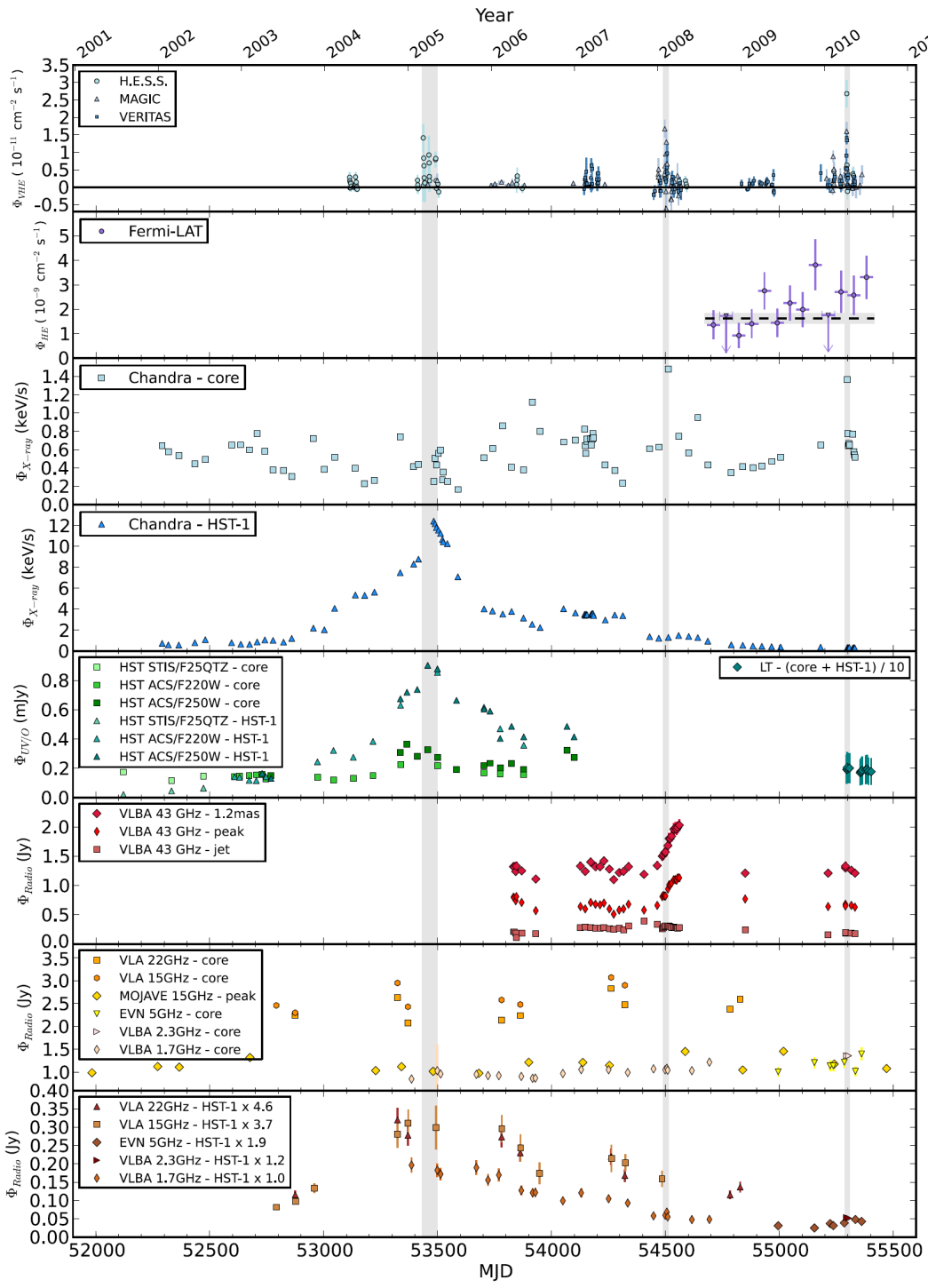

Figure 4.17: Multi-wavelength light curve of M87 from 2001 to 2011. The *Fermi*-LAT flux and weighted average (dashed line, second panel from top) is plotted against the VHE γ-ray flux from H.E.S.S., MAGIC, and VERITAS (top). Light curves for the emission cites at the core and at HST-1 are plotted separately for Chandra (third and fourth from top), along with optical and radio data of both core and HST-1 (panels 5-8) Adapted from [15].

[8, 31], has been found to demonstrate short timescale, rapid flaring on week to month timescales[65]. Both M87 and Perseus A are classified as low-power (FRI) radio galaxies, with broad low-energy synchrotron and high-energy inverse Compton (IC) components in their spectral energy distributions (SEDs), peaking roughly in the infrared and γ-ray bands, respectively. The shape of the SED in both sources is similar to that of the low synchrotron peaked (LSP) BL lacs, of which the FR1 radio galaxies are believed to be the parent population [305]. The difference in the variability properties is however not unique to the FR1 population, as steady HE emission over year timescales is also observed in some BL lac objects (see section 4.2.2.1 and 4.8).

Continued monitoring of M87 in the LAT energy range, coupled with simultaneous multiwavelength observations, will be crucial to reaching a full understanding of the origin of γ-ray emission in M87 in the years to come. The lack of variability seen from the source over the LAT mission, particularly in light of two separate TeV flares that occured during this time, is a compelling reason to reconsider previous assumptions that have gone into the modeling of γ-ray emission from the source. In particular, the possibility that the γ-ray emission could be taking place in less compact regions further along the jet, particularly beyond the parsec-scale core, should be considered in light of this emerging evidence. The question of whether this behavior is a trend among other γ-ray emitting source classes is also important to consider. With further monitoring of the full sky by the Fermi-LAT, the answers to these questions should become increasingly more evident as the observed time scales and statistics continue to improve.

Chapter 5
Development of Analysis Methods for the LAT Pass 8 Instrument Response Functions

5.1 Introduction

The Fermi-LAT is in many ways a state-of-the-art technology from its predecessors, implementing designs and methods that had previously been found only in particle accelerators into an instrument for detecting astrophysical γ-rays. The novelty of the LAT design has not only allowed for its vastly improved sensitivity, but also has opened up the possibility of implementing new analysis methods that had previously not been used for the detection of astronomical γ-rays.

One particular area of opportunity that is unique to the LAT lies in its ability to estimate the error in the angular reconstruction of each event via the Kalman fit (see Section 3.3.2.2). Normally, the angular uncertainty of the photons measured by a particular telescope is described by the point spread function (PSF). The PSF, which can be a function of one or more variables related to the instrument response, is obtained by fitting the angular deviation of a large number of events from their known true position to a functional form, then normalizing the function over all space. Thus the uncertainty of each event is described by the same PSF.

The LAT likelihood analysis is currently performed using this method, with each photon of measured energy and theta being described using the same PSF. Although this has historically been proven an effective and reliable method for performing likelihood analysis, the energy / theta parameterization inevitably results in all information about the event reconstruction being lost. Thus there is a great potential for improving the angular resolution of the LAT through the Kalman errors, due to the fact that the information from the event reconstruction is preserved.

In the following sections, the mathematical framework for performing likelihood analysis using the Kalman covariance matrix is outlined. Products from early developmental work of Pass 7 data using this method are presented. In particular, a method for performing smoothing of counts maps using the covariant errors is demonstrated. In addition, a method for obtaining the event-by-event errors for events that are measured only within the LAT calorimeter (CAL-only) is also presented.

5.2 Implementation & Development of Event-by-Event Covariant Errors

5.2.1 Overview of the 2d Covariance Matrix

As described in Section 3.3.2.2, the key product obtained from the Kalman Filter is the 2×2 covariance matrix that contains the information necessary for

describing the uncertainty in the measured direction of the reconstructed track. The covariance matrix is simply the multi-dimensional representation of the variance σ. A conceptual understanding of the covariance matrix can be made by examining its relationship to the equation for an ellipse rotated clockwise by a given angle θ:

$$1 = x^2 \left(\frac{\cos(\theta)^2}{a^2} + \frac{\sin(\theta)^2}{b^2} \right) + 2xy \cos(\theta)\sin(\theta) \left(\frac{1}{a^2} + \frac{1}{b^2} \right) + y^2 \left(\frac{\sin(\theta)^2}{a^2} + \frac{\cos(\theta)^2}{b^2} \right) \tag{5.1}$$

where a and b are the semimajor and semiminor axes, respectively, and the angle θ is defined with respect to the x-axis. Here we define the center of the ellipse to lie at the origin without the loss of generality.

To understand the ralationship to the covariance matrix, let us first define the following symmetric matrix:

$$C^{-1} = \begin{bmatrix} C_{xx}^{-1} & C_{xy}^{-1} \\ C_{xy}^{-1} & C_{yy}^{-1} \end{bmatrix} \tag{5.2}$$

where

$$C_{xx}^{-1} = \left(\frac{\cos(\theta)^2}{a^2} + \frac{\sin(\theta)^2}{b^2} \right), \tag{5.3}$$

$$C_{xy}^{-1} = \cos(\theta)\sin(\theta) \left(\frac{1}{a^2} + \frac{1}{b^2} \right), \tag{5.4}$$

$$C_{yy}^{-1} = \left(\frac{\sin(\theta)^2}{a^2} + \frac{\cos(\theta)^2}{b^2} \right) \tag{5.5}$$

From here, we note that Equation 5.1 can be re-expressed using the following matrix operation:

$$1 = r^T C^{-1} r = \begin{pmatrix} x & y \end{pmatrix} \begin{bmatrix} C_{xx}^{-1} & C_{xy}^{-1} \\ C_{xy}^{-1} & C_{yy}^{-1} \end{bmatrix} \begin{pmatrix} x \\ y \end{pmatrix} \tag{5.6}$$

Now consider a second ellipse with new semiminor and semimajor axes expressed as some common multiple (denoted here as n_σ) of the original semiminor and semimajor axes, $a \rightarrow n_\sigma a, b \rightarrow n_\sigma b$. Substituting these values into Equation 5.1 yields the following:

$$n_\sigma^2 = x^2 \left(\frac{\cos(\theta)^2}{a^2} + \frac{\sin(\theta)^2}{b^2} \right) + 2xy \cos(\theta)\sin(\theta) \left(\frac{1}{a^2} + \frac{1}{b^2} \right) + y^2 \left(\frac{\sin(\theta)^2}{a^2} + \frac{\cos(\theta)^2}{b^2} \right) \tag{5.7}$$

Thus, by relaxing the constraints on r to lie anywhere in the 2d plane, Equation 5.6 can be generalized to the following:

$$n_\sigma^2 = r^T C^{-1} r \tag{5.8}$$

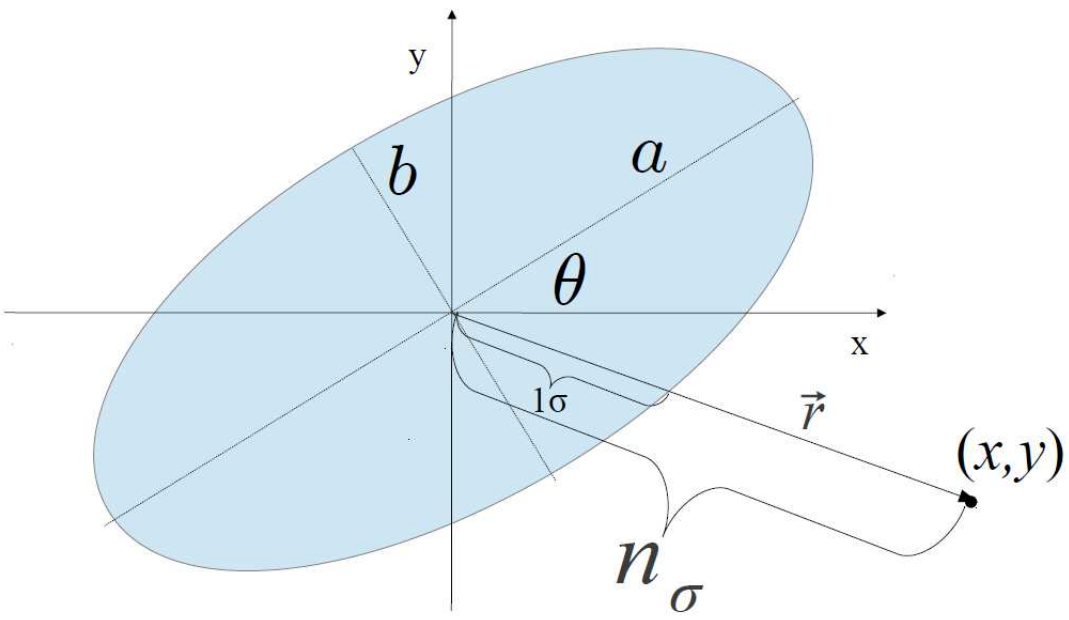

Figure 5.1: The operation $r^T C^{-1} r$ yields the number of sigma n_σ away from the ellipse along the direction of r.

where n_σ represents the number of sigma (where sigma is the length of the radius along the direction of r) from the center of the ellipse to the given point at r (See Figure 5.1). The interpretation of C^{-1} can thus be understood from Equation 5.8 as the multi-dimentional representation of $1/\sigma^2$, with its relationship to the covariance matrix being obtained through the standard inverse operation:

$$C^{-1} = \frac{1}{\det C} \begin{bmatrix} C_{yy} & -C_{xy} \\ -C_{xy} & C_{xx} \end{bmatrix} \tag{5.9}$$

The two-dimensional covariance matrix C therefore contains all the information necessary for expressing σ^2 in two dimensions:

$$C = \begin{bmatrix} \sigma_x^2 & \rho\sigma_x\sigma_y \\ \rho\sigma_x\sigma_y & \sigma_y^2 \end{bmatrix} \tag{5.10}$$

Here σ_x and σ_y represent the x and y standard deviations, which determine the width and height of the ellipse, while the correlation coefficient ρ, with constraints $-1 \leq \rho \leq 1$, determines the rotation of the ellipse from $-90°$ to $90°$.

The relationship between C and σ^2 is particularly useful for expanding an associated probability density to higher dimensions. For example, in one dimension the probability density that obeys Gaussian statistics is given by the normal distribution:

$$P(x) = \frac{1}{\sigma\sqrt{2\pi}} e^{-\frac{1}{2}\left(\frac{x-\mu}{\sigma}\right)^2} \tag{5.11}$$

This expression may be carried to multiple dimensions using the n-dimensional representation of equation 5.8 and the determinant of the covariance, along with the proper normalization for n dimensions:

$$P(\vec{x}) = \frac{1}{|C|^{\frac{1}{2}} (2\pi)^{\frac{n}{2}}} e^{-\frac{1}{2}(x-\mu)^T C^{-1}(x-\mu)} \tag{5.12}$$

where C in this case spans n dimensions. In 2 dimensions, this translates to the following expression:

$$P(x,y) = \frac{1}{\sigma_x \sigma_y \sqrt{1-\rho^2}(2\pi)} e^{-\frac{z}{2(1-\rho^2)}} \tag{5.13}$$

where

$$z \equiv \frac{(x-\mu_x)^2}{\sigma_x^2} - \frac{2\rho\,(x-\mu_x)\,(y-\mu_y)}{\sigma_x \sigma_y} + \frac{(y-\mu_y)^2}{\sigma_y^2} \tag{5.14}$$

This is known as the bivariate normal distribution.

5.2.2 Likelihood with Covariance Matrix

In section 5.2.1, it was shown that the covariance matrix C may be represented as a probability density through the bivariate normal distribution. Furthermore, in section,3.5.1 it was shown via Equation 3.21 that the predicted counts θ_{ij} could be obtained by convolving the model predicted counts density S with the instrument response R. The instrument response is in fact the normalized point spread function at the given energy ε and incoming angle Θ with respect to the LAT zenith and is therefore a probability density. In the unbinned likelihood case, the operation in Equation 3.21 is performed separately for each event and may therefore be replaced by the covariance-derived probability density.

One of the necessary steps for integrating the covariance information with the LAT likelihood analysis lies in the reconciliation of the event reconstruction and associated errors, which are performed in the LAT coordinate system, with that of the sources of interest, which lie on the celestial sphere. More specifically, the Kalman fit is performed over the LAT x-y tracker layers, with the final products for the covariance matrix elements lying in instrument slope coordinates (x/z, y/z, with z representing the direction of the LAT boresight; see Section 3.3.2.2). To make use of the Kalman errors, one of two possible approaches must be taken. The first approach, which is valid only in the small angle approximation, involves projecting the covariance matrix onto the sky by transforming the errors in s_1, s_2 space, to corresponding errors in θ, ϕ space:

$$\mathbf{C}' = \mathbf{J}\mathbf{C}\mathbf{J}^T \tag{5.15}$$

where $\mathbf{J}$ is the Jacobian matrix, with elements given by:

$$J_{ij} = \frac{\partial F_i}{\partial x_j} \tag{5.16}$$

Here $F : \mathbb{R}^n \rightarrow \mathbb{R}^m$ is the vector-valued function that transforms from Euclidean n-space to Euclidean m-space, given by m real-valued component functions $F_1(x_1, \cdots, x_n), \cdots, F_m(x_1, \cdots, x_n)$ [1]. In the transformation from instrument-slope to Cartesian coordinates, F is represented by $(\hat{v}_x, \hat{v}_y, \hat{v}_z)$, the components of which are obtained via the following transformations:

$$\hat{v}_z = -\left[1 + s_1^2 + s_2^2\right]^{-\frac{1}{2}} \tag{5.17}$$

$$\hat{v}_x = \hat{v}_z s_1 \tag{5.18}$$

$$\hat{v}_y = \hat{v}_z s_2 \tag{5.19}$$

where (s_1, s_2) are the instrument slope coordinates $(x/z, y/z)$. Using Equation 5.16, the Jacobian $\mathbf{A}$ is thus obtained:

$$\mathbf{A} = \begin{bmatrix} \hat{v}_z\left(1 - \hat{v}_x^2\right) & -\hat{v}_x\hat{v}_y\hat{v}_z \\ -\hat{v}_x\hat{v}_y\hat{v}_z & \hat{v}_z\left(1 - \hat{v}_y^2\right) \\ -\hat{v}_x\hat{v}_z^2 & -\hat{v}_y\hat{v}_z^2 \end{bmatrix} \tag{5.20}$$

At this point a simple linear rotation can be performed in 3d Cartesian space by finding the appropriate quaternion to map the instrument coordinate axes to the corresponding axes in the event frame.

Use of this method is valid only under the small angle approximation. This is most easily understood by considering the unit celestial sphere with the LAT positioned at its center (Figure 5.2). The LAT coordinate system is defined such that incoming events are reconstructed downward with respect to the LAT zenith (-$\hat{z}$), then projected onto the s_1, s_2 plane located at $z = 1$. Note that changes in distances along the celestial sphere do not have a 1-to-1 correspondence to changes in the s_1, s_2 plane. Therefore, the transformation of an error ellipse in s_1, s_2 space introduces angular distortions to the shape of the ellipse on the celestial sphere at large angles. Ultimately, the LAT errors are small enough that this approach is a valid approximation, although use of this method should be reserved primarily for source association and mapping error ellipses of individual events onto the sky (for example, when plotting the error ellipse against a source position in a counts map).

A second approach, which is valid for all angles, is to instead perform the likelihood analysis in the LAT frame by transforming the individual sky coordinates onto the s_1, s_2 plane. Because the LAT likelihood analysis requires only a finite list of sky coordinates (namely, the coordinates of the point sources, the pixel coordinates of any diffuse maps, and the coordinates of the events themselves), the coordinates may therefore be transformed prior to the calculation of the likelihood. This approach may also be taken without the loss of computational speed in the spectral fitting, due to the fact that the spatial probabilities may be pre-computed prior to performing a likelihood fit (see Section 3.5.1, Equations 3.21 and 3.22), and therefore the transformation only needs to be performed once.

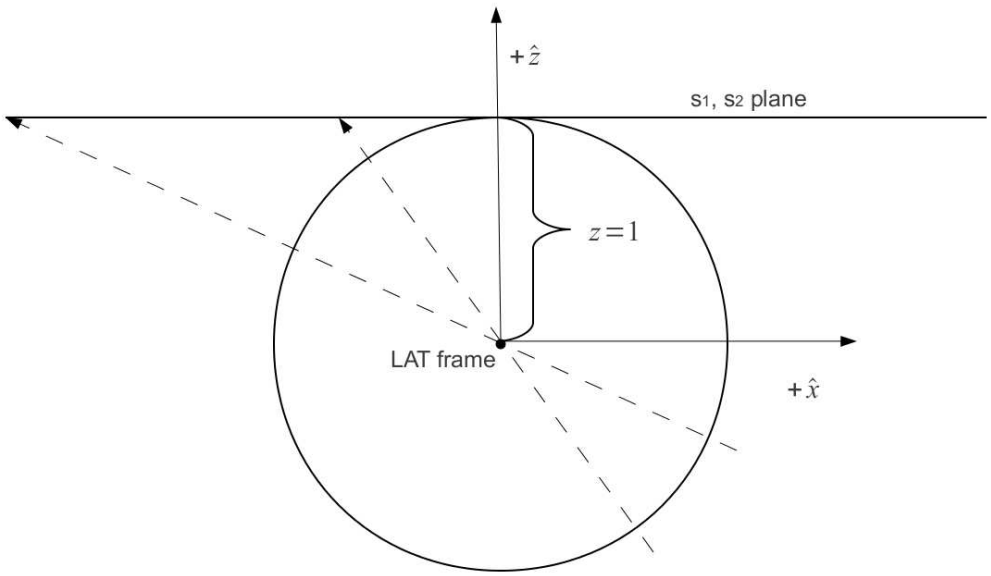

Figure 5.2: The LAT gnomonic projection. Events are reconstructed in the downward ($-\hat{z}$) direction, and projected onto the s_1, s_2 plane (located at $z = 1$), where $s_1 = \frac{x}{z}$ and $s_2 = \frac{y}{z}$.

5.2.3 Covariance Analysis Using HEALpix software

In order to perform the likelihood analysis using covariant errors, many of the steps described in Section 3.5.1 may be followed without any changes. More precisely, all of the cuts related to event selection, as well as the calculation of the livetime cube and exposure map, may be performed as described in Section 3.5.1. This is due to the fact that the event selection, livetime, and exposure are all calculated prior to convolution with the model in the unbinned analysis. All of the relevant likelihood calculations pertaining to the convolution with the model counts are thus contained in Equation 3.21. Thus, whenever there is not an explicit spectral dependence on the spatial distribution of source photons [1], the probability distribution function will be completely masked from the spectral fitting, and the same techniques described for the unbinned analysis in Section 3.5.1 can be applied.

To perform the calculation of θ_{ij} in Equation 3.21, an integration must be performed. In principle, any equal-area integration over the ROI is valid, however the simplest and most advantageous approach for covariant analysis is to discretize the function and perform the integral as a summation over the HEALpix sphere. HEALpix, which is an acronym for Hierarchical Equal Area isoLatitude Pixelization, is a method for pixelizing the celestial sphere in such a way that each pixel has the same surface area as every other pixel. Higher resolutions of the HEALpix grid are represented as subdivisions of each HEALpix pixel into four smaller pixels, with the lowest resolution grid being represented by 12 equal sized pixels, the second-highest resolution being 48 pixels, followed by 192, 768, and so on.

A discretization over the HEALpix sphere offers the most straightforward approach for normalizing the probability distribution. Normalization is performed by first transforming the discrete list of HEALpix coordinates into the LAT frame. This is done starting with a simple cartesian rotation from the sky coordinate frame to the LAT frame, followed by a transformation into the s_1, s_2 coordinate system. The differential probabilities for each sky coordinate are then obtained by solving Equation 5.12 in the s_1, s_2 coordinate system. The discrete function is then normalized by dividing by the sum of all probabilities.

HEALpix offers a number of important advantages in optimization. In principle, Equation 3.21 needs to be performed over the entire celestial sphere. However, in regions at large distances ($\gtrsim 3\sigma$ of the semimajor axis) from the source counts, the probabilities quickly approach zero. Thus, an optimization can be performed by querying a region of pixels that falls within n sigma of the measured photon, and setting all other probabilities to zero. The HEALpix software has the tools in place for performing such pixel queries. Another advantage in optimization is that the HEALpix resolution can easily be adjusted to accomodate the broad range of angular resolution in the LAT as a function of energy and theta. Lower energy events with errors on the order of degrees can in turn be performed over a lower resolution map than higher energy events, thus allowing for further optimization.

[1] no LAT source is modeled in this fashion using the standard analysis tools, primarily due to the computational power that would be required for such an analysis.

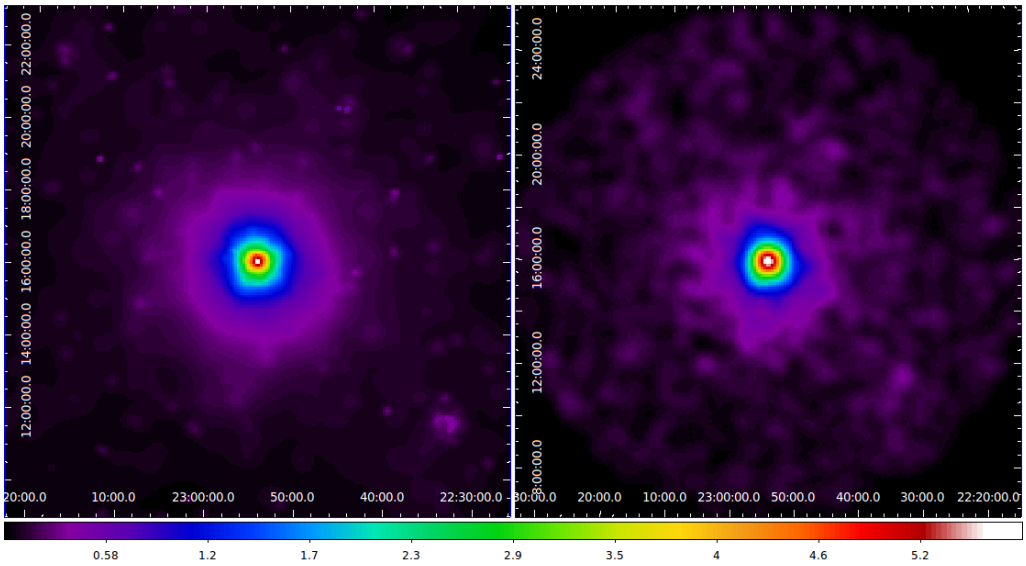

Figure 5.3: Comparison of covariance-smoothed counts map (left) of the FSRQ 3c454.3, against a standard counts map smoothed with a gaussian kernel of radius 6 pixels (right). The covariance-smoothed map shows greater symmetry, along with a sharper peak about the source position.

5.2.4 Initial Results: Covariance-Smoothed Counts Maps

One of the simplest tools that can demonstrate the potential of using event-by-event errors in the LAT is by producing counts maps in which each photon event is plotted by its corresponding probability distribution. In a standard counts map, a region of the sky is divided into a two-dimensional histogram of pixels, which are incremented for each count that falls within a given pixel. A convolution is then applied to the entire histogram using a kernel function, such as a gaussian of specified pixel width, in order to smooth the image.

By plotting each photon by its associated probability distribution, the smoothing is applied on a photon-by-photon basis, without the need to bin events, and in such a way as to maximize the amplitude of events with small errors, while lowering the amplitude of events with larger errors. For point sources, this will result in the peak amplitude being close to the original source location (see Figure 5.3). Another advantage that this has over standard counts maps is that the resolution of the map is effectively unbounded, being limited only by the computational power of the hardware used to produce the map.

Figure 5.4 demonstrates the potential of using event-by-event errors for detecting extended emission in LAT sources. Using two years of pass 7 data [2] covariance-smoothed counts maps of Fornax A, along with a sample of 2FGL extragalactic sources with index and flux similar to Fornax A[3], were created. The profiles of each

[2]The Kalman errors from pass 7 data should be considered preliminary, as further calibration of the Kalman errors was applied to the pass 8 data which had not been applied in pass 7.

[3]All sources with index and flux within 1σ of Fornax A were considered

source were then compared. Despite the sources being among the fairly low detection significance in the 2FGL catalog, their smoothed counts maps clearly show a visible signal over background. Interestingly, Fornax A demonstrates a far wider profile compared to the majority of the point sources, with the exception of PKS_2329-16.

5.3 Development of CAL-only Error Reconstruction for Pass 8

5.3.1 Overview of Calorimeter Clustering Methods

As discussed in Section 3.1.3, the LAT uses a hodoscopic calorimeter (abbreviated as CAL from here forward) to obtain a profile of the energy deposition. The profile can be described in three dimensions using the energy moment of inertia tensor $\mathbb{I}$ about the energy centroid $\mathbf{r}_c$ of the cluster.

For a given distribution of n CAL crystals, the energy centroid can be calculated using the position $\mathbf{r}_i$ and energy (denoted here as the weight w_i) of each crystal:

$$\mathbf{r}_c = \frac{\sum_{i=1}^{n} w_i \mathbf{r}_i}{W} \tag{5.21}$$

$$W = \sum_{i=1}^{n} w_i \tag{5.22}$$

where W represents the total weight or energy. To calculate the principal axis, we first must calculate the individual elements of the moment of inertia tensor $\mathbb{I}$, using the measured crystal energy as the weight instead of the standard mass:

$$\mathbb{I}_{xx} = \textstyle\sum_{i=1}^{n} w_i(r_i^2 - x_i^2),\ \mathbb{I}_{yy} = \sum_{i=1}^{n} w_i(r_i^2 - y_i^2),\ \mathbb{I}_{zz} = \sum_{i=1}^{n} w_i(r_i^2 - z_i^2), \tag{5.23}$$

$$\mathbb{I}_{xy} = -\textstyle\sum_{i=1}^{n} w_i x_i y_i,\ \mathbb{I}_{xz} = -\sum_{i=1}^{n} w_i x_i z_i,\ \mathbb{I}_{yz} = -\sum_{i=1}^{n} w_i y_i z_i \tag{5.24}$$

In the above equation, the index i runs over each of the n CAL crystals that fall above threshold for a given event, w_i is equal to the energy measured from the ith crystal, and x, y, z are the positional measurements for ith crystal defined with respect to the energy centroid $\mathbf{r}_c$ in instrument coordinates. The principal axis is thus obtained by diagonalizing the moment of inertia tensor and determining the principal axes via the secular equation:

$$\det(\mathbb{I} - \lambda \mathbb{1}) = \begin{vmatrix} \mathbb{I}_{xx} - \lambda & \mathbb{I}_{xy} & \mathbb{I}_{xz} \\ \mathbb{I}_{xy} & \mathbb{I}_{yy} - \lambda & \mathbb{I}_{yz} \\ \mathbb{I}_{xz} & \mathbb{I}_{yz} & \mathbb{I}_{zz} - \lambda \end{vmatrix} = 0 \tag{5.25}$$

From here the three eigenvalues for λ can be found by solving the cubic equation

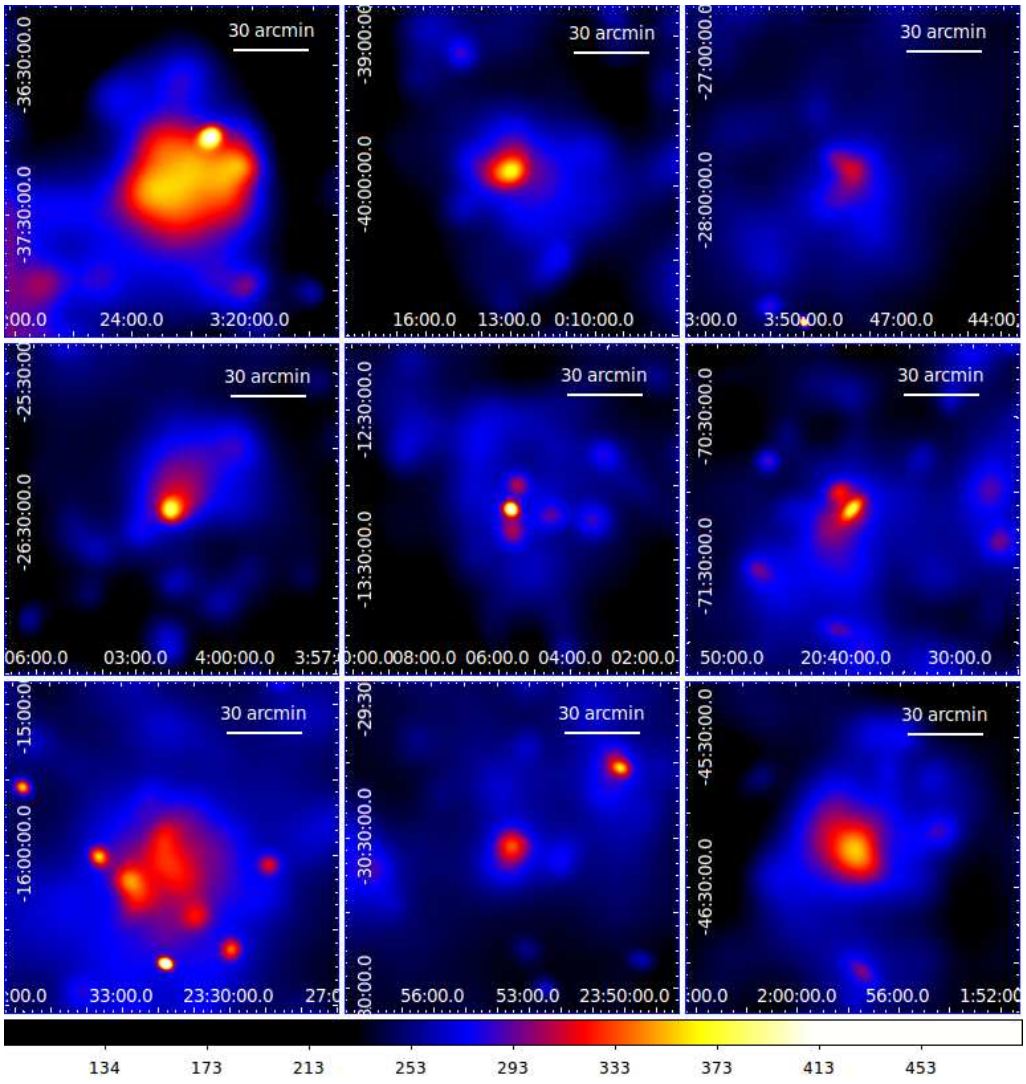

Figure 5.4: Comparison of covariance-smoothed counts maps using 2 years of preliminary pass 7 event data for AGN sources of similar 2FGL spectral index and $> 100\,\mathrm{MeV}$ flux. Starting from upper left to bottom right: Fornax A, PKS_0010-401, PKS_0346-27, PKS_0359-264, PKS_0403-13, PKS_2035-714, PKS_2329-16, PKS_2351-309, and PMN_J0157-4614. With the exception of PKS_2329-16, all point sources are peaked around their true source position. The extended emission around Fornax A holds significant promise for future analysis using event-by-event errors with the Pass 8 data. Note that the number scale does not represent source photon counts, but rather a counts density per unit area over the chosen pixel size.

$$\lambda^3 + a_2\lambda^2 + a_1\lambda + a_0 = 0 \tag{5.26}$$

where

$$a_2 = -(\mathbb{I}_{xx} + \mathbb{I}_{yy} + \mathbb{I}_{zz}) \tag{5.27}$$
$$a_1 = \mathbb{I}_{xx}\mathbb{I}_{yy} + \mathbb{I}_{yy}\mathbb{I}_{zz} + \mathbb{I}_{xx}\mathbb{I}_{zz} - (\mathbb{I}_{xy}^2 + \mathbb{I}_{yz}^2 + \mathbb{I}_{xz}^2) \tag{5.28}$$
$$a_0 = -\mathbb{I}_{xx}\mathbb{I}_{yy}\mathbb{I}_{zz} - 2\mathbb{I}_{xy}\mathbb{I}_{yz}\mathbb{I}_{xz} + \mathbb{I}_{xx}\mathbb{I}_{yz}^2 + \mathbb{I}_{yy}\mathbb{I}_{xz}^2 + \mathbb{I}_{zz}\mathbb{I}_{xy}^2 \tag{5.29}$$

Following [311], the cubic formula can be solved through the substitution $\lambda' = \lambda + a_2/3$, which yields the following form:

$$\lambda'^3 + p\lambda' - q = 0 \tag{5.30}$$

where

$$p \equiv \frac{3a_1 - a_2^2}{3} \tag{5.31}$$
$$q \equiv \frac{9a_1a_2 - 27a_0 - 2a_2^3}{27} \tag{5.32}$$

From here we apply the following substitutions:

$$Q = \frac{p}{3} \tag{5.33}$$
$$R = \frac{q}{2} \tag{5.34}$$
$$\theta \equiv \cos^{-1}\left(\frac{R}{\sqrt{-Q^3}}\right) \tag{5.35}$$

which yields the following solutions for λ:

$$\lambda_0 = 2\sqrt{-Q}\cos\left(\frac{\theta}{3}\right) - \frac{1}{3}a_2 \tag{5.36}$$
$$\lambda_1 = 2\sqrt{-Q}\cos\left(\frac{\theta + 2\pi}{3}\right) - \frac{1}{3}a_2 \tag{5.37}$$
$$\lambda_2 = 2\sqrt{-Q}\cos\left(\frac{\theta + 4\pi}{3}\right) - \frac{1}{3}a_2 \tag{5.38}$$

The corresponding eigenvectors $\mathbf{e}^i$ $(i = 1 \ldots 3)$ can thus be found by solving the following equation:

$$\mathbb{I}\mathbf{e}^i = \lambda_i\mathbf{e}^i \tag{5.39}$$

The principal axis thus corresponds to the eigenvector with the largest eigenvalue, which in this case is λ_1.

5.3.2 Implementation of the Error for CAL-only Events

Ultimately, the principal axis will point along the longitudinal direction of the shower profile, thus it can be used to obtain the incoming direction of γ-ray photons. Similarly, an error in the incoming direction of the photon can also be obtained by calculating the corresponding error in the principal eigenvector obtained from Equation 5.39. To calculate these errors, we follow the formalism (and corrigendum) outlined by Soler & van Gelder (1991) [277, 62] for obtaining the covariance matrices of eigenvalues and eigenvectors of second-rank 3-D symmetric tensors.

The individual elements Σ_{k-l} of the covariance matrix for the energy moment of inertia tensor can be calculated using the following equation:

$$\Sigma_{k-l} = \sum_{i=1}^{n} \frac{\partial \mathbb{I}_k}{\partial x_i}\frac{\partial \mathbb{I}_l}{\partial x_i}(\Delta x_i)^2 + \frac{\partial \mathbb{I}_k}{\partial y_i}\frac{\partial \mathbb{I}_l}{\partial y_i}(\Delta y_i)^2 + \frac{\partial \mathbb{I}_k}{\partial z_i}\frac{\partial \mathbb{I}_l}{\partial z_i}(\Delta z_i)^2 + \frac{\partial \mathbb{I}_k}{\partial w_i}\frac{\partial \mathbb{I}_l}{\partial w_i}(\Delta w_i)^2 \quad (5.40)$$

where k and l run over the 6 independent indices of the inertia tensor (xx, yy, zz, xy, xz, & yz), and Δx_i represents the positional error of the measured energy deposition in the ith LAT CAL crystal along the x direction of LAT coordinate frame. Next, The rotation matrix S that transforms from the LAT frame into the diagonalized frame is created from the eigenvectors obtained from Equation 5.39:

$$S = \begin{bmatrix} e_x^0 & e_y^0 & e_z^0 \\ e_x^1 & e_y^1 & e_z^1 \\ e_x^2 & e_y^2 & e_z^2 \end{bmatrix} \quad (5.41)$$

The remaining ingredients can be obtained by following the prescription of Soler & van Gelder (1991) as follows:

$$D = \begin{bmatrix} 1 & 0 & 0 & 0 & 0 & 0 & 0 & 0 & 0 \\ 0 & 0 & 0 & 0 & 1 & 0 & 0 & 0 & 0 \\ 0 & 0 & 0 & 0 & 0 & 0 & 0 & 0 & 1 \\ 0 & \frac{1}{2} & 0 & \frac{1}{2} & 0 & 0 & 0 & 0 & 0 \\ 0 & 0 & \frac{1}{2} & 0 & 0 & 0 & \frac{1}{2} & 0 & 0 \\ 0 & 0 & 0 & 0 & 0 & \frac{1}{2} & 0 & \frac{1}{2} & 0 \end{bmatrix} \quad (5.42)$$

$$v_d(\mathbb{I}) = Dvec(\mathbb{I}) = \begin{bmatrix} \mathbb{I}_{xx} \\ \mathbb{I}_{yy} \\ \mathbb{I}_{zz} \\ \mathbb{I}_{xy} \\ \mathbb{I}_{xz} \\ \mathbb{I}_{yz} \end{bmatrix} \quad (5.43)$$

The *vec* operation above stacks the tensor components into a single vector, while the D matrix rearranges the components and removes the duplicates. Thus, the 6×6 covariance matrix will be rearranged as follows:

$$\Sigma_{v_d(\mathbb{I})} = \begin{bmatrix} \Sigma_{xx-xx} & \Sigma_{xx-yy} & \Sigma_{xx-zz} & \Sigma_{xx-xy} & \Sigma_{xx-xz} & \Sigma_{xx-yz} \\ \Sigma_{xx-yy} & \Sigma_{yy-yy} & \Sigma_{yy-zz} & \Sigma_{yy-xy} & \Sigma_{yy-xz} & \Sigma_{yy-yz} \\ \Sigma_{xx-zz} & \Sigma_{yy-zz} & \Sigma_{zz-zz} & \Sigma_{zz-xy} & \Sigma_{zz-xz} & \Sigma_{zz-yz} \\ \Sigma_{xx-xy} & \Sigma_{yy-xy} & \Sigma_{zz-xy} & \Sigma_{xy-xy} & \Sigma_{xy-xz} & \Sigma_{xy-yz} \\ \Sigma_{xx-xz} & \Sigma_{yy-xz} & \Sigma_{zz-xz} & \Sigma_{xy-xz} & \Sigma_{xz-xz} & \Sigma_{xz-yz} \\ \Sigma_{xx-yz} & \Sigma_{yy-yz} & \Sigma_{zz-yz} & \Sigma_{xy-yz} & \Sigma_{xz-yz} & \Sigma_{yz-yz} \end{bmatrix} \tag{5.44}$$

The last three ingredients are:

$$D^+ = \begin{bmatrix} 1 & 0 & 0 & 0 & 0 & 0 \\ 0 & 0 & 0 & 1 & 0 & 0 \\ 0 & 0 & 0 & 0 & 1 & 0 \\ 0 & 0 & 0 & 1 & 0 & 0 \\ 0 & 1 & 0 & 0 & 0 & 0 \\ 0 & 0 & 0 & 0 & 0 & 1 \\ 0 & 0 & 0 & 0 & 1 & 0 \\ 0 & 0 & 0 & 0 & 0 & 1 \\ 0 & 0 & 1 & 0 & 0 & 0 \end{bmatrix} \tag{5.45}$$

followed by

$$S_p = \begin{bmatrix} 0 & S_{20} & -S_{10} \\ -S_{20} & 0 & S_{00} \\ S_{10} & -S_{00} & 0 \\ 0 & S_{21} & -S_{11} \\ -S_{21} & 0 & S_{01} \\ S_{11} & -S_{01} & 0 \\ 0 & S_{22} & -S_{12} \\ -S_{22} & 0 & S_{02} \\ S_{12} & -S_{02} & 1 \end{bmatrix} \tag{5.46}$$

and

$$G^+ = \begin{bmatrix} 1 & 0 & 0 & 0 & 0 & 0 & 0 & 0 & 0 \\ 0 & 0 & 0 & 0 & 1 & 0 & 0 & 0 & 0 \\ 0 & 0 & 0 & 0 & 0 & 0 & 0 & 0 & 1 \\ 0 & 0 & 0 & 0 & 0 & \frac{1}{2(\lambda_2-\lambda_1)} & 0 & \frac{1}{2(\lambda_2-\lambda_1)} & 0 \\ 0 & 0 & \frac{1}{2(\lambda_0-\lambda_2)} & 0 & 0 & 0 & \frac{1}{2(\lambda_0-\lambda_2)} & 0 & 0 \\ 0 & \frac{1}{2(\lambda_1-\lambda_0)} & 0 & \frac{1}{2(\lambda_1-\lambda_0)} & 0 & 0 & 0 & 0 & 0 \end{bmatrix} \tag{5.47}$$

The errors to the eigenvectors and eigenvalues, expressed in terms of LAT instrument coordinates, can then be obtained using the following transformations:

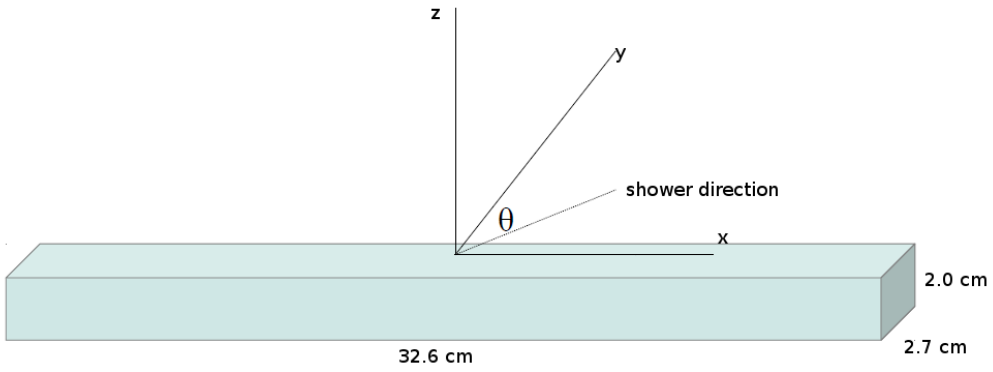

Figure 5.5: CAL crystal geometry. Errors in the positional measurements along the crystal length will increase with larger values of θ.

$$F^{-1} = G^{+}(S \otimes S)D^{+} \tag{5.48}$$

$$K = \begin{bmatrix} 0_{9\times3} & S_p \\ I_{3\times3} & 0_{3\times3} \end{bmatrix} F^{-1} \tag{5.49}$$

and finally

$$\Sigma_{vec(S),\lambda} = K\Sigma_{v_d(\mathbb{I})}K^{T} \tag{5.50}$$

The choice of Δx_i, Δy_i,Δz_i, and Δw_i to be used in Equation 5.40 is dependent on the geometry and energy readout response of the CAL crystals. For the energy w, a 10% error is chosen, consistent with the systematic errors estimated for individual CAL crystal readout [163]. The positional uncertainties were chosen as a function of the crystal geometry combined with the uncertainty of the longitudinal positional measurement obtained using the light asymmetry of the CAL crystals. More specifically, each CAL crystal has a geometry of 2.7 cm×2.0 cm×32.6 cm (see Figure 5.5), such that the uncertainty in a positional measurement using the crystal geometry alone would correspond to one half the length of the crystal dimension in any given direction. However, the positional uncertainty in the longitudinal direction can be better constrained using the light asymmetry in the crystal, as detailed in Johnson (2001) [163]. Using these calibration beam test results, a conservative starting estimate of 5 mm for the positional uncertainty was chosen (see [163], Figure 3 therein). Lastly, to account for additional uncertainty in the longitudinal position that arises from showers that are deposited off-axis (that is, with angular component lying along the crystal length), an additional component was added to the longitudinal undertainty equal to one half the traversed distance of the shower along the crystal.

5.3.3 Results & Conclusions

To test the method, 10000 all-gamma events were simulated using the GLEAM monte carlo software, with event selections for the number of CAL clusters (> 1),

CAL crystals (> 2), CAL raw energy ($> 5\,\mathrm{GeV}$), and CAL cluster moment x/y/z direction (not all = 0). The estimated value of the error for the principal axis along the direction of the monte carlo true position was then compared against the angular separation between the true and measured event directions (often referred to as a "pull plot"). The error estimation method described above was also compared against an estimate using only the crystal geometry, as well as an estimate where only the starting 5 mm errors were used, without an angular correction applied.

The results from this comparison are shown in Figure 5.6. From the resulting figure, we find that the proposed method utilizing the 5 mm positional uncertainty combined with the additional angular correction provides the most accurate description of the event errors. The events are well contained within the distribution, with 68% of events falling within 1σ and 95% of events falling within 2.5σ. In comparison, the method based on the crystal geometry alone significantly overestimates the error, with 95% of events being contained within 1σ, while the estimate using only the 5 mm uncertainty derived from the beam test at normal incidence tends to underestimate the error, with only 68% of events falling within 2.5σ, and 95% containment occurring at 6.5σ.

The above results are highly promising for implementation in future analysis. The ability to accurately describe the errors in each CAL cluster opens up the possibility to use events that convert in the calorimeter for analysis of point sources. While the angular uncertainty of these events will be on the order of several degrees, the improved effective area at VHE range, combined with the very low background at these energies, will ultimately aid in the likelihood analysis of VHE sources through improved statistics. This will in turn mean better spectral constraints at these energies, which will lead to improved science results in areas such as placing constraints on the EBL via the measurement of spectral attenuation in high redshift AGN as discussed in Sections 2.3.4.2 & 4.2.5.

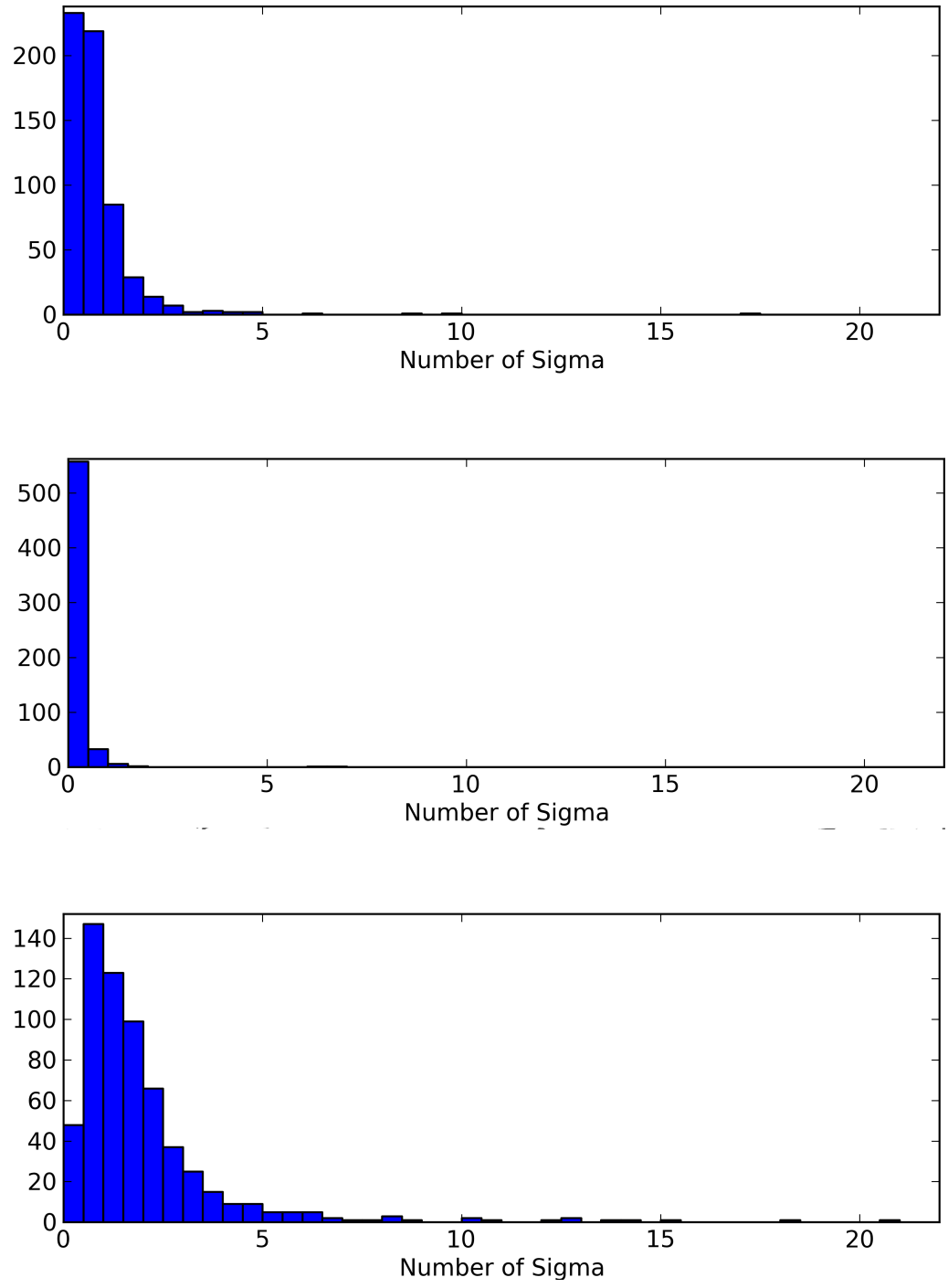

Figure 5.6: Event distribution of the pull (number of sigma) for each of the methods: 5 mm error plus angular correction (top), geometry-based error (middle), and 5 mm with no angular correction (bottom). Events are binned in intervals of 0.5 sigma.

Chapter 6
Final Thoughts

The Fermi-LAT has been a tremendous asset for studying the high energy sky, and its contribution to the study of AGN is no exception. Many of the results from its predecessors such as EGRET have been confirmed by the LAT, including the predominance of BL Lac and FSRQ blazars across the extragalactic sky, with their highly Doppler boosted emission leading to pronounced γ-ray variability on day-to-week timescales. The LAT has provided a great deal in advancing the wealth of knowledge that was obtained during the EGRET era. Yet equally important are the entirely new avenues that have been opened up by the LAT. The discovery of new source populations, and the many unexpected or groundbreaking results that have come to emerge from such discoveries, has given rise to many novel areas of study that hadn't been possible with previous γ-ray instruments.

This thesis has aimed to present a view of AGN that falls outside many of the well-established trends that had been "set in stone" prior to the launch of Fermi. Some might say it follows the mantra that while there is much to learn from studying the trend, it is often in the unusual that the greatest potential for discovery can be had. Yet many of the concepts that have been presented in this work are not "new", in the sense that the underlying processes such as synchrotron and inverse-Compton emission that are believed to be at work in these objects are well established to be key contributors in the production of γ-rays in AGN. In Chapter 1, I reviewed much of the key physics responsible for γ-ray production in AGN, while in Chapter 2, I established how this physics is applied to the underlying processes that give rise to the broadband properties of the various types of AGN seen by Fermi-LAT. The novelty in the objects studied here simply lies in how this physics is applied. Ultimately, this is done in a manner that is consistent with observations, which in some cases may require a re-evaluation of previous assumptions, such as with the steady emission seen in 4C+55.17 and M87, or in opening up new opportunities in areas of science that would otherwise not be possible when studying blazars, such as the application to EBL measurements with Fornax A.

Yet, for all that is discussed in Chapter 4, and for all that we are coming to understand about these objects, there is still much room for future discovery. Much of that discovery hinges on our ability to obtain better resolved, higher significance detections and tighter constraints on the spectral emission of these sources across their broadband spectra. And while there is much to be said for waiting for the next generation of γ-ray instruments to make such measurements possible, there nevertheless remains a tremendous untapped potential for achieving these goals using the Fermi-LAT. In Chapter 3, I detailed how the LAT is built upon many of the key technologies that are found in modern particle detectors, and I explain how these technologies are used in the LAT for detecting γ-rays in space. Yet some of the methods that are fundamental to the reconstruction of events in such detectors, such as the Kalman filter for estimating the errors in the event reconstructions,

are not yet implemented in the standard analysis. In Chapter 5, I outline some of the key concepts that can make such implementation possible. While adapting such information into the LAT analysis is in many ways a journey into completely uncharted territory, the promise that such methods could have in redifining the LAT are substantial.

Appendix A
Preparation of the 20 cm VLA Radio Image of Fornax A

The 20 cm VLA image from [120] was used to model the lobe emission. The higher resolution of the VLA map could allow for the core and lobes to be analyzed separately in a likelihood analysis so that the two could be compared. To prepare the spatial map for likelihood analysis, the point sources within the field of view (including the Fornax A core) were first removed by replacing them with their corresponding background levels, which were determined using the `funcnts` analysis tool. In addition, all negative pixel values were replaced with values of 0. Finally, the entire map was normalized to a flux of 1 ph cm^{-1} s^{-1} by dividing each pixel by a normalization factor. The following formula was used to obtain the normalization:

$$N = n_{pixels} * mean_{pixels} * \left(\frac{\pi}{180}\right)^2 * (\mathrm{CDELT2})^2 \tag{A.1}$$

where $mean_{pixels}$ is the mean value of all pixels in the map to be normalized and CDELT2 is the degrees per pixel in the image. Figure A.1 shows the before and after image with all point sources indicated in green, along with the cleaned image with all point sources removed.

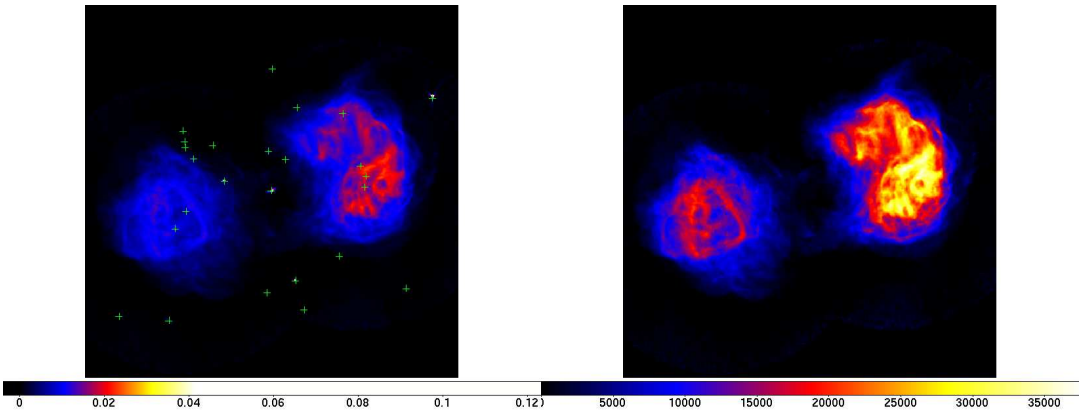

Figure A.1: Before (left) and after (right) images of the 20 cm VLA map for use as an extended source template in the LAT analysis. Indicated in green are the point sources removed from the map.

Appendix B
Association of the 145 GeV photon with 4C +55.17

To further investigate the VHE detection of the source, the 145 GeV event was analyzed in detail using the event display[1] and found to be a clean γ-ray event, going through more than half a tracker tower before interacting in the back planes and generating a well-behaved symmetric shower in the calorimeter (see Figure B.1). A full Monte Carlo simulation was also run in order to determine the accuracy of the energy reconstruction. A total of $500,000$ γ-rays between the energies 50 and 200 GeV were simulated at an incoming angle θ and ϕ equivalent to that of the measured event. Data selection cuts were applied on all similar variables, including cuts on the calorimeter raw energy, best measured energy, reconstructed direction, and event class level. The distribution in Monte Carlo energy for the remaining events was found to give a $\sim 1\sigma$ error of ± 11 GeV.

The probability of the 145 GeV event occurring by random coincidence from background contamination was calculated using the `gtsrcprob` analysis tool. Probabilities of each event are assigned via standard likelihood analysis to all sources within a provided best-fit model [209]. The probability that a photon is produced by a source i is proportional to $M_{\rm i}$, given by the formula:

$$M_{\rm i}(\varepsilon', \hat{p}', t) = \int_{\rm SR} d\varepsilon \, d\hat{p} \; S_{\rm i}(\varepsilon, \hat{p}) \; R(\varepsilon', \hat{p}'; \varepsilon, \hat{p}, t) \,, \tag{B.1}$$

where $S_{\rm i}(\varepsilon, \hat{p})$ is the predicted counts density from the source at energy ε and position $\hat{p}$, and $R(\varepsilon', \hat{p}'; \varepsilon, \hat{p}, t)$ is the convolution over the instrument response. In this way, all the surrounding point sources, the diffuse background, and their corresponding best-fit spectra are taken into account when assigning probabilities to individual photon events. For the 145 GeV event, the probability of spurious association with 4C +55.17 was found to be 6.3×10^{-4}, improving upon an independent method by [221], who quote a chance probability by background contamination of 3.1×10^{-3} for the same event.

[1] `http://glast-ground.slac.stanford.edu/DataPortalWired/`

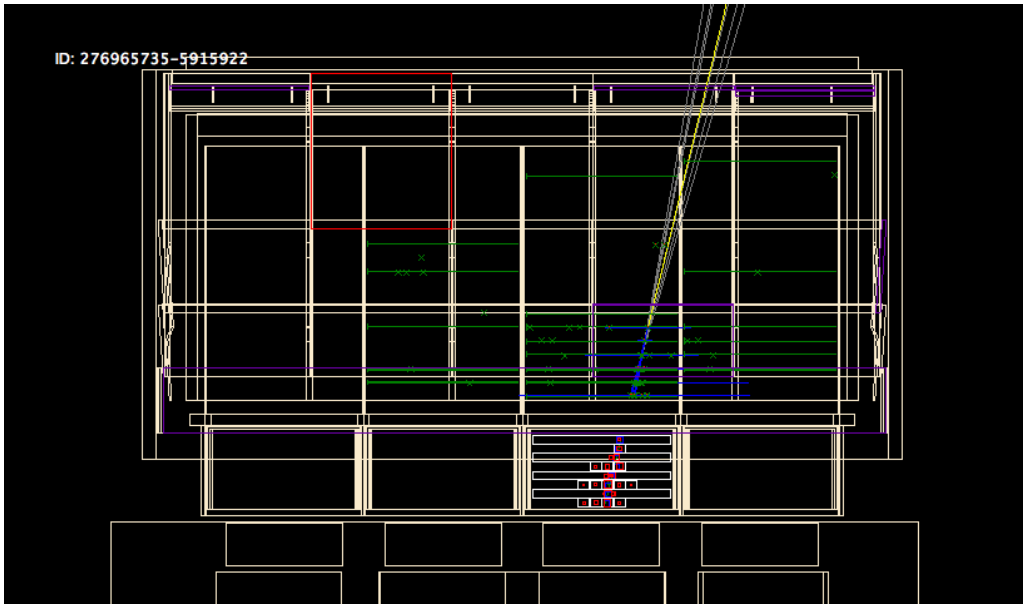

Figure B.1: Event display for the 145 GeV photon. Green "x"s denote hits in the tracker, while red squares indicate an energy deposit in a calorimeter crystal. The white and yellow lines indicate the track candidates and the best track for the event, respectively.

Appendix C
Calculation of the MAGIC II Differential Flux Sensitivity

Starting with the integral flux sensitivity curve of MAGIC II [32], the differential flux sensitivity can be derived for a given functional form. In the case of 4C +55.17, we represent the attenuated VHE spectrum with an exponential cutoff given by the formula:

$$\frac{dN}{dE} = N_0 \, E^{-\Gamma} \, e^{-(\frac{E}{E_c})} \tag{C.1}$$

where N_0, E_c, and Γ are free parameters of the fitted form of the function. The integral flux above some minimum energy E_o is thus given by:

$$N = N_0 \int_{E_0}^{\infty} dE \; E^{-\Gamma} \; e^{-\frac{E}{E_c}} \tag{C.2}$$

Defining the quantity

$$\Psi(E) \equiv \int_{E}^{\infty} dE' \; E'^{-\Gamma} \; e^{-\frac{E'}{E_c}} \tag{C.3}$$

the appropriate solution for N_0 may be substituted into equation C.1 to obtain:

$$\left.\frac{dN}{dE}\right|_{E_0} = \frac{N \, E_0^{-\Gamma} \, e^{-(\frac{E_0}{E_c})}}{\Psi(E_0)} \tag{C.4}$$

To construct the differential flux sensitivity curve, we obtained the values $\Gamma = 2.12$ and $E_c = 100$ GeV by performing a `gtlike` fit of the > 1.6 GeV data of 4C +55.17 to the exponential cutoff functional form. For each value N of the integral flux sensitivity, a corresponding differential flux sensitivity value could thus be obtained via numerical evaluation of equation C.4.

Bibliography

[1] Jacobian matrix and determinant. `http://en.wikipedia.org/wiki/Jacobian_matrix_and_determinant`.

[2] A. A. Abdo, M. Ackermann, I. Agudo, M. Ajello, A. Allafort, H. D. Aller, M. F. Aller, E. Antolini, A. A. Arkharov, M. Axelsson, and et al. Fermi Large Area Telescope and Multi-wavelength Observations of the Flaring Activity of PKS 1510-089 between 2008 September and 2009 June. *ApJ*, 721:1425–1447, Oct. 2010.

[3] A. A. Abdo, M. Ackermann, I. Agudo, M. Ajello, H. D. Aller, M. F. Aller, E. Angelakis, A. A. Arkharov, M. Axelsson, U. Bach, and et al. The Spectral Energy Distribution of Fermi Bright Blazars. *ApJ*, 716:30–70, June 2010.

[4] A. A. Abdo, M. Ackermann, M. Ajello, A. Allafort, E. Antolini, W. B. Atwood, M. Axelsson, L. Baldini, J. Ballet, G. Barbiellini, D. Bastieri, B. M. Baughman, K. Bechtol, R. Bellazzini, F. Belli, B. Berenji, D. Bisello, R. D. Blandford, E. D. Bloom, E. Bonamente, J. Bonnell, A. W. Borgland, A. Bouvier, J. Bregeon, A. Brez, M. Brigida, P. Bruel, T. H. Burnett, G. Busetto, S. Buson, G. A. Caliandro, R. A. Cameron, R. Campana, B. Canadas, P. A. Caraveo, S. Carrigan, J. M. Casandjian, E. Cavazzuti, M. Ceccanti, C. Cecchi, . elik, E. Charles, A. Chekhtman, C. C. Cheung, J. Chiang, A. N. Cillis, S. Ciprini, R. Claus, J. Cohen-Tanugi, J. Conrad, R. Corbet, D. S. Davis, M. DeKlotz, P. R. den Hartog, C. D. Dermer, A. de Angelis, A. de Luca, F. de Palma, S. W. Digel, M. Dormody, E. do Couto e Silva, P. S. Drell, R. Dubois, D. Dumora, D. Fabiani, C. Farnier, C. Favuzzi, S. J. Fegan, E. C. Ferrara, W. B. Focke, P. Fortin, M. Frailis, Y. Fukazawa, S. Funk, P. Fusco, F. Gargano, D. Gasparrini, N. Gehrels, S. Germani, G. Giavitto, B. Giebels, N. Giglietto, P. Giommi, F. Giordano, M. Giroletti, T. Glanzman, G. Godfrey, I. A. Grenier, M.-H. Grondin, J. E. Grove, L. Guillemot, S. Guiriec, M. Gustafsson, D. Hadasch, Y. Hanabata, A. K. Harding, M. Hayashida, E. Hays, S. E. Healey, A. B. Hill, D. Horan, R. E. Hughes, G. Iafrate, G. Jhannesson, A. S. Johnson, R. P. Johnson, T. J. Johnson, W. N. Johnson, T. Kamae, H. Katagiri, J. Kataoka, N. Kawai, M. Kerr, J. Kndlseder, D. Kocevski, M. Kuss, J. Lande, D. Landriu, L. Latronico, S.-H. Lee, M. Lemoine-Goumard, A. M. Lionetto, M. L. Garde, F. Longo, F. Loparco, B. Lott, M. N. Lovellette, P. Lubrano, G. M. Madejski, A. Makeev, B. Marangelli, M. Marelli, E. Massaro, M. N. Mazziotta, W. McConville, J. E. McEnery, P. F. Michelson, M. Minuti, W. Mitthumsiri, T. Mizuno, A. A. Moiseev, M. Mongelli, C. Monte, M. E. Monzani, E. Moretti, A. Morselli, I. V. Moskalenko, S. Murgia, H. Nakajima, T. Nakamori, M. Naumann-Godo, P. L. Nolan, J. P. Norris, E. Nuss, M. Ohno, T. Ohsugi, N. Omodei, E. Orlando, J. F. Ormes, M. Ozaki, A. Paccagnella, D. Paneque, J. H. Panetta, D. Parent, V. Pelassa, M. Pepe,

M. Pesce-Rollins, M. Pinchera, F. Piron, T. A. Porter, L. Poupard, S. Rain, R. Rando, P. S. Ray, M. Razzano, S. Razzaque, N. Rea, A. Reimer, O. Reimer, T. Reposeur, J. Ripken, S. Ritz, L. S. Rochester, A. Y. Rodriguez, R. W. Romani, M. Roth, H. F.-W. Sadrozinski, D. Salvetti, D. Sanchez, A. Sander, P. M. S. Parkinson, J. D. Scargle, T. L. Schalk, G. Scolieri, C. Sgr, M. S. Shaw, E. J. Siskind, D. A. Smith, P. D. Smith, G. Spandre, P. Spinelli, J.-L. Starck, T. E. Stephens, E. Striani, M. S. Strickman, A. W. Strong, D. J. Suson, H. Tajima, H. Takahashi, T. Takahashi, T. Tanaka, J. B. Thayer, J. G. Thayer, D. J. Thompson, L. Tibaldo, O. Tibolla, F. Tinebra, D. F. Torres, G. Tosti, A. Tramacere, Y. Uchiyama, T. L. Usher, A. V. Etten, V. Vasileiou, N. Vilchez, V. Vitale, A. P. Waite, E. Wallace, P. Wang, K. Watters, B. L. Winer, K. S. Wood, Z. Yang, T. Ylinen, and M. Ziegler. Fermi large area telescope first source catalog. *The Astrophysical Journal Supplement Series*, 188(2):405, 2010.

[5] A. A. Abdo, M. Ackermann, M. Ajello, A. Allafort, E. Antolini, W. B. Atwood, M. Axelsson, L. Baldini, J. Ballet, G. Barbiellini, D. Bastieri, B. M. Baughman, K. Bechtol, R. Bellazzini, B. Berenji, R. D. Blandford, E. D. Bloom, J. R. Bogart, E. Bonamente, A. W. Borgland, A. Bouvier, J. Bregeon, A. Brez, M. Brigida, P. Bruel, R. Buehler, T. H. Burnett, S. Buson, G. A. Caliandro, R. A. Cameron, A. Cannon, P. A. Caraveo, S. Carrigan, J. M. Casandjian, E. Cavazzuti, C. Cecchi, Ö. Çelik, A. Celotti, E. Charles, A. Chekhtman, A. W. Chen, C. C. Cheung, J. Chiang, S. Ciprini, R. Claus, J. Cohen-Tanugi, J. Conrad, L. Costamante, G. Cotter, S. Cutini, V. D'Elia, C. D. Dermer, A. de Angelis, F. de Palma, A. De Rosa, S. W. Digel, E. d. C. e. Silva, P. S. Drell, R. Dubois, D. Dumora, L. Escande, C. Farnier, C. Favuzzi, S. J. Fegan, E. C. Ferrara, W. B. Focke, P. Fortin, M. Frailis, Y. Fukazawa, S. Funk, P. Fusco, F. Gargano, D. Gasparrini, N. Gehrels, S. Germani, B. Giebels, N. Giglietto, P. Giommi, F. Giordano, M. Giroletti, T. Glanzman, G. Godfrey, P. Grandi, I. A. Grenier, M.-H. Grondin, J. E. Grove, S. Guiriec, D. Hadasch, A. K. Harding, M. Hayashida, E. Hays, S. E. Healey, A. B. Hill, D. Horan, R. E. Hughes, G. Iafrate, R. Itoh, G. Jóhannesson, A. S. Johnson, R. P. Johnson, T. J. Johnson, W. N. Johnson, T. Kamae, H. Katagiri, J. Kataoka, N. Kawai, M. Kerr, J. Knödlseder, M. Kuss, J. Lande, L. Latronico, C. Lavalley, M. Lemoine-Goumard, M. Llena Garde, F. Longo, F. Loparco, B. Lott, M. N. Lovellette, P. Lubrano, G. M. Madejski, A. Makeev, G. Malaguti, E. Massaro, M. N. Mazziotta, W. McConville, J. E. McEnery, S. McGlynn, P. F. Michelson, W. Mitthumsiri, T. Mizuno, A. A. Moiseev, C. Monte, M. E. Monzani, A. Morselli, I. V. Moskalenko, S. Murgia, P. L. Nolan, J. P. Norris, E. Nuss, M. Ohno, T. Ohsugi, N. Omodei, E. Orlando, J. F. Ormes, M. Ozaki, D. Paneque, J. H. Panetta, D. Parent, V. Pelassa, M. Pepe, M. Pesce-Rollins, S. Piranomonte, F. Piron, T. A. Porter, S. Rainò, R. Rando, M. Razzano, A. Reimer, O. Reimer, T. Reposeur, J. Ripken, S. Ritz, A. Y. Rodriguez, R. W. Romani, M. Roth, F. Ryde, H. F.-W. Sadrozinski, D. Sanchez, A. Sander, P. M. Saz Parkinson, J. D. Scargle, C. Sgrò, M. S. Shaw, E. J. Siskind, P. D.

Smith, G. Spandre, P. Spinelli, J.-L. Starck, Ł. Stawarz, M. S. Strickman, D. J. Suson, H. Tajima, H. Takahashi, T. Takahashi, T. Tanaka, G. B. Taylor, J. B. Thayer, J. G. Thayer, D. J. Thompson, L. Tibaldo, D. F. Torres, G. Tosti, A. Tramacere, P. Ubertini, Y. Uchiyama, T. L. Usher, V. Vasileiou, N. Vilchez, M. Villata, V. Vitale, A. P. Waite, E. Wallace, P. Wang, B. L. Winer, K. S. Wood, Z. Yang, T. Ylinen, and M. Ziegler. The First Catalog of Active Galactic Nuclei Detected by the Fermi Large Area Telescope. *ApJ*, 715:429–457, May 2010.

[6] A. A. Abdo, M. Ackermann, M. Ajello, A. Allafort, W. B. Atwood, L. Baldini, J. Ballet, G. Barbiellini, M. G. Baring, D. Bastieri, B. M. Baughman, K. Bechtol, R. Bellazzini, B. Berenji, P. N. Bhat, R. D. Blandford, E. D. Bloom, E. Bonamente, A. W. Borgland, A. Bouvier, T. J. Brandt, J. Bregeon, A. Brez, M. S. Briggs, M. Brigida, P. Bruel, R. Buehler, T. H. Burnett, S. Buson, G. A. Caliandro, R. A. Cameron, P. A. Caraveo, S. Carrigan, J. M. Casandjian, E. Cavazzuti, C. Cecchi, Ö. Çelik, E. Charles, A. Chekhtman, A. W. Chen, C. C. Cheung, J. Chiang, S. Ciprini, R. Claus, J. Cohen-Tanugi, V. Connaughton, J. Conrad, L. Costamante, C. D. Dermer, A. de Angelis, F. de Palma, S. W. Digel, B. L. Dingus, E. d. C. e. Silva, P. S. Drell, R. Dubois, C. Favuzzi, S. J. Fegan, J. Finke, P. Fortin, Y. Fukazawa, S. Funk, P. Fusco, F. Gargano, D. Gasparrini, N. Gehrels, S. Germani, N. Giglietto, R. C. Gilmore, P. Giommi, F. Giordano, M. Giroletti, T. Glanzman, G. Godfrey, J. Granot, J. Greiner, I. A. Grenier, J. E. Grove, S. Guiriec, M. Gustafsson, D. Hadasch, M. Hayashida, E. Hays, D. Horan, R. E. Hughes, G. Jóhannesson, A. S. Johnson, R. P. Johnson, W. N. Johnson, T. Kamae, H. Katagiri, J. Kataoka, J. Knödlseder, D. Kocevski, M. Kuss, J. Lande, L. Latronico, S.-H. Lee, M. Llena Garde, F. Longo, F. Loparco, B. Lott, M. N. Lovellette, P. Lubrano, A. Makeev, M. N. Mazziotta, W. McConville, J. E. McEnery, S. McGlynn, J. Mehault, P. Mészáros, P. F. Michelson, T. Mizuno, A. A. Moiseev, C. Monte, M. E. Monzani, E. Moretti, A. Morselli, I. V. Moskalenko, S. Murgia, T. Nakamori, M. Naumann-Godo, P. L. Nolan, J. P. Norris, E. Nuss, M. Ohno, T. Ohsugi, A. Okumura, N. Omodei, E. Orlando, J. F. Ormes, M. Ozaki, D. Paneque, J. H. Panetta, D. Parent, V. Pelassa, M. Pepe, M. Pesce-Rollins, F. Piron, T. A. Porter, J. R. Primack, S. Rainò, R. Rando, M. Razzano, S. Razzaque, A. Reimer, O. Reimer, L. C. Reyes, J. Ripken, S. Ritz, R. W. Romani, M. Roth, H. F.-W. Sadrozinski, D. Sanchez, A. Sander, J. D. Scargle, T. L. Schalk, C. Sgrò, M. S. Shaw, E. J. Siskind, P. D. Smith, G. Spandre, P. Spinelli, F. W. Stecker, M. S. Strickman, D. J. Suson, H. Tajima, H. Takahashi, T. Takahashi, T. Tanaka, J. B. Thayer, J. G. Thayer, D. J. Thompson, L. Tibaldo, D. F. Torres, G. Tosti, A. Tramacere, Y. Uchiyama, T. L. Usher, J. Vandenbroucke, V. Vasileiou, N. Vilchez, V. Vitale, A. von Kienlin, A. P. Waite, P. Wang, C. Wilson-Hodge, B. L. Winer, K. S. Wood, R. Yamazaki, Z. Yang, T. Ylinen, and M. Ziegler. Fermi Large Area Telescope Constraints on the Gamma-ray Opacity of the Universe. *ApJ*, 723:1082–1096, Nov. 2010.

[7] A. A. Abdo, M. Ackermann, M. Ajello, A. Allafort, L. Baldini, J. Ballet, G. Barbiellini, D. Bastieri, R. Bellazzini, B. Berenji, R. D. Blandford, E. D. Bloom, E. Bonamente, A. W. Borgland, A. Bouvier, J. Bregeon, M. Brigida, P. Bruel, R. Buehler, S. Buson, G. A. Caliandro, R. A. Cameron, P. A. Caraveo, J. M. Casandjian, E. Cavazzuti, C. Cecchi, E. Charles, A. Chekhtman, C. C. Cheung, J. Chiang, S. Ciprini, R. Claus, J. Conrad, S. Cutini, F. D'Ammando, A. de Angelis, F. de Palma, C. D. Dermer, S. W. Digel, E. d. C. e. Silva, P. S. Drell, R. Dubois, D. Dumora, L. Escande, C. Favuzzi, S. J. Fegan, E. C. Ferrara, P. Fortin, Y. Fukazawa, P. Fusco, F. Gargano, D. Gasparrini, N. Gehrels, S. Germani, N. Giglietto, P. Giommi, F. Giordano, M. Giroletti, T. Glanzman, G. Godfrey, I. A. Grenier, J. E. Grove, S. Guiriec, D. Hadasch, M. Hayashida, E. Hays, D. Horan, R. Itoh, G. Jóhannesson, A. S. Johnson, T. Kamae, H. Katagiri, J. Kataoka, J. Knödlseder, M. Kuss, J. Lande, S. Larsson, L. Latronico, S.-H. Lee, F. Longo, F. Loparco, B. Lott, M. N. Lovellette, P. Lubrano, G. M. Madejski, A. Makeev, M. N. Mazziotta, W. McConville, J. E. McEnery, P. F. Michelson, W. Mitthumsiri, T. Mizuno, A. A. Moiseev, C. Monte, M. E. Monzani, A. Morselli, I. V. Moskalenko, S. Murgia, M. Naumann-Godo, S. Nishino, P. L. Nolan, J. P. Norris, E. Nuss, T. Ohsugi, A. Okumura, E. Orlando, J. F. Ormes, D. Paneque, V. Pelassa, M. Pesce-Rollins, M. Pierbattista, F. Piron, T. A. Porter, S. Rainò, R. Rando, S. Razzaque, A. Reimer, O. Reimer, S. Ritz, M. Roth, H. F.-W. Sadrozinski, D. Sanchez, J. D. Scargle, T. L. Schalk, C. Sgrò, E. J. Siskind, P. D. Smith, G. Spandre, P. Spinelli, M. S. Strickman, H. Takahashi, T. Takahashi, T. Tanaka, Y. Tanaka, J. G. Thayer, J. B. Thayer, D. J. Thompson, L. Tibaldo, D. F. Torres, G. Tosti, A. Tramacere, E. Troja, J. Vandenbroucke, V. Vasileiou, G. Vianello, N. Vilchez, V. Vitale, A. P. Waite, P. Wang, B. L. Winer, K. S. Wood, Z. Yang, and M. Ziegler. Fermi Gamma-ray Space Telescope Observations of the Gamma-ray Outburst from 3C454.3 in November 2010. *ApJ*, 733:L26, June 2011.

[8] A. A. Abdo, M. Ackermann, M. Ajello, K. Asano, L. Baldini, J. Ballet, G. Barbiellini, D. Bastieri, B. M. Baughman, K. Bechtol, R. Bellazzini, R. D. Blandford, E. D. Bloom, E. Bonamente, A. W. Borgland, J. Bregeon, A. Brez, M. Brigida, P. Bruel, T. H. Burnett, G. A. Caliandro, R. A. Cameron, P. A. Caraveo, J. M. Casandjian, E. Cavazzuti, C. Cecchi, A. Celotti, A. Chekhtman, C. C. Cheung, J. Chiang, S. Ciprini, R. Claus, J. Cohen-Tanugi, S. Colafrancesco, L. R. Cominsky, J. Conrad, L. Costamante, C. D. Dermer, A. de Angelis, F. de Palma, S. W. Digel, D. Donato, E. do Couto e Silva, P. S. Drell, R. Dubois, D. Dumora, C. Farnier, C. Favuzzi, J. Finke, W. B. Focke, M. Frailis, Y. Fukazawa, S. Funk, P. Fusco, F. Gargano, M. Georganopoulos, S. Germani, B. Giebels, N. Giglietto, F. Giordano, T. Glanzman, I. A. Grenier, M.-H. Grondin, J. E. Grove, L. Guillemot, S. Guiriec, Y. Hanabata, A. K. Harding, R. C. Hartman, M. Hayashida, E. Hays, R. E. Hughes, G. Jóhannesson, A. S. Johnson, R. P. Johnson, W. N. Johnson, M. Kadler, T. Kamae, Y. Kanai, H. Katagiri, J. Kataoka, N. Kawai, M. Kerr,

J. Knödlseder, F. Kuehn, M. Kuss, L. Latronico, M. Lemoine-Goumard, F. Longo, F. Loparco, B. Lott, M. N. Lovellette, P. Lubrano, G. M. Madejski, A. Makeev, M. N. Mazziotta, J. E. McEnery, C. Meurer, P. F. Michelson, W. Mitthumsiri, T. Mizuno, A. A. Moiseev, C. Monte, M. E. Monzani, A. Morselli, I. V. Moskalenko, S. Murgia, T. Nakamori, P. L. Nolan, J. P. Norris, E. Nuss, T. Ohsugi, N. Omodei, E. Orlando, J. F. Ormes, D. Paneque, J. H. Panetta, D. Parent, M. Pepe, M. Pesce-Rollins, F. Piron, T. A. Porter, S. Rainò, M. Razzano, A. Reimer, O. Reimer, T. Reposeur, S. Ritz, A. Y. Rodriguez, R. W. Romani, F. Ryde, H. F.-W. Sadrozinski, R. Sambruna, D. Sanchez, A. Sander, R. Sato, P. M. S. Parkinson, C. Sgrò, D. A. Smith, P. D. Smith, G. Spandre, P. Spinelli, J.-L. Starck, M. S. Strickman, A. W. Strong, D. J. Suson, H. Tajima, H. Takahashi, T. Takahashi, T. Tanaka, G. B. Taylor, J. G. Thayer, D. J. Thompson, D. F. Torres, G. Tosti, Y. Uchiyama, T. L. Usher, N. Vilchez, V. Vitale, A. P. Waite, K. S. Wood, T. Ylinen, M. Ziegler, H. D. Aller, M. F. Aller, K. I. Kellermann, Y. Y. Kovalev, Y. A. Kovalev, M. L. Lister, and A. B. Pushkarev. Fermi Discovery of Gamma-ray Emission from NGC 1275. *ApJ*, 699:31–39, July 2009.

[9] A. A. Abdo, M. Ackermann, M. Ajello, W. B. Atwood, M. Axelsson, L. Baldini, J. Ballet, D. L. Band, G. Barbiellini, D. Bastieri, and et al. Fermi/Large Area Telescope Bright Gamma-Ray Source List. *ApJS*, 183:46–66, July 2009.

[10] A. A. Abdo, M. Ackermann, M. Ajello, W. B. Atwood, M. Axelsson, L. Baldini, J. Ballet, G. Barbiellini, D. Bastieri, B. M. Baughman, K. Bechtol, R. Bellazzini, R. D. Blandford, E. D. Bloom, E. Bonamente, A. W. Borgland, A. Bouvier, J. Bregeon, A. Brez, M. Brigida, P. Bruel, T. H. Burnett, G. A. Caliandro, R. A. Cameron, P. A. Caraveo, J. M. Casandjian, E. Cavazzuti, C. Cecchi, E. Charles, A. Chekhtman, A. W. Chen, C. C. Cheung, J. Chiang, S. Ciprini, R. Claus, J. Cohen-Tanugi, S. Colafrancesco, W. Collmar, L. R. Cominsky, J. Conrad, L. Costamante, S. Cutini, C. D. Dermer, A. de Angelis, F. de Palma, S. W. Digel, E. do Couto e Silva, P. S. Drell, R. Dubois, D. Dumora, C. Farnier, C. Favuzzi, S. J. Fegan, E. C. Ferrara, J. Finke, W. B. Focke, L. Foschini, M. Frailis, L. Fuhrmann, Y. Fukazawa, S. Funk, P. Fusco, F. Gargano, D. Gasparrini, N. Gehrels, S. Germani, B. Giebels, N. Giglietto, P. Giommi, F. Giordano, M. Giroletti, T. Glanzman, G. Godfrey, I. A. Grenier, M.-H. Grondin, J. E. Grove, L. Guillemot, S. Guiriec, Y. Hanabata, A. K. Harding, R. C. Hartman, M. Hayashida, E. Hays, S. E. Healey, D. Horan, R. E. Hughes, G. Jóhannesson, A. S. Johnson, R. P. Johnson, T. J. Johnson, W. N. Johnson, M. Kadler, T. Kamae, H. Katagiri, J. Kataoka, M. Kerr, J. Knödlseder, M. L. Kocian, F. Kuehn, M. Kuss, J. Lande, L. Latronico, M. Lemoine-Goumard, F. Longo, F. Loparco, B. Lott, M. N. Lovellette, P. Lubrano, G. M. Madejski, A. Makeev, E. Massaro, M. N. Mazziotta, W. McConville, J. E. McEnery, S. McGlynn, C. Meurer, P. F. Michelson, W. Mitthumsiri, T. Mizuno, A. A. Moiseev, C. Monte, M. E. Monzani, E. Moretti, A. Morselli, I. V. Moskalenko, S. Murgia, P. L. Nolan, J. P. Norris, E. Nuss,

T. Ohsugi, N. Omodei, E. Orlando, J. F. Ormes, M. Ozaki, D. Paneque, J. H. Panetta, D. Parent, V. Pelassa, M. Pepe, M. Pesce-Rollins, F. Piron, T. A. Porter, S. Rainò, R. Rando, M. Razzano, S. Razzaque, A. Reimer, O. Reimer, T. Reposeur, L. C. Reyes, S. Ritz, L. S. Rochester, A. Y. Rodriguez, R. W. Romani, F. Ryde, H. F.-W. Sadrozinski, D. Sanchez, A. Sander, P. M. Saz Parkinson, J. D. Scargle, T. L. Schalk, A. Sellerholm, C. Sgrò, M. S. Shaw, D. A. Smith, P. D. Smith, G. Spandre, P. Spinelli, J.-L. Starck, M. S. Strickman, D. J. Suson, H. Tajima, H. Takahashi, T. Takahashi, T. Tanaka, G. B. Taylor, J. B. Thayer, J. G. Thayer, D. J. Thompson, L. Tibaldo, D. F. Torres, G. Tosti, A. Tramacere, Y. Uchiyama, T. L. Usher, N. Vilchez, M. Villata, V. Vitale, A. P. Waite, B. L. Winer, K. S. Wood, T. Ylinen, and M. Ziegler. Bright Active Galactic Nuclei Source List from the First Three Months of the Fermi Large Area Telescope All-Sky Survey. *ApJ*, 700:597–622, July 2009.

[11] A. A. Abdo, M. Ackermann, M. Ajello, W. B. Atwood, M. Axelsson, L. Baldini, J. Ballet, G. Barbiellini, D. Bastieri, K. Bechtol, R. Bellazzini, B. Berenji, R. D. Blandford, E. D. Bloom, E. Bonamente, A. W. Borgland, J. Bregeon, A. Brez, M. Brigida, P. Bruel, T. H. Burnett, G. A. Caliandro, R. A. Cameron, A. Cannon, P. A. Caraveo, J. M. Casandjian, E. Cavazzuti, C. Cecchi, Ö. Çelik, E. Charles, C. C. Cheung, J. Chiang, S. Ciprini, R. Claus, J. Cohen-Tanugi, S. Colafrancesco, J. Conrad, L. Costamante, S. Cutini, D. S. Davis, C. D. Dermer, A. de Angelis, F. de Palma, S. W. Digel, D. Donato, E. d. C. e. Silva, P. S. Drell, R. Dubois, D. Dumora, Y. Edmonds, C. Farnier, C. Favuzzi, S. J. Fegan, J. Finke, W. B. Focke, P. Fortin, M. Frailis, Y. Fukazawa, S. Funk, P. Fusco, F. Gargano, D. Gasparrini, N. Gehrels, M. Georganopoulos, S. Germani, B. Giebels, N. Giglietto, P. Giommi, F. Giordano, M. Giroletti, T. Glanzman, G. Godfrey, I. A. Grenier, M.-H. Grondin, J. E. Grove, L. Guillemot, S. Guiriec, Y. Hanabata, A. K. Harding, M. Hayashida, E. Hays, D. Horan, G. Jóhannesson, A. S. Johnson, R. P. Johnson, T. J. Johnson, W. N. Johnson, T. Kamae, H. Katagiri, J. Kataoka, N. Kawai, M. Kerr, J. Knödlseder, M. L. Kocian, M. Kuss, J. Lande, L. Latronico, M. Lemoine-Goumard, F. Longo, F. Loparco, B. Lott, M. N. Lovellette, P. Lubrano, G. M. Madejski, A. Makeev, M. N. Mazziotta, W. McConville, J. E. McEnery, C. Meurer, P. F. Michelson, W. Mitthumsiri, T. Mizuno, A. A. Moiseev, C. Monte, M. E. Monzani, A. Morselli, I. V. Moskalenko, S. Murgia, P. L. Nolan, J. P. Norris, E. Nuss, T. Ohsugi, N. Omodei, E. Orlando, J. F. Ormes, M. Ozaki, D. Paneque, J. H. Panetta, D. Parent, V. Pelassa, M. Pepe, M. Pesce-Rollins, F. Piron, T. A. Porter, S. Rainò, R. Rando, M. Razzano, A. Reimer, O. Reimer, T. Reposeur, S. Ritz, L. S. Rochester, A. Y. Rodriguez, R. W. Romani, M. Roth, F. Ryde, H. F.-W. Sadrozinski, R. Sambruna, D. Sanchez, A. Sander, P. M. Saz Parkinson, J. D. Scargle, C. Sgrò, M. S. Shaw, D. A. Smith, P. D. Smith, G. Spandre, P. Spinelli, M. S. Strickman, D. J. Suson, H. Tajima, H. Takahashi, T. Tanaka, G. B. Taylor, J. B. Thayer, D. J. Thompson, L. Tibaldo, D. F. Torres, G. Tosti, A. Tramacere, Y. Uchiyama, T. L. Usher, V. Vasileiou, N. Vilchez, A. P. Waite, P. Wang,

B. L. Winer, K. S. Wood, T. Ylinen, M. Ziegler, D. E. Harris, F. Massaro, and Ł. Stawarz. Fermi Large Area Telescope Gamma-Ray Detection of the Radio Galaxy M87. *ApJ*, 707:55–60, Dec. 2009.

[12] A. A. Abdo, M. Ackermann, M. Ajello, W. B. Atwood, M. Axelsson, L. Baldini, J. Ballet, G. Barbiellini, D. Bastieri, K. Bechtol, R. Bellazzini, B. Berenji, E. D. Bloom, E. Bonamente, A. W. Borgland, J. Bregeon, A. Brez, M. Brigida, P. Bruel, T. H. Burnett, G. A. Caliandro, R. A. Cameron, P. A. Caraveo, J. M. Casandjian, E. Cavazzuti, C. Cecchi, Ö. Çelik, E. Charles, A. Chekhtman, C. C. Cheung, J. Chiang, S. Ciprini, R. Claus, J. Cohen-Tanugi, J. Conrad, C. D. Dermer, A. de Angelis, F. de Palma, S. W. Digel, E. d. C. e. Silva, P. S. Drell, A. Drlica-Wagner, R. Dubois, D. Dumora, C. Farnier, C. Favuzzi, S. J. Fegan, W. B. Focke, L. Foschini, M. Frailis, Y. Fukazawa, S. Funk, P. Fusco, F. Gargano, D. Gasparrini, N. Gehrels, S. Germani, B. Giebels, N. Giglietto, F. Giordano, T. Glanzman, G. Godfrey, I. A. Grenier, M.-H. Grondin, J. E. Grove, L. Guillemot, S. Guiriec, Y. Hanabata, A. K. Harding, M. Hayashida, E. Hays, R. E. Hughes, G. Jóhannesson, A. S. Johnson, R. P. Johnson, W. N. Johnson, T. Kamae, H. Katagiri, J. Kataoka, N. Kawai, M. Kerr, J. Knödlseder, M. L. Kocian, M. Kuss, J. Lande, L. Latronico, M. Lemoine-Goumard, F. Longo, F. Loparco, B. Lott, M. N. Lovellette, P. Lubrano, G. M. Madejski, A. Makeev, M. N. Mazziotta, W. McConville, J. E. McEnery, C. Meurer, P. F. Michelson, W. Mitthumsiri, T. Mizuno, A. A. Moiseev, C. Monte, M. E. Monzani, A. Morselli, I. V. Moskalenko, S. Murgia, T. Nakamori, P. L. Nolan, J. P. Norris, E. Nuss, T. Ohsugi, N. Omodei, E. Orlando, J. F. Ormes, M. Ozaki, D. Paneque, J. H. Panetta, D. Parent, V. Pelassa, M. Pepe, M. Pesce-Rollins, F. Piron, T. A. Porter, S. Rainò, R. Rando, M. Razzano, A. Reimer, O. Reimer, T. Reposeur, S. Ritz, A. Y. Rodriguez, R. W. Romani, M. Roth, F. Ryde, H. F.-W. Sadrozinski, A. Sander, P. M. Saz Parkinson, J. D. Scargle, A. Sellerholm, C. Sgrò, M. S. Shaw, D. A. Smith, P. D. Smith, G. Spandre, P. Spinelli, M. S. Strickman, A. W. Strong, D. J. Suson, H. Takahashi, T. Tanaka, J. B. Thayer, J. G. Thayer, D. J. Thompson, L. Tibaldo, O. Tibolla, D. F. Torres, G. Tosti, A. Tramacere, Y. Uchiyama, T. L. Usher, V. Vasileiou, N. Vilchez, V. Vitale, A. P. Waite, P. Wang, B. L. Winer, K. S. Wood, T. Ylinen, M. Ziegler, and Fermi LAT Collaboration. Detection of Gamma-Ray Emission from the Starburst Galaxies M82 and NGC 253 with the Large Area Telescope on Fermi. *ApJ*, 709:L152–L157, Feb. 2010.

[13] A. A. Abdo, M. Ackermann, M. Ajello, L. Baldini, J. Ballet, G. Barbiellini, D. Bastieri, K. Bechtol, R. Bellazzini, B. Berenji, R. D. Blandford, E. D. Bloom, E. Bonamente, A. W. Borgland, A. Bouvier, T. J. Brandt, J. Bregeon, A. Brez, M. Brigida, P. Bruel, R. Buehler, T. H. Burnett, S. Buson, G. A. Caliandro, R. A. Cameron, A. Cannon, P. A. Caraveo, S. Carrigan, J. M. Casandjian, E. Cavazzuti, C. Cecchi, Ö. Çelik, A. Celotti, E. Charles, A. Chekhtman, A. W. Chen, C. C. Cheung, J. Chiang, S. Ciprini, R. Claus,

J. Cohen-Tanugi, S. Colafrancesco, J. Conrad, D. S. Davis, C. D. Dermer, A. de Angelis, F. de Palma, E. d. C. e. Silva, P. S. Drell, R. Dubois, C. Favuzzi, S. J. Fegan, E. C. Ferrara, P. Fortin, M. Frailis, Y. Fukazawa, P. Fusco, F. Gargano, D. Gasparrini, N. Gehrels, S. Germani, N. Giglietto, P. Giommi, F. Giordano, M. Giroletti, T. Glanzman, G. Godfrey, P. Grandi, I. A. Grenier, J. E. Grove, L. Guillemot, S. Guiriec, D. Hadasch, M. Hayashida, E. Hays, D. Horan, R. E. Hughes, M. S. Jackson, G. Jóhannesson, A. S. Johnson, W. N. Johnson, T. Kamae, H. Katagiri, J. Kataoka, J. Knödlseder, M. Kuss, J. Lande, L. Latronico, S.-H. Lee, M. Lemoine-Goumard, M. Llena Garde, F. Longo, F. Loparco, B. Lott, M. N. Lovellette, P. Lubrano, G. M. Madejski, A. Makeev, G. Malaguti, M. N. Mazziotta, W. McConville, J. E. McEnery, P. F. Michelson, G. Migliori, W. Mitthumsiri, T. Mizuno, C. Monte, M. E. Monzani, A. Morselli, I. V. Moskalenko, S. Murgia, M. Naumann-Godo, I. Nestoras, P. L. Nolan, J. P. Norris, E. Nuss, T. Ohsugi, A. Okumura, N. Omodei, E. Orlando, J. F. Ormes, D. Paneque, J. H. Panetta, D. Parent, V. Pelassa, M. Pepe, M. Persic, M. Pesce-Rollins, F. Piron, T. A. Porter, S. Rainò, R. Rando, M. Razzano, S. Razzaque, A. Reimer, O. Reimer, L. C. Reyes, M. Roth, H. F.-W. Sadrozinski, D. Sanchez, A. Sander, J. D. Scargle, C. Sgrò, E. J. Siskind, P. D. Smith, G. Spandre, P. Spinelli, Ł. Stawarz, F. W. Stecker, M. S. Strickman, D. J. Suson, H. Takahashi, T. Tanaka, J. B. Thayer, J. G. Thayer, D. J. Thompson, L. Tibaldo, D. F. Torres, E. Torresi, G. Tosti, A. Tramacere, Y. Uchiyama, T. L. Usher, J. Vandenbroucke, V. Vasileiou, N. Vilchez, M. Villata, V. Vitale, A. P. Waite, P. Wang, B. L. Winer, K. S. Wood, Z. Yang, T. Ylinen, and M. Ziegler. Fermi Large Area Telescope Observations of Misaligned Active Galactic Nuclei. *ApJ*, 720:912–922, Sept. 2010.

[14] A. U. Abeysekara, R. Alfaro, C. Alvarez, J. D. Álvarez, R. Arceo, J. C. Arteaga-Velázquez, H. A. Ayala Solares, A. S. Barber, B. M. Baughman, N. Bautista-Elivar, E. Belmont, S. Y. BenZvi, D. Berley, M. Bonilla Rosales, J. Braun, R. A. Caballero-Lopez, A. Carramiñana, M. Castillo, U. Cotti, J. Cotzomi, E. de la Fuente, C. De León, T. DeYoung, R. Diaz Hernandez, J. C. Diaz-Velez, B. L. Dingus, M. A. DuVernois, R. W. Ellsworth, A. Fernandez, D. W. Fiorino, N. Fraija, A. Galindo, J. L. Garcia-Luna, G. Garcia-Torales, F. Garfias, L. X. González, M. M. González, J. A. Goodman, V. Grabski, M. Gussert, Z. Hampel-Arias, C. M. Hui, P. Hüntemeyer, A. Imran, A. Iriarte, P. Karn, D. Kieda, G. J. Kunde, A. Lara, R. J. Lauer, W. H. Lee, D. Lennarz, H. León Vargas, E. C. Linares, J. T. Linnemann, M. Longo, R. Luna-García, A. Marinelli, O. Martinez, J. Martínez-Castro, J. A. J. Matthews, P. Miranda-Romagnoli, E. Moreno, M. Mostafá, J. Nava, L. Nellen, M. Newbold, R. Noriega-Papaqui, T. Oceguera-Becerra, B. Patricelli, R. Pelayo, E. G. Pérez-Pérez, J. Pretz, C. Rivière, J. Ryan, D. Rosa-González, H. Salazar, F. Salesa, A. Sandoval, E. Santos, M. Schneider, S. Silich, G. Sinnis, A. J. Smith, K. Sparks, R. W. Springer, I. Taboada, P. A. Toale, K. Tollefson, I. Torres, T. N. Ukwatta, L. Villaseñor, T. Weisgarber, S. Westerhoff, I. G. Wisher, J. Wood, G. B. Yodh, P. W. Younk, D. Zaborov, A. Zepeda, and

H. Zhou. Sensitivity of the high altitude water Cherenkov detector to sources of multi-TeV gamma rays. *Astroparticle Physics*, 50:26–32, Dec. 2013.

[15] A. Abramowski, F. Acero, F. Aharonian, A. G. Akhperjanian, G. Anton, A. Balzer, A. Barnacka, U. Barres de Almeida, Y. Becherini, J. Becker, and et al. The 2010 Very High Energy γ-Ray Flare and 10 Years of Multi-wavelength Observations of M 87. *ApJ*, 746:151, Feb. 2012.

[16] V. A. Acciari, E. Aliu, T. Arlen, M. Bautista, M. Beilicke, W. Benbow, S. M. Bradbury, J. H. Buckley, V. Bugaev, Y. Butt, and et al. Radio Imaging of the Very-High-Energy γ-Ray Emission Region in the Central Engine of a Radio Galaxy. *Science*, 325:444–, July 2009.

[17] V. A. Acciari, M. Beilicke, G. Blaylock, S. M. Bradbury, J. H. Buckley, V. Bugaev, Y. Butt, O. Celik, A. Cesarini, L. Ciupik, P. Cogan, P. Colin, W. Cui, M. K. Daniel, C. Duke, T. Ergin, A. D. Falcone, S. J. Fegan, J. P. Finley, G. Finnegan, P. Fortin, L. F. Fortson, K. Gibbs, G. H. Gillanders, J. Grube, R. Guenette, G. Gyuk, D. Hanna, E. Hays, J. Holder, D. Horan, S. B. Hughes, M. C. Hui, T. B. Humensky, A. Imran, P. Kaaret, M. Kertzman, D. B. Kieda, J. Kildea, A. Konopelko, H. Krawczynski, F. Krennrich, M. J. Lang, S. LeBohec, K. Lee, G. Maier, A. McCann, M. McCutcheon, J. Millis, P. Moriarty, R. Mukherjee, T. Nagai, R. A. Ong, D. Pandel, J. S. Perkins, M. Pohl, J. Quinn, K. Ragan, P. T. Reynolds, H. J. Rose, M. Schroedter, G. H. Sembroski, A. W. Smith, D. Steele, S. P. Swordy, A. Syson, J. A. Toner, L. Valcarcel, V. V. Vassiliev, S. P. Wakely, J. E. Ward, T. C. Weekes, A. Weinstein, R. J. White, D. A. Williams, S. A. Wissel, M. D. Wood, and B. Zitzer. Observation of Gamma-Ray Emission from the Galaxy M87 above 250 GeV with VERITAS. *ApJ*, 679:397–403, May 2008.

[18] M. Ackermann, M. Ajello, A. Allafort, E. Antolini, W. B. Atwood, M. Axelsson, L. Baldini, J. Ballet, G. Barbiellini, D. Bastieri, K. Bechtol, R. Bellazzini, B. Berenji, R. D. Blandford, E. D. Bloom, E. Bonamente, A. W. Borgland, E. Bottacini, A. Bouvier, J. Bregeon, M. Brigida, P. Bruel, R. Buehler, T. H. Burnett, S. Buson, G. A. Caliandro, R. A. Cameron, P. A. Caraveo, J. M. Casandjian, E. Cavazzuti, C. Cecchi, E. Charles, C. C. Cheung, J. Chiang, S. Ciprini, R. Claus, J. Cohen-Tanugi, J. Conrad, L. Costamante, S. Cutini, A. de Angelis, F. de Palma, C. D. Dermer, S. W. Digel, E. d. C. e. Silva, P. S. Drell, R. Dubois, L. Escande, C. Favuzzi, S. J. Fegan, E. C. Ferrara, J. Finke, W. B. Focke, P. Fortin, M. Frailis, Y. Fukazawa, S. Funk, P. Fusco, F. Gargano, D. Gasparrini, N. Gehrels, S. Germani, B. Giebels, N. Giglietto, P. Giommi, F. Giordano, M. Giroletti, T. Glanzman, G. Godfrey, I. A. Grenier, J. E. Grove, S. Guiriec, M. Gustafsson, D. Hadasch, M. Hayashida, E. Hays, S. E. Healey, D. Horan, X. Hou, R. E. Hughes, G. Iafrate, G. Jóhannesson, A. S. Johnson, W. N. Johnson, T. Kamae, H. Katagiri, J. Kataoka, J. Knödlseder, M. Kuss, J. Lande, S. Larsson, L. Latronico, F. Longo, F. Loparco, B. Lott,

M. N. Lovellette, P. Lubrano, G. M. Madejski, M. N. Mazziotta, W. McConville, J. E. McEnery, P. F. Michelson, W. Mitthumsiri, T. Mizuno, A. A. Moiseev, C. Monte, M. E. Monzani, E. Moretti, A. Morselli, I. V. Moskalenko, S. Murgia, T. Nakamori, M. Naumann-Godo, P. L. Nolan, J. P. Norris, E. Nuss, M. Ohno, T. Ohsugi, A. Okumura, N. Omodei, M. Orienti, E. Orlando, J. F. Ormes, M. Ozaki, D. Paneque, D. Parent, M. Pesce-Rollins, M. Pierbattista, S. Piranomonte, F. Piron, G. Pivato, T. A. Porter, S. Rainò, R. Rando, M. Razzano, S. Razzaque, A. Reimer, O. Reimer, S. Ritz, L. S. Rochester, R. W. Romani, M. Roth, D. A. Sanchez, C. Sbarra, J. D. Scargle, T. L. Schalk, C. Sgrò, M. S. Shaw, E. J. Siskind, G. Spandre, P. Spinelli, A. W. Strong, D. J. Suson, H. Tajima, H. Takahashi, T. Takahashi, T. Tanaka, J. G. Thayer, J. B. Thayer, D. J. Thompson, L. Tibaldo, M. Tinivella, D. F. Torres, G. Tosti, E. Troja, Y. Uchiyama, J. Vandenbroucke, V. Vasileiou, G. Vianello, V. Vitale, A. P. Waite, E. Wallace, P. Wang, B. L. Winer, D. L. Wood, K. S. Wood, and S. Zimmer. The Second Catalog of Active Galactic Nuclei Detected by the Fermi Large Area Telescope. *ApJ*, 743:171, Dec. 2011.

[19] M. Ackermann, M. Ajello, A. Allafort, L. Baldini, J. Ballet, G. Barbiellini, D. Bastieri, K. Bechtol, R. Bellazzini, B. Berenji, E. D. Bloom, E. Bonamente, A. W. Borgland, J. Bregeon, M. Brigida, P. Bruel, R. Buehler, S. Buson, G. A. Caliandro, R. A. Cameron, P. A. Caraveo, J. M. Casandjian, E. Cavazzuti, C. Cecchi, E. Charles, A. Chekhtman, C. C. Cheung, J. Chiang, S. Ciprini, R. Claus, J. Cohen-Tanugi, J. Conrad, S. Cutini, F. D'Ammando, A. de Angelis, F. de Palma, C. D. Dermer, E. d. C. e. Silva, P. S. Drell, A. Drlica-Wagner, T. Enoto, C. Favuzzi, S. J. Fegan, E. C. Ferrara, P. Fortin, Y. Fukazawa, P. Fusco, F. Gargano, D. Gasparrini, N. Gehrels, S. Germani, N. Giglietto, P. Giommi, F. Giordano, M. Giroletti, G. Godfrey, J. E. Grove, S. Guiriec, D. Hadasch, M. Hayashida, E. Hays, R. E. Hughes, G. Jóhannesson, A. S. Johnson, T. Kamae, H. Katagiri, J. Kataoka, J. Knödlseder, M. Kuss, J. Lande, M. Llena Garde, F. Longo, F. Loparco, B. Lott, M. N. Lovellette, P. Lubrano, G. M. Madejski, M. N. Mazziotta, P. F. Michelson, T. Mizuno, C. Monte, M. E. Monzani, A. Morselli, I. V. Moskalenko, S. Murgia, S. Nishino, J. P. Norris, E. Nuss, M. Ohno, T. Ohsugi, A. Okumura, E. Orlando, M. Ozaki, D. Paneque, M. Pesce-Rollins, M. Pierbattista, F. Piron, G. Pivato, T. A. Porter, S. Rainò, R. Rando, M. Razzano, A. Reimer, O. Reimer, S. Ritz, M. Roth, D. A. Sanchez, C. Sbarra, C. Sgrò, E. J. Siskind, G. Spandre, P. Spinelli, Ł. Stawarz, A. W. Strong, H. Takahashi, T. Takahashi, T. Tanaka, J. B. Thayer, D. J. Thompson, L. Tibaldo, M. Tinivella, D. F. Torres, G. Tosti, E. Troja, Y. Uchiyama, T. L. Usher, J. Vandenbroucke, V. Vasileiou, G. Vianello, V. Vitale, A. P. Waite, B. L. Winer, K. S. Wood, M. Wood, Z. Yang, and S. Zimmer. Search for Gamma-ray Emission from X-Ray-selected Seyfert Galaxies with Fermi-LAT. *ApJ*, 747:104, Mar. 2012.

[20] M. Ackermann, M. Ajello, A. Allafort, P. Schady, L. Baldini, J. Ballet, G. Barbiellini, D. Bastieri, R. Bellazzini, R. D. Blandford, E. D. Bloom, A. W. Bor-

gland, E. Bottacini, A. Bouvier, J. Bregeon, M. Brigida, P. Bruel, R. Buehler, S. Buson, G. A. Caliandro, R. A. Cameron, P. A. Caraveo, E. Cavazzuti, C. Cecchi, E. Charles, R. C. G. Chaves, A. Chekhtman, C. C. Cheung, J. Chiang, G. Chiaro, S. Ciprini, R. Claus, J. Cohen-Tanugi, J. Conrad, S. Cutini, F. D'Ammando, F. de Palma, C. D. Dermer, S. W. Digel, E. do Couto e Silva, A. Domínguez, P. S. Drell, A. Drlica-Wagner, C. Favuzzi, S. J. Fegan, W. B. Focke, A. Franckowiak, Y. Fukazawa, S. Funk, P. Fusco, F. Gargano, D. Gasparrini, N. Gehrels, S. Germani, N. Giglietto, F. Giordano, M. Giroletti, T. Glanzman, G. Godfrey, I. A. Grenier, J. E. Grove, S. Guiriec, M. Gustafsson, D. Hadasch, M. Hayashida, E. Hays, M. S. Jackson, T. Jogler, J. Kataoka, J. Knödlseder, M. Kuss, J. Lande, S. Larsson, L. Latronico, F. Longo, F. Loparco, M. N. Lovellette, P. Lubrano, M. N. Mazziotta, J. E. McEnery, J. Mehault, P. F. Michelson, T. Mizuno, C. Monte, M. E. Monzani, A. Morselli, I. V. Moskalenko, S. Murgia, A. Tramacere, E. Nuss, J. Greiner, M. Ohno, T. Ohsugi, N. Omodei, M. Orienti, E. Orlando, J. F. Ormes, D. Paneque, J. S. Perkins, M. Pesce-Rollins, F. Piron, G. Pivato, T. A. Porter, S. Rainò, R. Rando, M. Razzano, S. Razzaque, A. Reimer, O. Reimer, L. C. Reyes, S. Ritz, A. Rau, C. Romoli, M. Roth, M. Sánchez-Conde, D. A. Sanchez, J. D. Scargle, C. Sgrò, E. J. Siskind, G. Spandre, P. Spinelli, Ł. Stawarz, D. J. Suson, H. Takahashi, T. Tanaka, J. G. Thayer, D. J. Thompson, L. Tibaldo, M. Tinivella, D. F. Torres, G. Tosti, E. Troja, T. L. Usher, J. Vandenbroucke, V. Vasileiou, G. Vianello, V. Vitale, A. P. Waite, B. L. Winer, K. S. Wood, and M. Wood. The Imprint of the Extragalactic Background Light in the Gamma-Ray Spectra of Blazars. *Science*, 338:1190–, Nov. 2012.

[21] J. K. Adelman-McCarthy, M. A. Agüeros, S. S. Allam, C. Allende Prieto, K. S. J. Anderson, S. F. Anderson, J. Annis, N. A. Bahcall, C. A. L. Bailer-Jones, I. K. Baldry, J. C. Barentine, B. A. Bassett, A. C. Becker, T. C. Beers, E. F. Bell, A. A. Berlind, M. Bernardi, M. R. Blanton, J. J. Bochanski, W. N. Boroski, J. Brinchmann, J. Brinkmann, R. J. Brunner, T. Budavári, S. Carliles, M. A. Carr, F. J. Castander, D. Cinabro, R. J. Cool, K. R. Covey, I. Csabai, C. E. Cunha, J. R. A. Davenport, B. Dilday, M. Doi, D. J. Eisenstein, M. L. Evans, X. Fan, D. P. Finkbeiner, S. D. Friedman, J. A. Frieman, M. Fukugita, B. T. Gänsicke, E. Gates, B. Gillespie, K. Glazebrook, J. Gray, E. K. Grebel, J. E. Gunn, V. K. Gurbani, P. B. Hall, P. Harding, M. Harvanek, S. L. Hawley, J. Hayes, T. M. Heckman, J. S. Hendry, R. B. Hindsley, C. M. Hirata, C. J. Hogan, D. W. Hogg, J. B. Hyde, S.-i. Ichikawa, Ž. Ivezić, S. Jester, J. A. Johnson, A. M. Jorgensen, M. Jurić, S. M. Kent, R. Kessler, S. J. Kleinman, G. R. Knapp, R. G. Kron, J. Krzesinski, N. Kuropatkin, D. Q. Lamb, H. Lampeitl, S. Lebedeva, Y. S. Lee, R. F. Leger, S. Lépine, M. Lima, H. Lin, D. C. Long, C. P. Loomis, J. Loveday, R. H. Lupton, O. Malanushenko, V. Malanushenko, R. Mandelbaum, B. Margon, J. P. Marriner, D. Martínez-Delgado, T. Matsubara, P. M. McGehee, T. A. McKay, A. Meiksin, H. L. Morrison, J. A. Munn, R. Nakajima, E. H. Neilsen, Jr., H. J. Newberg, R. C.

Nichol, T. Nicinski, M. Nieto-Santisteban, A. Nitta, S. Okamura, R. Owen, H. Oyaizu, N. Padmanabhan, K. Pan, C. Park, J. Peoples, Jr., J. R. Pier, A. C. Pope, N. Purger, M. J. Raddick, P. Re Fiorentin, G. T. Richards, M. W. Richmond, A. G. Riess, H.-W. Rix, C. M. Rockosi, M. Sako, D. J. Schlegel, D. P. Schneider, M. R. Schreiber, A. D. Schwope, U. Seljak, B. Sesar, E. Sheldon, K. Shimasaku, T. Sivarani, J. A. Smith, S. A. Snedden, M. Steinmetz, M. A. Strauss, M. SubbaRao, Y. Suto, A. S. Szalay, I. Szapudi, P. Szkody, M. Tegmark, A. R. Thakar, C. A. Tremonti, D. L. Tucker, A. Uomoto, D. E. Vanden Berk, J. Vandenberg, S. Vidrih, M. S. Vogeley, W. Voges, N. P. Vogt, Y. Wadadekar, D. H. Weinberg, A. A. West, S. D. M. White, B. C. Wilhite, B. Yanny, D. R. Yocum, D. G. York, I. Zehavi, and D. B. Zucker. The Sixth Data Release of the Sloan Digital Sky Survey. *ApJS*, 175:297–313, Apr. 2008.

[22] I. Agudo, J. L. Gómez, C. Casadio, T. V. Cawthorne, and M. Roca-Sogorb. A Recollimation Shock 80 mas from the Core in the Jet of the Radio Galaxy 3C 120: Observational Evidence and Modeling. *ApJ*, 752:92, June 2012.

[23] F. Aharonian, A. Akhperjanian, M. Beilicke, K. Bernlöhr, H.-G. Börst, H. Bojahr, O. Bolz, T. Coarasa, J. L. Contreras, J. Cortina, S. Denninghoff, M. V. Fonseca, M. Girma, N. Götting, G. Heinzelmann, G. Hermann, A. Heusler, W. Hofmann, D. Horns, I. Jung, R. Kankanyan, M. Kestel, A. Kohnle, A. Konopelko, H. Kornmeyer, D. Kranich, H. Lampeitl, M. Lopez, E. Lorenz, F. Lucarelli, O. Mang, H. Meyer, R. Mirzoyan, A. Moralejo, E. Ona-Wilhelmi, M. Panter, A. Plyasheshnikov, G. Pühlhofer, R. de los Reyes, W. Rhode, J. Ripken, G. Rowell, V. Sahakian, M. Samorski, M. Schilling, M. Siems, D. Sobzynska, W. Stamm, M. Tluczykont, V. Vitale, H. J. Völk, C. A. Wiedner, and W. Wittek. Is the giant radio galaxy M 87 a TeV gamma-ray emitter? *A&A*, 403:L1–L5, May 2003.

[24] F. Aharonian, A. G. Akhperjanian, A. R. Bazer-Bachi, M. Beilicke, W. Benbow, D. Berge, K. Bernlöhr, C. Boisson, O. Bolz, V. Borrel, I. Braun, F. Breitling, A. M. Brown, P. M. Chadwick, L.-M. Chounet, R. Cornils, L. Costamante, B. Degrange, H. J. Dickinson, A. Djannati-Ataï, L. O. Drury, G. Dubus, D. Emmanoulopoulos, P. Espigat, F. Feinstein, G. Fontaine, Y. Fuchs, S. Funk, Y. A. Gallant, B. Giebels, S. Gillessen, J. F. Glicenstein, P. Goret, C. Hadjichristidis, D. Hauser, M. Hauser, G. Heinzelmann, G. Henri, G. Hermann, J. A. Hinton, W. Hofmann, M. Holleran, D. Horns, A. Jacholkowska, O. C. de Jager, B. Khélifi, S. Klages, N. Komin, A. Konopelko, I. J. Latham, R. Le Gallou, A. Lemière, M. Lemoine-Goumard, N. Leroy, T. Lohse, J. M. Martin, O. Martineau-Huynh, A. Marcowith, C. Masterson, T. J. L. McComb, M. de Naurois, S. J. Nolan, A. Noutsos, K. J. Orford, J. L. Osborne, M. Ouchrif, M. Panter, G. Pelletier, S. Pita, G. Pühlhofer, M. Punch, B. C. Raubenheimer, M. Raue, J. Raux, S. M. Rayner, A. Reimer, O. Reimer, J. Ripken, L. Rob, L. Rolland, G. Rowell, V. Sahakian, L. Saugé, S. Schlenker, R. Schlickeiser, C. Schuster, U. Schwanke, M. Siewert, H. Sol, D. Spangler, R. Steenkamp, C. Stegmann, J.-P. Tavernet, R. Terrier, C. G.

Théoret, M. Tluczykont, C. van Eldik, G. Vasileiadis, C. Venter, P. Vincent, H. J. Völk, and S. J. Wagner. A low level of extragalactic background light as revealed by γ-rays from blazars. *Nature*, 440:1018–1021, Apr. 2006.

[25] F. Aharonian, A. G. Akhperjanian, A. R. Bazer-Bachi, M. Beilicke, W. Benbow, D. Berge, K. Bernlöhr, C. Boisson, O. Bolz, V. Borrel, I. Braun, A. M. Brown, R. Bühler, I. Büsching, S. Carrigan, P. M. Chadwick, L.-M. Chounet, G. Coignet, R. Cornils, L. Costamante, B. Degrange, H. J. Dickinson, A. Djannati-Ataï, L. O. Drury, G. Dubus, K. Egberts, D. Emmanoulopoulos, P. Espigat, F. Feinstein, E. Ferrero, A. Fiasson, G. Fontaine, S. Funk, S. Funk, M. Füßling, Y. A. Gallant, B. Giebels, J. F. Glicenstein, P. Goret, C. Hadjichristidis, D. Hauser, M. Hauser, G. Heinzelmann, G. Henri, G. Hermann, J. A. Hinton, A. Hoffmann, W. Hofmann, M. Holleran, S. Hoppe, D. Horns, A. Jacholkowska, O. C. de Jager, E. Kendziorra, M. Kerschhaggl, B. Khélifi, N. Komin, A. Konopelko, K. Kosack, G. Lamanna, I. J. Latham, R. Le Gallou, A. Lemière, M. Lemoine-Goumard, J.-P. Lenain, T. Lohse, J. M. Martin, O. Martineau-Huynh, A. Marcowith, C. Masterson, G. Maurin, T. J. L. McComb, E. Moulin, M. de Naurois, D. Nedbal, S. J. Nolan, A. Noutsos, K. J. Orford, J. L. Osborne, M. Ouchrif, M. Panter, G. Pelletier, S. Pita, G. Pühlhofer, M. Punch, S. Ranchon, B. C. Raubenheimer, M. Raue, S. M. Rayner, A. Reimer, J. Ripken, L. Rob, L. Rolland, S. Rosier-Lees, G. Rowell, V. Sahakian, A. Santangelo, L. Saugé, S. Schlenker, R. Schlickeiser, R. Schröder, U. Schwanke, S. Schwarzburg, S. Schwemmer, A. Shalchi, H. Sol, D. Spangler, F. Spanier, R. Steenkamp, C. Stegmann, G. Superina, P. H. Tam, J.-P. Tavernet, R. Terrier, M. Tluczykont, C. van Eldik, G. Vasileiadis, C. Venter, J. P. Vialle, P. Vincent, H. J. Völk, S. J. Wagner, and M. Ward. Fast Variability of Tera-Electron Volt γ Rays from the Radio Galaxy M87. *Science*, 314:1424–1427, Dec. 2006.

[26] F. A. Aharonian. The Project of the HEGRA Imaging Cherenkov Telescope System: Status and Motivations. In R. C. Lamb, editor, *Towards a Major Atmospheric Cherenkov Detector – II for TeV Astro/Particle Physics*, page 81, 1993.

[27] F. A. Aharonian, D. Khangulyan, and L. Costamante. Formation of hard very high energy gamma-ray spectra of blazars due to internal photon-photon absorption. *MNRAS*, 387:1206–1214, July 2008.

[28] M. Ajello, L. Costamante, R. M. Sambruna, N. Gehrels, J. Chiang, A. Rau, A. Escala, J. Greiner, J. Tueller, J. V. Wall, and R. F. Mushotzky. The Evolution of Swift/BAT Blazars and the Origin of the MeV Background. *ApJ*, 699:603–625, July 2009.

[29] M. Ajello, A. Rau, J. Greiner, G. Kanbach, M. Salvato, A. W. Strong, S. D. Barthelmy, N. Gehrels, C. B. Markwardt, and J. Tueller. The Swift BAT X-Ray Survey. III. X-Ray Spectra and Statistical Properties. *ApJ*, 673:96–113, Jan. 2008.

[30] J. Albert, E. Aliu, H. Anderhub, L. A. Antonelli, P. Antoranz, M. Backes, C. Baixeras, J. A. Barrio, H. Bartko, D. Bastieri, J. K. Becker, W. Bednarek, K. Berger, E. Bernardini, C. Bigongiari, A. Biland, R. K. Bock, G. Bonnoli, P. Bordas, V. Bosch-Ramon, T. Bretz, I. Britvitch, M. Camara, E. Carmona, A. Chilingarian, S. Commichau, J. L. Contreras, J. Cortina, M. T. Costado, S. Covino, V. Curtef, F. Dazzi, A. De Angelis, E. De Cea del Pozo, R. de los Reyes, B. De Lotto, M. De Maria, F. De Sabata, C. Delgado Mendez, A. Dominguez, D. Dorner, M. Doro, M. Errando, M. Fagiolini, D. Ferenc, E. Fernández, R. Firpo, M. V. Fonseca, L. Font, N. Galante, R. J. García López, M. Garczarczyk, M. Gaug, F. Goebel, M. Hayashida, A. Herrero, D. Höhne, J. Hose, C. C. Hsu, S. Huber, T. Jogler, D. Kranich, A. La Barbera, A. Laille, E. Leonardo, E. Lindfors, S. Lombardi, F. Longo, M. López, E. Lorenz, P. Majumdar, G. Maneva, N. Mankuzhiyil, K. Mannheim, L. Maraschi, M. Mariotti, M. Martínez, D. Mazin, M. Meucci, M. Meyer, J. M. Miranda, R. Mirzoyan, S. Mizobuchi, M. Moles, A. Moralejo, D. Nieto, K. Nilsson, J. Ninkovic, N. Otte, I. Oya, M. Panniello, R. Paoletti, J. M. Paredes, M. Pasanen, D. Pascoli, F. Pauss, R. G. Pegna, M. A. Perez-Torres, M. Persic, L. Peruzzo, A. Piccioli, F. Prada, E. Prandini, N. Puchades, A. Raymers, W. Rhode, M. Ribó, J. Rico, M. Rissi, A. Robert, S. Rügamer, A. Saggion, T. Y. Saito, M. Salvati, M. Sanchez-Conde, P. Sartori, K. Satalecka, V. Scalzotto, V. Scapin, T. Schweizer, M. Shayduk, K. Shinozaki, S. N. Shore, N. Sidro, A. Sierpowska-Bartosik, A. Sillanpää, D. Sobczynska, F. Spanier, A. Stamerra, L. S. Stark, L. Takalo, F. Tavecchio, P. Temnikov, D. Tescaro, M. Teshima, M. Tluczykont, D. F. Torres, N. Turini, H. Vankov, A. Venturini, V. Vitale, R. M. Wagner, W. Wittek, V. Zabalza, F. Zandanel, R. Zanin, and J. Zapatero. Very High Energy Gamma-Ray Observations of Strong Flaring Activity in M87 in 2008 February. *ApJ*, 685:L23–L26, Sept. 2008.

[31] J. Aleksić, E. A. Alvarez, L. A. Antonelli, P. Antoranz, M. Asensio, M. Backes, U. Barres de Almeida, J. A. Barrio, D. Bastieri, J. Becerra González, W. Bednarek, K. Berger, E. Bernardini, A. Biland, O. Blanch, R. K. Bock, A. Boller, G. Bonnoli, D. Borla Tridon, T. Bretz, A. Cañellas, E. Carmona, A. Carosi, P. Colin, E. Colombo, J. L. Contreras, J. Cortina, L. Cossio, S. Covino, P. da Vela, F. Dazzi, A. de Angelis, G. de Caneva, E. de Cea Del Pozo, B. de Lotto, C. Delgado Mendez, A. Diago Ortega, M. Doert, A. Domínguez, D. Dominis Prester, D. Dorner, M. Doro, D. Eisenacher, D. Elsaesser, D. Ferenc, M. V. Fonseca, L. Font, C. Fruck, R. J. García López, M. Garczarczyk, D. Garrido, G. Giavitto, N. Godinović, S. R. Gozzini, D. Hadasch, D. Häfner, A. Herrero, D. Hildebrand, D. Höhne-Mönch, J. Hose, D. Hrupec, B. Huber, T. Jogler, V. Kadenius, H. Kellermann, S. Klepser, T. Krähenbühl, J. Krause, A. La Barbera, D. Lelas, E. Leonardo, N. Lewandowska, E. Lindfors, S. Lombardi, M. López, R. López-Coto, A. López-Oramas, E. Lorenz, M. Makariev, G. Maneva, N. Mankuzhiyil, K. Mannheim, L. Maraschi, M. Mariotti, M. Martínez, D. Mazin, M. Meucci,

J. M. Miranda, R. Mirzoyan, J. Moldón, A. Moralejo, P. Munar-Adrover, A. Niedzwiecki, D. Nieto, K. Nilsson, N. Nowak, R. Orito, S. Paiano, D. Paneque, R. Paoletti, S. Pardo, J. M. Paredes, S. Partini, M. A. Perez-Torres, M. Persic, L. Peruzzo, M. Pilia, J. Pochon, F. Prada, P. G. Prada Moroni, E. Prandini, I. Puerto Gimenez, I. Puljak, I. Reichardt, R. Reinthal, W. Rhode, M. Ribó, J. Rico, S. Rügamer, A. Saggion, K. Saito, T. Y. Saito, M. Salvati, K. Satalecka, V. Scalzotto, V. Scapin, C. Schultz, T. Schweizer, M. Shayduk, S. N. Shore, A. Sillanpää, J. Sitarek, I. Snidaric, D. Sobczynska, F. Spanier, S. Spiro, V. Stamatescu, A. Stamerra, B. Steinke, J. Storz, N. Strah, S. Sun, T. Surić, L. Takalo, H. Takami, F. Tavecchio, P. Temnikov, T. Terzić, D. Tescaro, M. Teshima, O. Tibolla, D. F. Torres, A. Treves, M. Uellenbeck, P. Vogler, R. M. Wagner, Q. Weitzel, V. Zabalza, F. Zandanel, R. Zanin, C. Pfrommer, and A. Pinzke. Detection of very-high energy γ-ray emission from ¡ASTROBJ¿NGC 1275¡/ASTROBJ¿ by the MAGIC telescopes. *A&A*, 539:L2, Mar. 2012.

[32] J. Aleksić, E. A. Alvarez, L. A. Antonelli, P. Antoranz, M. Asensio, M. Backes, J. A. Barrio, D. Bastieri, J. Becerra González, W. Bednarek, A. Berdyugin, K. Berger, E. Bernardini, A. Biland, O. Blanch, R. K. Bock, A. Boller, G. Bonnoli, D. Borla Tridon, I. Braun, T. Bretz, A. Cañellas, E. Carmona, A. Carosi, P. Colin, E. Colombo, J. L. Contreras, J. Cortina, L. Cossio, S. Covino, F. Dazzi, A. de Angelis, G. de Caneva, E. de Cea Del Pozo, B. de Lotto, C. Delgado Mendez, A. Diago Ortega, M. Doert, A. Domínguez, D. Dominis Prester, D. Dorner, M. Doro, D. Elsaesser, D. Ferenc, M. V. Fonseca, L. Font, C. Fruck, R. J. García López, M. Garczarczyk, D. Garrido, G. Giavitto, N. Godinović, D. Hadasch, D. Häfner, A. Herrero, D. Hildebrand, D. Höhne-Mönch, J. Hose, D. Hrupec, B. Huber, T. Jogler, H. Kellermann, S. Klepser, T. Krähenbühl, J. Krause, A. La Barbera, D. Lelas, E. Leonardo, E. Lindfors, S. Lombardi, M. López, A. López-Oramas, E. Lorenz, M. Makariev, G. Maneva, N. Mankuzhiyil, K. Mannheim, L. Maraschi, M. Mariotti, M. Martínez, D. Mazin, M. Meucci, J. M. Miranda, R. Mirzoyan, H. Miyamoto, J. Moldón, A. Moralejo, P. Munar-Adrover, D. Nieto, K. Nilsson, R. Orito, I. Oya, D. Paneque, R. Paoletti, S. Pardo, J. M. Paredes, S. Partini, M. Pasanen, F. Pauss, M. A. Perez-Torres, M. Persic, L. Peruzzo, M. Pilia, J. Pochon, F. Prada, P. G. Prada Moroni, E. Prandini, I. Puljak, I. Reichardt, R. Reinthal, W. Rhode, M. Ribó, J. Rico, S. Rügamer, A. Saggion, K. Saito, T. Y. Saito, M. Salvati, K. Satalecka, V. Scalzotto, V. Scapin, C. Schultz, T. Schweizer, M. Shayduk, S. N. Shore, A. Sillanpää, J. Sitarek, I. Snidaric, D. Sobczynska, F. Spanier, S. Spiro, V. Stamatescu, A. Stamerra, B. Steinke, J. Storz, N. Strah, T. Surić, L. Takalo, H. Takami, F. Tavecchio, P. Temnikov, T. Terzić, D. Tescaro, M. Teshima, O. Tibolla, D. F. Torres, A. Treves, M. Uellenbeck, H. Vankov, P. Vogler, R. M. Wagner, Q. Weitzel, V. Zabalza, F. Zandanel, and R. Zanin. Performance of the MAGIC stereo system obtained with Crab Nebula data. *Astroparticle Physics*, 35:435–448, Feb. 2012.

[33] J. Aleksić, L. A. Antonelli, P. Antoranz, M. Backes, J. A. Barrio, D. Bastieri, J. Becerra González, W. Bednarek, A. Berdyugin, K. Berger, E. Bernardini, A. Biland, O. Blanch, R. K. Bock, A. Boller, G. Bonnoli, D. Borla Tridon, I. Braun, T. Bretz, A. Cañellas, E. Carmona, A. Carosi, P. Colin, E. Colombo, J. L. Contreras, J. Cortina, L. Cossio, S. Covino, F. Dazzi, A. De Angelis, E. De Cea del Pozo, B. De Lotto, C. Delgado Mendez, A. Diago Ortega, M. Doert, A. Domínguez, D. Dominis Prester, D. Dorner, M. Doro, D. Elsaesser, D. Ferenc, M. V. Fonseca, L. Font, C. Fruck, R. J. García López, M. Garczarczyk, D. Garrido, G. Giavitto, N. Godinović, D. Hadasch, D. Häfner, A. Herrero, D. Hildebrand, D. Höhne-Mönch, J. Hose, D. Hrupec, B. Huber, T. Jogler, S. Klepser, T. Krähenbühl, J. Krause, A. La Barbera, D. Lelas, E. Leonardo, E. Lindfors, S. Lombardi, M. López, E. Lorenz, M. Makariev, G. Maneva, N. Mankuzhiyil, K. Mannheim, L. Maraschi, M. Mariotti, M. Martínez, D. Mazin, M. Meucci, J. M. Miranda, R. Mirzoyan, H. Miyamoto, J. Moldón, A. Moralejo, D. Nieto, K. Nilsson, R. Orito, I. Oya, D. Paneque, R. Paoletti, S. Pardo, J. M. Paredes, S. Partini, M. Pasanen, F. Pauss, M. A. Perez-Torres, M. Persic, L. Peruzzo, M. Pilia, J. Pochon, F. Prada, P. G. Prada Moroni, E. Prandini, I. Puljak, I. Reichardt, R. Reinthal, W. Rhode, M. Ribó, J. Rico, S. Rügamer, A. Saggion, K. Saito, T. Y. Saito, M. Salvati, K. Satalecka, V. Scalzotto, V. Scapin, C. Schultz, T. Schweizer, M. Shayduk, S. N. Shore, A. Sillanpää, J. Sitarek, D. Sobczynska, F. Spanier, S. Spiro, A. Stamerra, B. Steinke, J. Storz, N. Strah, T. Surić, L. Takalo, F. Tavecchio, P. Temnikov, T. Terzić, D. Tescaro, M. Teshima, M. Thom, O. Tibolla, D. F. Torres, A. Treves, H. Vankov, P. Vogler, R. M. Wagner, Q. Weitzel, V. Zabalza, F. Zandanel, R. Zanin, MAGIC Collaboration, Y. T. Tanaka, D. L. Wood, and S. Buson. MAGIC Discovery of Very High Energy Emission from the FSRQ PKS 1222+21. *ApJ*, 730:L8, Mar. 2011.

[34] D. R. Altschuler and J. F. C. Wardle. Observations of the flux density and linear polarization of compact extragalactic radio sources at 3.7- and 11.1-cm wavelength. *MmRAS*, 82:1–67, 1976.

[35] R. R. J. Antonucci and J. S. Miller. Spectropolarimetry and the nature of NGC 1068. *ApJ*, 297:621–632, Oct. 1985.

[36] R. Atkins, W. Benbow, D. Berley, E. Blaufuss, J. Bussons, D. G. Coyne, R. S. Delay, T. De Young, B. L. Dingus, D. E. Dorfan, R. W. Ellsworth, A. Falcone, L. Fleysher, R. Fleysher, G. Gisler, M. M. Gonzalez, J. A. Goodman, T. J. Haines, E. Hays, C. M. Hoffman, L. A. Kelley, R. W. Laird, J. McCullough, J. E. McEnery, R. S. Miller, A. I. Mincer, M. F. Morales, P. Nemethy, D. Noyes, J. M. Ryan, F. W. Samuelson, M. Schneider, B. Shen, A. Shoup, G. Sinnis, A. J. Smith, G. W. Sullivan, O. T. Tumer, K. Wang, M. Wascko, D. A. Williams, S. Westerhoff, M. E. Wilson, X. Xu, and G. B. Yodh. Observation of TeV Gamma Rays from the Crab Nebula with Milagro Using a New Background Rejection Technique. *ApJ*, 595:803–811, Oct. 2003.

[37] W. B. Atwood, A. A. Abdo, M. Ackermann, W. Althouse, B. Anderson, M. Axelsson, L. Baldini, J. Ballet, D. L. Band, G. Barbiellini, and et al. The Large Area Telescope on the Fermi Gamma-Ray Space Telescope Mission. *ApJ*, 697:1071–1102, June 2009.

[38] W. B. Atwood, J. A. Hernando, M. Hirayama, R. P. Johnson, W. Kröger, and H. F.-W. Sadrozinski. The silicon tracker/converter for the gamma-ray large area space telescope. *Nuclear Instruments and Methods in Physics Research A*, 435:224–232, Oct. 1999.

[39] P. Augusto, J. I. Gonzalez-Serrano, I. Perez-Fournon, and P. N. Wilkinson. Flat-spectrum symmetric objects with ˜1kpc sizes - I. The candidates. *MNRAS*, 368:1411–1428, May 2006.

[40] L. Baldini, A. Brez, T. Himel, M. Hirayama, R. Johnson, W. Kroeger, L. Latronico, M. Minuti, D. Nelson, R. Rando, H.-W. Sadrozinski, C. Sgro, G. Spandre, E. Spencer, M. Sugizaki, H. Tajima, J. Cohen-Tanugi, and M. Ziegler. The silicon tracker readout electronics of the gamma-ray large area space telescope. *Nuclear Science, IEEE Transactions on*, 53(2):466 – 473, april 2006.

[41] M. Baloković, A. Comastri, F. A. Harrison, D. M. Alexander, D. R. Ballantyne, F. E. Bauer, S. E. Boggs, W. N. Brandt, M. Brightman, F. E. Christensen, W. W. Craig, A. Del Moro, P. Gandhi, C. J. Hailey, M. Koss, G. B. Lansbury, B. Luo, G. M. Madejski, A. Marinucci, G. Matt, C. B. Markwardt, S. Puccetti, C. S. Reynolds, G. Risaliti, E. Rivers, D. Stern, D. J. Walton, and W. W. Zhang. The NuSTAR View of Nearby Compton-thick AGN: The Cases of NGC 424, NGC 1320 and IC 2560. *ArXiv e-prints*, Aug. 2014.

[42] S. A. Baum, C. P. O'Dea, D. W. Murphy, and A. G. de Bruyn. 0108 + 388 - A compact double source with surprising properties. *A&A*, 232:19–26, June 1990.

[43] M. C. Begelman. *Baby Cygnus A's*, page 209. 1996.

[44] M. C. Begelman. Young radio galaxies and their environments. In H. J. A. Röttgering, P. N. Best, and M. D. Lehnert, editors, *The Most Distant Radio Galaxies*, page 173, 1999.

[45] A. R. Bell. The acceleration of cosmic rays in shock fronts. I. *MNRAS*, 182:147–156, Jan. 1978.

[46] A. R. Bell. The acceleration of cosmic rays in shock fronts. II. *MNRAS*, 182:443–455, Feb. 1978.

[47] R. Bellazzini, F. Angelini, R. Bagagli, L. Baldini, A. Brez, M. Ceccanti, J. Cohen Tanugi, M. Kuss, L. Latronico, M. M. Massai, M. Minuti, N. Omodei, G. Spandre, L. Vigiani, and F. Zetti. The silicon-strip tracker of the Gamma ray Large Area Space Telescope. *Nuclear Instruments and Methods in Physics Research A*, 512:136–142, Oct. 2003.

[48] K. Bernlöhr, O. Carrol, R. Cornils, S. Elfahem, P. Espigat, S. Gillessen, G. Heinzelmann, G. Hermann, W. Hofmann, D. Horns, I. Jung, R. Kankanyan, A. Katona, B. Khelifi, H. Krawczynski, M. Panter, M. Punch, S. Rayner, G. Rowell, M. Tluczykont, and R. van Staa. The optical system of the H.E.S.S. imaging atmospheric Cherenkov telescopes. Part I: layout and components of the system. *Astroparticle Physics*, 20:111–128, Nov. 2003.

[49] S. Bianchi, R. Maiolino, and G. Risaliti. AGN Obscuration and the Unified Model. *Advances in Astronomy*, 2012, 2012.

[50] G. V. Bicknell and M. C. Begelman. Understanding the Kiloparsec-Scale Structure of M87. *ApJ*, 467:597, Aug. 1996.

[51] G. V. Bicknell, M. A. Dopita, and C. P. O. O'Dea. Unification of the Radio and Optical Properties of Gigahertz Peak Spectrum and Compact Steep-Spectrum Radio Sources. *ApJ*, 485:112–124, Aug. 1997.

[52] G. F. Bignami, G. Boella, J. J. Burger, B. G. Taylor, P. Keirle, J. A. Paul, H. A. Mayer-Hasselwander, E. Pfeffermann, L. Scarsi, and B. N. Swanenburg. The COS-B experiment for gamma-ray astronomy. *Space Science Instrumentation*, 1:245–268, Aug. 1975.

[53] J. A. Biretta, W. B. Sparks, and F. Macchetto. Hubble Space Telescope Observations of Superluminal Motion in the M87 Jet. *ApJ*, 520:621–626, Aug. 1999.

[54] J. A. Biretta, C. P. Stern, and D. E. Harris. The radio to X-ray spectrum of the M87 jet and nucleus. *AJ*, 101:1632–1646, May 1991.

[55] R. D. Blandford and A. Königl. Relativistic jets as compact radio sources. *ApJ*, 232:34–48, Aug. 1979.

[56] M. Błażejowski, M. Sikora, R. Moderski, and G. M. Madejski. Comptonization of Infrared Radiation from Hot Dust by Relativistic Jets in Quasars. *ApJ*, 545:107–116, Dec. 2000.

[57] S. D. Bloom and A. P. Marscher. An Analysis of the Synchrotron Self-Compton Model for the Multi–Wave Band Spectra of Blazars. *ApJ*, 461:657, Apr. 1996.

[58] S. D. Bloom, A. P. Marscher, W. K. Gear, H. Terasranta, E. Valtaoja, H. D. Aller, and M. F. Aller. Radio, millimeter-submillimeter, and infrared spectra of flat-spectrum extragalactic radio sources. *AJ*, 108:398–404, Aug. 1994.

[59] P. Boinee, G. Cabras, A. de Angelis, D. Favretto, M. Frailis, R. Giannitrapani, E. Milotti, F. Longo, M. Brigida, F. Gargano, N. Giglietto, M. N. Mazziotta, C. Cecchi, P. Lubrano, M. Pepe, L. Baldini, J. Cohen-Tanugi, M. Kuss, L. Latronico, N. Omodei, G. Spandre, J. Bogart, R. Dubois, T. Kamae, L. Rochester, T. Usher, T. Burnett, and S. Robinson. Gleam: the

GLAST Large Area Telescope Simulation Framework. In S. Ciprini, A. de Angelis, P. Lubrano, and O. Mansutti, editors, *Science with the New Generation of High Energy Gamma-Ray Experiments : Between Astrophysics and Astroparticle Physics*, page 141, Aug. 2003.

[60] M. Böttcher, C. D. Dermer, and J. D. Finke. The Hard VHE γ-Ray Emission in High-Redshift TeV Blazars: Comptonization of Cosmic Microwave Background Radiation in an Extended Jet? *ApJ*, 679:L9–L12, May 2008.

[61] M. Böttcher, R. Mukherjee, and A. Reimer. Predictions of the High-Energy Emission from BL Lacertae Objects: The Case of W Comae. *ApJ*, 581:143–154, Dec. 2002.

[62] G. Bressan, P. L. Bragato, and C. Venturini. Corrigendum. *Geophysical Journal International*, 165:382–382, Apr. 2006.

[63] A. H. Bridle and R. A. Perley. Extragalactic Radio Jets. *ARA&A*, 22:319–358, 1984.

[64] M. Brigida, M. N. Mazziotta, F. Gargano, and F. Loparco. LAT TKR trigger and hit capture efficiency studies. *LAT-TD-04184*, pages 1–9, June 2004.

[65] A. M. Brown and J. Adams. High-energy γ-ray properties of the Fanaroff-Riley type I radio galaxy NGC 1275. *MNRAS*, 413:2785–2790, June 2011.

[66] A. M. Brown and J. Adams. Discovery of γ-ray emission from the broad-line radio galaxy Pictor A. *MNRAS*, 421:2303–2309, Apr. 2012.

[67] B. J. Burn. On the depolarization of discrete radio sources by Faraday dispersion. *MNRAS*, 133:67, 1966.

[68] D. N. Burrows, J. E. Hill, J. A. Nousek, J. A. Kennea, A. Wells, J. P. Osborne, A. F. Abbey, A. Beardmore, K. Mukerjee, A. D. T. Short, G. Chincarini, S. Campana, O. Citterio, A. Moretti, C. Pagani, G. Tagliaferri, P. Giommi, M. Capalbi, F. Tamburelli, L. Angelini, G. Cusumano, H. W. Bräuninger, W. Burkert, and G. D. Hartner. The Swift X-Ray Telescope. *Space Sci. Rev.*, 120:165–195, Oct. 2005.

[69] M. Cappellari, E. Emsellem, D. Krajnović, R. M. McDermid, N. Scott, G. A. Verdoes Kleijn, L. M. Young, K. Alatalo, R. Bacon, L. Blitz, M. Bois, F. Bournaud, M. Bureau, R. L. Davies, T. A. Davis, P. T. de Zeeuw, P.-A. Duc, S. Khochfar, H. Kuntschner, P.-Y. Lablanche, R. Morganti, T. Naab, T. Oosterloo, M. Sarzi, P. Serra, and A.-M. Weijmans. The ATLAS^{3D} project - I. A volume-limited sample of 260 nearby early-type galaxies: science goals and selection criteria. *MNRAS*, 413:813–836, May 2011.

[70] J. A. Cardelli, G. C. Clayton, and J. S. Mathis. The relationship between infrared, optical, and ultraviolet extinction. *ApJ*, 345:245–256, Oct. 1989.

[71] M. T. Carini, H. R. Miller, J. C. Noble, and A. C. Sadun. The timescales of the optical variability of blazars. II - AP Librae. *AJ*, 101:1196–1201, Apr. 1991.

[72] J. C. Carvalho. The age of GHz-peaked-spectrum radio sources. *A&A*, 292:392–394, Dec. 1994.

[73] J. C. Carvalho. The evolution of GHz-peaked-spectrum radio sources. *A&A*, 329:845–852, Jan. 1998.

[74] J.-M. Casandjian and I. A. Grenier. A revised catalogue of EGRET γ-ray sources. *A&A*, 489:849–883, Oct. 2008.

[75] A. Celotti and G. Ghisellini. The power of blazar jets. *MNRAS*, 385:283–300, Mar. 2008.

[76] A. Celotti, P. Padovani, and G. Ghisellini. Jets and accretion processes in active galactic nuclei: further clues. *MNRAS*, 286:415–424, Apr. 1997.

[77] C. C. Cheung, D. E. Harris, and Ł. Stawarz. Superluminal Radio Features in the M87 Jet and the Site of Flaring TeV Gamma-Ray Emission. *ApJ*, 663:L65–L68, July 2007.

[78] M. Chiaberge, A. Capetti, and A. Celotti. The BL Lac heart of Centaurus A. *MNRAS*, 324:L33–L37, July 2001.

[79] M. Cohen, W. A. Wheaton, and S. T. Megeath. Spectral Irradiance Calibration in the Infrared. XIV. The Absolute Calibration of 2MASS. *AJ*, 126:1090–1096, Aug. 2003.

[80] S. Collier and B. M. Peterson. Characteristic Ultraviolet/Optical Timescales in Active Galactic Nuclei. *ApJ*, 555:775–785, July 2001.

[81] A. Comastri, G. Fossati, G. Ghisellini, and S. Molendi. On the Soft X-Ray Spectra of γ-Loud Blazars. *ApJ*, 480:534–546, May 1997.

[82] A. Comastri, M. Mignoli, P. Ciliegi, P. Severgnini, R. Maiolino, M. Brusa, F. Fiore, A. Baldi, S. Molendi, R. Morganti, C. Vignali, F. La Franca, G. Matt, and G. C. Perola. The HELLAS2XMM Survey. II. Multiwavelength Observations of P3: An X-Ray-bright, Optically Inactive Galaxy. *ApJ*, 571:771–778, June 2002.

[83] R. Cornils, S. Gillessen, I. Jung, W. Hofmann, M. Beilicke, K. Bernlöhr, O. Carrol, S. Elfahem, G. Heinzelmann, G. Hermann, D. Horns, R. Kankanyan, A. Katona, H. Krawczynski, M. Panter, S. Rayner, G. Rowell, M. Tluczykont, and R. van Staa. The optical system of the H.E.S.S. imaging atmospheric Cherenkov telescopes. Part II: mirror alignment and point spread function. *Astroparticle Physics*, 20:129–143, Nov. 2003.

[84] J. H. Croston, M. J. Hardcastle, D. E. Harris, E. Belsole, M. Birkinshaw, and D. M. Worrall. An X-Ray Study of Magnetic Field Strengths and Particle Content in the Lobes of FR II Radio Sources. *ApJ*, 626:733–747, June 2005.

[85] R. M. Cutri, M. F. Skrutskie, S. van Dyk, C. A. Beichman, J. M. Carpenter, T. Chester, L. Cambresy, T. Evans, J. Fowler, J. Gizis, E. Howard, J. Huchra, T. Jarrett, E. L. Kopan, J. D. Kirkpatrick, R. M. Light, K. A. Marsh, H. McCallon, S. Schneider, R. Stiening, M. Sykes, M. Weinberg, W. A. Wheaton, S. Wheelock, and N. Zacarias. *2MASS All Sky Catalog of point sources.* June 2003.

[86] B. Czerny, A. Siemiginowska, A. Janiuk, B. Nikiel-Wroczyński, and Ł. Stawarz. Accretion Disk Model of Short-Timescale Intermittent Activity in Young Radio Sources. *ApJ*, 698:840–851, June 2009.

[87] D. Dallacasa, C. Stanghellini, M. Centonza, and R. Fanti. High frequency peakers. I. The bright sample. *A&A*, 363:887–900, Nov. 2000.

[88] F. D'Ammando, G. Tosti, M. Orienti, J. Finke, and on behalf of the Fermi Large Area Telescope Collaboration. Four Years of Fermi LAT Observations of Narrow-Line Seyfert 1 Galaxies. *ArXiv e-prints*, Mar. 2013.

[89] M. de Naurois, J. Holder, R. Bazer-Bachi, H. Bergeret, P. Bruel, A. Cordier, G. Debiais, J.-P. Dezalay, D. Dumora, E. Durand, P. Eschstruth, P. Espigat, B. Fabre, P. Fleury, N. Hérault, M. Hrabovsky, S. Incerti, R. Le Gallou, F. Münz, A. Musquère, J.-F. Olive, E. Paré, J. Québert, R. C. Rannot, T. Reposeur, L. Rob, P. Roy, T. Sako, P. Schovanek, D. A. Smith, P. Snabre, and A. Volte. Measurement of the Crab Flux above 60 GeV with the CELESTE Cerenkov Telescope. *ApJ*, 566:343–357, Feb. 2002.

[90] W. H. de Vries, P. D. Barthel, and C. P. O'Dea. Radio spectra of Gigahertz Peaked Spectrum radio sources. *A&A*, 321:105–110, May 1997.

[91] D. S. De Young. The evolution of compact steep spectrum sources. *ApJ*, 402:95–108, Jan. 1993.

[92] D. S. De Young. Jet Interaction and the Evolution of Compact Symmetric Radio Sources. *ApJ*, 490:L55–L58, Nov. 1997.

[93] R. P. Deo, D. M. Crenshaw, and S. B. Kraemer. The Host Galaxies of Narrow-Line Seyfert 1 Galaxies: Nuclear Dust Morphology and Starburst Rings. *AJ*, 132:321–346, July 2006.

[94] S. M. Derdeyn, C. H. Ehrmann, C. E. Fichtel, D. A. Kniffen, and R. W. Ross. SAS-B digitized spark chamber gamma ray telescope. *Nuclear Instruments and Methods*, 98:557–566, 1972.

[95] C. D. Dermer and G. Menon. *High Energy Radiation From Black Holes.* Princeton University Press, 2009.

[96] C. D. Dermer and R. Schlickeiser. Model for the High-Energy Emission from Blazars. *ApJ*, 416:458, Oct. 1993.

[97] C. D. Dermer, R. Schlickeiser, and A. Mastichiadis. High-energy gamma radiation from extragalactic radio sources. *A&A*, 256:L27–L30, Mar. 1992.

[98] V. Despringre, D. Fraix-Burnet, and E. Davoust. First millimeter mapping of the jet and nucleus of M 87. *A&A*, 309:375–380, May 1996.

[99] T. Di Matteo, S. W. Allen, A. C. Fabian, A. S. Wilson, and A. J. Young. Accretion onto the Supermassive Black Hole in M87. *ApJ*, 582:133–140, Jan. 2003.

[100] A. Domínguez, J. R. Primack, D. J. Rosario, F. Prada, R. C. Gilmore, S. M. Faber, D. C. Koo, R. S. Somerville, M. A. Pérez-Torres, P. Pérez-González, J.-S. Huang, M. Davis, P. Guhathakurta, P. Barmby, C. J. Conselice, M. Lozano, J. A. Newman, and M. C. Cooper. Extragalactic background light inferred from AEGIS galaxy-SED-type fractions. *MNRAS*, 410:2556–2578, Feb. 2011.

[101] D. Donato, G. Ghisellini, G. Tagliaferri, and G. Fossati. Hard X-ray properties of blazars. *A&A*, 375:739–751, Sept. 2001.

[102] A. W. F. Edwards. *Likelihood*. Johns Hopkins University Press, Baltimore, 1992.

[103] R. D. Ekers, W. M. Goss, K. J. Wellington, A. Bosma, R. M. Smith, and F. Schweizer. The large-scale radio structure of Fornax A. *A&A*, 127:361–365, Nov. 1983.

[104] B. L. Fanaroff and J. M. Riley. The morphology of extragalactic radio sources of high and low luminosity. *MNRAS*, 167:31P–36P, May 1974.

[105] C. Fanti, R. Fanti, D. Dallacasa, R. T. Schilizzi, R. E. Spencer, and C. Stanghellini. Are compact steep-spectrum sources young? *A&A*, 302:317, Oct. 1995.

[106] R. Fanti, C. Fanti, R. T. Schilizzi, R. E. Spencer, Nan Rendong, P. Parma, W. J. M. van Breugel, and T. Venturi. On the nature of compact steep spectrum radio sources. *A&A*, 231:333–346, May 1990.

[107] G. G. Fazio, H. F. Helmken, G. H. Rieke, and T. C. Weekes. An experiment to search for discrete sources of cosmic gamma rays in the 10^{11} to 10^{12} eV region. *Canadian Journal of Physics Supplement*, 46:451, 1968.

[108] I. J. Feain, T. J. Cornwell, R. D. Ekers, M. R. Calabretta, R. P. Norris, M. Johnston-Hollitt, J. Ott, E. Lindley, B. M. Gaensler, T. Murphy, E. Middelberg, S. Jiraskova, S. O'Sullivan, N. M. McClure-Griffiths, and J. Bland-Hawthorn. The Radio Continuum Structure of Centaurus A at 1.4 GHz. *ApJ*, 740:17, Oct. 2011.

[109] E. D. Feigelson, S. A. Laurent-Muehleisen, R. I. Kollgaard, and E. B. Fomalont. Discovery of Inverse-Compton X-Rays in Radio Lobes. *ApJ*, 449:L149, Aug. 1995.

[110] Fermi-LAT Collaboration. Fermi Gamma-Ray Imaging of a Radio Galaxy. *Science*, 328:725–, May 2010.

[111] Fermi-LAT Collaboration. Observations of the Young Supernova Remnant RX J1713.7-3946 with the Fermi Large Area Telescope. *ApJ*, 734:28, June 2011.

[112] Fermi-LAT Collaboration. Fermi Large Area Telescope Observations of the Supernova Remnant G8.7-0.1. *ApJ*, 744:80, Jan. 2012.

[113] Fermi-LAT Collaboration. The Fermi Large Area Telescope On Orbit: Event Classification, Instrument Response Functions, and Calibration. *ArXiv e-prints*, June 2012.

[114] O. Ferreira, G. Bogaert, A. Bonnemaison, G. Drevillon, P. Fleury, B. Giebels, P. Prat, D. Bdrde, P. Bourgeois, B. Cordier, F. X. Gentit, B. Horeau, and Y. Piret. Environmental tests of the glast validation module calorimeter. *Nuclear Instruments and Methods in Physics Research Section A: Accelerators, Spectrometers, Detectors and Associated Equipment*, 530(3):323 – 329, 2004.

[115] A. L. Fey, C. Ma, E. F. Arias, P. Charlot, M. Feissel-Vernier, A.-M. Gontier, C. S. Jacobs, J. Li, and D. S. MacMillan. The Second Extension of the International Celestial Reference Frame: ICRF-EXT.1. *AJ*, 127:3587–3608, June 2004.

[116] C. E. Fichtel, R. C. Hartman, D. A. Kniffen, D. J. Thompson, H. Ogelman, M. E. Ozel, T. Tumer, and G. F. Bignami. High-energy gamma-ray results from the second small astronomy satellite. *ApJ*, 198:163–182, May 1975.

[117] J. D. Finke, C. D. Dermer, and M. Böttcher. Synchrotron Self-Compton Analysis of TeV X-Ray-Selected BL Lacertae Objects. *ApJ*, 686:181–194, Oct. 2008.

[118] J. D. Finke, S. Razzaque, and C. D. Dermer. Modeling the Extragalactic Background Light from Stars and Dust. *ApJ*, 712:238–249, Mar. 2010.

[119] R. A. Fisher. Statistical methods for research workers. *The Eugenics Review*, 18(2):148–150, 1926.

[120] E. B. Fomalont, K. A. Ebneter, W. J. M. van Breugel, and R. D. Ekers. Depolarization silhouettes and the filamentary structure in the radio source Fornax A. *ApJ*, 346:L17–L20, Nov. 1989.

[121] L. Foschini, M. Berton, A. Caccianiga, S. Ciroi, V. Cracco, B. M. Peterson, E. Angelakis, V. Braito, L. Fuhrmann, L. Gallo, D. Grupe, E. Järvelä, S. Kaufmann, S. Komossa, Y. Y. Kovalev, A. Lähteenmäki, M. M. Lisakov, M. L. Lister, S. Mathur, J. L. Richards, P. Romano, A. Sievers, G. Tagliaferri, J. Tammi, O. Tibolla, M. Tornikoski, S. Vercellone, G. La Mura, L. Maraschi, and P. Rafanelli. Properties of flat-spectrum radio-loud Narrow-Line Seyfert 1 Galaxies. *ArXiv e-prints*, Sept. 2014.

[122] L. Foschini, G. Ghisellini, Y. Y. Kovalev, M. L. Lister, F. D'Ammando, D. J. Thompson, A. Tramacere, E. Angelakis, D. Donato, A. Falcone, L. Fuhrmann, M. Hauser, Y. A. Kovalev, K. Mannheim, L. Maraschi, W. Max-Moerbeck, I. Nestoras, V. Pavlidou, T. J. Pearson, A. B. Pushkarev, A. C. S. Readhead, J. L. Richards, M. A. Stevenson, G. Tagliaferri, O. Tibolla, F. Tavecchio, and S. Wagner. The first gamma-ray outburst of a narrow-line Seyfert 1 galaxy: the case of PMN J0948+0022 in 2010 July. *MNRAS*, 413:1671–1677, May 2011.

[123] G. Fossati, L. Maraschi, A. Celotti, A. Comastri, and G. Ghisellini. A unifying view of the spectral energy distributions of blazars. *MNRAS*, 299:433–448, Sept. 1998.

[124] A. Franceschini, G. Rodighiero, and M. Vaccari. Extragalactic optical-infrared background radiation, its time evolution and the cosmic photon-photon opacity. *A&A*, 487:837–852, Sept. 2008.

[125] P. J. Francis, P. C. Hewett, C. B. Foltz, F. H. Chaffee, R. J. Weymann, and S. L. Morris. A high signal-to-noise ratio composite quasar spectrum. *ApJ*, 373:465–470, June 1991.

[126] R. Frühwirth, M. Regler, R. K. Bock, H. Grote, and D. Notz. *Data Analysis Techniques for High Energy Physics*. Cambridge Univ. Press, second edition, 2000.

[127] S. García-Burillo, F. Combes, R. Neri, A. Fuente, A. Usero, S. Leon, and J. Lim. Fueling the central engine of radio galaxies. I. The molecular/dusty disk of 4C 31.04. *A&A*, 468:L71–L75, June 2007.

[128] K. Gebhardt and J. Thomas. The Black Hole Mass, Stellar Mass-to-Light Ratio, and Dark Halo in M87. *ApJ*, 700:1690–1701, Aug. 2009.

[129] N. Gehrels, G. Chincarini, P. Giommi, K. O. Mason, J. A. Nousek, A. A. Wells, N. E. White, S. D. Barthelmy, D. N. Burrows, L. R. Cominsky, K. C. Hurley, F. E. Marshall, P. Mészáros, P. W. A. Roming, L. Angelini, L. M. Barbier, T. Belloni, S. Campana, P. A. Caraveo, M. M. Chester, O. Citterio, T. L. Cline, M. S. Cropper, J. R. Cummings, A. J. Dean, E. D. Feigelson, E. E. Fenimore, D. A. Frail, A. S. Fruchter, G. P. Garmire, K. Gendreau, G. Ghisellini, J. Greiner, J. E. Hill, S. D. Hunsberger, H. A. Krimm, S. R.

Kulkarni, P. Kumar, F. Lebrun, N. M. Lloyd-Ronning, C. B. Markwardt, B. J. Mattson, R. F. Mushotzky, J. P. Norris, J. Osborne, B. Paczynski, D. M. Palmer, H.-S. Park, A. M. Parsons, J. Paul, M. J. Rees, C. S. Reynolds, J. E. Rhoads, T. P. Sasseen, B. E. Schaefer, A. T. Short, A. P. Smale, I. A. Smith, L. Stella, G. Tagliaferri, T. Takahashi, M. Tashiro, L. K. Townsley, J. Tueller, M. J. L. Turner, M. Vietri, W. Voges, M. J. Ward, R. Willingale, F. M. Zerbi, and W. W. Zhang. The Swift Gamma-Ray Burst Mission. *ApJ*, 611:1005–1020, Aug. 2004.

[130] B. J. Geldzahler and E. B. Fomalont. Radio observations of the jet in Fornax A. *AJ*, 89:1650–1657, Nov. 1984.

[131] M. Georganopoulos, J. D. Finke, and L. C. Reyes. A Method for Setting Upper Limits to the Extragalactic Background Light with Fermi-lat and TeV Observations of Blazars. *ApJ*, 714:L157–L161, May 2010.

[132] M. Georganopoulos and D. Kazanas. Decelerating Flows in TeV Blazars: A Resolution to the BL Lacertae-FR I Unification Problem. *ApJ*, 594:L27–L30, Sept. 2003.

[133] M. Georganopoulos, R. M. Sambruna, D. Kazanas, A. N. Cillis, C. C. Cheung, E. S. Perlman, K. M. Blundell, and D. S. Davis. A Novel Method for Measuring the Extragalactic Background Light: Fermi Application to the Lobes of Fornax A. *ApJ*, 686:L5–L8, Oct. 2008.

[134] G. Ghisellini, A. Celotti, G. Fossati, L. Maraschi, and A. Comastri. A theoretical unifying scheme for gamma-ray bright blazars. *MNRAS*, 301:451–468, Dec. 1998.

[135] G. Ghisellini and P. Madau. On the origin of the gamma-ray emission in blazars. *MNRAS*, 280:67–76, May 1996.

[136] G. Ghisellini and L. Maraschi. Bulk acceleration in relativistic jets and the spectral properties of blazars. *ApJ*, 340:181–189, May 1989.

[137] G. Ghisellini and F. Tavecchio. The blazar sequence: a new perspective. *MNRAS*, 387:1669–1680, July 2008.

[138] R. C. Gilmore, P. Madau, J. R. Primack, R. S. Somerville, and F. Haardt. GeV gamma-ray attenuation and the high-redshift UV background. *MNRAS*, 399:1694–1708, Nov. 2009.

[139] R. C. Gilmore, R. S. Somerville, J. R. Primack, and A. Domínguez. Semi-analytic modelling of the extragalactic background light and consequences for extragalactic gamma-ray spectra. *MNRAS*, 422:3189–3207, June 2012.

[140] V. L. Ginzburg and S. I. Syrovatskii. Developments in the Theory of Synchrotron Radiation and its Reabsorption. *ARA&A*, 7:375, 1969.

[141] M. Giroletti and A. Polatidis. Samples and statistics of CSS and GPS sources. *Astronomische Nachrichten*, 330:193, Feb. 2009.

[142] P. Goudfrooij, M. V. Alonso, C. Maraston, and D. Minniti. The star cluster system of the 3-Gyr-old merger remnant NGC 1316: clues from optical and near-infrared photometry. *MNRAS*, 328:237–256, Nov. 2001.

[143] E. J. Grove. Scenarios for Flight Trigger and Filter Configuration. *LAT-SS-286*, pages 1–26, Sept. 2007.

[144] N. E. Gugliucci, G. B. Taylor, A. B. Peck, and M. Giroletti. Polarimetry of Compact Symmetric Objects. *ApJ*, 661:78–87, May 2007.

[145] H. E. S. S. Collaboration and Fermi-LAT collaborations. The high-energy γ-ray emission of AP Librae. *ArXiv e-prints*, Oct. 2014.

[146] D. S. Hanna, D. Bhattacharya, L. M. Boone, M. C. Chantell, Z. Conner, C. E. Covault, M. Dragovan, P. Fortin, D. T. Gregorich, J. A. Hinton, R. Mukherjee, R. A. Ong, S. Oser, K. Ragan, R. A. Scalzo, D. R. Schuette, C. G. Théoret, T. O. Tümer, D. A. Williams, and J. A. Zweerink. The STACEE-32 ground based gamma-ray detector. *Nuclear Instruments and Methods in Physics Research A*, 491:126–151, Sept. 2002.

[147] M. J. Hardcastle, C. C. Cheung, I. J. Feain, and Ł. Stawarz. High-energy particle acceleration and production of ultra-high-energy cosmic rays in the giant lobes of Centaurus A. *MNRAS*, 393:1041–1053, Mar. 2009.

[148] D. E. Harris and J. E. Grindlay. The prospects for X-ray detection of inverse-Compton emission from radio source electrons and photons of the microwave background. *MNRAS*, 188:25–37, July 1979.

[149] F. A. Harrison, W. W. Craig, F. E. Christensen, C. J. Hailey, W. W. Zhang, S. E. Boggs, D. Stern, W. R. Cook, K. Forster, P. Giommi, B. W. Grefenstette, Y. Kim, T. Kitaguchi, J. E. Koglin, K. K. Madsen, P. H. Mao, H. Miyasaka, K. Mori, M. Perri, M. J. Pivovaroff, S. Puccetti, V. R. Rana, N. J. Westergaard, J. Willis, A. Zoglauer, H. An, M. Bachetti, N. M. Barrière, E. C. Bellm, V. Bhalerao, N. F. Brejnholt, F. Fuerst, C. C. Liebe, C. B. Markwardt, M. Nynka, J. K. Vogel, D. J. Walton, D. R. Wik, D. M. Alexander, L. R. Cominsky, A. E. Hornschemeier, A. Hornstrup, V. M. Kaspi, G. M. Madejski, G. Matt, S. Molendi, D. M. Smith, J. A. Tomsick, M. Ajello, D. R. Ballantyne, M. Baloković, D. Barret, F. E. Bauer, R. D. Blandford, W. N. Brandt, L. W. Brenneman, J. Chiang, D. Chakrabarty, J. Chenevez, A. Comastri, F. Dufour, M. Elvis, A. C. Fabian, D. Farrah, C. L. Fryer, E. V. Gotthelf, J. E. Grindlay, D. J. Helfand, R. Krivonos, D. L. Meier, J. M. Miller, L. Natalucci, P. Ogle, E. O. Ofek, A. Ptak, S. P. Reynolds, J. R. Rigby, G. Tagliaferri, S. E. Thorsett, E. Treister, and C. M. Urry. The Nuclear Spectroscopic Telescope Array (NuSTAR) High-energy X-Ray Mission. *ApJ*, 770:103, June 2013.

[150] J. Hartle. *Gravity: An Introduction to Einstein's General Relativity.* Addison-Wesley, Boston, 2003.

[151] R. C. Hartman, D. L. Bertsch, S. D. Bloom, A. W. Chen, P. Deines-Jones, J. A. Esposito, C. E. Fichtel, D. P. Friedlander, S. D. Hunter, L. M. McDonald, P. Sreekumar, D. J. Thompson, B. B. Jones, Y. C. Lin, P. F. Michelson, P. L. Nolan, W. F. Tompkins, G. Kanbach, H. A. Mayer-Hasselwander, A. Mücke, M. Pohl, O. Reimer, D. A. Kniffen, E. J. Schneid, C. von Montigny, R. Mukherjee, and B. L. Dingus. The Third EGRET Catalog of High-Energy Gamma-Ray Sources. *ApJS*, 123:79–202, July 1999.

[152] M. G. Hauser and E. Dwek. The Cosmic Infrared Background: Measurements and Implications. *ARA&A*, 39:249–307, 2001.

[153] J. F. Helmboldt, G. B. Taylor, S. Tremblay, C. D. Fassnacht, R. C. Walker, S. T. Myers, L. O. Sjouwerman, T. J. Pearson, A. C. S. Readhead, L. Weintraub, N. Gehrels, R. W. Romani, S. Healey, P. F. Michelson, R. D. Blandford, and G. Cotter. The VLBA Imaging and Polarimetry Survey at 5 GHz. *ApJ*, 658:203–216, Mar. 2007.

[154] J. Holder, R. W. Atkins, H. M. Badran, G. Blaylock, S. M. Bradbury, J. H. Buckley, K. L. Byrum, D. A. Carter-Lewis, O. Celik, Y. C. K. Chow, P. Cogan, W. Cui, M. K. Daniel, I. de la Calle Perez, C. Dowdall, P. Dowkontt, C. Duke, A. D. Falcone, S. J. Fegan, J. P. Finley, P. Fortin, L. F. Fortson, K. Gibbs, G. Gillanders, O. J. Glidewell, J. Grube, K. J. Gutierrez, G. Gyuk, J. Hall, D. Hanna, E. Hays, D. Horan, S. B. Hughes, T. B. Humensky, A. Imran, I. Jung, P. Kaaret, G. E. Kenny, D. Kieda, J. Kildea, J. Knapp, H. Krawczynski, F. Krennrich, M. J. Lang, S. LeBohec, E. Linton, E. K. Little, G. Maier, H. Manseri, A. Milovanovic, P. Moriarty, R. Mukherjee, P. A. Ogden, R. A. Ong, D. Petry, J. S. Perkins, F. Pizlo, M. Pohl, J. Quinn, K. Ragan, P. T. Reynolds, E. T. Roache, H. J. Rose, M. Schroedter, G. H. Sembroski, G. Sleege, D. Steele, S. P. Swordy, A. Syson, J. A. Toner, L. Valcarcel, V. V. Vassiliev, S. P. Wakely, T. C. Weekes, R. J. White, D. A. Williams, and R. Wagner. The first VERITAS telescope. *Astroparticle Physics*, 25:391–401, July 2006.

[155] L.-h. Huang, D.-r. Jiang, and X.-w. Cao. Relation Between Millimeter Wavelengths Emission and High-Energy Emission for Active Galactic Nuclei. *Chinese Physics Letters*, 15:856–858, Nov. 1998.

[156] R. Hughes, J. E. Grove, M. Kocian, S. Ritz, J. J. Russell, E. Siskind, P. Smith, T. Usher, B. Winer, and L. Collaboration. The trigger and onboard filter of the glast large area telescope. *AIP Conference Proceedings*, 921(1):568–569, 2007.

[157] C. M. Hui and for the VERITAS collaboration. VERITAS observations of M87 from 2007 to present. *ArXiv e-prints*, July 2009.

[158] N. Isobe, K. Makishima, M. Tashiro, K. Itoh, N. Iyomoto, I. Takahashi, and H. Kaneda. The XMM-Newton Examination of Energetics in the East Lobe of the Nearby Radio Galaxy Fornax A (NGC 1316). *ApJ*, 645:256–263, July 2006.

[159] J. D. Jackson. *Classical Electrodynamics - 3rd Edition*. John Wiley & Sons Inc., 1998.

[160] N. Jackson, R. A. Battye, I. W. A. Browne, S. Joshi, T. W. B. Muxlow, and P. N. Wilkinson. Polarisation of flat-spectrum radio sources (Jackson+, 2007). *VizieR Online Data Catalog*, 837:60371, Sept. 2007.

[161] J. V. Jelley and N. A. Porter. Čerenkov Radiation from the Night Sky, and its Application to γ-Ray Astronomy. *QJRAS*, 4:275, Sept. 1963.

[162] T. Jenness, E. I. Robson, and J. A. Stevens. Observations of flat-spectrum radio sources at $\lambda 850\mu$m from the James Clerk Maxwell Telescope II. April 2000 to June 2005. *MNRAS*, 401:1240–1254, Jan. 2010.

[163] W. Johnson, J. Grove, B. Phlips, J. Ampe, S. Singh, and E. Ponslet. The construction and performance of the csi hodoscopic calorimeter for the glast beam test engineering module. *Nuclear Science, IEEE Transactions on*, 48(4):1182 –1189, aug 2001.

[164] W. Junor, J. A. Biretta, and M. Livio. Formation of the radio jet in M87 at 100 Schwarzschild radii from the central black hole. *Nature*, 401:891–892, Oct. 1999.

[165] H. Kaneda, M. Tashiro, Y. Ikebe, Y. Ishisaki, H. Kubo, K. Makshima, T. Ohashi, Y. Saito, H. Tabara, and T. Takahashi. Detection of Inverse-Compton X-Rays from Lobes of the Radio Galaxy Fornax A. *ApJ*, 453:L13, Nov. 1995.

[166] J. Kataoka, G. Madejski, M. Sikora, P. Roming, M. M. Chester, D. Grupe, Y. Tsubuku, R. Sato, N. Kawai, G. Tosti, D. Impiombato, Y. Y. Kovalev, Y. A. Kovalev, P. G. Edwards, S. J. Wagner, R. Moderski, Ł. Stawarz, T. Takahashi, and S. Watanabe. Multiwavelength Observations of the Powerful Gamma-Ray Quasar PKS 1510-089: Clues on the Jet Composition. *ApJ*, 672:787–799, Jan. 2008.

[167] J. Kataoka and Ł. Stawarz. X-Ray Emission Properties of Large-Scale Jets, Hot Spots, and Lobes in Active Galactic Nuclei. *ApJ*, 622:797–810, Apr. 2005.

[168] J. Kataoka, Ł. Stawarz, Y. Takahashi, C. C. Cheung, M. Hayashida, P. Grandi, T. H. Burnett, A. Celotti, S. J. Fegan, P. Fortin, K. Maeda, T. Nakamori, G. B. Taylor, G. Tosti, S. W. Digel, W. McConville, J. Finke, and F. D'Ammando. Broad-line Radio Galaxies Observed with Fermi-LAT: The Origin of the GeV γ-Ray Emission. *ApJ*, 740:29, Oct. 2011.

[169] N. Kawakatu and M. Kino. On the dynamical evolution of hotspots in powerful radio-loud active galactic nuclei. *MNRAS*, 370:1513–1518, Aug. 2006.

[170] R. C. Keenan, A. J. Barger, L. L. Cowie, and W.-H. Wang. The Resolved Near-infrared Extragalactic Background. *ApJ*, 723:40–46, Nov. 2010.

[171] K. I. Kellermann and MOJAVE Collaboration. Kinematics of the Active Radio Source at The Nucleus of NGC1275 (3C84). In *American Astronomical Society Meeting Abstracts #217*, volume 43 of *Bulletin of the American Astronomical Society*, page 408.07, Jan. 2011.

[172] K. I. Kellermann, R. Sramek, M. Schmidt, D. B. Shaffer, and R. Green. VLA observations of objects in the Palomar Bright Quasar Survey. *AJ*, 98:1195–1207, Oct. 1989.

[173] M. Kerr. *Likelihood methods for the detection and characterization of gamma-ray pulsars with the Fermi large area telescope*. PhD thesis, University of Washington, 2010.

[174] I. King. The structure of star clusters. I. an empirical density law. *AJ*, 67:471, Oct. 1962.

[175] M. Kino and K. Asano. Mini-radio lobes in AGN core illumination and their hadronic gamma-ray afterlight. *MNRAS*, 412:L20–L24, Mar. 2011.

[176] M. Kino, H. Ito, N. Kawakatu, and H. Nagai. New prediction of extragalactic GeV γ-ray emission from radio lobes of young AGN jets. *MNRAS*, 395:L43–L47, May 2009.

[177] M. Kino, N. Kawakatu, and H. Ito. Extragalactic MeV γ-ray emission from cocoons of young radio galaxies. *MNRAS*, 376:1630–1634, Apr. 2007.

[178] T. M. Kneiske, T. Bretz, K. Mannheim, and D. H. Hartmann. Implications of cosmological gamma-ray absorption. II. Modification of gamma-ray spectra. *A&A*, 413:807–815, Jan. 2004.

[179] T. M. Kneiske and H. Dole. A lower-limit flux for the extragalactic background light. *A&A*, 515:A19, June 2010.

[180] S. Komossa, W. Voges, D. Xu, S. Mathur, H.-M. Adorf, G. Lemson, W. J. Duschl, and D. Grupe. Radio-loud Narrow-Line Type 1 Quasars. *AJ*, 132:531–545, Aug. 2006.

[181] A. Konigl. Relativistic jets as X-ray and gamma-ray sources. *ApJ*, 243:700–709, Feb. 1981.

[182] Y. Y. Kovalev, H. D. Aller, M. F. Aller, D. C. Homan, M. Kadler, K. I. Kellermann, Y. A. Kovalev, M. L. Lister, M. J. McCormick, A. B. Pushkarev, E. Ros, and J. A. Zensus. The Relation Between AGN Gamma-Ray Emission and Parsec-Scale Radio Jets. *ApJ*, 696:L17–L21, May 2009.

[183] Y. Y. Kovalev, M. L. Lister, D. C. Homan, and K. I. Kellermann. The Inner Jet of the Radio Galaxy M87. *ApJ*, 668:L27–L30, Oct. 2007.

[184] W. Kraushaar, G. W. Clark, G. Garmire, H. Helmken, P. Higbie, and M. Agogino. Explorer XI Experiment on Cosmic Gamma Rays. *ApJ*, 141:845, Apr. 1965.

[185] J. H. Krolik and M. C. Begelman. Molecular tori in Seyfert galaxies - Feeding the monster and hiding it. *ApJ*, 329:702–711, June 1988.

[186] D. Kumar. Active galactic nuclei - definition. `http://dmr-astronomersclub.blogspot.com/2012/08/active-galactic-nuclei-agn-definition.html`.

[187] R. C. Lamb and T. C. Weekes. Very high energy gamma-ray binary stars. *Science*, 238:1528–1534, Dec. 1987.

[188] J. Lande, M. Ackermann, A. Allafort, J. Ballet, K. Bechtol, T. H. Burnett, J. Cohen-Tanugi, A. Drlica-Wagner, S. Funk, F. Giordano, M.-H. Grondin, M. Kerr, and M. Lemoine-Goumard. Search for Spatially Extended Fermi Large Area Telescope Sources Using Two Years of Data. *ApJ*, 756:5, Sept. 2012.

[189] A. Lawrence and M. Elvis. Misaligned Disks as Obscurers in Active Galaxies. *ApJ*, 714:561–570, May 2010.

[190] J.-P. Lenain, C. Ricci, M. Türler, D. Dorner, and R. Walter. Seyfert 2 galaxies in the GeV band: jets and starburst. *A&A*, 524:A72, Dec. 2010.

[191] M. L. Lister, M. Aller, H. Aller, T. Hovatta, K. I. Kellermann, Y. Y. Kovalev, E. T. Meyer, A. B. Pushkarev, E. Ros, MOJAVE Collaboration, M. Ackermann, E. Antolini, L. Baldini, J. Ballet, G. Barbiellini, D. Bastieri, K. Bechtol, R. Bellazzini, B. Berenji, R. D. Blandford, E. D. Bloom, M. Boeck, E. Bonamente, A. W. Borgland, J. Bregeon, M. Brigida, P. Bruel, R. Buehler, S. Buson, G. A. Caliandro, R. A. Cameron, P. A. Caraveo, J. M. Casandjian, E. Cavazzuti, C. Cecchi, C. S. Chang, E. Charles, A. Chekhtman, C. C. Cheung, J. Chiang, S. Ciprini, R. Claus, J. Cohen-Tanugi, J. Conrad, S. Cutini, F. de Palma, C. D. Dermer, E. d. C. e. Silva, P. S. Drell, A. Drlica-Wagner, C. Favuzzi, S. J. Fegan, E. C. Ferrara, J. Finke, W. B. Focke, P. Fortin, Y. Fukazawa, P. Fusco, F. Gargano, D. Gasparrini, N. Gehrels, S. Germani, N. Giglietto, F. Giordano, M. Giroletti, T. Glanzman, G. Godfrey, I. A. Grenier, S. Guiriec, D. Hadasch, M. Hayashida, E. Hays, D. Horan, R. E. Hughes, G. Jóhannesson, A. S. Johnson, M. Kadler, H. Katagiri, J. Kataoka, J. Knödlseder, M. Kuss, J. Lande, F. Longo, F. Loparco, B. Lott, M. N. Lovellette, P. Lubrano, G. M. Madejski, M. N. Mazziotta, W. McConville, J. E. McEnery, J. Mehault, P. F. Michelson, T. Mizuno, C. Monte, M. E. Monzani, A. Morselli, I. V. Moskalenko, S. Murgia, M. Naumann-Godo, S. Nishino, P. L. Nolan, J. P. Norris, E. Nuss, M. Ohno, T. Ohsugi, A. Okumura, N. Omodei,

E. Orlando, M. Ozaki, D. Paneque, D. Parent, M. Pesce-Rollins, M. Pierbattista, F. Piron, G. Pivato, S. Rainò, A. Readhead, A. Reimer, O. Reimer, J. L. Richards, S. Ritz, H. F.-W. Sadrozinski, C. Sgrò, M. S. Shaw, E. J. Siskind, G. Spandre, P. Spinelli, H. Takahashi, T. Tanaka, J. G. Thayer, J. B. Thayer, D. J. Thompson, G. Tosti, A. Tramacere, E. Troja, T. L. Usher, J. Vandenbroucke, V. Vasileiou, G. Vianello, V. Vitale, A. P. Waite, P. Wang, B. L. Winer, K. S. Wood, S. Zimmer, and Fermi LAT Collaboration. γ-Ray and Parsec-scale Jet Properties of a Complete Sample of Blazars From the MOJAVE Program. *ApJ*, 742:27, Nov. 2011.

[192] M. L. Lister, M. F. Aller, H. D. Aller, D. C. Homan, K. I. Kellermann, Y. Y. Kovalev, A. B. Pushkarev, J. L. Richards, E. Ros, and T. Savolainen. MOJAVE. X. Parsec-scale Jet Orientation Variations and Superluminal Motion in Active Galactic Nuclei. *AJ*, 146:120, Nov. 2013.

[193] M. Longair. Radiation processes in high energy astrophysics iii. `http://eud.gsfc.nasa.gov/Volker.Beckmann/school/download/Longair_Radiation3.pdf`, 2006.

[194] E. Lorenz and The MAGIC Collaboration. Status of the 17 m MAGIC telescope. *"New Astronomy Reviews"*, 48:339–344, Apr. 2004.

[195] W.-F. Luo, J. Yang, L. Cui, X. Liu, and Z.-Q. Shen. Seven-frequency VLBI Observations of the GHz-Peaked-Spectrum Source OQ 208. *Chinese Journal of Astronomy and Astrophysics*, 7:611–619, Oct. 2007.

[196] C. Ly, R. C. Walker, and W. Junor. High-Frequency VLBI Imaging of the Jet Base of M87. *ApJ*, 660:200–205, May 2007.

[197] F. Macchetto, A. Marconi, D. J. Axon, A. Capetti, W. Sparks, and P. Crane. The Supermassive Black Hole of M87 and the Kinematics of Its Associated Gaseous Disk. *ApJ*, 489:579–600, Nov. 1997.

[198] G. Mackie and G. Fabbiano. Evolution of gas and stars in the merger galaxy NGC 1316 (Fornax A). *AJ*, 115:514, Feb. 1998.

[199] P. Madau and L. Pozzetti. Deep galaxy counts, extragalactic background light and the stellar baryon budget. *MNRAS*, 312:L9–L15, Feb. 2000.

[200] MAGIC Collaboration, J. Albert, E. Aliu, H. Anderhub, L. A. Antonelli, P. Antoranz, M. Backes, C. Baixeras, J. A. Barrio, H. Bartko, D. Bastieri, J. K. Becker, W. Bednarek, K. Berger, E. Bernardini, C. Bigongiari, A. Biland, R. K. Bock, G. Bonnoli, P. Bordas, V. Bosch-Ramon, T. Bretz, I. Britvitch, M. Camara, E. Carmona, A. Chilingarian, S. Commichau, J. L. Contreras, J. Cortina, M. T. Costado, S. Covino, V. Curtef, F. Dazzi, A. De Angelis, E. D. Cea del Pozo, R. de los Reyes, B. De Lotto, M. De Maria, F. De Sabata, C. D. Mendez, A. Dominguez, D. Dorner, M. Doro, M. Errando, M. Fagiolini, D. Ferenc, E. Fernández, R. Firpo, M. V. Fonseca, L. Font, N. Galante,

R. J. García López, M. Garczarczyk, M. Gaug, F. Goebel, M. Hayashida, A. Herrero, D. Höhne, J. Hose, C. C. Hsu, S. Huber, T. Jogler, T. M. Kneiske, D. Kranich, A. La Barbera, A. Laille, E. Leonardo, E. Lindfors, S. Lombardi, F. Longo, M. López, E. Lorenz, P. Majumdar, G. Maneva, N. Mankuzhiyil, K. Mannheim, L. Maraschi, M. Mariotti, M. Martínez, D. Mazin, M. Meucci, M. Meyer, J. M. Miranda, R. Mirzoyan, S. Mizobuchi, M. Moles, A. Moralejo, D. Nieto, K. Nilsson, J. Ninkovic, N. Otte, I. Oya, M. Panniello, R. Paoletti, J. M. Paredes, M. Pasanen, D. Pascoli, F. Pauss, R. G. Pegna, M. A. Perez-Torres, M. Persic, L. Peruzzo, A. Piccioli, F. Prada, E. Prandini, N. Puchades, A. Raymers, W. Rhode, M. Ribó, J. Rico, M. Rissi, A. Robert, S. Rügamer, A. Saggion, T. Y. Saito, M. Salvati, M. Sanchez-Conde, P. Sartori, K. Satalecka, V. Scalzotto, V. Scapin, R. Schmitt, T. Schweizer, M. Shayduk, K. Shinozaki, S. N. Shore, N. Sidro, A. Sierpowska-Bartosik, A. Sillanpää, D. Sobczynska, F. Spanier, A. Stamerra, L. S. Stark, L. Takalo, F. Tavecchio, P. Temnikov, D. Tescaro, M. Teshima, M. Tluczykont, D. F. Torres, N. Turini, H. Vankov, A. Venturini, V. Vitale, R. M. Wagner, W. Wittek, V. Zabalza, F. Zandanel, R. Zanin, and J. Zapatero. Very-High-Energy gamma rays from a Distant Quasar: How Transparent Is the Universe? *Science*, 320:1752–, June 2008.

[201] M. A. Malkan and F. W. Stecker. An Empirically Based Calculation of the Extragalactic Infrared Background. *ApJ*, 496:13–16, Mar. 1998.

[202] M. A. Malkan and F. W. Stecker. An Empirically Based Model for Predicting Infrared Luminosity Functions, Deep Infrared Galaxy Counts, and the Diffuse Infrared Background. *ApJ*, 555:641–649, July 2001.

[203] K. Mannheim. The proton blazar. *A&A*, 269:67–76, Mar. 1993.

[204] K. Mannheim, P. L. Biermann, and W. M. Kruells. A novel mechanism for nonthermal X-ray emission. *A&A*, 251:723–731, Nov. 1991.

[205] A. P. Marscher. Turbulent, Extreme Multi-zone Model for Simulating Flux and Polarization Variability in Blazars. *ApJ*, 780:87, Jan. 2014.

[206] A. P. Marscher and W. K. Gear. Models for high-frequency radio outbursts in extragalactic sources, with application to the early 1983 millimeter-to-infrared flare of 3C 273. *ApJ*, 298:114–127, Nov. 1985.

[207] A. P. Marscher, S. G. Jorstad, J. R. Mattox, and A. E. Wehrle. High-Frequency VLBA Total and Polarized Intensity Images of Gamma-Ray Bright Blazars. *ApJ*, 577:85–97, Sept. 2002.

[208] H. L. Marshall, B. P. Miller, D. S. Davis, E. S. Perlman, M. Wise, C. R. Canizares, and D. E. Harris. A High-Resolution X-Ray Image of the Jet in M87. *ApJ*, 564:683–687, Jan. 2002.

[209] J. R. Mattox, D. L. Bertsch, J. Chiang, B. L. Dingus, S. W. Digel, J. A. Esposito, J. M. Fierro, R. C. Hartman, S. D. Hunter, G. Kanbach, D. A. Kniffen, Y. C. Lin, D. J. Macomb, H. A. Mayer-Hasselwander, P. F. Michelson, C. von Montigny, R. Mukherjee, P. L. Nolan, P. V. Ramanamurthy, E. Schneid, P. Sreekumar, D. J. Thompson, and T. D. Willis. The Likelihood Analysis of EGRET Data. *ApJ*, 461:396, Apr. 1996.

[210] J. R. Mattox, R. C. Hartman, and O. Reimer. A Quantitative Evaluation of Potential Radio Identifications for 3EG EGRET Sources. *ApJS*, 135:155–175, Aug. 2001.

[211] W. McConville, L. Ostorero, R. Moderski, Ł. Stawarz, C. C. Cheung, M. Ajello, A. Bouvier, J. Bregeon, D. Donato, J. Finke, A. Furniss, J. E. McEnery, M. E. Monzani, M. Orienti, L. C. Reyes, A. Rossetti, and D. A. Williams. Fermi Large Area Telescope Observations of the Active Galaxy 4C +55.17: Steady, Hard Gamma-Ray Emission and Its Implications. *ApJ*, 738:148, Sept. 2011.

[212] R. Moderski, M. Sikora, and M. Błażejowski. Numerical simulations of radiation from blazar jets. *A&A*, 406:855–865, Aug. 2003.

[213] R. Moderski, M. Sikora, P. S. Coppi, and F. Aharonian. Klein-Nishina effects in the spectra of non-thermal sources immersed in external radiation fields. *MNRAS*, 363:954–966, Nov. 2005.

[214] A. A. Moiseev, P. L. Deering, R. C. Hartman, T. E. Johnson, T. R. Nebel, J. F. Ormes, and D. J. Thompson. High efficiency plastic scintillator detector with wavelength-shifting fiber readout for the GLAST Large Area Telescope. *Nuclear Instruments and Methods in Physics Research A*, 583:372–381, Dec. 2007.

[215] A. A. Moiseev, R. C. Hartman, J. F. Ormes, D. J. Thompson, M. J. Amato, T. E. Johnson, K. N. Segal, and D. A. Sheppard. The anti-coincidence detector for the GLAST large area telescope. *Astroparticle Physics*, 27:339–358, June 2007.

[216] P. Morrison. On gamma-ray astronomy. *Il Nuovo Cimento*, 7(6):858–865, 1958.

[217] A. Mücke, R. J. Protheroe, R. Engel, J. P. Rachen, and T. Stanev. BL Lac objects in the synchrotron proton blazar model. *Astroparticle Physics*, 18:593–613, Mar. 2003.

[218] C. Müller, M. Kadler, R. Ojha, M. Böck, F. Krauß, G. B. Taylor, J. Wilms, J. Blanchard, B. Carpenter, T. Dauser, M. Dutka, P. G. Edwards, N. Gehrels, C. Großberger, H. Hase, S. Horiuchi, A. Kreikenbohm, J. E. J. Lovell, W. McConville, C. Phillips, C. Plötz, T. Pursimo, J. Quick, E. Ros, R. Schulz,

J. Stevens, S. J. Tingay, J. Trüstedt, A. K. Tzioumis, and J. A. Zensus. The unusual multiwavelength properties of the gamma-ray source PMN J1603-4904. *A&A*, 562:A4, Feb. 2014.

[219] M. Murgia. Spectral Ages of CSOs and CSS Sources. *"Publications of the Astronomical Society of Australia"*, 20:19–24, 2003.

[220] S. T. Myers, N. J. Jackson, I. W. A. Browne, A. G. de Bruyn, T. J. Pearson, A. C. S. Readhead, P. N. Wilkinson, A. D. Biggs, R. D. Blandford, C. D. Fassnacht, L. V. E. Koopmans, D. R. Marlow, J. P. McKean, M. A. Norbury, P. M. Phillips, D. Rusin, M. C. Shepherd, and C. M. Sykes. The Cosmic Lens All-Sky Survey - I. Source selection and observations. *MNRAS*, 341:1–12, May 2003.

[221] A. Neronov, D. Semikoz, and I. Vovk. High Galactic latitude Fermi sources of γ-rays with energies above 100 GeV. *A&A*, 529:A59, May 2011.

[222] J. Neyman and E. Pearson. On the use and interpretation of certain test criteria. *Biometrika*, 20A:128, 1928.

[223] E. Nieppola, M. Tornikoski, and E. Valtaoja. Spectral energy distributions of a large sample of BL Lacertae objects. *A&A*, 445:441–450, Jan. 2006.

[224] E. Nieppola, E. Valtaoja, M. Tornikoski, T. Hovatta, and M. Kotiranta. Blazar sequence - an artefact of Doppler boosting. *A&A*, 488:867–872, Sept. 2008.

[225] P. L. Nolan, A. A. Abdo, M. Ackermann, M. Ajello, A. Allafort, E. Antolini, W. B. Atwood, M. Axelsson, L. Baldini, J. Ballet, and et al. Fermi Large Area Telescope Second Source Catalog. *ApJS*, 199:31, Apr. 2012.

[226] L. Observatory, H. Curtis, W. Campbell, J. Moore, R. Wilson, and W. Wright. *Studies of the Nebulae: Made at the Lick Observatory, University of California, at Mount Hamilton, California, and Santiago, Chile.* Number v. 13 in Publications. University of California Press, 1918.

[227] C. P. O'Dea. The Compact Steep-Spectrum and Gigahertz Peaked-Spectrum Radio Sources. *PASP*, 110:493–532, May 1998.

[228] C. P. O'Dea and S. A. Baum. Constraints on Radio Source Evolution from the Compact Steep Spectrum and GHz Peaked Spectrum Radio Sources. *AJ*, 113:148–161, Jan. 1997.

[229] M. Orienti and D. Dallacasa. Are young radio sources in equipartition? *A&A*, 487:885–894, Sept. 2008.

[230] M. Orienti and D. Dallacasa. Physical properties of young radio sources: VLBA observations of high-frequency peaking radio sources. *MNRAS*, 438:463–475, Feb. 2014.

[231] M. R. Orr, F. Krennrich, and E. Dwek. Strong New Constraints on the Extragalactic Background Light in the Near- to Mid-infrared. *ApJ*, 733:77, June 2011.

[232] L. Ostorero, R. Moderski, Ł. Stawarz, A. Diaferio, I. Kowalska, C. C. Cheung, J. Kataoka, M. C. Begelman, and S. J. Wagner. X-ray-emitting GHz-peaked-spectrum Galaxies: Testing a Dynamical-Radiative Model with Broadband Spectra. *ApJ*, 715:1071–1093, June 2010.

[233] F. N. Owen, J. A. Eilek, and N. E. Kassim. M87 at 90 Centimeters: A Different Picture. *ApJ*, 543:611–619, Nov. 2000.

[234] I. Owsianik and J. E. Conway. First detection of hotspot advance in a Compact Symmetric Object. Evidence for a class of very young extragalactic radio sources. *A&A*, 337:69–79, Sept. 1998.

[235] P. Padovani and P. Giommi. The connection between x-ray- and radio-selected BL Lacertae objects. *ApJ*, 444:567–581, May 1995.

[236] A. B. Peck, G. B. Taylor, and J. E. Conway. Obscuration of the Parsec-Scale Jets in the Compact Symmetric Object 1946+708. *ApJ*, 521:103–111, Aug. 1999.

[237] R. A. Perley, J. W. Dreher, and J. J. Cowan. The jet and filaments in Cygnus A. *ApJ*, 285:L35–L38, Oct. 1984.

[238] E. S. Perlman, W. B. Sparks, J. Radomski, C. Packham, R. S. Fisher, R. Piña, and J. A. Biretta. Deep 10 Micron Imaging of M87. *ApJ*, 561:L51–L54, Nov. 2001.

[239] E. S. Perlman and A. S. Wilson. The X-Ray Emissions from the M87 Jet: Diagnostics and Physical Interpretation. *ApJ*, 627:140–155, July 2005.

[240] M. Perucho and J. M. Martí. Physical Parameters in the Hot Spots and Jets of Compact Symmetric Objects. *ApJ*, 568:639–650, Apr. 2002.

[241] B. M. Peterson. *An Introduction to Active Galactic Nuclei*. Cambridge University Press, 1997.

[242] R. B. Phillips and R. L. Mutel. On symmetric structure in compact radio sources. *A&A*, 106:21–24, Feb. 1982.

[243] R. W. Pogge. Narrow-line Seyfert 1s: 15 years later. *"New Astronomy Reviews"*, 44:381–385, Sept. 2000.

[244] A. G. Polatidis and J. E. Conway. Proper Motions in Compact Symmetric Objects. *"Publications of the Astronomical Society of Australia"*, 20:69–74, 2003.

[245] A. G. Polatidis, P. N. Wilkinson, W. Xu, A. C. S. Readhead, T. J. Pearson, G. B. Taylor, and R. C. Vermeulen. The First Caltech–Jodrell Bank VLBI Survey. I. lambda = 18 Centimeter Observations of 87 Sources. *ApJS*, 98:1, May 1995.

[246] E. Pons and M. G. Watson. A new sample of X-ray selected narrow emission-line galaxies. I. The nature of optically elusive AGN. *A&A*, 568:A108, Aug. 2014.

[247] J. R. Primack, J. S. Bullock, and R. S. Somerville. Observational Gamma-ray Cosmology. In F. A. Aharonian, H. J. Völk, and D. Horns, editors, *High Energy Gamma-Ray Astronomy*, volume 745 of *American Institute of Physics Conference Series*, pages 23–33, Feb. 2005.

[248] R. J. Protheroe and P. L. Biermann. A new estimate of the extragalactic radio background and implications for ultra-high-energy γ-ray propagation. *Astroparticle Physics*, 6:45–54, Dec. 1996.

[249] A. C. S. Readhead, G. B. Taylor, W. Xu, T. J. Pearson, P. N. Wilkinson, and A. G. Polatidis. The Statistics and Ages of Compact Symmetric Objects. *ApJ*, 460:612, Apr. 1996.

[250] W. Reich, P. Reich, M. Pohl, R. Kothes, and R. Schlickeiser. Flux density monitoring of radio sources with detected or supposed gamma-ray emission. *A&AS*, 131:11–16, July 1998.

[251] A. Reid, D. L. Shone, C. E. Akujor, I. W. A. Browne, D. W. Murphy, J. Pedelty, L. Rudnick, and D. Walsh. High resolution radio maps of quasars from the Jodrell Bank 966MHz survey. *A&AS*, 110:213, Apr. 1995.

[252] A. Reimer, R. J. Protheroe, and A.-C. Donea. M 87 as a misaligned synchrotron-proton blazar. *A&A*, 419:89–98, May 2004.

[253] O. Reimer, M. Pohl, P. Sreekumar, and J. R. Mattox. EGRET Upper Limits on the High-Energy Gamma-Ray Emission of Galaxy Clusters. *ApJ*, 588:155–164, May 2003.

[254] L. C. Reyes. *Detecting the EBL attenuation of blazars with GLAST*. PhD thesis, University of Maryland, College Park, 2007.

[255] C. S. Reynolds and M. C. Begelman. Intermittant Radio Galaxies and Source Statistics. *ApJ*, 487:L135–L138, Oct. 1997.

[256] C. S. Reynolds, T. Di Matteo, A. C. Fabian, U. Hwang, and C. R. Canizares. The 'quiescent' black hole in M87. *MNRAS*, 283:L111–L116, Dec. 1996.

[257] G. H. Rieke and M. J. Lebofsky. The interstellar extinction law from 1 to 13 microns. *ApJ*, 288:618–621, Jan. 1985.

[258] P. W. A. Roming, T. E. Kennedy, K. O. Mason, J. A. Nousek, L. Ahr, R. E. Bingham, P. S. Broos, M. J. Carter, B. K. Hancock, H. E. Huckle, S. D. Hunsberger, H. Kawakami, R. Killough, T. S. Koch, M. K. McLelland, K. Smith, P. J. Smith, J. C. Soto, P. T. Boyd, A. A. Breeveld, S. T. Holland, M. Ivanushkina, M. S. Pryzby, M. D. Still, and J. Stock. The Swift Ultra-Violet/Optical Telescope. *Space Sci. Rev.*, 120:95–142, Oct. 2005.

[259] A. Rossetti, F. Mantovani, D. Dallacasa, C. Fanti, and R. Fanti. Multi-frequency VLBA observations of compact sources from the Peacock and Wall catalogue. *A&A*, 434:449–458, May 2005.

[260] J. J. Russell. LAT Global Trigger Conceptual Design. *LAT-SS-286*, pages 1–14, June 2001.

[261] G. B. Rybicki and A. P. Lightman. *Radiative Processes in Astrophysics*. Wiley-VCH Verlag GmbH, 2007.

[262] M. H. Salamon and F. W. Stecker. Absorption of High-Energy Gamma Rays by Interactions with Extragalactic Starlight Photons at High Redshifts and the High-Energy Gamma-Ray Background. *ApJ*, 493:547–554, Jan. 1998.

[263] D. J. Schlegel, D. P. Finkbeiner, and M. Davis. Maps of Dust Infrared Emission for Use in Estimation of Reddening and Cosmic Microwave Background Radiation Foregrounds. *ApJ*, 500:525–553, June 1998.

[264] D. P. Schneider, P. B. Hall, G. T. Richards, M. A. Strauss, D. E. Vanden Berk, S. F. Anderson, W. N. Brandt, X. Fan, S. Jester, J. Gray, J. E. Gunn, M. U. SubbaRao, A. R. Thakar, C. Stoughton, A. S. Szalay, B. Yanny, D. G. York, N. A. Bahcall, J. Barentine, M. R. Blanton, H. Brewington, J. Brinkmann, R. J. Brunner, F. J. Castander, I. Csabai, J. A. Frieman, M. Fukugita, M. Harvanek, D. W. Hogg, Ž. Ivezić, S. M. Kent, S. J. Kleinman, G. R. Knapp, R. G. Kron, J. Krzesiński, D. C. Long, R. H. Lupton, A. Nitta, J. R. Pier, D. H. Saxe, Y. Shen, S. A. Snedden, D. H. Weinberg, and J. Wu. The Sloan Digital Sky Survey Quasar Catalog. IV. Fifth Data Release. *AJ*, 134:102–117, July 2007.

[265] F. Schweizer. An optical study of the giant radio galaxy NGC 1316 /Fornax A/. *ApJ*, 237:303–318, Apr. 1980.

[266] G. A. Seielstad, T. J. Pearson, and A. C. S. Readhead. 10.8-GHz flux density variations among a complete sample of sources from the NRAO-Bonn 84 survey. *PASP*, 95:842–872, Nov. 1983.

[267] H. Seta, M. S. Tashiro, and S. Inoue. Suzaku Detection of Thermal X-Ray Emission Associated with the Western Radio Lobe of Fornax A. *PASJ*, 65:106, Oct. 2013.

[268] E. J. Shaya, D. M. Dowling, D. G. Currie, S. M. Faber, E. A. Ajhar, T. R. Lauer, E. J. Groth, C. J. Grillmair, R. Lynd, and E. J. O'Neil, Jr. Hubble Space Telescope Planetary Camera Images of NGC 1316 (Fornax A). *AJ*, 111:2212, June 1996.

[269] Y. Shi, G. H. Rieke, D. C. Hines, K. D. Gordon, and E. Egami. Thermal and Nonthermal Infrared Emission from M87. *ApJ*, 655:781–789, Feb. 2007.

[270] A. Siemiginowska. X-ray emission from GPS and CSS sources. *Astronomische Nachrichten*, 330:264–269, Feb. 2009.

[271] A. Siemiginowska, C. C. Cheung, S. LaMassa, D. J. Burke, T. L. Aldcroft, J. Bechtold, M. Elvis, and D. M. Worrall. X-Ray Cluster Associated with the z = 1.063 CSS Quasar 3C 186: The Jet is Not Frustrated. *ApJ*, 632:110–121, Oct. 2005.

[272] A. Siemiginowska, S. LaMassa, T. L. Aldcroft, J. Bechtold, and M. Elvis. X-Ray Properties of the Gigahertz Peaked and Compact Steep Spectrum Sources. *ApJ*, 684:811–821, Sept. 2008.

[273] A. Siemiginowska, Ł. Stawarz, C. C. Cheung, D. E. Harris, M. Sikora, T. L. Aldcroft, and J. Bechtold. The 300 kpc Long X-Ray Jet in PKS 1127-145, z = 1.18 Quasar: Constraining X-Ray Emission Models. *ApJ*, 657:145–158, Mar. 2007.

[274] M. Sikora, M. C. Begelman, and M. J. Rees. Comptonization of diffuse ambient radiation by a relativistic jet: The source of gamma rays from blazars? *ApJ*, 421:153–162, Jan. 1994.

[275] M. Sikora, R. Moderski, and G. M. Madejski. 3C 454.3 Reveals the Structure and Physics of Its "Blazar Zone". *ApJ*, 675:71–78, Mar. 2008.

[276] I. A. G. Snellen, R. T. Schilizzi, G. K. Miley, A. G. de Bruyn, M. N. Bremer, and H. J. A. Röttgering. On the evolution of young radio-loud AGN. *MNRAS*, 319:445–456, Dec. 2000.

[277] T. Soler and B. H. W. Gelder. On covariances of eigenvalues and eigenvectors of second-rank symmetric tensors. *Geophysical Journal International*, 105:537–546, May 1991.

[278] W. B. Sparks, J. A. Biretta, and F. Macchetto. The Jet of M87 at Tenth-Arcsecond Resolution: Optical, Ultraviolet, and Radio Observations. *ApJ*, 473:254, Dec. 1996.

[279] T. Stanev and A. Franceschini. Constraints on the Extragalactic Infrared Background from Gamma-Ray Observations of Markarian 501. *ApJ*, 494:L159–L162, Feb. 1998.

[280] Ł. Stawarz, F. Aharonian, J. Kataoka, M. Ostrowski, A. Siemiginowska, and M. Sikora. Dynamics and high-energy emission of the flaring HST-1 knot in the M 87 jet. *MNRAS*, 370:981–992, Aug. 2006.

[281] Ł. Stawarz, L. Ostorero, M. C. Begelman, R. Moderski, J. Kataoka, and S. Wagner. Evolution of and High-Energy Emission from GHz-Peaked Spectrum Sources. *ApJ*, 680:911–925, June 2008.

[282] Ł. Stawarz, A. Siemiginowska, M. Ostrowski, and M. Sikora. On the Magnetic Field in the Kiloparsec-Scale Jet of Radio Galaxy M87. *ApJ*, 626:120–127, June 2005.

[283] F. W. Stecker, M. G. Baring, and E. J. Summerlin. Blazar γ-Rays, Shock Acceleration, and the Extragalactic Background Light. *ApJ*, 667:L29–L32, Sept. 2007.

[284] F. W. Stecker and O. C. de Jager. New Upper Limits on Intergalactic Infrared Radiation from High-Energy Astrophysics. *ApJ*, 415:L71, Oct. 1993.

[285] F. W. Stecker, M. A. Malkan, and S. T. Scully. Intergalactic Photon Spectra from the Far-IR to the UV Lyman Limit for 0 ¡ z ¡ 6 and the Optical Depth of the Universe to High-Energy Gamma Rays. *ApJ*, 648:774–783, Sept. 2006.

[286] A. Strandlie and R. Frühwirth. Track and vertex reconstruction: From classical to adaptive methods. *Rev. Mod. Phys.*, 82:1419–1458, May 2010.

[287] M. Stritzinger, C. R. Burns, M. M. Phillips, G. Folatelli, K. Krisciunas, S. Kattner, S. E. Persson, L. Boldt, A. Campillay, C. Contreras, W. Krzeminski, N. Morrell, F. Salgado, W. L. Freedman, M. Hamuy, B. F. Madore, M. Roth, and N. B. Suntzeff. The Distance to NGC 1316 (Fornax A) from Observations of Four Type Ia Supernovae. *AJ*, 140:2036–2051, Dec. 2010.

[288] A. W. Strong. Data analysis in gamma-ray astronomy - Multivariate likelihood method for correlation studies. *A&A*, 150:273–275, Sept. 1985.

[289] A. W. Strong, I. V. Moskalenko, and O. Reimer. Diffuse Galactic Continuum Gamma Rays: A Model Compatible with EGRET Data and Cosmic-Ray Measurements. *ApJ*, 613:962–976, Oct. 2004.

[290] B. N. Swanenburg, K. Bennett, G. F. Bignami, R. Buccheri, P. Caraveo, W. Hermsen, G. Kanbach, G. G. Lichti, J. L. Masnou, H. A. Mayer-Hasselwander, J. A. Paul, B. Sacco, L. Scarsi, and R. D. Wills. Second COS B catalog of high-energy gamma-ray sources. *ApJ*, 243:L69–L73, Jan. 1981.

[291] J. C. Tan, H. Beuther, F. Walter, and E. G. Blackman. A Search for Molecular Gas in the Nucleus of M87 and Implications for the Fueling of Supermassive Black Holes. *ApJ*, 689:775–781, Dec. 2008.

[292] Y. T. Tanaka, Ł. Stawarz, D. J. Thompson, F. D'Ammando, S. J. Fegan, B. Lott, D. L. Wood, C. C. Cheung, J. Finke, S. Buson, L. Escande, S. Saito, M. Ohno, T. Takahashi, D. Donato, J. Chiang, M. Giroletti, F. K. Schinzel, G. Iafrate, F. Longo, and S. Ciprini. Fermi Large Area Telescope Detection of Bright γ-Ray Outbursts from the Peculiar Quasar 4C +21.35. *ApJ*, 733:19, May 2011.

[293] M. S. Tashiro, N. Isobe, H. Seta, K. Matsuta, and Y. Yaji. Hard X-Ray Spectrum from West Lobe of Radio Galaxy Fornax A Observed with Suzaku. *PASJ*, 61:327, Jan. 2009.

[294] F. Tavecchio and G. Ghisellini. Spine-sheath layer radiative interplay in subparsec-scale jets and the TeV emission from M87. *MNRAS*, 385:L98–L102, Mar. 2008.

[295] F. Tavecchio, L. Maraschi, A. Wolter, C. C. Cheung, R. M. Sambruna, and C. M. Urry. Chandra and Hubble Space Telescope Observations of Gamma-Ray Blazars: Comparing Jet Emission at Small and Large Scales. *ApJ*, 662:900–908, June 2007.

[296] G. B. Taylor, S. E. Healey, J. F. Helmboldt, S. Tremblay, C. D. Fassnacht, R. C. Walker, L. O. Sjouwerman, T. J. Pearson, A. C. S. Readhead, L. Weintraub, N. Gehrels, R. W. Romani, P. F. Michelson, R. D. Blandford, and G. Cotter. Characteristics of EGRET Blazars in the VLBA Imaging and Polarimetry Survey (VIPS). *ApJ*, 671:1355–1364, Dec. 2007.

[297] G. B. Taylor, A. C. S. Readhead, and T. J. Pearson. Pinpointing the Center of Activity in Compact Symmetric Objects. I. Sources from the Pearson-Readhead Survey. *ApJ*, 463:95, May 1996.

[298] H. Teraesranta, M. Tornikoski, A. Mujunen, K. Karlamaa, T. Valtonen, N. Henelius, S. Urpo, M. Lainela, T. Pursimo, K. Nilsson, S. Wiren, A. Laehteenmaeki, M. Korpi, R. Rekola, P. Heinaemaeki, M. Hanski, P. Nurmi, K. Kokkonen, P. Keinaenen, O. Joutsamo, J. Oksanen, H. Pietilae, E. Valtaoja, M. Valtonen, and P. Koenoenen. Fifteen years monitoring of extragalactic radio sources at 22, 37 and 87 GHz. *A&AS*, 132:305–331, Nov. 1998.

[299] H. Teräsranta, J. Achren, M. Hanski, J. Heikkilä, J. Holopainen, O. Joutsamo, M. Juhola, K. Karlamaa, S. Katajainen, P. Keinänen, P. Koivisto, M. Koskimies, P. Könönen, M. Lainela, A. Lähtenmäki, K. Mäkinen, T. Niemelä, P. Nurmi, T. Pursimo, R. Rekola, T. Savolainen, M. Tornikoski, J. Torppa, T. Valtonen, N. Varjonen, E. Vilenius, J. Virtanen, and S. Wiren. Twenty years monitoring of extragalactic sources at 22, 37 and 87 GHz. *A&A*, 427:769–771, Nov. 2004.

[300] H. Teräsranta, S. Wiren, P. Koivisto, V. Saarinen, and T. Hovatta. 24 year monitoring of extragalactic sources at 22 and 37 GHz. *A&A*, 440:409–410, Sept. 2005.

[301] D. J. Thompson, D. L. Bertsch, C. E. Fichtel, R. C. Hartman, R. Hofstadter, E. B. Hughes, S. D. Hunter, B. W. Hughlock, G. Kanbach, D. A. Kniffen, Y. C. Lin, J. R. Mattox, H. A. Mayer-Hasselwander, C. von Montigny, P. L. Nolan, H. I. Nel, K. Pinkau, H. Rothermel, E. J. Schneid, M. Sommer, P. Sreekumar, D. Tieger, and A. H. Walker. Calibration of the Energetic Gamma-Ray Experiment Telescope (EGRET) for the Compton Gamma-Ray Observatory. *ApJS*, 86:629–656, June 1993.

[302] J. L. Tonry. Surface brightness fluctuations - A bridge from M31 to the Hubble constant. *ApJ*, 373:L1–L4, May 1991.

[303] I. Torniainen, M. Tornikoski, A. Lähteenmäki, M. F. Aller, H. D. Aller, and M. G. Mingaliev. Radio continuum spectra of gigahertz-peaked spectrum galaxies. *A&A*, 469:451–457, July 2007.

[304] J. R. Trump, C. D. Impey, Y. Taniguchi, M. Brusa, F. Civano, M. Elvis, J. M. Gabor, K. Jahnke, B. C. Kelly, A. M. Koekemoer, T. Nagao, M. Salvato, Y. Shioya, P. Capak, J. P. Huchra, J. S. Kartaltepe, G. Lanzuisi, P. J. McCarthy, V. Maineri, and N. Z. Scoville. The Nature of Optically Dull Active Galactic Nuclei in COSMOS. *ApJ*, 706:797–809, Nov. 2009.

[305] C. M. Urry and P. Padovani. Unified Schemes for Radio-Loud Active Galactic Nuclei. *PASP*, 107:803, Sept. 1995.

[306] W. van Breugel, G. Miley, and T. Heckman. Studies of kiloparsec-scale, steep-spectrum radio cores. I VLA maps. *AJ*, 89:5–22, Jan. 1984.

[307] V. V. Vassiliev. Extragalactic background light absorption signal in the TeV γ-ray spectra of blazars. *Astroparticle Physics*, 12:217–238, Jan. 2000.

[308] M.-P. Véron-Cetty and P. Véron. A catalogue of quasars and active nuclei: 12th edition. *A&A*, 455:773–777, Aug. 2006.

[309] S. J. Wagner, B. Behera, and H.E.S.S. Collaboration. Hess Observations Of Quasars. In *AAS/High Energy Astrophysics Division #11*, volume 42 of *Bulletin of the American Astronomical Society*, page 660, Feb. 2010.

[310] J. F. C. Wardle, A. H. Bridle, and M. J. L. Kesteven. Variability of extragalactic sources at 2.7 GHz. IV Evidence for weak extended emission and for rapid variability. *AJ*, 86:848–853, June 1981.

[311] E. W. Weisstein. Cubic formula. `http://mathworld.wolfram.com/CubicFormula.html`.

[312] S. Wilkes. The large-sample distribution of the likelihood ratio for testing composite hypotheses. *Ann. Math. Stat.*, 150:273, 1938.

[313] P. N. Wilkinson, A. G. Polatidis, A. C. S. Readhead, W. Xu, and T. J. Pearson. Two-sided ejection in powerful radio sources: The compact symmetric objects. *ApJ*, 432:L87–L90, Sept. 1994.

[314] B. J. Wills, K. L. Thompson, M. Han, H. Netzer, D. Wills, J. A. Baldwin, G. J. Ferland, I. W. A. Browne, and M. S. Brotherton. Hubble Space Telescope Sample of Radio-loud Quasars: Ultraviolet Spectra of the First 31 Quasars. *ApJ*, 447:139, July 1995.

[315] E. L. Wright, X. Chen, N. Odegard, C. L. Bennett, R. S. Hill, G. Hinshaw, N. Jarosik, E. Komatsu, M. R. Nolta, L. Page, D. N. Spergel, J. L. Weiland, E. Wollack, J. Dunkley, B. Gold, M. Halpern, A. Kogut, D. Larson, M. Limon, S. S. Meyer, and G. S. Tucker. Five-Year Wilkinson Microwave Anisotropy Probe Observations: Source Catalog. *ApJS*, 180:283–295, Feb. 2009.

[316] W. Xu. PhD thesis, California Institute of Technology, 1994.